



HAL
open science

New material for energy : oxynitride thin films for photoelectrodes

Anyssa Derj

► **To cite this version:**

Anyssa Derj. New material for energy : oxynitride thin films for photoelectrodes. Condensed Matter [cond-mat]. Université Paris-Saclay, 2023. English. NNT : 2023UPASP130 . tel-04672743

HAL Id: tel-04672743

<https://theses.hal.science/tel-04672743v1>

Submitted on 19 Aug 2024

HAL is a multi-disciplinary open access archive for the deposit and dissemination of scientific research documents, whether they are published or not. The documents may come from teaching and research institutions in France or abroad, or from public or private research centers.

L'archive ouverte pluridisciplinaire **HAL**, est destinée au dépôt et à la diffusion de documents scientifiques de niveau recherche, publiés ou non, émanant des établissements d'enseignement et de recherche français ou étrangers, des laboratoires publics ou privés.

*New material for energy:
Oxynitride thin films for photoelectrodes*

*Nouveaux matériaux pour l'énergie :
Des couches minces d'oxynitrides pour photoélectrodes*

Thèse de doctorat de l'université Paris-Saclay

École doctorale n° 564 - Physique en Ile de France (PIF)

Spécialité de doctorat : Physique

Graduate school : Physique

Référent : Faculté des Sciences d'Orsay

Thèse préparée au **Service de Physique de l'Etat Condensé** (Université Paris-Saclay, CEA, CNRS), sous la direction d'**Antoine BARBIER**, Directeur de recherche CEA, et le co-encadrement d'**Hélène MAGNAN**, Ingénieure-chercheuse CEA

Thèse soutenue à Paris-Saclay, le 20 octobre 2023, par

Anyssa Leila DERJ

Composition du Jury

Membres du jury avec voix délibérative

Bruno DOMENICHINI Professeur, Université de Bourgogne	Président & Rapporteur
José PENUELAS Maître de conférences, HDR, École Centrale de Lyon	Rapporteur & Examineur
Marie D'ANGELO Maître de conférences, Sorbonne Université	Examinatrice
Valérie KELLER Directrice de recherches, Université de Strasbourg	Examinatrice

Titre : Nouveaux matériaux pour l'énergie : Des couches minces d'oxynitrides pour photoélectrodes

Mots clés : Oxynitrides, photoélectrodes, couches minces

Résumé : Le fractionnement photoélectrochimique de l'eau à l'aide de semi-conducteurs est une solution prometteuse à la course aux ressources alternatives d'énergie renouvelable. Ce processus exploite l'énergie solaire abondante pour fractionner les molécules d'eau et générer de l'hydrogène comme vecteur d'énergie propre, exempt de émissions de dioxyde de carbone lors de son utilisation.

Cependant, les oxydes conventionnels utilisés en tant que photoanodes sont confrontés à une capacité d'absorption limitée des photons solaires et à une mauvaise séparation des charges, qui entravent leur efficacité de conversion. Pour surmonter ces limitations, nous proposons l'utilisation d'oxynitrides pour la photoélectrolyse de l'eau. En théorie, ces oxynitrides présentent une meilleure absorption de la lumière visible et des positions de bord de bande de conduction/valence adéquates par rapport aux niveaux redox de l'eau. Expérimentalement, ces composés présentent toutefois, souvent de mauvaises activités photochimiques attribuées à notamment, des concentrations élevées de défauts.

Afin de pallier les inconvénients des méthodes de chimie du solide impliquant la nitruration à haute température de poudres d'oxydes, dans cette thèse, les films minces épitaxiés sont préparés sous ultra-vide, en utilisant l'épitaxie par jet moléculaire assistée par une source plasma hybride d'azote atomique/ionique pour fournir l'azote nécessaire à la croissance des films épitaxiés dopés N.

Plus précisément, nous étudions l'influence du dopage sur la structure cristalline, électronique et les propriétés des photoanodes pour la photoélectrolyse de l'eau.

Nous avons étudié dans un premier temps, des films déposés sur un substrat d'oxyde en utilisant uniquement un plasma atomique d'azote. Le substrat d'oxyde permet en l'occurrence, de fournir l'oxygène nécessaire à la croissance des films épitaxiés de BaTiO_3 dopés N (~3.8 at% par rapport à Ti). Une étude comparative avec des films non dopés de BaTiO_3 d'une épaisseur identique fabriqués à l'aide d'un plasma d'oxygène atomique suggère que le dopage en azote est auto-limitant en raison de l'incorporation de lacunes d'oxygène, assurant ainsi la neutralité de charge. Malgré, des niveaux de dopage faible, la structure électronique du matériau subit des modifications améliorant l'absorption du spectre lumineux.

De plus, pour obtenir une structure de réseau plus stable pour les réactions d'oxydation de l'eau, ce travail présente également des résultats préliminaires concernant le co-dopage de BaTiO_3 à l'aide d'atome de tantale. Même en l'absence de cristallinité du $\text{BaTa}_x\text{Ti}_{1-x}\text{O}_{3-x}\text{N}_x$, la présence de Ta a permis de multiplier par deux le taux de dopage en azote levant ainsi, les conditions limitantes qui affectaient l'incorporation de N dans le matériau.

Dans un second temps, sur un substrat non oxyde, de platine, en utilisant à la fois un plasma d'oxygène atomique et un plasma hybride d'azote, nous avons pu montrer qu'en faisant varier le taux d'ions d'azote ainsi que la température du substrat, nous pouvions élaborer des films minces épitaxiés de TiO_2 dopés N de structures cristallographiques différentes. De plus, la réduction de Ti^{4+} en Ti^{3+} , conduit à la formation d'états de défauts peu profonds qui peuvent piéger les trous et permettre une meilleure séparation de charges. La photoanode de meilleure efficacité a été obtenue pour un film de structure quasi-rutile contenant 9 % de Ti^{3+} avec un photocourant deux fois plus important que celui du TiO_2 rutile non dopé. Cependant, dès lors que la surface est réoxydée, par exemple, par un traitement au plasma d'oxygène, la surface adopte un comportement similaire à celle du TiO_2 entraînant ainsi un photocourant différent sans toutefois modifier les propriétés de volume.

En somme, l'objectif de cette thèse était d'examiner ces matériaux en étudiant un paramètre à la fois, ce qui la distingue des études traditionnelles en chimie du solide qui traitent de multiples paramètres simultanément.

Title : New material for energy: Oxynitride thin films for photoelectrodes

Keywords : Oxynitrides, photoelectrodes, thin films

Abstract : Photoelectrochemical water splitting using semiconductors has emerged as a promising solution in the search for alternative green and renewable energy sources. This process harnesses abundant solar energy to split water molecules and generate hydrogen as a clean energy vector, producing when used, energy free from carbon dioxide emissions.

Conventional oxides used as photoanodes face challenges such as limited absorption of solar photons and poor charge separation, which hinder their conversion efficiency. To overcome these limitations, we propose the use of oxynitrides for solar water splitting. In theory, these oxynitrides exhibit strong sensitivity to visible light and suitable conduction/valence band edge positions with respect to water redox levels. However, these compounds experimentally, often exhibit poor photochemical activities attributed to high defect concentrations.

In order to avoid the drawbacks of traditional solid-state chemistry methods involving the high-temperature nitriding of oxide powders, in this thesis, epitaxial thin films are prepared under ultra-high vacuum, using molecular beam epitaxy assisted by a hybrid atomic/ionic nitrogen plasma source to provide the nitrogen necessary for the growth of N-doped epitaxial films.

More precisely, we study the influence of N doping on the crystal structure, the electronic structure and the photoanode properties for photoelectrolysis.

First, we studied films deposited on an oxide substrate using only nitrogen atomic plasma. The oxide substrate allowing in this case to provide the oxygen necessary for the growth of N doped BaTiO_3 epitaxial films (~3.8at% versus Ti). A comparative study with undoped BaTiO_3 films of identical thickness fabricated using an atomic oxygen plasma suggests that nitrogen doping is self-limiting due to the incorporation of oxygen vacancies, thereby ensuring charge neutrality.

Even modest doping levels lead to modifications in the material electronic structure, enhancing the visible light absorption.

To address the challenges of achieving a more stable lattice structure for solar water splitting reactions, the presented work also investigates preliminary results on the co-doping of BaTiO_3 through tantalum incorporation. Even in the absence of $\text{BaTa}_x\text{Ti}_{1-x}\text{O}_{3-x}\text{N}_x$ crystallinity, the presence of Ta allowed the reduction of Ti^{4+} to Ti^{3+} , the creation of oxygen vacancies and a level of nitrogen doping twice as high compared to the previous conditions. These changes removed the limiting conditions that affected the incorporation of nitrogen into the material.

In a second step, we studied films deposited on a non-oxide substrate (Platinum) using both an atomic oxygen plasma source as well as a hybrid nitrogen plasma source. We demonstrated that by varying the rate of nitrogen ions and the temperature of the substrate, one obtained epitaxial thin films of N-doped TiO_2 with different crystallographic structures. Moreover, the reduction of Ti^{4+} to Ti^{3+} , leads to the formation of shallow defect states that can trap holes and allow better charge separation. The most efficient photoanode was a film of quasi-rutile structure containing 9% Ti^{3+} with a photocurrent twice as high as the undoped rutile TiO_2 . However, once the surface is reoxidized, for example by oxygen plasma treatment, the surface starts to behave more like TiO_2 , leading to a different photocurrent without any change in the volume properties.

In summary, the objective of this thesis was to examine materials by studying one parameter at a time, which sets it apart from traditional solid-state chemistry studies that deal with multiple parameters simultaneously.

Acknowledgements:

Writing this thesis has been an arduous yet fulfilling journey, and I would be remiss if I did not take a moment to express my gratitude to those who have supported me along the way.

First and foremost, I would like to express my gratitude to my co-supervisor and mentor, Hélène Magnan, as well as my thesis advisor, Antoine Barbier. I hope that our paths will cross again for the better. I extend my deepest appreciation to them, whose guidance and expertise have been invaluable throughout this entire process. Your unwavering commitment to academic excellence and your ability to challenge and inspire me have shaped this thesis into what it is today. I am truly grateful for your patience, encouragement, and the countless hours you dedicated to reviewing and providing constructive feedback.

I would like to thank Patrice Roche for welcoming me to his department, the Service de Physique de l'Etat Condensé (SPEC) and all its members, as well as Michel Viret in his laboratory, the Laboratoire de Nanomagnétisme et Oxydes (LNO).

I am also indebted to the synchrotron staff with whom I collaborated during this work, especially during the synchrotron runs at SOLEIL, Patrick Le Fèvre from the CASSIOPEE beamline, Emiliano Fonda from the SAMBA beamline, at Diffabs, Cristian Mocuta beamline and at Tempo, Mathieu Silly. Thank you, for your valuable insights and suggestions. Your expertise and critical analysis have helped me refine my ideas and deepen my understanding of the subject matter. I am grateful for the time and effort you invested in evaluating my work and for the thought-provoking discussions that have expanded my intellectual horizons.

I warmly thank the members of the jury for their remarks and clarifications regarding this manuscript and the thesis defense: the rapporteurs Bruno Domenichini and José Penuelas, as well as the examiners Marie D'angelo and Valérie Keller.

In the Oxides group, I owe a great deal to our seasoned technician Frédéric Merlet, who helped us untangle numerous problematic situations, from maintaining the Oxide MBE to digital attacks. As well as Dana Stanescu, whose experience on water photoelectrolysis provided a shoulder to lean on during challenging times.

I would like to express my heartfelt appreciation to my monitoring committee Jean-Baptiste Moussy, Patrick Le Fèvre and François Ladieu who have been a constant source of support and encouragement throughout this undertaking.

I am grateful to the secretarial staff for their assistance with administrative procedures: Corinne

Kopec-Coelho and Nathalie Royer.

Thanks to a group of young PhD students/postdocs/engineers whom I wish nothing but the best, my time at CEA was elevated to a magnificent human experience. Omar, Maikane, Gr goire, Binh, Paul and Kevin thank you for our exciting discussions and crazy adventures, which will undoubtedly be missed! ; I will remember for a long time those relaxing moments exchanging thoughts about life and beyond.

A very special thought for my office colleague Haowen, with whom I shared these three years of galley and will defend his thesis few months after me, good luck friend, stay strong and focus.

To those who have offered me kindness and compassion along the way, to my friends my family and my husband. I am forever grateful for your unwavering love, understanding, and belief in my abilities. Your unyielding support and encouragement have been my foundation, providing the strength and motivation to persevere even when faced with obstacles. Your sacrifices and enduring presence in my life have been a source of inspiration and a reminder of the importance of pursuing one's passions. My faithful patient and loving husband Pierre-jean alias Yahya, if you ever read this, know that, without realizing it, you contributed in your own way to the successful completion of this thesis, helping me relax or overcome writer's block during the writing process (at any time of day or night). Thank you very much for your love, support, assistance, and unwavering encouragement, which maximized the happiness derived from this adventure.

Big brother, Amine, you have been my role model, teaching me the values of perseverance, resilience, and dedication. Your unwavering work ethic and commitment to excellence have inspired me to give my best in every endeavor. I aspire to one day establish a family and create a warm and loving home similar to yours. Sending my affection and well wishes to my sister Yousra and my delightful and spirited niece Aya.

Finally, I sincerely want to thank my parents Aziz and Mouna who have never stopped believe in me, to support me and above all to allow me to take all these steps to get there today at the rank of Doctor in Physics. Thank you, Dad, for working so hard to offer us a comfort life full of opportunities and possibilities, which only depends on what, we would like to do with it. Dad, you have gone beyond to ensure that I had the resources needed to succeed. Thank you, Mom, being a listening ear, comforting and especially to always find solutions to all my problems even if they do not really exist. Mom, you have been my guiding light, my rock, and my biggest cheerleader. From the moment I embarked on this academic pursuit, you believed in me wholeheartedly, even during times when I

doubted my own abilities.

I hope one day to be able to give it back to you a hundredfold because without you I could not have gone very far!

I want to acknowledge the deep well of gratitude that resides within me. I am grateful for the unwavering support of my loved ones, who have stood by my side through thick and thin. Their unwavering belief in me has been a constant source of strength, and for that, I am eternally indebted. It is with great emotion that I conclude these three years of thesis within our laboratory. It has been a real pleasure for me to work with all of you. I am ready to face whatever lies ahead.

Content:

General introduction.....	26
a. Solar energy to fuel approach.....	26
b. Methods to produce a solar fuel.....	27
c. State of the art of photoelectrochemical cells.....	28
d. Photoelectrochemical systems.....	30
e. Semiconductors and photo-electrode materials.....	32
f. This thesis: Improving hydrogen production by using oxynitrides as photoelectrodes.....	34
g. References.....	38
Chapter I: Oxynitrides as a potential photoanode for solar water splitting	42
1.1 Hydrogen production from water splitting.....	42
1.1.1 Making hydrogen.....	42
1.1.2 Choosing Electrolysis.....	44
1.1.2.1 Electrolytic cell for water splitting.....	44
1.1.2.2 Types of electrolyzers for water splitting.....	45
1.1.3 Photoelectrochemical cell for solar water splitting requirements.....	45
1.1.3.1 The semiconductor.....	47
1.1.3.2 The electrolyte.....	48
1.1.3.3 Semiconductor/electrolyte interaction.....	49
1.1.3.3.1 n-type semiconductor-electrolyte junction in dark-SC (semiconductor) side.....	49
1.1.3.3.2 n-type semiconductor-electrolyte junction in dark in the electrolyte side.....	51
1.1.3.3.3 n-type semiconductor-electrolyte junction under illumination.....	52
1.2 Photoelectrodes requirements: photoanode improvements.....	52
1.2.1 Band gap.....	53
1.2.2 Band edges positions.....	54
1.2.3 Charge carriers' separation and recombination.....	57
1.2.4 Stability in aqueous media.....	57
1.3 Nitrogen doping metal oxide photoanodes for efficient photoelectrochemical water splitting.....	58
1.3.1 General improvement methods.....	59
1.3.2 Our improvement method.....	61
1.3.3 N-doping influence.....	62
1.3.4 Oxygen vacancies effect.....	64
1.3.5 Epitaxial thin film photoanodes.....	64
1.3.6 Summary.....	66
1.4 References.....	67
Chapter II: Experimental details.....	72
2.1 Epitaxy and epitaxial thin films.....	72
2.1.1 Epitaxy.....	72
2.1.1.1 Definition.....	72
2.1.1.2 Important factors for epitaxial growth.....	73

2.2 Film deposition technique of metal oxide films.....	73
2.2.1 Oxygen and Nitrogen plasma assisted molecular beam epitaxy (O&NPA-MBE).....	76
2.2.1.1 Radio frequency oxygen plasma source (RF).....	77
2.2.1.2 Electron cyclotron resonance nitrogen plasma source (ECR).....	78
2.2.2 Substrates preparation.....	81
2.2.2.1 Undoped and 1 at.% Niobium doped SrTiO ₃ (001) in film.....	81
2.2.2.2 Platinum (111).....	81
2.3 Characterization techniques <i>in situ</i> and in laboratory.....	82
2.3.1 Reflexion high energy electron diffraction (RHEED).....	82
2.3.2 X-ray Photoelectron Spectroscopy (XPS).....	86
2.3.3 Auger Spectroscopy (AES).....	88
2.3.4 X-ray Reflectivity (XRR).....	89
2.4 Photoelectrochemical characterization.....	91
2.4.1 Experimental setup.....	91
2.4.2 I-V voltammetry.....	92
2.4.3 I-λ measurement.....	94
2.4.4 Electrochemical impedance spectroscopy.....	95
2.5 Further characterization methods.....	98
2.5.1 Synchrotron X-ray Diffraction (XRD).....	98
2.5.2 Resonant Photoemission (RPE).....	99
2.5.3 X-ray absorption spectroscopy (XAS) and Extended X-ray absorption fine structure (EXAFS).....	101
2.6 References.....	105
 Chapter III: Self-oxidized single crystalline perovskite N-doped BaTiO ₃ oxynitrides.....	 109
3.1 Photoelectrochemical properties of perovskite oxides layers.....	109
3.1.1 Structure of perovskite oxides.....	109
3.1.2 BaTiO ₃ a perovskite material.....	110
3.1.3 BaTiO ₃ ferroelectric material.....	110
3.2 Growth and epitaxial single crystalline BaTiO ₃ layer on 1 at.% Nb :SrTiO ₃ (001)	112
3.2.1 Nitride Materials by Molecular Beam Epitaxy.....	112
3.2.1.2 ECR nitrogen source calibration: Atomic Nitrogen.....	113
3.2.2 Deposition of Ti+N on SrTiO ₃ (001) and 1% Nb :SrTiO ₃ (001)	114
3.2.2.1 Crystal growth of TiN: Synthesis of our first nitride.....	115
3.2.2.2 Chemical composition of Ti+N on SrTiO ₃ (001) and 1% Nb :SrTiO ₃ (001)	119
3.2.2.3 The crystal structure of Ti+N on SrTiO ₃ (001) and 1% Nb :SrTiO ₃ (001)	120
3.2.2.4 Influence of nitriding on photoelectrolysis.....	122
3.2.2.5 Conclusion on the firsts experiments on nitriding.....	124
3.3 Growth of epitaxial single crystalline film of Ba+Ti+ N on 1 at.% Nb :SrTiO ₃ (001)....	125
3.3.1 <i>In situ</i> analysis of the sample.....	125
3.3.1.1 <i>In situ</i> RHEED.....	125
3.3.1.2 <i>In situ</i> AES measurements.....	127
3.3.2 <i>Ex situ</i> investigation of the samples.....	128
3.3.2.1 <i>Ex situ</i> XPS measurements.....	128
3.3.2.2 XRD measurements.....	132
3.3.2.3 XRR measurements.....	136
3.3.2.4 Electronic structure investigation by XAS and RPES.....	137

3.3.2.4.1 XAS at the Ti-L _{2,3} edges and O-K edge	137
3.3.2.4.2 Resonant photoelectron spectroscopy on doped and undoped BaTiO ₃	140
3.3.3 Photoelectrochemical properties analysis	142
3.3.3.1 Photocurrent measurements	143
3.3.3.2 Absorption measurements	145
3.3.3.2.1 The spectral response	145
3.3.3.2.2 The photoelectrochemical gap	146
3.3.4 Discussion and conclusions	148
3.4 Stable photoanode oxynitride perovskite by lattice charge compensation: Preliminary results	149
3.4.1 Stability of oxynitrides perovskite structure	149
3.4.2 Activating BaTaO ₂ N by Ti modification for water oxidation reactions	150
3.4.3 E-Beam evaporator for charge compensation	150
3.4.3.1 Charge compensation	150
3.4.3.2 Electron beam evaporation calibration	150
3.4.4 Growth of BaTa _x Ti _{1-x} O _{3-x} N _x on 1 at.% Nb :SrTiO ₃ (001)	151
3.4.4.1 Crystallographic structure investigation	152
3.4.4.2 <i>In situ</i> electronic structure study	152
3.4.4.2.1 Chemical composition	152
3.4.4.2.2 Surface electronic environment	153
3.4.5 Solar water splitting efficiency	155
3.5 Summary	155
3.6 References	156
Chapter IV: Nitrogen incorporation into TiO ₂ epitaxial thin films	162
4.1 Properties of TiO ₂	162
4.1.1 TiO ₂ a popular semiconductor	162
4.1.2 TiO ₂ rutile phase for solar water splitting	163
4.1.3 TiO ₂ limitations and improvements for PEC water splitting	165
4.1.4 Nitrogen doped TiO ₂	166
4.2 Growth and epitaxial single crystalline TiO ₂ layer	169
4.2.1 Single-crystalline growth on Pt (111)	169
4.2.2 Nitrogen doping TiO ₂ thin films	169
4.2.2.1 Nitriding using hybrid ECR plasma Source	169
4.2.2.2 Growth conditions	171
4.3 N-doped TiO ₂ single layer on Pt (111)	172
4.3.1 Crystallographic structure investigated by <i>in situ</i> RHEED	175
4.3.2 Electronic structure analyzed by <i>ex situ</i> XPS measurements	178
4.3.3 PEC measurements	185
4.3.3.1 I-V measurements	185
4.3.3.2 The spectral response	186
4.3.3.3 The photoelectrochemical gap	188
4.3.3.4 Electrochemical impedance spectroscopy	189
4.3.4 Crystal structure: EXAFS measurements analysis	191
4.3.5 Influence of Ti ³⁺ species, oxygen vacancies and nitrogen content on the crystal structure	195

4.3.5.1 The photocurrent as a function of the N/Ti ratio and the Ti^{3+} content.....	196
4.3.5.2 The width of the depletion zone.....	198
4.3.5.3 Discussion and conclusions.....	200
4.3.6 Influence of the growth temperature: N-doped TiO_2 single layer on Pt (111).....	201
4.3.6.1 Crystalline characterization.....	201
4.3.6.2 Investigation of the right crystallographic structure: EXAFS measurement.....	203
4.3.6.3 Electronic environment.....	206
4.3.6.4 Photoelectrochemical properties.....	207
4.3.6.5 Discussion and conclusion.....	207
4.3.7 Influence of water reaction.....	208
4.3.7.1 Experimental set-up of the reactor.....	211
4.3.7.2 Model used for <i>post mortem</i> surface.....	211
4.3.7.3 Results and discussion.....	213
4.4 General summary.....	228
4.5 References.....	220
General conclusion and perspectives.....	228
Résumé étendu en français.....	231

Acronyms:

AES	Auger Spectroscopy
ALD	Atomic layer deposition
AM	Air mass
AEL	Alkaline electrolyzer
BTO	BaTiO ₃
CB	Conduction band
CBM	Conduction band minimum
CE	Counter electrode
CIS	Constant initial state
CPE	Constant phase element
DNOSC	Dye-sensitized nanostructured solar cells
DSSC	Dye sensitized solar cells
ECR	Electron cyclotron resonance nitrogen plasma source
EIS	Electrochemical impedance spectroscopy
EXAFS	Extended X-ray absorption fine structure
FWHM	Full width at half maximum
HER	Hydrogen evolution reaction
hMBE	Hybrid vapor phase MBE
IR	Infrared radiation
MBE	Molecular beam epitaxy
MOCVD	Metal-organic chemical vapor deposition
MSD	Mean square displacement
NHE	Normal hydrogen electrode
OER	Oxygen evolution reaction
O&NPA-MBE	Oxygen and Nitrogen plasma assisted molecular beam epitaxy
PEC	Photoelectrochemical cell
PEM	Polymer electrolyte membrane
PVD	Physical vapor deposition processes
PV	Photovoltaic
Pt	Platinum
QCM	Quartz crystal microbalance

RE	Reference electrode
RF	Radio frequency oxygen plasma source
RHEED	Reflexion high energy electron diffraction
RP	Resonant Photoemission
SC	Semiconductor
SCLJ	Semiconductor liquid junction
STO	SrTiO ₃
UHV	Ultra-high-vacuum
UV	Ultraviolet-visible
VB	Valence band
VBE	Valence band edge
VBM	Valence band maximum
WE	Working electrode
XAS	X-ray absorption spectroscopy
XPS	X-ray photoelectron Spectroscopy
XRD	X-ray diffraction
XRR	X-ray Resonant Reflectivity

Figures:

General introduction:

- *Figure 1: Schematic representation of the operating principle of PEC cells based on a photosynthetic cell that generates a chemical fuel through the photon driven water splitting*
- *Figure 2: At short circuit, a the energy level diagram of an n-type semiconductor photoanode and metal cathode photoelectrochemical cell (PEC), b the energy level diagram of a p-type semiconductor photocathode and metal anode regenerative PEC.*
- *Figure 3: Simplistic representation of the band diagram of; a a PEC cell system using a photoanode and a photocathode. And b a double photoelectrode PEC cell system using a photoanode, a metallic cathode, and an external bias.*
- *Figure 4: The lower edge of the conduction band (red color) and upper edge of the valence band (green color) are presented along with the band gap in electron volts. The energy scale is indicated in electron volts using either the normal hydrogen electrode (NHE) or the vacuum level as a reference at pH=0. On the right side the standard potentials of several redox couples are presented against the standard hydrogen electrode potential.*
- *Figure 5: Periodic table of the elements with data for production, price and implied value for the year 2010. The color coding (green, light-green, orange and red) corresponds to overall production level (medium to high, low, very low and extremely low, respectively). Solid color is used for elements which are chiefly main economic products of their respective ores while a diagonal gradient in color is used for elements which are mostly by-products of other elements.*
- *Figure 6: Energy diagram for the synthesis of a nitrides b oxides.*

Chapter I: Oxynitrides as a potential photoanode for solar water splitting

- *Figure 1.1: Various energy-driven water-splitting routes using thermal, electrical, biochemical, and photonic energy or their combinations.*
- *Figure 1.2: Schematic representation of the photoelectrochemical (PEC) water splitting process in a common PEC water splitting system consisting of a photoanode and a metal counterpart.*
- *Figure 1.3: Schematic band-gap representation for a intrinsic; b n-type doped and c p-type*

doped semiconductor.

- *Figure 1.4: n-type semiconductor-electrolyte interface. (left) before contact, (right) after contact. After contact, the system reaches electronic equilibrium (E_{Eq}) when the energy of the Fermi level (E_F) in the semiconductor is equivalent to the redox potential of the electrolyte (E_{Redox}). The space charge layer, which is the area where the charge distribution differs from the bulk material, has a width ω and a height ΔE . The electric field in the space layer favors the separation of charge carriers.*
- *Figure 1.5: The structure model of the n-type semiconductor/electrolyte interface under equilibrium conditions and the potential (ϕ) profile across this interface (blue line). $\Delta\phi_{sc}$, $\Delta\phi_H$, and $\Delta\phi_G$ are the potential drops in the space charge layer (I), Helmholtz layer (II), and Gouy layer (III), respectively (NB: this figure is in reverse potential of figure 1.5).*
- *Figure 1.6: Charge carriers separation in an n-type semiconductor under illumination.*
- *Figure 1.7: AM 1.5 solar spectrum in tempered zones, taking into account atmosphere absorptions (1 sun conditions with power intensity of 100 mW cm^{-2}). Zone I (II) corresponds to the part of the solar spectrum absorbed by a semiconductor having a gap of 2 eV. The energy / wavelength equivalence is given by $E = hc/\lambda$.*
- *Figure 1.8: a Conduction band (left bar) and valence band (right bar) positions vs NHE at $\text{pH}=0$ of common semiconductors used in photoelectrolysis cells. The band gap value is in parentheses, and the ordinate indicates the maximum theoretical photocurrent under Air Mass 1.5 illumination. The dotted lines indicate the thermodynamic potentials for water reduction and oxidation, respectively. Reproduced from. b Band positions of various semiconductors with respect to the redox potentials of water splitting at $\text{pH}=14$.*
- *Figure 1.9: Elements used to construct photoelectrodes for water splitting and their roles.*
- *Figure 1.10: Schematic band structure of an insulating titanium oxynitride (Ti-N-O compound). The valence band consists mainly of hybridized orbitals from N-2p and O-2p states, whereas the conduction band is dominated by empty Ti-3d orbitals. Octahedral coordination around Ti atoms splits the 3d band into lower and upper levels.*
- *Figure 1.11 Representation of narrowing the band gap of a semiconductor by doping.*
- *Figure 1.12: Schematic representation of N doping via increasing nitrification temperature and respective bandgaps and the presence of interband states related to interstitial and substitutional doping.*

Chapter II: Experimental details

- *Figure 2.1: Schematic illustration of lattice matched, strained and relaxed epitaxy.*
- *Figure 2.2: The ABO_3 perovskite family of complex oxides hosting a wide array of functional properties and electronic phases. The basic BO_6 octahedral unit is located at the center of the unit cell with A sites on the corner (top left). This simple building block enables a large configurational space for functional heterostructures of structurally similar films with diverse properties (top right).*
- *Figure 2.3: Intrinsic $SrTiO_3$ film lattice parameter reported for different growth rates using scalable oxide thin film growth techniques: Pulsed Laser Deposition (PLD), sputtering, Metal-Organic Chemical Vapor Deposition (MOCVD), Atomic Layer Deposition (ALD), Molecular Beam Epitaxy (MBE), and hybrid Molecular Beam Epitaxy (hMBE). The defect concentration δ due to nonstoichiometric growth condition was determined from the intrinsic film lattice parameter expansion.*
- *Figure 2.4: O&NPA-MBE deposition chamber : a schematic representation.*
- *Figure 2.5: Schematic drawing of the principal of the RF source.*
- *Figure 2.6: Schematic mechanism of an ECR nitrogen plasma source.*
- *Figure 2.7: Features on the ECR source used during this study*
- *Figure 2.8 : Aperture producing Hybrid mode.*
- *Figure 2.9: Classification of different electromagnetic waves.*
- *Figure 2.10: a Schematic diagram of RHEED apparatus b The simplest RHEED set up includes an electron gun, a (here a plasma clean substrate of Pt (111)), and a fluorescence screen.*
- *Figure 2.11: Different types of morphologies of single crystal surfaces; in real-space morphology (left), associated reciprocal space (middle), and corresponding RHEED patterns (right).*
- *Figure 2.12: Principle of RHEED pattern analysis in order to calculate the surface lattice parameters in the case of a the 1% Nb doped $SrTiO_3$ (001) and c $BaTiO_3$ deposited on 1% Nb doped $SrTiO_3$ (001) surfaces, with their corresponding RHEED pattern (green contrast) with blue (gray) dashed rectangles highlighting the integration box used to obtain the curves of the integrated RHEED images. b and d the surface reciprocal geometry indicating two different azimuths for each sample surface reciprocal lattice $(10)^*_s$ and $(11)^*_s$.*

- *Figure 2.13: Energy level diagram depicting the photoelectric effect. An incoming photon is absorbed such to provide a sufficient energy to an electron to overcome the binding energy (E_b). Because of the quantification of the electronic levels, the kinetic energy of the emitted electron has elemental specificity and hence allows for surface chemical identification.*
- *Figure 2.14: Simplified universal curve for the electron inelastic mean free path in elements based on the equation in the inset.*
- *Figure 2.15: Ex situ widescan XPS spectrum taken for a N-doped TiO_2 film which highlights the presence of Ti, O and C at the surface. The N ratio is too low to be seen in the wide scan.*
- *Figure 2.16: Energy level depicting the process by which an Auger electron is emitted.*
- *Figure 2.17: Auger scan for an N-doped BaTiO_3 layer deposited on 1% Nb: SrTiO_3 (001).*
- *Figure 2.18: Schematic representation of the resulting momentum transfer Q_z in XRR.*
- *Figure 2.19: Typical features of a reflectivity curve.*
- *Figure 2.20: a Photoelectrochemistry setup, and b details of the mounting within the cell.*
- *Figure 2.21: Schematic representation of the measurement system.*
- *Figure 2.22: $I(V)$ curves: $J_D(V)$ (red curve) and $J_L(V)$ (green curve) and ON/OFF chopped (blue curve).*
- *Figure 2.23: Light flux of the Xe arc lamp after the monochromator as a function of the wavelength.*
- *Figure 2.24: Electrochemical absorption as a function of the wavelength at 0.4 V vs. Ag/AgCl of TiO_2 deposited on (001) and normalized at 270 nm.*
- *Figure 2.25: Direct band gaps determined using the ‘efficient Tauc plot method’, for TiO_2 deposited on Pt (111).*
- *Figure 2.26: Photoelectrochemical cells of 3 electrodes with the working (WE), counter (CE), and reference (RE) electrodes and its equivalent RS-RCPE circuit model.*
- *Figure 2.27: Schematic illustration of Bragg's law.*
- *Figure 2.28: Schematic diagram of the Resonant phenomena when investigating the valence band in RPES: interference between the photoemission from the valence band and the Auger relaxation. E_F stands for the Fermi level of the sample.*
- *Figure 2.29: Ti-K edge absorption spectra for a TiO_2/Pt (111) film. The different remarkable regions are highlighted in red.*
- *Figure 2.30: Ti-K edge EXAFS data post-processing illustration: (a) raw absorption spectra recorded in normal incidence with glitches (black line, glitches are indicated by asterisks)*

and glitch-free (red line), (b) corresponding experimental EXAFS oscillations obtained by the Athena software (black thick line) and the fitted data by FEFF calculations assuming a rutile crystallographic structure (grey thin line) using the Artemis software. Sample: $\text{TiO}_2/\text{Pt}(111)$.

Chapter III: Self-oxidized single crystalline perovskite N-doped BaTiO_3 oxynitrides

- Figure 3.1: a Example of the representation of a perovskite crystallographic structure (SrTiO_3 used as substrate in this study) b (001) orientation of SrTiO_3 .
- Figure 3.2: Behavior of the BaTiO_3 perovskite below and above the ferroelectric ordering temperature.
- Figure 3.3 Evolution of the concentration of each species O, N, and C during nitridation of Al using the ECR source with a single hole aperture. The solid lines are guides to the eyes.
- Figure 3.4 Calibration of the **a** operating pressure and **b** the source current for nitriding.
- Figure 3.5: a the observed RHEED patterns along the $(10)_s^*$ and $(11)_s^*$ azimuths during growth for a 4 nm thick film and their corresponding integrated profiles along the streak directions, at 0 and 180 min. b The upper (resp. bottom) line shows the data for the SrTiO_3 (001) substrate (resp. $\text{Ti+N}/\text{SrTiO}_3$ (001) film). c the corresponding surface reciprocal lattice is represented, making explicit the diffraction directions, the elementary cell (in the reciprocal space) is also shown. d TiN Rocksalt structure. e Evolution of the TiN in-plane lattice parameter ($a_{//}$) derived from the $(10)_s^*$ direction RHEED pattern assuming rocksalt structure as a function of the film thickness compared with of the lattice parameter of bulk TiN (dark red), SrTiO_3 (dark bleu) and TiO_2 rutile (purple) at the deposition temperature (450 °C) (taking into account the thermal expansion).
- Figure 3.6: a The observed RHEED patterns along the $(10)_s^*$ and $(11)_s^*$ azimuths during growth for a 9 nm thick film and their corresponding integrated profiles along the streak directions, at 0 and 360 min. b The upper (resp. bottom) line shows the data for the 1%Nb: SrTiO_3 (001) substrate (resp. $\text{Ti+N}/1\%\text{Nb}:\text{SrTiO}_3$ (001) film). c The corresponding surface reciprocal lattice is represented, making explicit the diffraction directions, the elementary cell (in the reciprocal space) is also shown. d Evolution of the TiN in-plane lattice parameter ($a_{//}$) as a function of the film thickness deduced from the $(10)_s^*$ direction RHEED pattern. Dashed lines stand for the in-plane lattice parameter of bulk TiN (dark red), SrTiO_3 (dark blue) and TiO_2 (purple) at the deposition temperature (450°C) (taking into account the

- thermal expansion).*
- *Figure 3.7: In situ, AES spectra of the thin Ti+N (180min deposition) deposited on SrTiO₃ (001) and the thick Ti+N (360min deposition) deposited on 1%Nb:SrTiO₃ layers normalized at 418 eV.*
 - *Figure 3.8: X-ray photoemission spectra of thin Ti+N (180min deposition) deposited on SrTiO₃(001) for a Wide scan b Ti-2p core level, c N-1s core level and d O-1s core level.*
 - *Figure 3.9: Wide angle X-ray diffraction along specular directions for a thin TiO_xN_{1-x} (180min deposition) sample and for b thick TiO_xN_{1-x} (360min deposition) sample*
 - *Figure 3.10: a Efficient absorption photocurrent density as a function of the wavelength at 0.5 V vs. Ag/AgCl normalized at 320nm, (inset) light flux of the Xe arc lamp as a function of the wavelength, d Photocurrent density versus the applied voltage (vs. Ag/AgCl), for thick TiO_xN_{1-x} (360min deposition) (blue) and (black) thick TiO₂ (360min deposition) layers.*
 - *Figure 3.11: a RHEED patterns along (10)_s^{*} and (11)_s^{*} azimuths observed during the growth of BaTiO₃ and Ba+Ti+N on 1%Nb doped SrTiO₃. The total thickness is about 14 nm after 180 min of deposition. b growth steps. c The corresponding surface reciprocal lattice is represented, making explicit the diffraction directions, the elementary cell (in the reciprocal space) is also shown. d The corresponding integrated profiles of the RHEED patterns of Nb:SrTiO₃ plasma cleaned and BaTiO₃ and Ba+Ti+N deposited on after Nb:SrTiO₃ 180min along the streak directions. e Evolution of the Ba+Ti+N/Nb:SrTiO₃ in-plane lattice parameter (denoted by a_{//}) derived from RHEED patterns recorded during growth at a sample temperature of 450 °C. Horizontal green and gray lines indicate the SrTiO₃ and BaTiO₃ bulk cubic lattice parameters at 450 °C, thermal expansion coefficients were taken into account (ca.7.4×10⁻⁶ K⁻¹ and 1.3×10⁻⁵ K⁻¹, respectively).*
 - *Figure 3.12: Auger scans for BTO and N:BTO layers deposited on Nb:STO (350eV to 450eV and 470eV to 640eV).*
 - *Figure 3.13: a Photoemission O-1s core levels of undoped (black) and N-doped (red) BaTiO₃ layers. b Wide photoemission scans of undoped (black) and N-doped (red) BaTiO₃ layers.*
 - *Figure 3.14 : Photoemission spectra of undoped (black) and N-doped (red) BaTiO₃ layers for (a) Ti-2p, (b) N-1s core levels, (c) the valence band region, (d) Ba-3d, (e) Ba-3d_{5/2} (undoped), the green contribution corresponds to the α component and the blue one to the β component, and (f) Ba-3d_{5/2} (doped). For (e, f) symbols stand for experimental data. For (b, e, f) thin bottom lines correspond to Shirley type backgrounds and thick straight lines to best fits. The*

best-fit parameters are reported in Table 4

- *Figure 3.15: Wide angle X-ray diffraction along specular direction for N : BTO sample. (inset) In surface plane scan along the [HH0] direction across the (110) Bragg peaks of N : BTO and Nb : STO corresponding to the best fit.*
- *Figure 3.16: Scherrer plot for the N-doped BaTiO₃ layers. The measured data is represented by the solid squares and the linear fit by the red line.*
- *Figure 3.17: FWHM widths of all accessible in surface plane Bragg peaks of the N-doped BaTiO₃ layer as a function of 1/Q² (black) and best linear fit (red line).*
- *Figure 3.18: Specular reflectivity measurements (1) and best fit (–) for the N:BTO sample deposited on SrTiO₃ : 1% Nb. The inset shows the electronic density profile.*
- *Figure 3.19: a Schematic of the splitting of the 3d orbital of Ti in the TiO₆ octahedron and TiO₅ pyramid; b O-K edge XAS of c-BTO and s-BTO, with the outlined area is obtained by subtracting the intensity of s-BTO from that of c-BTO.*
- *Figure 3.20: a Ti-L_{2,3} edge with a zoom on the Ti-L₃ edge on inset and b O-K edge XAS of undoped (blue) and N-doped (red) BaTiO₃ layers. Black arrows indicate the peak intensity coming from Ti³⁺*
- *Figure 3.21: Resonant photoemission maps of VB at the Ti-L_{3,2} edge for a undoped BTO and b N-doped BTO. The inset on top is the valence band (VB) recorded at the photon energy indicated by the yellow horizontal line, the inset on the right is the Constant Initial State (CIS), i.e the resonance of electron of binding energy indicated by the vertical yellow line.*
- *Figure 3.22: the Constant Initial State (CIS) for undoped (bleu) and N-doped BTO (red).*
- *Figure 3.23: I(V) voltammetry curves, light ON (green curves), light OFF (red curves), light switched between ON and OFF (blue curves) for a a bare SrTiO₃:Nb substrate, b a BaTiO₃ overlayer and c a N doped BaTiO₃ overlayer.*
- *Figure 3.24: Photocurrent density versus the applied voltage (vs. Ag/AgCl) for undoped (blue) and N-doped (red) BaTiO₃ layers.*
- *Figure 3.25: Efficient absorption photocurrent density as a function of the wavelength at 0 V vs. Ag/AgCl, (inset) light flux of the Xe arc lamp as a function of the wavelength for undoped (blue) and N-doped (red) BaTiO₃ layers.*
- *Figure 3.26: Direct band gaps determined using the ‘efficient Tauc plot method’, for undoped (blue) and N-doped (red) BaTiO₃ layers for undoped (blue) and N-doped (red) BaTiO₃ layers.*

- *Figure 3.27: a Crystal structure and b band structure of typical d^0 -type transition metal oxynitride perovskite $ABO_{3-x}N_x$*
- *Figure 3.28: AES scans; before and after deposition of Ta on a polished and outgassed Cu substrate*
- *Figure 3.29: RHEED patterns, along $(10)_s^*$ and $(11)_s^*$ azimuths, observed during the growth of Ta-N:BTO on Nb:STO substrate.*
- *Figure 3.30: Auger spectra for Ta-N:BTO, N:BTO and a reference $BaTiO_3$ sample deposited on Nb:STO(001)*
- *Figure 3.31: Photoemission spectra of a codoped $BaTiO_3$ layer with N and Ta atoms, for a Ta-4f, b Ti-2p, c O-1s d Ba-3d and e N-1s core levels*

Chapter IV: Nitrogen incorporation into TiO_2 epitaxial thin films

- *Figure 4.1: Crystal configurations of a anatase, b rutile, and c brookite TiO_2 . The small red sphere and large grey sphere represent the O and Ti atoms, respectively.*
- *Figure 4.2: Calculated edge positions of conduction band and valence band for pure and non-metal doped anatase TiO_2 at pH=0.*
- *Figure 4.3: Nitrogen source calibration curves for $P_N = 1.10^{-6}$ mbar.*
- *Figure 4.4: Nitrogen source condition parameters.*
- *Figure 4.5: a Parameters for the synthesis of N-doped and undoped TiO_2 on Pt(111) b the corresponding RHEED patterns obtained along the $(10)_s^*$ and $(11)_s^*$ at 180 min of deposition. (i.e end of deposition)*
- *Figure 4.6: a Growth condition parameters for the synthesis of rutile $TiO_2/Pt(111)$ b RHEED pattern obtained along the $(10)_s^*$ with the corresponding integrated profiles at 0 and 180 min of r- TiO_2 , c corresponding surface reciprocal lattices for the N- TiO_2 on Pt (111) samples. On c, the transparent red, green and grey rectangles highlight the elementary unit cell for r- TiO_2 .*
- *Figure 4.7: Integrated profiles of the RHEED patterns obtained along the $(10)_s^*$ and the $(11)_s^*$ directions at 180 min for undoped (black), N-doped at I-H- K_e -O (purple), N-doped at I-L- K_e (pink), N-doped at I-H- K_e (green) and N-doped at A (blue) growth conditions of TiO_2 layers deposited on Pt(111).*
- *Figure 4.8: N1s photoemission spectra of N-doped at I-H- K_e -O (purple), N-doped at I-L- K_e (pink), N-doped at I-H- K_e (green) and N-doped at A (blue) conditions of TiO_2 layers deposited*

- on Pt(111). The red contribution corresponds to the $N_{(Ti-O-N)}$ component and the orange one to the $N_{(Ti-N)}$ component, thin bottom lines correspond to Linear type backgrounds and thick straight lines to best fits. The best-fit parameters are reported in Table 3.
- Figure 4.9: Ti-2p photoemission spectra of undoped (black), N-doped at I-H- K_e -O (purple), N-doped at I-L- K_e (pink), N-doped at I-H- K_e (green) and N-doped at A (blue) conditions of TiO_2 layers deposited on Pt(111). The red contribution corresponds to the Ti^{4+} component and the orange one to the Ti^{3+} component, thin bottom lines correspond to Shirley type backgrounds and thick straight lines to best fits. The best-fit parameters are reported in Table 3.
 - Figure 4.10: O-1s photoemission spectra of undoped (black), N-doped at I-H- K_e -O (purple), N-doped at I-L- K_e (pink), N-doped at I-H- K_e (green) and N-doped at A (blue) conditions of TiO_2 layers deposited on Pt(111). The red contribution corresponds to the oxygen bulk component and the orange one to the hydroxyl component, thin bottom lines correspond to Shirley type backgrounds and thick straight lines to best fits. The best-fit parameters are reported in Table 3.
 - Figure 4.11: Valence band of undoped (black), N-doped at I-H- K_e -O (purple), N-doped at I-L- K_e (pink), N-doped at I-H- K_e (green) and N-doped at A (blue) conditions of TiO_2 layers deposited on Pt(111), Thick red dot lines the valence band edge (VBE). NB: O-2p bonding state (a) and non-bonding state (b).
 - Figure 4.12: Photocurrent density curves undoped (black), N-doped at I-H- K_e -O (purple), N-doped at I-L- K_e (pink), N-doped at I-H- K_e (green) and N-doped at A (blue) conditions of TiO_2 layers deposited on Pt(111).
 - Figure 4.13: Efficient absorption spectra of undoped (black), N-doped at I-H- K_e -O (purple), N-doped at I-L- K_e (pink), N-doped at I-H- K_e (green) and N-doped at A (blue) conditions of TiO_2 layers deposited on Pt(111), as a function of the wavelength at 0.4 V vs. Ag/AgCl. For comparison between samples, the curves are normalized with the light flux of the Xe arc lamp used during the experiment at 270 nm.
 - Figure 4.14 : Efficient Tauc plot deduced from curves of Figure 4.19 of undoped (black), N-doped at I-H- K_e -O (purple), N-doped at I-L- K_e (pink), N-doped at I-H- K_e (green) and N-doped at A (blue) conditions of TiO_2 layers deposited on Pt(111), as a function of the energy. The straight lines with open circles give an indication of the indirect efficient gap for different thin films.

- Figure 4.15: Mott–Schottky plots for undoped (black), N-doped at I-H- K_e -O (purple), N-doped at I-L- K_e (pink), N-doped at I-H- K_e (green) and N-doped at A (blue) growth conditions of TiO_2 layers deposited on Pt(111). Straight lines indicate the linear fit of each curve.
- Figure 4.16: Experimental (colored thick lines) $k^3\chi(k)$ EXAFS oscillations and fit (gray thin line) by FEFF calculations (assuming a rutile structure) obtained in **a** grazing and **b** normal. Sample : undoped (black), N-doped at I-H- K_e -O (purple), N-doped at I-L- K_e (pink), N-doped at I-H- K_e (green) and N-doped at A (bleu) conditions of TiO_2 layers deposited on Pt(111).
- Figure 4.17: Evolution of the dilatation parameters; α parameter parallel to the surface (dark red unfilled stars) and β parameter perpendicular to the surface (dark green filled stars) as a function of the N/Ti ratios and the Ti^{3+} content.
- Figure 4.18: Evolution of $c_{in\ plane}$ lattice parameter as a function of the N/Ti(%) and the Ti^{3+} ratio and content in the films
- Figure 4.19: Evolution of the $a_{in\ plane}$ (blue squares) the $c_{in\ plane}$ (red circles) lattice parameters of TiO_2 as a function of the N-doping extent and Ti^{3+} ratio.
- Figure 4.20: Comparison between the photocurrent of undoped (black), N-doped at I-H- K_e -O (purple), N-doped at I-L- K_e (pink), N-doped at I-H- K_e (green) and N-doped at A (blue) conditions of TiO_2 layers deposited on Pt(111) at 0.4V and their respective a N/Ti ratio and b Ti^{3+} content.
- Figure 4.21: Evolution of the depletion width and the photocurrent both at 0.4 V vs Ag/AgCl as a function of the N/Ti ratio and Ti^{3+} content on the films.
- Figure 4.22: Electronic parameters of each sample and their resulted photocurrent.
- Figure 4.23: a Growth condition parameters for the synthesis of corundum N- TiO_2 /Pt(111) b RHEED patterns along two particular azimuths the $(10)^*_s$ and the $(11)^*_s$ with the corresponding integrated profiles at 0 and 180 min. c a scheme of the film deposited Pt (111). d corresponding surface reciprocal lattices, the elementary cell (in the reciprocal space) is also shown red square.
- Figure 4.24: Raw (salmon lines) Ti K-edge $k^3\chi(k)$ EXAFS data N- TiO_2 Corundum/Pt(111) (I-L- K_e) in normal incidence (upper panel) and in grazing incidence (bottom panel) and fit of the data by FEFF calculation assuming the rutile (100) structure with the bulk lattice parameter (gray lines) and corundum (0001) with the bulk lattice parameter (black lines), with parameters indicated in Table 7 (best fit, black line).
- Figure 4.25: Experimental XANES spectra of three films; TiO_2 Rutile , N- TiO_2 at I-H- K_e

- deposited at 450°C and N-TiO₂ at I-L-K_e nitriding conditions deposited at 550°C, all samples are deposited on Pt (111).
- Figure 4.26: a Ti2p, b O1s, c N1s, and d VB XPS spectra of nitrogen doped TiO₂ corundum phase deposited on Pt (111)
 - Figure 4.27: Photocurrent density at 0.4V for as a function of the content of Ti³⁺ in the lattice of studied samples
 - Figure 4.28: Evolution of the photocurrent at 0.4V vs Ag/AgCl before and after plasma O₂ cleaning process of doped and undoped films.
 - Figure 4.29: Comparison of the evolution of the Ti³⁺ contribution in the Ti-2p core levels before and after plasma O₂ cleaning process of doped and undoped films.
 - Figure 4.29: Comparison of the evolution of the Ti³⁺ contribution in the Ti-2p core levels before and after plasma O₂ cleaning process of doped and undoped films.
 - Figure 4.30: a picture of the reactor set-up. b simplified scheme of the model studied
 - Figure 4.31: Examples of O1s XPS fitting for N-TiO₂ Rutile/ Pt (111) (I-H-K_e) at select situation. The color-coding is as follows: Ox, (red); OH, (purple); H₂O, (blue); raw data, green lines; background black lines and envelopes, gray lines.
 - Figure 4.32: a Thickness of monolayers OH and b H₂O of three films ; undoped TiO₂, N-TiO₂ Rutile at I-H-K_e conditions and N-TiO₂ corundum at I-L-K_e deposited on Pt (111) as a function of each situation; plasma cleaned, under water, cleaned again and under water light on and two times . The values are the cumulative result of the fitting analysis from the three experiments. The data are analyzed by the multilayer model.
 - Figure 4.33: Ti-2p and N-1s core levels of N-TiO₂ Rutile /Pt (111) (I-H-K_e) during the reactivity with water and light study

Tables:

Chapter III: Self-oxidized single crystalline perovskite N-doped BaTiO₃ oxynitrides

- *Table 1: Summary of significant sample growth parameters deduced from the in-plane RHEED measurements and both in-plane and out-of-plane parameters deduced from XRD measurements for each sample.*
- *Table 2: Summary of significant sample photoelectrochemical properties investigated in the present work. The FWHM and the photoelectrochemical band gap deduced from the efficient T_{auc} plot and the photocurrent measured at 0.5V for thick TiO_xN_{1-x} (360min deposition) and thick TiO₂ (360min deposition) layers deposited on 1%Nb doped SrTiO₃.*
- *Table 3: Summary of significant sample growth conditions*
- *Table 4: Best fit parameters for Ba-3d photo-emission lines deconvolution for undoped and N-doped BaTiO₃/SrTiO₃:Nb samples. E_B stands for binding energy, Δ for peak width (full width at half maximum values), ρ for the relative weight of each line.*
- *Table 5: Summary of significant sample growth conditions and properties examined in the present work. a (respectively c) are the in-plane (respectively out-of-plane) parameters deduced from XRD measurements.*

Chapter IV: Nitrogen incorporation into TiO₂ epitaxial thin films

- *Table 1: Structural data and optical gap for anatase, rutile, and brookite TiO₂*
- *Table 2: Condition parameters for the synthesis of N-doped and undoped TiO₂ deposited on Pt (111) for 180 min.*
- *Table 3: Concentrations (at. %) of the components in layers of nitrogen doped and undoped TiO₂ on Pt (111) and their VBE.*
- *Table 4: Photoelectrochemical parameters of N-doped and undoped TiO₂ deposited on Pt (111)*
- *Table 5: Electrochemical impedance parameters deduced from the fit of $1/C^2 = f(V)$ of N-doped and undoped TiO₂ deposited on Pt (111)*
- *Table 6: Structural parameters deduced from EXAFS experiment.*

- *Table 7: Structural Parameters (Distance, Dilatation Factors) obtained by EXAFS for N-TiO₂ at I-L-K_e nitriding conditions deposited on Pt (111) at 550°C using rutile (100) and corundum (0001) structures.*
- *Table 8: Evolution of the C1s/O1s ratio and the FWHM of the Ox peak under every situation*

General introduction:

a. Solar energy to fuel approach

“The Terawatt Challenge” or the way the world might provide a future global energy prosperity proposed by Richard Smalley is intended to solve the nowadays energy problem [1-Smalley 2005]. The main purpose of this strategy is to find what he named “the new oil”, the prosperous Eldorado of the 21st century that is as enabling as oil and gas have been for the past century. Distressingly, almost certainly within this decade, at some point, we will reach the shortage of the dwindling fossil fuel that is produced worldwide. This is an appropriate expression since society currently consumes 16.0 TW_{avg} (terawatt per year in average) of primary power of which 87% is based on burning fossil fuels [2-BP 2011] and it is estimated that by 2050 the demand for primary power will be approximately 30 TW_{avg} [3-Lewis 2006, 4-Armaroli 2007]. Nonetheless, thanks to the increasing public awareness, we are currently witnessing a new ‘green’ gold rush. Wherein, any technology for energy harvesting, conversion or storage in a sustainable future are in competition to scale up to the TW-level and make a relevant impact at the global energy needs. This requirement is true for photovoltaics, wind turbines, solar fuels, biomass conversion catalysts, electrification of automotive vehicles, fuel cells, storage batteries, flow batteries and any other energy conversion technology.

Undoubtedly, conversion of sunlight into electrical energy is one of the most promising routes to meet the global electricity demand. Indeed, in one hour, solar energy striking earth provides the actual energy demand for one year [5-Nature 2008, 6-Abbasi 2011]. Therefore, on one hand, technologies such as photovoltaic (PV) solar cells, are in constant improvement, currently provide 0.1 TW of power and are right on track to produce 1 TW by 2025 [7-Zakutayev 2016]. However, concerns remain about the sustainability of the manufacturing [8-Powell 2015], as well as the abundance of critical chemical elements for thin film PV technologies [9-Wadia 2009]. On the other hand, the idea of synthesizing solar cell absorbers capable of storing electricity like in batteries, or converting solar energy to fuels for mobile and transport applications, seems even more attractive than reaching 30 TW. A solar fuel is a synthetic chemical fuel produced from solar energy. Nevertheless, the lack of suitable semiconductor materials for photoelectrochemical (PEC) fuels production in particular, which is much more pressing than for PV electricity generation is due to demanding characteristics. As well as being environmentally friendly, the solar absorber materials used in these novel technologies should be inexpensive, efficient, and reliable.

b. Solar fuel produced by photoelectrochemistry

The history of photoelectrochemical cells has been described by Michael Grätzel in 2001 [10-Grätzel 2001]. Since the discovery of the photoelectric effect by Edmond Becquerel [11-Becquerel 1839] in 1839, the key goal of the scientific community is to convert light into electric power or chemical fuels such as hydrogen. Initially, the discovery of photoelectrochemistry was driven by photographic purposes and imaging improvement [10-Grätzel 2001]. However, respectively in 1955 and 1966, the field took a new turn up thanks to Brattain and Garret and subsequently Gerischer, who undertook the first detailed electrochemical and photoelectrochemical studies of the semiconductor–electrolyte interface [12-Brattain 1955, 13-Gerischer 1966]. In addition, since the first oil embargo in 1973, when the worldwide quest for alternative energy sources began.

Photovoltaics are based on photons absorbed on a p-n junction of semiconductors creating an electron–hole pair, generating an electric potential difference across the interface. So far, the junction of these types of devices are made from polluting or not recyclable inorganic solid-state materials. Increasingly, there is an awareness of the possible advantages of replacing the phase in contact with the semiconductor by the electrolyte (liquid, gel or organic solid), and thereby forming a photoelectrochemical device. In such a device, absorption of light occurs at the electrode/electrolyte interface in order to produce electrical energy (like in a Dye Sensitized Solar Cell) or solar fuel (like in the case of photoelectrolysis of water).

In a photoelectrochemical device, photons are absorbed in order to produce charge carriers necessary for electrochemical reaction. Basically, photoelectrochemical cells (PECs) consists of one or two semiconducting electrodes used as and an optional reference electrodes immersed in an electrolyte. During operation, light is absorbed in the photoelectrode, and the photoelectron can be transferred toward the electrical circuit. Due to the strong interaction between the electrons and the atomic constituents of the lattice, the excess energy is distributed rapidly over the solid and is converted into lattice vibrations and heat. Resultantly in a waste of energy since electron emission from a solid surface by excitation with light has a very small cross section.

c. State of the art of photoelectrochemical cells

The most two investigated PECs types are regenerative photovoltaic cell and photoelectrosynthetic cells. The regenerative photovoltaic cell, as indicated by its name, during illumination no chemical change occur on this type of cell also known as Dye Sensitized Solar Cells (DSSC).

In 1991, Grätzel and O'Regan made a significant breakthrough in Dye-Sensitized Solar Cells (DSSCs) by introducing a mesoporous structure in the semiconductor. This advancement led to a notable increase in energy conversion efficiency from 1% to 7.9% [14- O'Regan, B., & Grätzel, M. 1991]. Despite their relatively lower performance compared to other solar cell technologies, DSSCs have found practical applications due to their low cost, flexible form factor, and ease of fabrication. Furthermore, the fundamental understanding gained from DSSCs has contributed to the development of photoelectrosynthetic cells [15-Eom 2018].

Photoelectrosynthetic cells consists of two face-to-face electrodes separated by a redox active electrolyte. The working photoelectrode (WE) is composed of a mesoporous semiconducting material, a monolayer of a specific dye capable of absorbing visible light is added to the surface of the semiconducting particles. In the 'Grätzel cell' or dye-sensitized nanostructured solar cells (DNSCs), the dye absorbs light, causing electrons to be excited. To complete the circuit, the excited electrons diffuse through the nanoparticles of the semiconductor and reach a transparent conducting substrate. The electrons are then transported through an external circuit to the cathode (or back-contact). At the cathode, the electrons reduce the oxidized form of the electrolyte, while the reduced form of the electrolyte diffuses towards the working photoelectrode and reacts with the cationic dye, regenerating the dye.

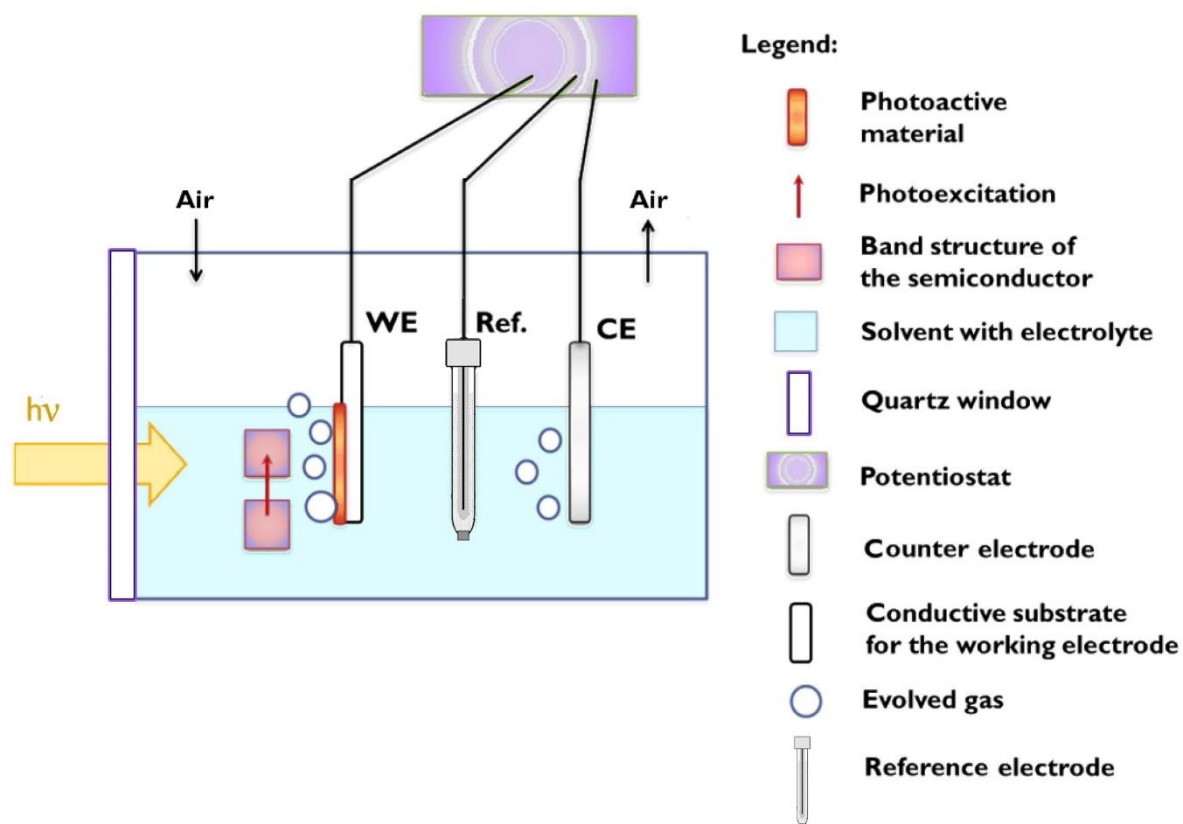


Figure 3: Schematic representation of the operating principle of PEC cells based on a photosynthetic cell that generates a chemical fuel through the photon driven water splitting

Direct conversion of solar energy into a fuel mimicking the catalytic processes of photosynthesis would be a way to solve the problem of storing solar energy. A direct process would minimize the number of steps needed from light to fuel, and therefore potentially allow for higher conversion efficiencies. These are the promises made by the second type of PEC cells, currently described as photoelectrosynthetic cells. Based on a similar principle except that instead of, electrical energy, these PECs may produce useful fuels in a process such as the photoelectrolysis of water to hydrogen and oxygen or the reduction of CO_2 to methane [16-Fujishima 1972, 17-Walter 2010]. As depicted in figure 1 the basic experimental setup is usually composed of a three electrode configuration, comprising a working photoelectrode (WE) (photoanode or photocathode, sometimes both), a counter

electrode (CE) (a metallic material for instance) and a reference electrode (RE) to observe half reactions in the cell. This electrode system is mainly immersed in an aqueous electrolyte (NaOH in our case). The reactor is either transparent to light or comprises an optical window that allows irradiation to reach the photoelectrode, in this case, a visible light permeable quartz window.

d. Photoelectrochemical systems

In these photosynthetic cells, the absorbing material is often the electrode (i.e. the semiconductor itself) [18-Shinde 2018, 19-Klotz 2016]. Although, photoelectrode architectures exhibiting a dye for solar water splitting have also been reported [20-Swierk 2013]. For example, the recent report published by Ager et al. about what is often referred to tandem systems where light absorption is not performed by the semiconductor but by an organic dye [21-Ager 2015]. Another possibility is the surface modification of semiconducting materials with molecular organometallics, favoring either the water oxidation or the reduction reactions [22-Krawicz 2013]. In fact, depending on the conductivity type of the semiconductor, the photoelectrode can be the seat of the oxygen evolution reaction (OER) that forms O_2 by water oxidation (Figure 2a). In other words, O_2 evolution will involve an electron (-) transfer from the electrolyte to the photoactive electrode (i.e. a hole (+) transfer from the photoelectrode to the electrolyte). In such cases, these materials are n-type semiconductors (hematite [23-Klahr 2012] and $BiVO_4$ [24-Trzeźniewski 2016] are typical examples). Otherwise, the semiconductor is a p-type material and therefore, the seat of the hydrogen evolution reaction (HER) that forms H_2 from water reduction (for instance, Rh: $SrTiO_3$ [25-Iwashina 2011]) (Figure 2b). H_2 evolution will then, involve an electron transfer from the photoelectrode to the electrolyte.

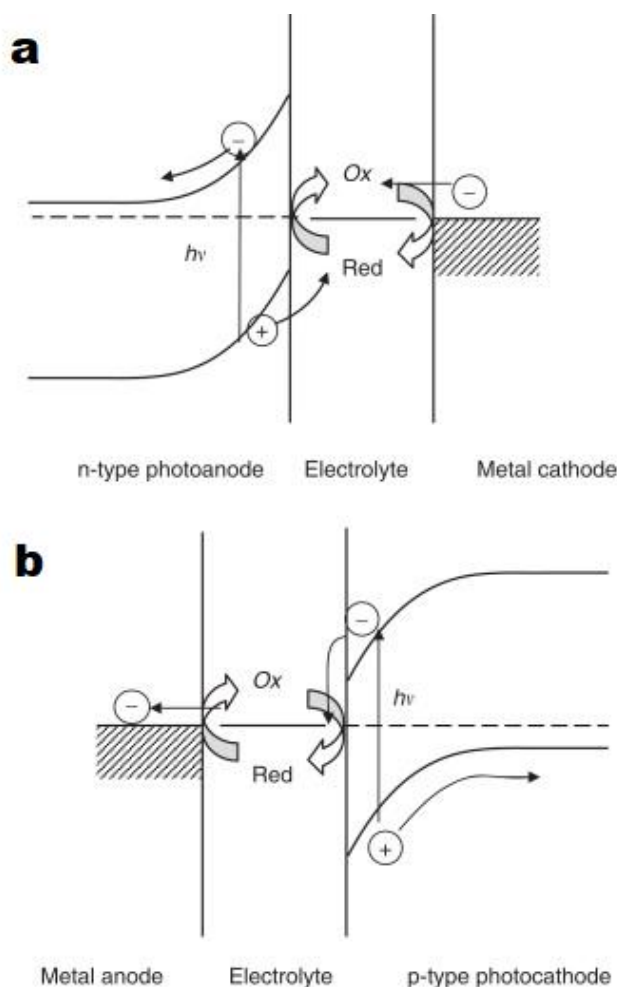


Figure 4: At short circuit, **a** the energy level diagram of an n-type semiconductor photoanode and metal cathode photoelectrochemical cell (PEC), **b** the energy level diagram of a p-type semiconductor photocathode and metal anode regenerative PEC [26-Decker 2009].

Therefore, a last example of interest in photoelectrosynthetic cells systems (Figure 3a). The use of simultaneously two photoelectrodes in a unique cell. The photogenerated electrons are consumed to reduce H^+ into H_2 at the photocathode, while holes take part in oxidation of water into O_2 at the photoanode. At laboratory scale, the cell may use an extra input voltage to drive the charges transfer from the photoelectrodes to the electrolyte. It can be furnished through the application of an external bias (Figure 3b) by a generator or an external power supply unit. This thesis is completely devoted to the analysis of this last kind of PEC systems (photoanode + metallic counter cathode (in this case a platinum (Pt) as CE).

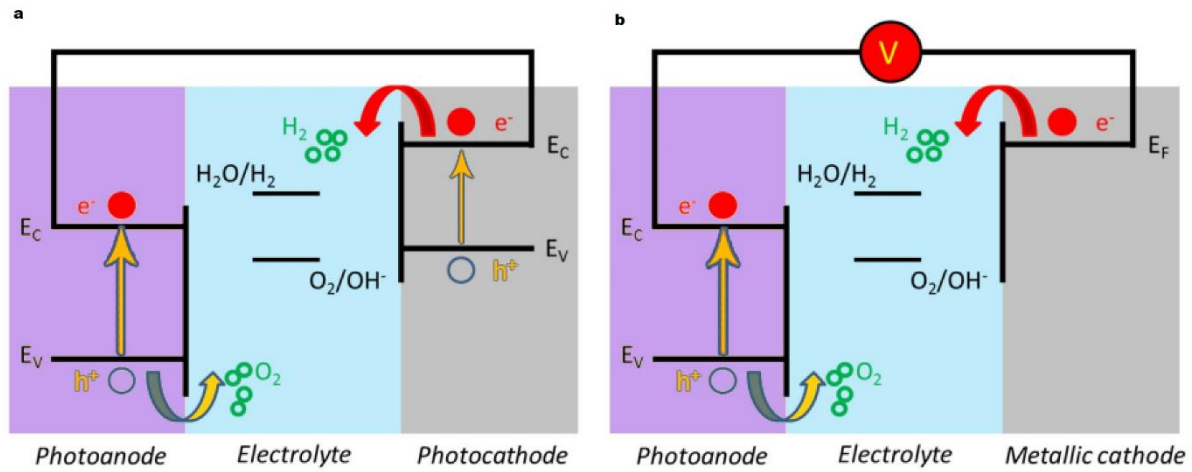


Figure 5: Simplistic representation of the band diagram of; **a** a PEC cell system using a photoanode and a photocathode. And **b** a double photoelectrode PEC cell system using a photoanode, a metallic cathode, and an external bias [27- Rioult 2015]

e. Semiconductors and photo-anode materials for solar water splitting

The overall reaction in a PEC cell for solar water splitting is the splitting of water by sunlight. Under normal operating conditions, room temperature and atmospheric pressure. The reaction may not be spontaneous and an additional potential must be applied [28-Choudhary 2012]. The semiconductor should have an optimum bandgap value about 2.3 eV and moreover, accurate positions of conduction and valence bands for spontaneous water splitting [29-Minggu 2010].

For the OER application, transition metal oxide surfaces have received much attention due to their natural stability in water and under the highly oxidative conditions. The Fujishima and Honda team was the pioneer research group who triggered the potential of TiO₂-based photoelectrochemical reactions for the decomposition of water into H₂ and O₂ [16-Fujishima 1972]. Unfortunately, because of its large band gap (3.0 to 3.2 eV, as shown in figure 4), TiO₂ absorbs mostly the ultraviolet part of the visible spectrum and thus has low conversion efficiency. Numerous attempts to shift the spectral response of TiO₂ better into the visible or to develop alternative oxides and so-called structured materials have so far faced very challenging requirements with uncertain results [30-Lewerenz 2013].

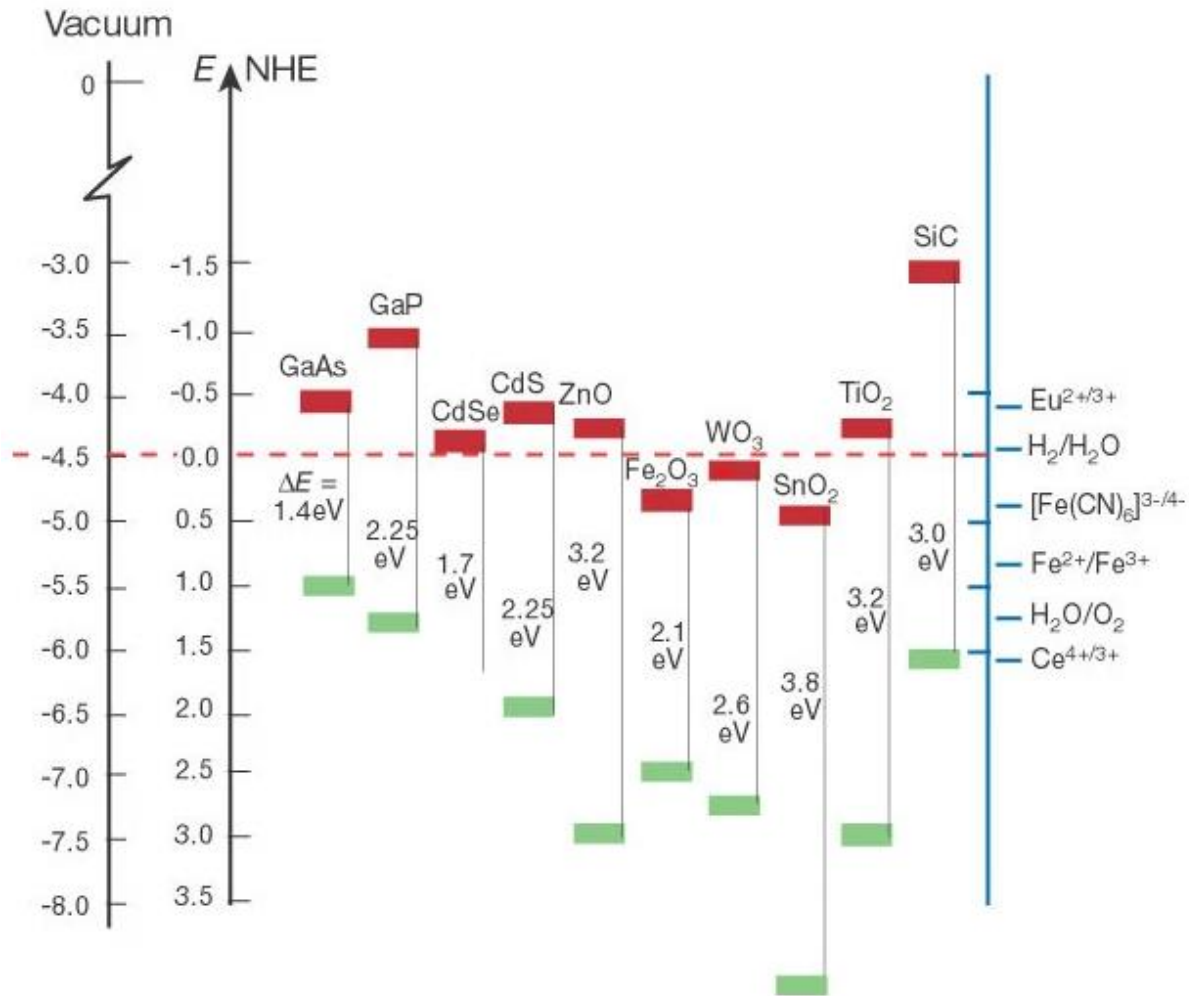


Figure 4: The lower edge of the conduction band (red color) and upper edge of the valence band (green color) are presented along with the band gap in electron volts. The energy scale is indicated in electron volts using either the normal hydrogen electrode (NHE) or the vacuum level as a reference at pH=0. On the right side the standard potentials of several redox couples are presented against the standard hydrogen electrode potential [11-Grätzel M 2001].

In fact, if water is targeted as the new environmentally friendly source for energy storage (H₂). The desirable photon absorber material must as well, be essentially inexhaustible, cheap, and widely available (see figure 5). It is however, not only a question of light absorption efficiency but also of photo-generated carrier collection, ion transport, catalysis, and gas collection. Moreover, the most common and available methods for hydrogen production processes are thermolysis, cracking, reforming, gasification and through thermochemical cycles. All these methods require high temperatures and produce toxic waste. Our strategy drives efforts toward a viable solution to overcome these drawbacks

of solar energy. Accordingly, this following thesis describes a research progress in the development of visible light-driven photoanodes, focusing on the refinement of *oxynitride materials*. They are expected to harvest visible photons (~450–700 nm) and work as stable photoelectrodes for water reduction and oxidation under visible light.

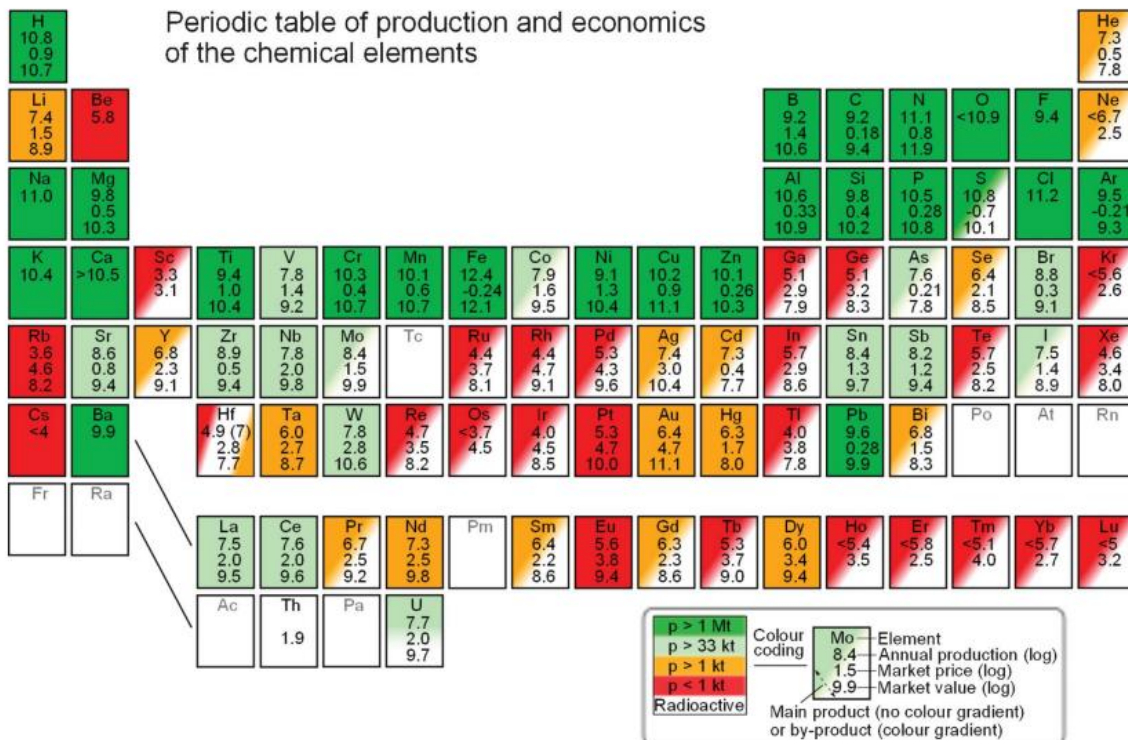


Figure 5: Periodic table of the elements with data for production, price and implied value for the year 2010. The color coding (green, light-green, orange and red) corresponds to overall production level (medium to high, low, very low and extremely low, respectively). Solid color is used for elements which are chiefly main economic products of their respective ores while a diagonal gradient in color is used for elements which are mostly by-products of other elements [31-Vesborg 2012].

f. This thesis: Improving hydrogen production by using oxynitrides as photoelectrodes

Oxygen has the ability to form stable compounds with the majority of metals in a great variety of compositions and structures. Some of multinary oxides such as hematite (Fe₂O₃), SrTiO₃ or BaTiO₃, are of great technological relevance due to their properties and applications in various domains. Ox-

xygen and nitrogen show close ionic radius that makes possible to substitute one by the other preserving eventually, the crystal structure. Nitrogen shows lower electronegativity and higher polarizability than oxygen and the nitride anion is more charged than the oxide one. The insertion of nitrogen in the lattice of an oxide will then, add new $2p$ energy levels in the valence band above the O- $2p$ levels, as a consequence of the lower electronegativity of nitrogen. This leads to a decrease of the optical band gap value, E_g , and thus to a modification of the visible light-driven photoelectrochemical behavior [30-Lewerenz 2013].

Nitrides are essential for a number of electronic applications, owing to the unique combination of electronic, optical and structural properties [30-Lewerenz 2013, 32-Yan 2018,]. For solar water splitting applications, nitrides hold promise due to their adjustable band gaps. However, one major challenge associated with nitrides is their susceptibility to corrosion [16-Fujishima 1972]. Furthermore, nitrides have received relatively less attention compared to other material classes, partly because their synthesis is challenging [7-Zakutayev 2016]. There is a thermodynamic imbalance between nitrating and oxidation, with the formation of oxide phases being energetically more favorable than the synthesis of nitrides. As a result, the synthesis of nitrides often requires exceptionally clean or highly energetic environments [33-Breternitz 2022].

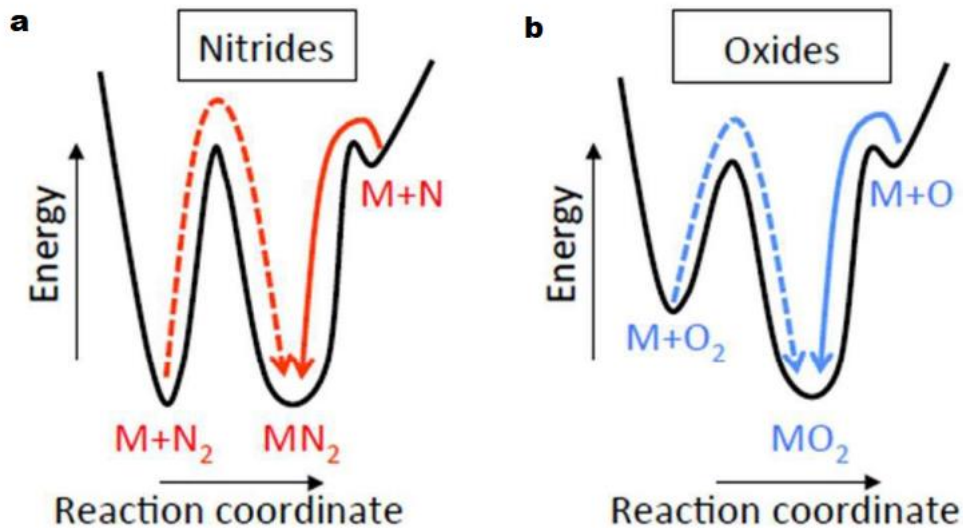


Figure 6: Energy diagram for the synthesis of **a** nitrides **b** oxides [7-Zakutayev 2016]

In this work, we aim at elaborating nanometric single crystalline thin films based on oxynitrides, *i.e.* materials which contains oxygen and nitrogen, and used them as photoelectrodes for photoelectrolysis purposes. This new class of materials has been proposed in a number of theoretical studies promising for this application [34-Aoki 2019, 35-Wu 2013]. Respectfully, to the earlier requirements, our oxynitrides are composed of barium, titanium, oxygen and nitrogen, which are affordable, abundant species as shown in figure 5.

Herein, the study focuses on the fundamental understanding of the potential photoelectrochemical properties of these materials for solar water splitting (water oxidation, hydrogen production). In addition, our films are deposited by oxygen and nitrogen plasma assisted molecular beam epitaxy (O&N PA-MBE), on single crystalline substrates (Pt(111) and SrTiO₃(001)) which makes it possible to elaborate epitaxial films with controlled parameters (dopants concentration, crystallographic structure) suitable for model studies. The use of highly sensitive characterization techniques, in particular using synchrotron radiation light, makes possible the determination of the relevant physical parameters affecting the photoelectrochemical properties. In addition, a photoelectrochemical characterization setup allows to establish the correlation between physical and water splitting properties on the very same sample. In order to properly treat the subject, we divided it into four chapters. In chapter 1, the basic concepts of hydrogen production from solar water splitting with semiconducting photoanodes, as well as the challenging requirements concerning photoelectrochemical properties of photoanodes are presented. Chapter 2 presents the experimental techniques used for the elaboration and characterization of our thin films (O&NPA-MBE, laboratory and synchrotron characterization techniques, photoelectrochemical characterization setup). Chapter 3 presents results about self-oxidized single crystalline N-doped oxide layers, where we investigate the effects of the crystallographic structure, the electronic and chemical composition, the optical properties and the photoelectrochemical efficiency of the doped perovskite. Preliminary results for elaborating a stable photoanode oxynitride perovskite by lattice charge compensation are presented at the end of this chapter. In Chapter 4 we study the effects of N-doping on titanium dioxide (crystallographic and electronic structures, photoelectrochemical and electronic properties), unravelling the intimate crystallographic structure of N-doped TiO₂ and demonstrating the existence of an optimal Ti³⁺ doping level and an increase of the charge separation inducing a high photocurrent gain. In addition, the investigation of the reactivity

under water and light, enabling a further understanding of the chemical interaction between the surfaces under water and light. Lastly, the final section is dedicated to a general conclusion and presents some open perspectives.

g. References:

- [1]. R.E. Smalley. (2005) Future global energy prosperity: the terawatt challenge. *MRS Bull*, 30 pp. 412-417
- [2]. BP Statistical Review of World Energy, Bp plc technical report, (2011)
- [3]. Lewis, N. S., & Nocera, D. G. (2006). Powering the planet: Chemical challenges in solar energy utilization. *Proceedings of the National Academy of Sciences*, 103(43), 15729-15735.
- [4]. Armaroli, N., & Balzani, V. (2007). The future of energy supply: challenges and opportunities. *Angewandte Chemie International Edition*, 46(1-2), 52-66.
- [5]. A task of terawatts. (2008) *Nature* 454, 805 (2008)
- [6]. Abbasi, T., & Abbasi, S. A. (2011). 'Renewable' hydrogen: prospects and challenges. *Renewable and Sustainable Energy Reviews*, 15(6), 3034-3040.
- [7]. Zakutayev, A. (2016). Design of nitride semiconductors for solar energy conversion. *Journal of Materials Chemistry A*, 4(18), 6742-6754.
- [8]. Powell, D. M., Fu, R., Horowitz, K., Basore, P. A., Woodhouse, M., & Buonassisi, T. (2015). The capital intensity of photovoltaics manufacturing: barrier to scale and opportunity for innovation. *Energy & Environmental Science*, 8(12), 3395-3408.
- [9]. Wadia, C., Alivisatos, A. P., & Kammen, D. M. (2009). Materials availability expands the opportunity for large-scale photovoltaics deployment. *Environmental science & technology*, 43(6), 2072-2077.
- [10]. Grätzel, M. (2001). Photoelectrochemical cells. *nature*, 414(6861), 338-344.
- [11]. Becquerel, E. *C.R. Acad. Sci.* 9, 145–149 1839
- [12]. Brattain, W. H., & Garrett, C. G. B. (1955). Experiments on the interface between germanium and an electrolyte. *Bell System Technical Journal*, 34(1), 129-176.
- [13]. Gerischer, H. (1966). Electrochemical behavior of semiconductors under illumination. *Journal of the electrochemical society*, 113(11), 1174.

- [14]. O'regan, B., & Grätzel, M. (1991). A low-cost, high-efficiency solar cell based on dye-sensitized colloidal TiO₂ films. *nature*, 353(6346), 737-740.
- [15]. Eom, Y. K., Nhon, L., Leem, G., Sherman, B. D., Wang, D., Troian-Gautier, L., ... & Schanze, K. S. (2018). Visible-light-driven photocatalytic water oxidation by a π -conjugated donor–acceptor–donor chromophore/catalyst assembly. *ACS Energy Letters*, 3(9), 2114-2119.
- [16]. Fujishima, A., & Honda, K. (1972). Electrochemical photolysis of water at a semiconductor electrode. *nature*, 238(5358), 37-38.
- [17]. Walter, M. G., Warren, E. L., McKone, J. R., Boettcher, S. W., Mi, Q., Santori, E. A., & Lewis, N. S. (2010). Solar water splitting cells. *Chemical reviews*, 110(11), 6446-6473.
- [18]. Shinde, P. S., Peng, X., Wang, J., Ma, Y., McNamara, L. E., Hammer, N. I., ... & Pan, S. (2018). Rapid screening of photoanode materials using scanning photoelectrochemical microscopy technique and formation of Z-scheme solar water splitting system by coupling p-and n-type heterojunction photoelectrodes. *ACS Applied Energy Materials*, 1(5), 2283-2294.
- [19]. Klotz, D., Ellis, D. S., Dotan, H., & Rothschild, A. (2016). Empirical in operando analysis of the charge carrier dynamics in hematite photoanodes by PEIS, IMPS and IMVS. *Physical Chemistry Chemical Physics*, 18(34), 23438-23457.
- [20]. Swierk, J. R., & Mallouk, T. E. (2013). Design and development of photoanodes for water-splitting dye-sensitized photoelectrochemical cells. *Chemical Society Reviews*, 42(6), 2357-2387.
- [21]. Ager, J. W., Shaner, M. R., Walczak, K. A., Sharp, I. D., & Ardo, S. (2015). Experimental demonstrations of spontaneous, solar-driven photoelectrochemical water splitting. *Energy & Environmental Science*, 8(10), 2811-2824.
- [22]. Krawicz, A., Yang, J., Anzenberg, E., Yano, J., Sharp, I. D., & Moore, G. F. (2013). Photo-functional construct that interfaces molecular cobalt-based catalysts for H₂ production to a visible-light-absorbing semiconductor. *Journal of the American Chemical Society*, 135(32), 11861-11868.

- [23]. Klahr, B., Gimenez, S., Fabregat-Santiago, F., Hamann, T., & Bisquert, J. (2012). Water oxidation at hematite photoelectrodes: the role of surface states. *Journal of the American Chemical Society*, 134(9), 4294-4302.
- [24]. Trześniewski, B. J., & Smith, W. A. (2016). Photocharged BiVO₄ photoanodes for improved solar water splitting. *Journal of Materials Chemistry A*, 4(8), 2919-2926.
- [25]. Iwashina, K., & Kudo, A. (2011). Rh-doped SrTiO₃ photocatalyst electrode showing cathodic photocurrent for water splitting under visible-light irradiation. *Journal of the American Chemical Society*, 133(34), 13272-13275.
- [26]. F. Decker, S. Cattarin, (2009) *Encyclopedia of Electrochemical Power Sources*
- [27]. Rioult, M. (2015). Hematite-based epitaxial thin films as photoanodes for solar water splitting (Doctoral dissertation, Ecole Polytechnique).
- [28]. Choudhary, S., Upadhyay, S., Kumar, P., Singh, N., Satsangi, V. R., Shrivastav, R., & Dass, S. (2012). Nanostructured bilayered thin films in photoelectrochemical water splitting—A review. *International journal of hydrogen energy*, 37(24), 18713-18730.
- [29]. Minggu, L. J., Daud, W. R. W., & Kassim, M. B. (2010). An overview of photocells and photoreactors for photoelectrochemical water splitting. *International journal of hydrogen energy*, 35(11), 5233-5244.
- [30]. Lewerenz, H. J., & Peter, L. (Eds.). (2013). *Photoelectrochemical water splitting: materials, processes and architectures*. Royal Society of Chemistry.
- [31]. Vesborg, P. C., & Jaramillo, T. F. (2012). Addressing the terawatt challenge: scalability in the supply of chemical elements for renewable energy. *Rsc Advances*, 2(21), 7933-7947.
- [32]. Yan, R., Khalsa, G., Vishwanath, S., Han, Y., Wright, J., Rouvimov, S., ... & Jena, D. (2018). GaN/NbN epitaxial semiconductor/superconductor heterostructures. *Nature*, 555(7695), 183-189
- [33]. Breternitz, J., & Schorr, S. (2022). Zinc germanium nitrides and oxide nitrides: the influence of oxygen on electronic and structural properties. *Faraday Discussions*, 239, 219-234.

- [34]. Aoki, Y., Sakurai, M., Coh, S., Chelikowsky, J. R., Louie, S. G., Cohen, M. L., & Saito, S. (2019). Insulating titanium oxynitride for visible light photocatalysis. *Physical Review B*, 99(7), 075203.
- [35]. Wu, Y., Lazic, P., Hautier, G., Persson, K., & Ceder, G. (2013). First principles high throughput screening of oxynitrides for water-splitting photocatalysts. *Energy & environmental science*, 6(1), 157-168.

Chapter I

Oxynitrides as a potential photoanode for solar water splitting

Summary: In this chapter, the development of hydrogen fuel technologies and its potential role in the transition to a more sustainable and secure energy system are discussed. However, there are still challenges that must be overcome in terms of cost, infrastructure, and public acceptance in order for hydrogen fuel to reach its full potential. Moreover, we will highlight how solar energy storage by photoelectrochemical water splitting has garnered significant research attention in recent years. Subsequently, we will discuss why the oxynitrides, a class of promising materials, are being investigated for their potential use as photoelectrodes in solar water splitting applications.

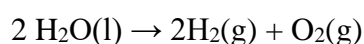
Meeting mankind's thirst for sustainable energy is one of the scientific grand challenges of our time. The limited reserves of fossil fuels and their negative impact on the environment pose significant challenges to our energy security and sustainability. As a result, researchers are actively seeking renewable energy sources, to meet the energy needs of a growing global population. However, solar energy is intermittent, with significant variation depending on the time of day, season, and geographic location. Hydrogen produced by solar energy is considered a promising clean energy vector with the features of high energy capacity of 122 kJ/g [1-NREL] and zero-carbon emission.

1.1 Hydrogen production from water splitting

1.1.1 Making hydrogen

Henry Cavendish first, isolated hydrogen gas in 1766 through a series of experiments involving the reaction of metals with acids [3-Cavendish 1766].

However, it was not until the development of the modern electrolysis process in the late 1800s that large-scale production of hydrogen became possible. The general chemical reaction for the electrolysis of water, [4-Nicholson1800, 5-Ritter1801] is given by:



In 1800, Nicholson and his colleague Anthony Carlisle used electrolysis to decompose water into its constituent elements, and they observed the formation of hydrogen and oxygen gases at the cathode

and anode, respectively. This discovery was significant because it showed that water could be broken down into its component parts using an electric current, providing a way to obtain pure hydrogen and oxygen gases.

Later, in 1801, Ritter improved on Nicholson and Carlisle's work by demonstrating that the production of hydrogen and oxygen gases during electrolysis was in proportion to the amount of electrical charge passing through the water. He also showed that the hydrogen and oxygen gases could be collected and measured separately, and that the volume ratio of hydrogen to oxygen was always 2:1, consistent with the chemical formula for water (H₂O).

The overall water splitting is an uphill (endergonic) reaction. The ΔG (Gibb's free energy) for the reaction is +237 kJ mol⁻¹, i.e. the reaction is not spontaneous under standard conditions, and energy must be supplied to overcome the activation energy barrier for the reaction to occur. This is because the products of the reaction (hydrogen gas and oxygen gas) have higher energy content than the reactant (water). The energy required to drive this reaction can be provided by various sources, including thermal, electrical, photonic, or biochemical energy (Figure 1.1)

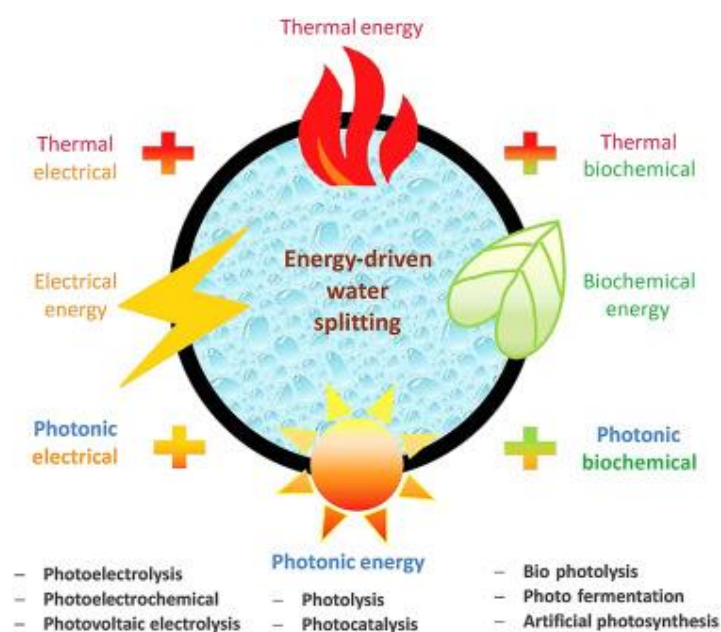


Figure 1.1: Various energy-driven water-splitting routes using thermal, electrical, biochemical, and photonic energy or their combinations [6-Tee 2017].

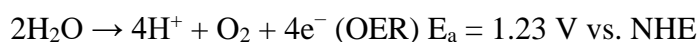
1.1.2 Choosing Electrolysis

The process of electrolysis is based on passing an electric current through water to produce high-purity hydrogen and oxygen gases. As a mature method for water splitting, with a large-scale hydrogen production, electrolysis still faces challenges to overcome including improving the efficiency, durability, and cost of the technology.

1.1.2.1 Electrolytic cell for water splitting

The electrolytic cell, also known as an electrolyser, uses an electrical current to split water (H₂O) into its constituent hydrogen (H₂) and oxygen (O₂) gas through a process called electrolysis. This electrochemical device typically consists of two electrodes (an anode and a cathode) immersed in a solution of water and an electrolyte, which can be an acid, base, or salt. When an electric current is applied two important half-cell reactions, namely, the anodic oxygen evolution reaction (OER) and the cathodic hydrogen evolution reaction (HER) occur.

In acidic conditions (pH < 7), the water is oxidized at the anode according to the following equation:



Electrons and protons are combined at the cathode to generate H₂:



- In alkaline conditions (pH > 7), the OER and HER proceed according to the equations below, respectively.



According to the energy cost on each mechanism, the water oxidation half reaction is more difficult both thermodynamically and kinetically compared to the water reduction half reaction in PEC water splitting. This is because the energy barrier for water oxidation is much higher and the process is more complex than water reduction. In fact, it takes four holes to produce one mole of oxygen while only two electrons participate in the reaction for generating one mole of hydrogen. Therefore, the water oxidation half reaction is often considered one of the most challenging steps in PEC water splitting.

1.1.2.2 Types of electrolyzers for water splitting

Different technologies have been developed from these two previous grand categories and according to the electrolyte used in the electrolytic cell, herein four under categories: Polymer Electrolyte membrane or PEM Electrolyzer [7-Hosseini 2016, 8-El Emam 2023], Solid Oxide Electrolyzer or high-Temperature steam electrolysis [9-Wang 2018], Alkaline Electrolyzer (AEL) [10-Gallandat 2017] and what used here a Photoelectrochemical cell (PEC) [11-Grätzel 2001, 12-Lianos 2011]

1.1.3 Photoelectrochemical cell for solar water splitting requirements

To use solar energy for hydrogen production through electrolysis, there are two main approaches:

-Conventional electrolyzer with a photovoltaic (PV) cell: In this configuration, a PV cell is used to directly convert solar energy into electricity. This electricity is then utilized to power an electrolyzer, which separates water into hydrogen and oxygen. The conventional electrolyzer requires specific electrode catalyst materials to facilitate the oxidation and reduction reactions.

-Photoelectrochemical cell (PEC): In this approach, a PEC cell is employed, where the electrode is a semiconductor that absorbs solar energy to generate photoexcited charge carriers. These charge carriers can then transfer to the electrolyte to drive chemical reactions, such as water oxidation or reduction. The following diagram illustrates the basic principle of a PEC cell:

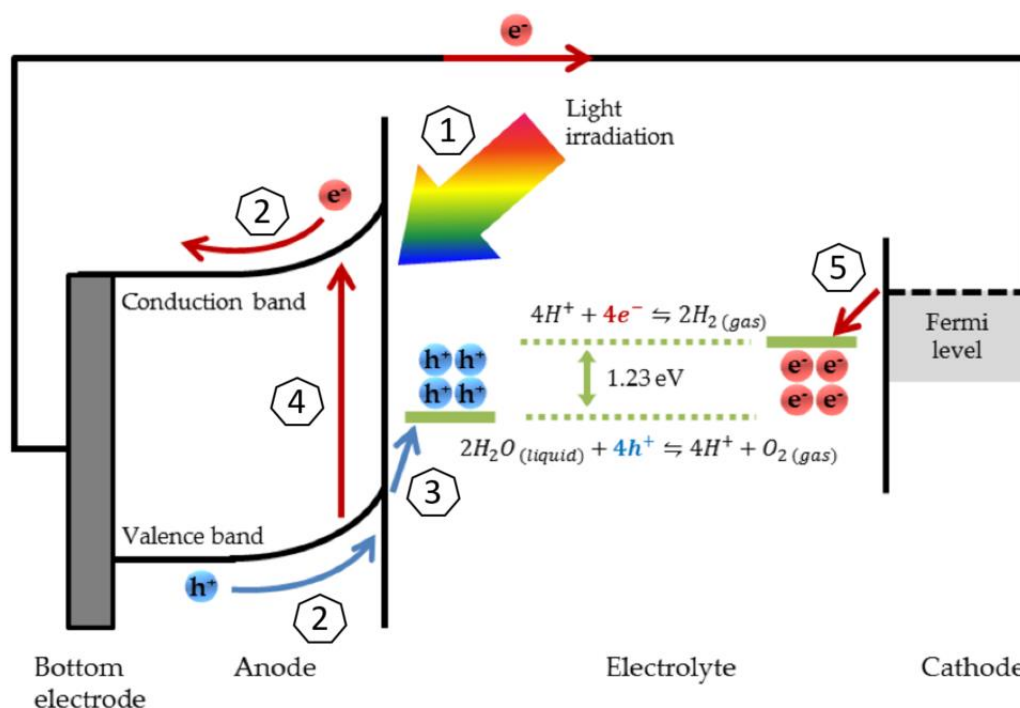


Figure 1.2: Schematic representation of the photoelectrochemical (PEC) water splitting process in a common PEC water splitting system consisting of a photoanode and a metal counterpart [13-Jeong 2018].

The process of photoelectrochemical (PEC) water splitting involves several key steps (see Figure 1.2):

1. Absorption of solar radiation: The photoelectrode absorbs solar radiation, typically in the visible light range, leading to the photoexcitation of electrons in the valence band of the photoelectrode.
2. Charge carrier generation and separation: The photoexcited electrons and the corresponding holes are generated in the photoelectrode. It is crucial to prevent recombination, which can reduce the overall efficiency of the PEC system. This separation can be achieved through internal or external bias applied through the circuit.
3. Water oxidation at the anode: The photoexcited holes participate in the oxidation of water molecules at the anode. This leads to the release of oxygen gas (O_2) and the generation of protons (H^+). Therefore, a stable anode against oxidation is compulsory.

4. Transport of charge carriers: The protons (H^+) produced at the anode move towards the surface, while the photoexcited electrons are transported to the bottom electrode, and towards the cathode through an external circuit.
5. Hydrogen evolution at the cathode: At the cathode, electrons (e^-) combine with water to form hydrogen gas (H_2)

Understanding the electronic processes at the interface between the semiconductor and the electrolyte is crucial for comprehending the underlying chemistry of electrochemical reactions. This in-depth understanding of electronic processes aids in optimizing the design of PEC cells and developing suitable photoelectrodes to enhance the efficiency of chemical reactions.

1.1.3.1 The semiconductor

Molecular bonding theory explains that the combination of atomic orbitals from multiple atoms forms bonding and anti-bonding energy levels, which constitute energy bands. The valence band VB (highest occupied molecular orbital) and conduction band CB (lowest unoccupied molecular orbital) are formed from these energy levels, with a band-gap (E_g) representing the energy difference between them. Semiconductors typically have a band-gap in the range of 0.5-3.5 eV. The position of the Fermi level, which is the energy level that separates the occupied and unoccupied electronic states, depends on the doping concentration and temperature of the material. When an external energy source like a photon excites the semiconductor, charge-carriers are generated; an electron in the valence band is promoted to the conduction band, leaving a hole in the valence band, which leads to some degree of conduction. These electron-hole pairs are important in water splitting reactions.

Intrinsic semiconductors have a balanced number of positively charged holes and negatively charged electrons, making them electrically neutral (Figure 1.3a). Also known as undoped semiconductors, they have low conductivity. Once doped with impurity atoms they become extrinsic semiconductors. Donor-doped semiconductors have impurity atoms with more valence electrons, creating an electron-rich (n-type) semiconductor (Figure 1.3b), while acceptor-doped semiconductors have impurity atoms with fewer valence electrons, creating a hole-rich (p-type) semiconductor (Figure 1.3c). Consequently, n-type semiconductors have electrons as majority carriers, while in p-type semiconductors, holes are the majority carriers [14-Shockley 1958].

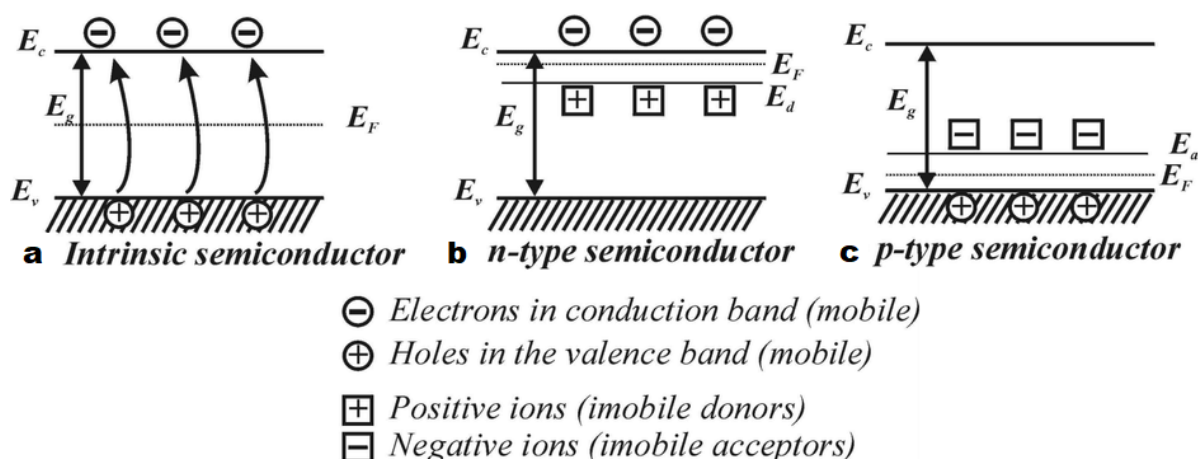


Figure 1.3: Schematic band-gap representation for **a** intrinsic; **b** n-type doped and **c** p-type doped semiconductor.

Thus, in this study, we are investigating methods to reduce the band gap of traditional oxides by employing doping techniques. Our objective is to find a suitable semiconductor material with a band gap of around 2.3 eV.

1.1.3.2 The electrolyte

In a PEC cell, the electrolyte acts as a medium for the transport of ions, *i.e.* the flow of electrical current. The redox potential of the electrolyte (E_{redox}) determines the band alignment at the semiconductor-electrolyte interface. For the charge transfer, the conduction band minimum (CBM) of the semiconductor should be more negative than the reduction potential of the electrolyte, while the valence band maximum (VBM) should be more positive than the oxidation potential of the electrolyte (see figure 1.2). This ensures that photoexcited electrons can transfer to the electrolyte and reduce species such as water or oxygen, while photoexcited holes can oxidize species such as water or hydroxide ions [15-Walter 2010].

The pH modifies the position of E_{redox} with respect of semiconductor bands and can change the stability of the PEC cell. Usually, the optimum pH for PEC water splitting, in the case of photoanode, is in the basic range, where the concentration of the water-splitting intermediate (OH^\cdot) is relatively high, but the concentration of interfering species, such as H_2 and O_2 , is low, and where valence band is below oxidation level of water

The electrolyte used in this thesis is a NaOH solution at a concentration of 0.1 M, (*i.e.* pH=13). These conditions are typically used for the water oxidation reaction at the semiconductor/electrolyte interface. This is because the relevant redox couple in this reaction is O_2/OH^- , and the hydroxide ion (OH^-) is the ionic charge carrier in the electrolyte. The high pH of the NaOH solution helps to maintain a

stable and basic environment for the reaction to occur, while the relatively high concentration of the electrolyte helps to promote the conductivity of the solution [16-Biswas 2019].

1.1.3.3 Semiconductor/electrolyte interaction

1.1.3.3.1 n-type semiconductor-electrolyte junction in dark –SC (semiconductor) side

When two semiconductors come into contact, the two materials exchange charges until their Fermi levels are equalized. This process results in a bending of the semiconductor energy bands near the interface, known as band bending. Analogously, if a semiconductor is in contact with an electrolyte, the same process occurs. The equivalent of Fermi level for an electrolyte is the E_{redox} (see figure 1.4).

The band bending creates a space charge region near the interface in the semiconductor, which acts as a potential barrier for charge carriers, affecting their transport across the interface. The extent of the space charge region and the height of the potential barrier depend on the doping concentration and the degree of band bending, via the formula:

$$\omega = \sqrt{\Delta E_{\phi SC} \frac{2\epsilon\epsilon_0}{e_0 N_D}}$$

Where ω is the width of the depletion layer, ΔE the height of depletion layer, ϵ the dielectric constant of the semiconductor, ϵ_0 the vacuum permittivity, e_0 the elemental charge and N_D the donor concentration in the semiconductor. This equation is very similar to the Mott-Schottky equation for a semiconductor-metal interface [17-Schmikler 2010].

In the case of n-type semiconductors, the Fermi level of the semiconductor is initially above that of E_{redox} of the electrolyte. This leads to an upward band bending, where the conduction band and the valence band are raised relative to the Fermi level. This upward band bending favors the hole transfer from the semiconductor towards the electrolyte, and is therefore suitable for photoanode.

Conversely, in p-type semiconductors, the Fermi level of the semiconductor is initially below that of E_{redox} of the electrolyte. This leads to a downward band bending, favoring the electron transfer toward the electrolyte, and is therefore suitable for photocathode. In this thesis, we focus on developing n-type semiconductors to use them as photoanode in PEC cells, where the oxidation reaction occurs.

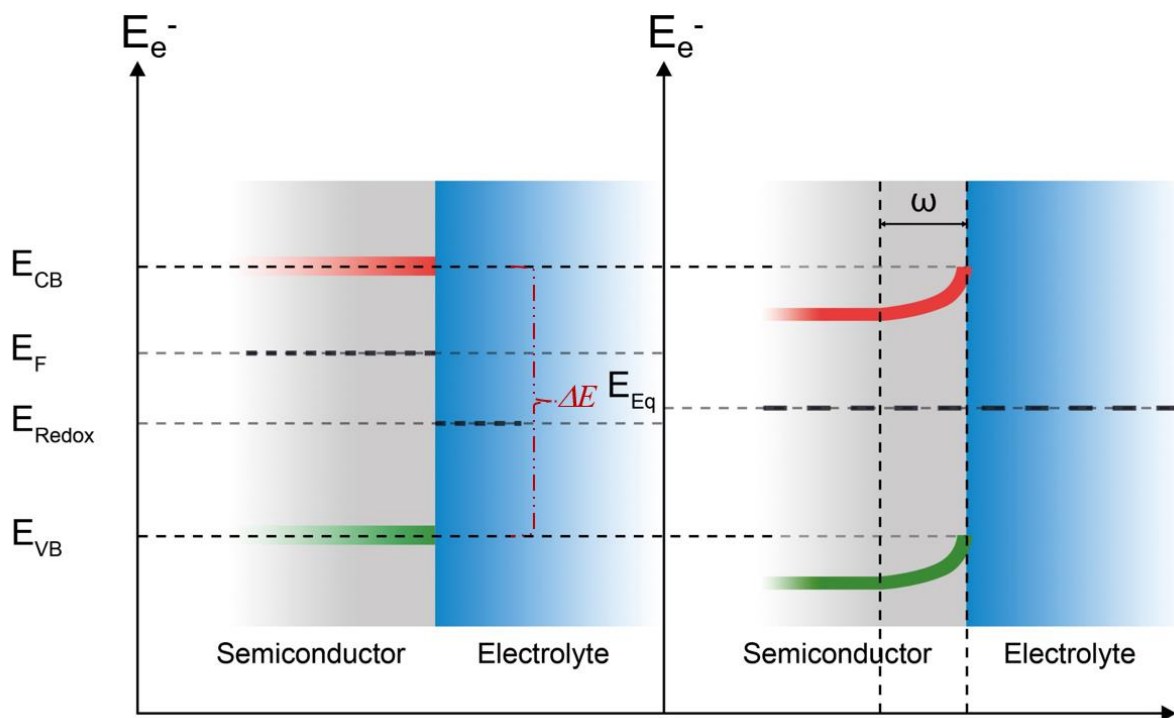


Figure 1.4: n-type semiconductor-electrolyte interface. (left) before contact, (right) after contact. After contact, the system reaches electronic equilibrium (E_{Eq}) when the energy of the Fermi level (E_F) in the semiconductor is equivalent to the redox potential of the electrolyte (E_{Redox}). The space charge layer, which is the area where the charge distribution differs from the bulk material, has a width ω and a height ΔE . The electric field in the space layer favors the separation of charge carriers.

1.1.3.3.2 n-type semiconductor-electrolyte junction in dark in the electrolyte side

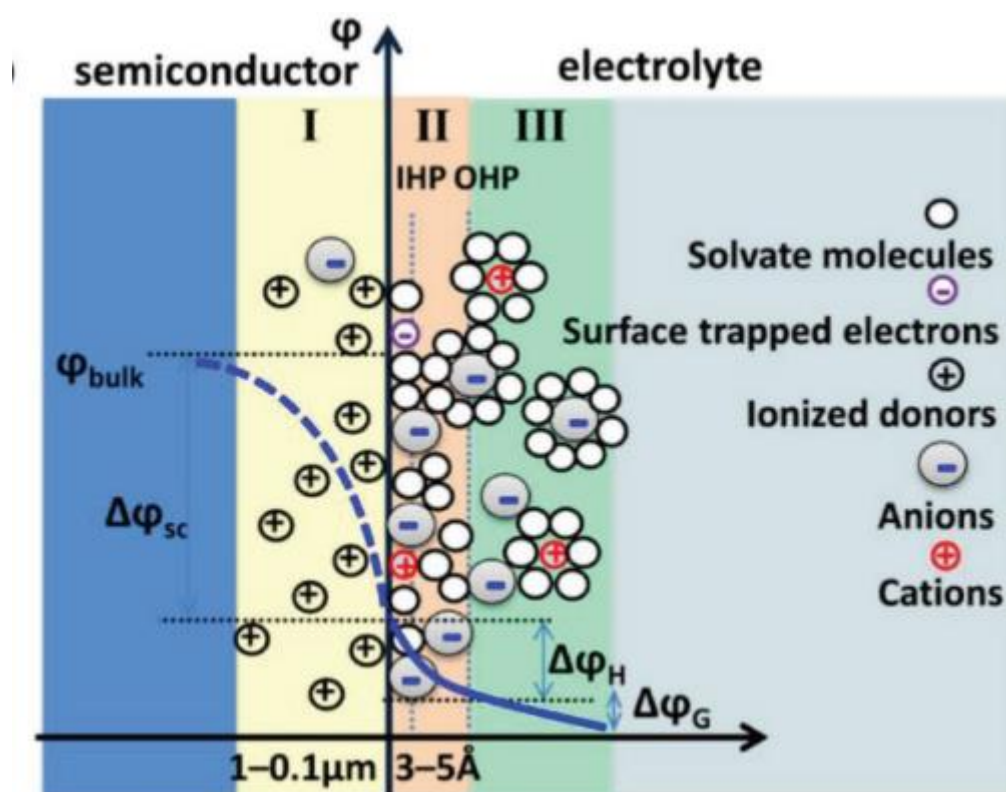


Figure 1.5: The structure model of the n-type semiconductor/electrolyte interface under equilibrium conditions and the potential (ϕ) profile across this interface (blue line). $\Delta\phi_{sc}$, $\Delta\phi_H$, and $\Delta\phi_G$ are the potential drops in the space charge layer (I), Helmholtz layer (II), and Gouy layer (III), respectively (NB: this figure is in reverse potential of figure 1.5) [18-Xu 2019].

If we want to describe more precisely the interface between the semiconductor and the electrolyte in PEC cells, there are three distinct layers (Figure 1.5) to consider. The first layer (I), is the space charge region in the SC described above. In the case of n-type SC it is positively charged.

The electron transfer during the contact also leads to the formation of an electric field in the electrolyte at the semiconductor liquid junction (SCLJ). The second layer (II), in the electrolyte, is known as the Helmholtz layer and is negatively charged. This layer comprises trapped electrons in surface states, adsorbed ions, and oriented water molecule dipoles. The third layer (III), adjacent to the Helmholtz layer, is the Gouy diffuse layer, which has the lowest potential among the three layers. It mainly contains anions and a small number of cations. The varying electron densities across these three layers give rise to a potential drop, resulting in upward band bending [18-Xu 2019].

1.1.3.3.3 n-type semiconductor-electrolyte junction under illumination

When a photon with energy greater than E_g hits the semiconductor an electron/hole pair is generated. In the absence of an external electric field, these carriers can recombine, and the energy is converted into light or heat. However, if the semiconductor is connected to an external circuit, and/or if the carriers are situated in the space charge layer, the electron/hole pair can be separated by the built-in electric field or an external bias voltage, leading to a flow of current. In the case of an n-type SC, the electrons move toward the bulk of the semiconductor while the holes move to the solution. The Fermi level is defined by the energy level where there is a 50% probability of finding an electron. Under illumination the Fermi level for electrons ($E_{F,e}$) and the Fermi level of holes ($E_{F,p}$) split into two quasi-Fermi levels, reflecting the fact that the electron and hole densities are no longer equal. This difference between the two quasi-Fermi levels defines the open circuit potential (VOC) of the n-SC / electrolyte junction under illumination (Figure 1.6) [19-Sze 2006].

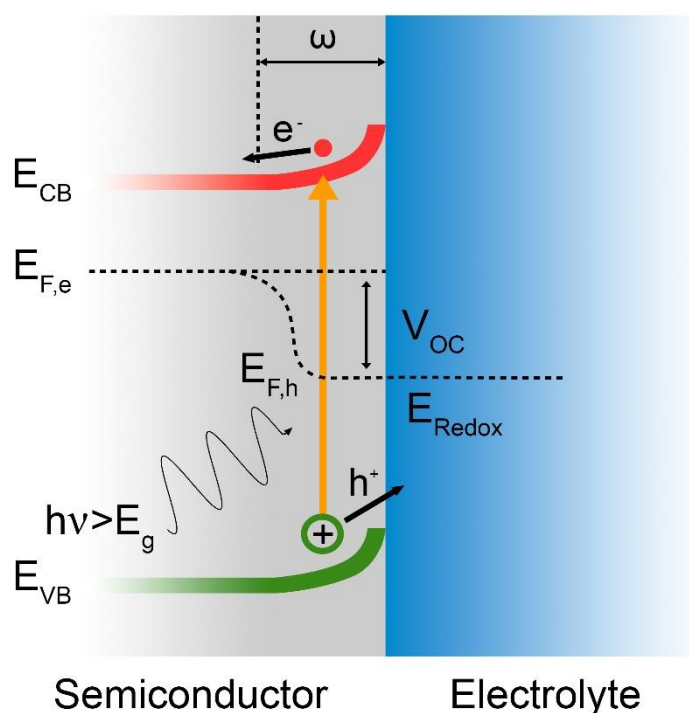


Figure 1.6: Charge carriers separation in an n-type semiconductor under illumination.

1.2 Photoelectrochemical cells improvement : Photoanode requirements

The anodic reaction in PEC water splitting for H_2 production, involves water oxidation on photoanodes. Due to the nature of multi-electron and multi-proton transfers, water oxidation typically

requires substantial overpotentials [20- Cook 2010]. This thesis aims at innovating promising photoanode materials for highly efficient PEC water splitting, starting from existing materials. To function as an oxygen evolving photoanode material, a semiconductor should possess n-type conductivity, which causes band bending to generate an electric field driving holes towards the surface. It must possess appropriate band-edge positions and band gap values. Furthermore, the semiconductor must have suitable electrical properties such as resistivity to enable effective collection of charge carriers and no recombination. It is also necessary for the semiconductor to remain stable when subjected to water oxidation conditions.

1.2.1 Band gap

Natural sunlight consists of 5% UV (280–400 nm), 43% visible (400–700 nm), and 52% infrared radiation (700–2500 nm) (Figure 1.7). Therefore, to increase efficiency, the band gap of semiconductors must ensure substantial absorption of the solar spectrum. Since the proton reduction potential (H^+/H_2) is located at 0 V vs. NHE (Normal Hydrogen Electrode) and the water oxidation ($\text{O}_2/\text{H}_2\text{O}$) potential at 1.23 V vs. NHE (pH = 0), the theoretical minimum band-gap for water splitting requires incident photons with a minimum energy of 1.23 eV, which corresponds to a wavelength of light of ~ 1100 nm. However, when considering the thermodynamic energy losses occurring during charge carrier transportation (0.3-0.4 eV) and the overpotential requirement for acceptable surface reaction kinetics (0.4-0.6 eV), a minimum band-gap of ~ 1.8 eV is required, corresponding to light absorption at *ca.* 700 nm.

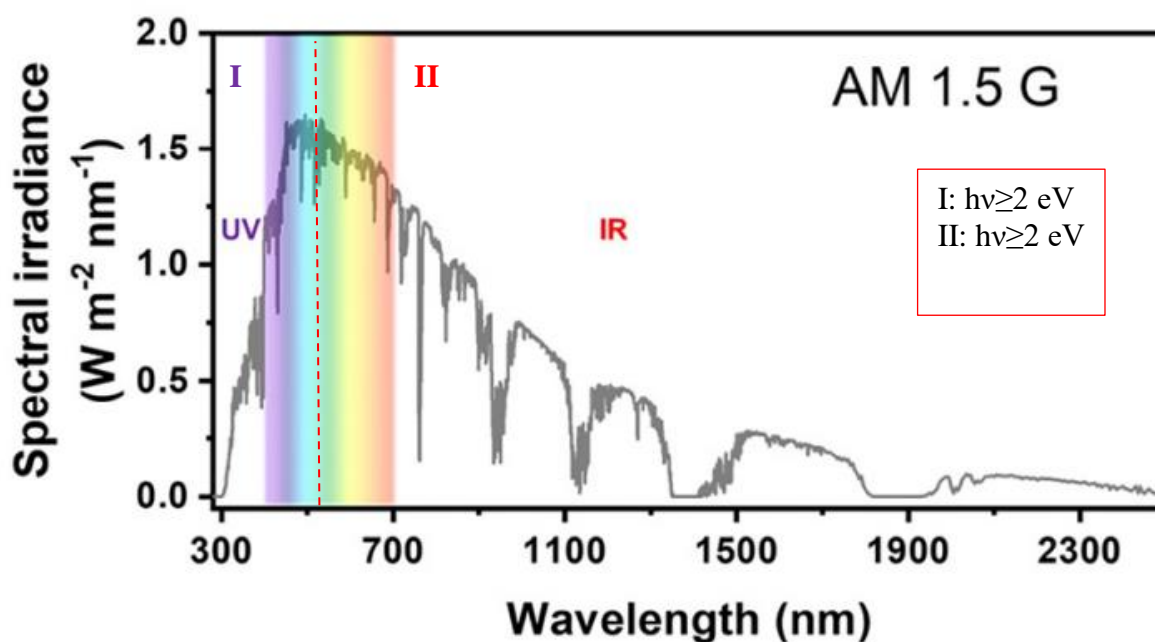


Figure 1.7: AM 1.5 solar spectrum in temperated zones, taking into account atmosphere absorptions (1 sun conditions with power intensity of 100 mW cm^{-2}). Zone I (II) corresponds to the part of the solar spectrum absorbed by a semiconductor having a gap of 2 eV. The energy / wavelength equivalence is given by $E = hc/\lambda$ [24- Meng 2021].

For this reason and for a single semiconductor photoelectrode, the band-gap energy between 1.9 eV and 3.2 eV is desirable, with a preferred band-gap of around 2.0 eV for optimal sunlight utilization [21-Jiang 2017, 22-Zhang 2012].

1.2.2 Band edges positions

In an ideal case with single semiconductor material, in order to perform both HER and OER, the band edges must straddle the redox potentials of H₂O (0.00 eV and 1.23 eV). If it is not the case the SC cannot be used alone, and a second photoelectrode and/or bias is needed. Figure 1.8 displays the band-edge positions of common p- and n-type semiconductor materials with respect to the normal hydrogen electrode, and the position of water redox potentials. The graph plots the semiconductor band-edge positions against their maximum photocurrent, integrated under Air Mass 1.5 illumination, based on the Shockley-Queisser limit for solar energy conversion. η_{STH} has been the most important and commonly used parameter [25-Vayssieres 2010]. It is defined as the ratio of chemical energy (H₂) output to the solar energy input, as expressed in:

$$\begin{aligned}\eta_{STH}(\%) &= \left(\frac{\text{chemical energy produced}}{\text{Solar energy input}} \right) \\ &= \left[\frac{H_2 \text{ production rate (mmol } H_2 \text{ s}^{-1}) \times \Delta G^\circ (\text{kJ mol}^{-1})}{P_{\text{solar}} (\text{mW cm}^{-2}) \times \text{Illuminated area (cm}^2)} \right]_{AM\ 1.5G} \\ &= J_{ph} (\text{mA cm}^{-2} \times 1.23)\end{aligned}$$

Some n-type semiconductors with large band gaps partially cover the potentials of the O₂/H₂O redox couple, but they are unable to generate high photocurrent densities under AM 1.5 illumination. In contrast, p-type semiconductors with smaller band gaps (and higher photocurrent) exhibit more negative conduction/valence bands that can facilitate reactions at the H⁺/H₂ potential (Figure 1.8a), but they cannot be used alone. Metal oxide semiconductors materials are suitable for use as photoanodes since their valence band (VB) energy level is generally well below the energy level of O₂/OH⁻, promoting the water oxidation reaction (see figure 1.9b). However, for materials such as TiO₂, SrTiO₃, and KTaO₃ with large band gaps, the photoconversion efficiency is restricted to only a few percent.

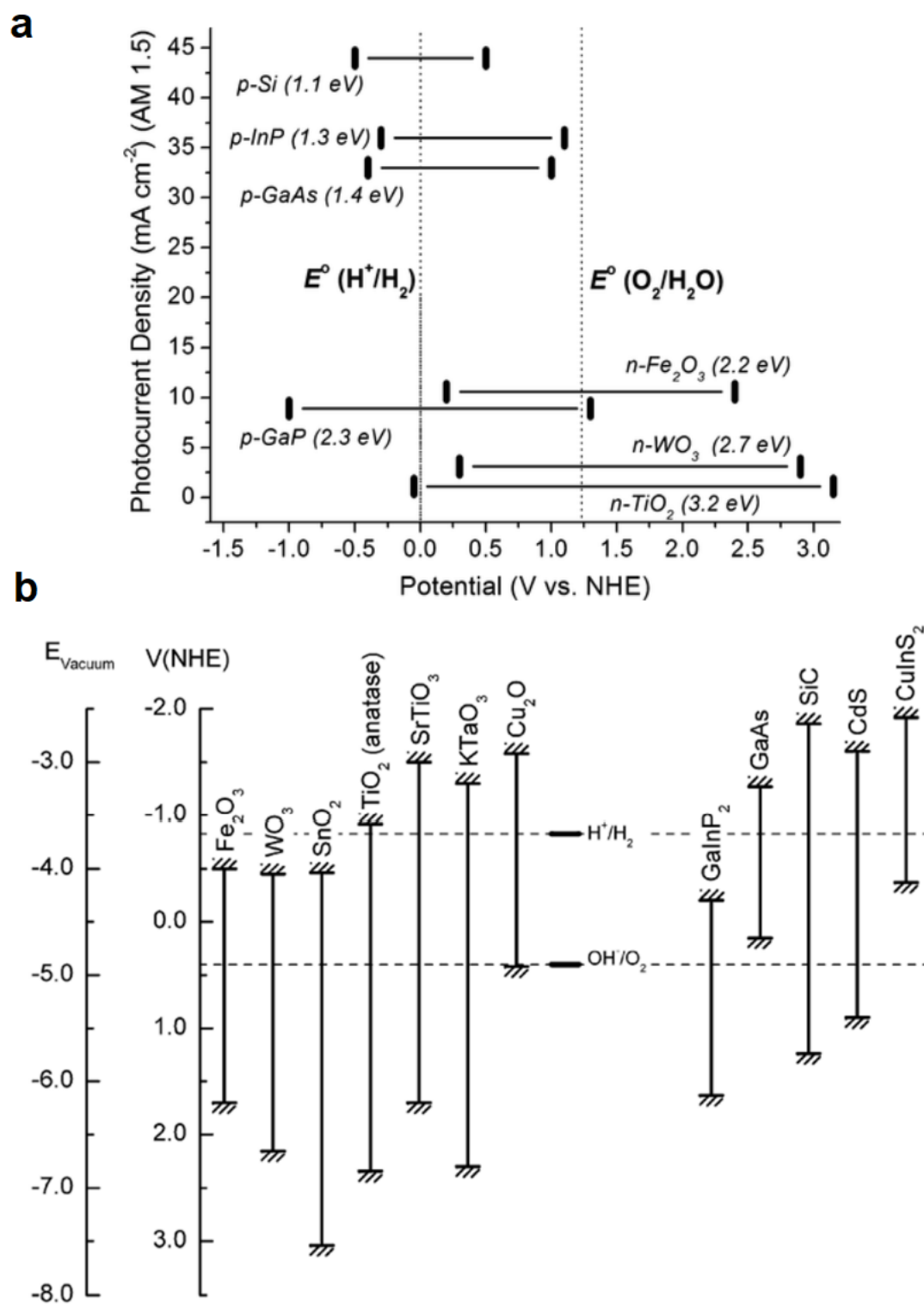


Figure 1.8: **a** Conduction band (left bar) and valence band (right bar) positions vs NHE at pH=0 of common semiconductors used in photoelectrolysis cells. The band gap value is in parentheses, and the ordinate indicates the maximum theoretical photocurrent under Air Mass 1.5 illumination.

*The dotted lines indicate the thermodynamic potentials for water reduction and oxidation, respectively. Reproduced from [15-Walter 2010]. **b** Band positions of various semiconductors with respect to the redox potentials of water splitting at pH=14 [26-van de Krol 2008].*

In this thesis, we will focus on systems made of n-type semiconductors with valence bands well below the O₂/H₂O potential suitable to drive water oxidation, and water reduction at a metallic cathode (Pt).

1.2.2 Charge carriers' separation and recombination

Recombination can occur through two pathways: direct and indirect. Direct recombination occurs when electrons and holes recombine within the photoanode, resulting in a loss of photocurrent. Indirect recombination occurs when electrons and holes are first separated, but then recombine at a later stage within the photoanode or at its interface with the electrolyte or other layers of the cell [22-Zhang 2012, 23-Pinaud 2013].

Photoanode recombination is a significant issue that limits the efficiency of PEC cells. To minimize recombination, photoanode materials are often designed to have high carrier mobility, low defect density, and appropriate energy band positions. Additionally, passivation layers or coatings can be applied to reduce surface recombination and enhance charge transport within the photoanode.

1.2.3 Stability in aqueous media

Ensuring the stability of materials in aqueous medium is a crucial necessity, at least for a minimum of 20 years (the average lifetime of these type of devices). To be a suitable water splitting semiconductor, a material should exhibit strong catalytic activity and stability while maintaining rapid surface reaction kinetics to avoid electron-hole recombination. Despite initial reports of high efficiencies in experiments, the process eventually degrades over time, primarily due to material oxidation, ultimately resulting in complete cessation of the process [22-Zhang 2012]. Hence, maintaining material stability is crucial to ensure the sustained performance of the process over time. Photocorrosion is a common issue for many water splitting semiconductors, particularly metal sulfides. Photocorrosion can occur if the semiconductor's band edges and decomposition potentials are not in favorable positions, causing the photoelectrode to decompose instead of oxidizing or reducing water. The anodic photocorrosion occur when the anodic decomposition potential is above the valence band potential of the semiconductor. While the cathodic photocorrosion occur when the cathodic decomposition

potential is below the conduction band of the semiconductor. As the actual values of the decomposition potentials depend on the pH value, some metal oxides, such as BiVO_4 and ZnO , and metal sulfides, such as MoS_2 and CdS , can easily undergo anodic photocorrosion due to the pH of the electrolyte. However, common photoanode materials such as TiO_2 and Fe_2O_3 , even though their anodic deposition potential is above the valence band potential, are thermodynamically stable because of their very slow decomposition reaction kinetics. Photocorrosion can also be influenced by other factors such as the crystal structure, morphology, and surface chemistry of the semiconductor [21-Jiang 2017].

Nonetheless, for practical applications and economical scale-up, it is crucial for the photoelectrode materials to be low-cost, composed of earth-abundant elements and stable in water. Therefore, we choose to work with BaTiO_3 and TiO_2 .

1.3 Nitrogen doping metal oxide photoanodes for efficient photoelectrochemical water splitting

Metal oxide photoanodes have been extensively studied for PEC water splitting due to their chemical stability, abundance, and ease of synthesis. However, the efficiency in PEC water splitting remains limited due to several factors such as charge carrier recombination, low light absorption, and slow charge transfer kinetics.

1.3.1 General improvement methods of metal oxide photoanode

Improving the efficiency of photoelectrodes is a key goal in the field of renewable energy. Here are some general ways to enhance photoelectrode efficiencies:

- *Doping*: Doping metal oxides with impurities can modify their electronic structure and improve their charge transfer kinetics. It is a widely used technique to modify the properties of semiconductor materials, including photoanodes used in solar water splitting applications. n-type doping introduces impurities that donate electrons to the material, thereby increasing its conductivity and carrier mobilities. In undoped or lightly doped semiconductors, the Fermi level is typically closer to the middle of the band gap. With increased n-type doping, the Fermi level can be shifted closer to the bottom of the conduction band. This shift increases the flat band potential, *i.e.* the potential difference between the surface of the photoanode and the electrolyte. This leads to a higher band bending at the interface between the photoanode and the electrolyte, providing more favorable conditions for charge separation

and efficient charge transfer at the photoanode-electrolyte interface [27-Zaleska 2008 to 33-Ihara 2003].

- *Surface modification*: Surface modification of metal oxide photoanodes with co-catalysts or passivating layers can improve their charge transfer kinetics and reduce surface charge carrier recombination [34-Sivula 2013, 35-Xi 2018].
- *Nanostructuring*: Nanostructuring involves the fabrication of metal oxide photoanodes with nanoscale features in order to increase the surface area and improve exchange with the electrode and to reduce the travel distance of the charge carriers. This can be achieved through techniques such as sol-gel processing, hydrothermal synthesis, and electrodeposition [36-Kay 2006, 37-Wang 2019].
- *Heterojunction formation*: Heterojunction formation involves the integration of two or more semiconducting materials with different bandgaps in order to improve light absorption and/or to create a built-in potential at the interface, which can improve the charge separation. For example, integrating a metal oxide photoanode with a metal sulfide or metal oxide catalyst can create a heterojunction that enhances the overall PEC water splitting efficiency [38-Chaves 2020, 39-Zhou 2012]
- *Electrolyte engineering*: The choice of electrolyte can also affect the efficiency of PEC water splitting. For example, using an electrolyte with a high concentration of a redox couple can increase the charge transfer efficiency and reduce charge carrier recombination [40-Tan 2021].

1.3.2 Our improvement method

The approach taken in this thesis, involves modifying the light absorption of oxide photoanodes through the introduction of dopants or defects that can modify the electronic properties of the material. More precisely, we have grown epitaxial oxide films of BaTiO_3 , TiO_2 and $\text{BaTa}_{1-x}\text{O}_{3-x}\text{N}_x$, to improve their photoanode efficiency by nitrogen doping and/or introducing oxygen vacancies.

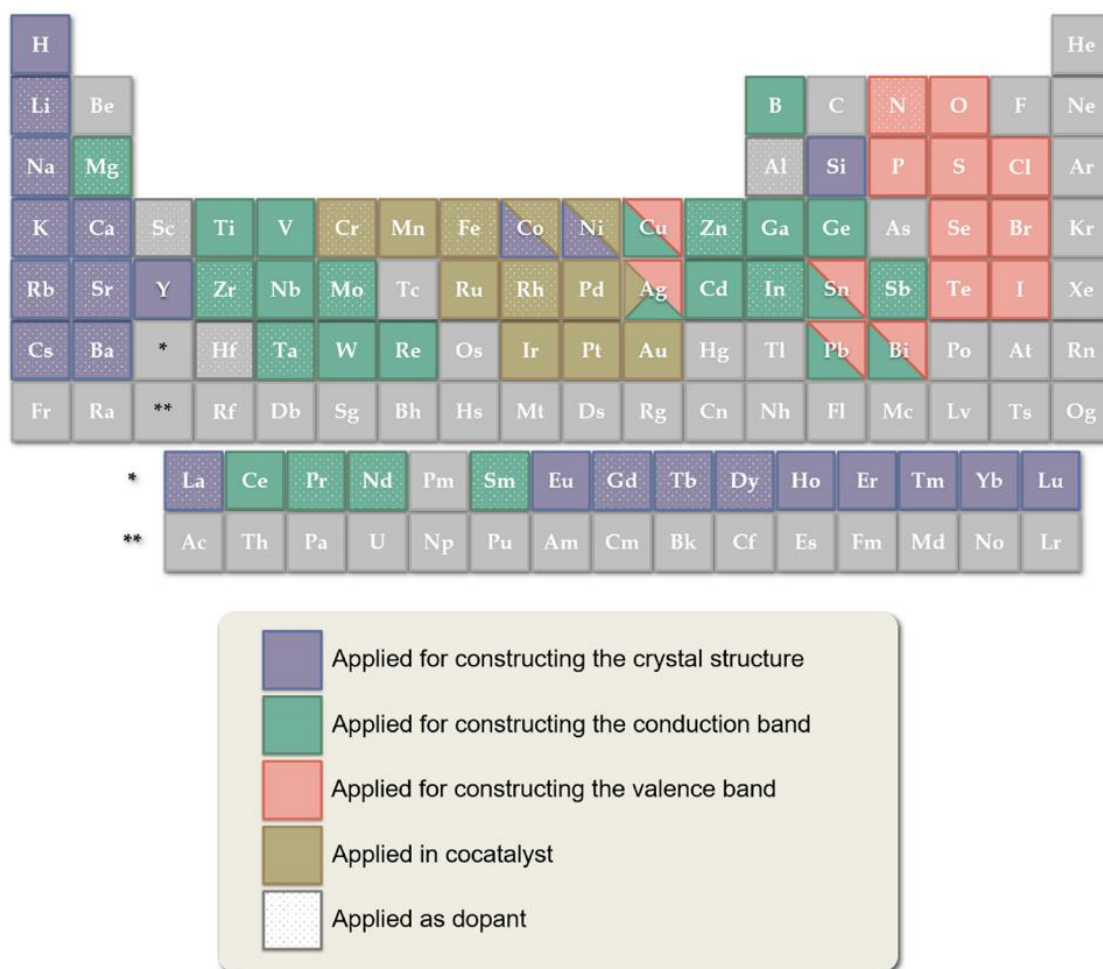


Figure 1.9: Elements used to construct photoelectrodes for water splitting and their roles [41-Wang 2019]

Wang et al. [41-wang 2019] have studied material design strategies for PEC and have summarized the role of each compound (Figure 1.9). Taking the examples of samples studied in this thesis (N doped-BaTiO₃, N doped-TiO₂ and BaTiO₃, and codoped Ta and N doped BaTiO₃), one expects that the conduction bands are influenced by the metal cations (Ti⁴⁺ and Ta⁵⁺), while the valence band is influenced by O-2p and N-2p orbitals. According to this study, barium does not directly influence the band structure and instead plays a role in constructing the perovskite crystal structure of the metal oxide. Nitrogen will then be in competition with the oxygen orbitals and contribute to the valence band. According to Wang and his team, one of the major challenges during the elaboration of material will be to maintain the symmetry of the metal oxygen octahedral/tetrahedral coordination, as well as the VB and CB structures, without compromising the efficiency of the photoanodes [41-Wang 2019].

1.3.3 N-Doping influence

Doping with anionic nonmetals, such as nitrogen, has been a popular approach for enhancing the visible light response of semiconductors. This is because anionic dopants create localized energy states in the bandgap of the semiconductor, which extends the efficient absorption for water oxidation from the UV-light region (≤ 400 nm) to the visible-light region ($\leq \sim 550$ nm), and generate electron-hole pairs. Compared to cationic doping, anionic doping may result in fewer recombination centers, and better photoelectrochemical activity [27-Zaleska 2008- 28-Di Valentin 2004].

For example, nitrogen doping into TiO_2 , introduces energy levels within the bandgap of the metal oxide, allowing a better absorption of visible light [27-Zaleska 2008 to 33-Ihara 2003]. Therefore one can expect an increased electron-hole pair generation and, consequently, higher photocurrent. The band gap narrowing can be explained by the schematic band structure (figure 1.10).

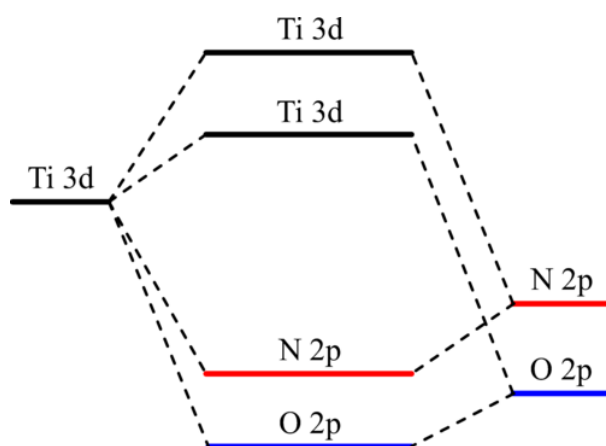


Figure 1.10: Schematic band structure of an insulating titanium oxynitride (Ti-N-O compound). The valence band consists mainly of hybridized orbitals from N-2p and O-2p states, whereas the conduction band is dominated by empty Ti-3d orbitals. Octahedral coordination around Ti atoms splits the 3d band into lower and upper levels [42-Aoki 2014].

The valence band consists mainly of hybridized orbitals from N-2p and O-2p states. As a result of the lower electronegativity of nitrogen compared to oxygen, the N-2p is above O-2p, leading to a shift of the valence band with respect to undoped TiO_2 , and therefore a gap reduction.

A second example is the case of DFT calculations on tantalum (oxy)nitride compounds as a function of the O/N ratio (Figure 1.11). It shows that not only the band gap can be tuned to ideal values for visible light absorption, but also that the valence and conduction bands can be ideally positioned with respect to the water redox potentials.

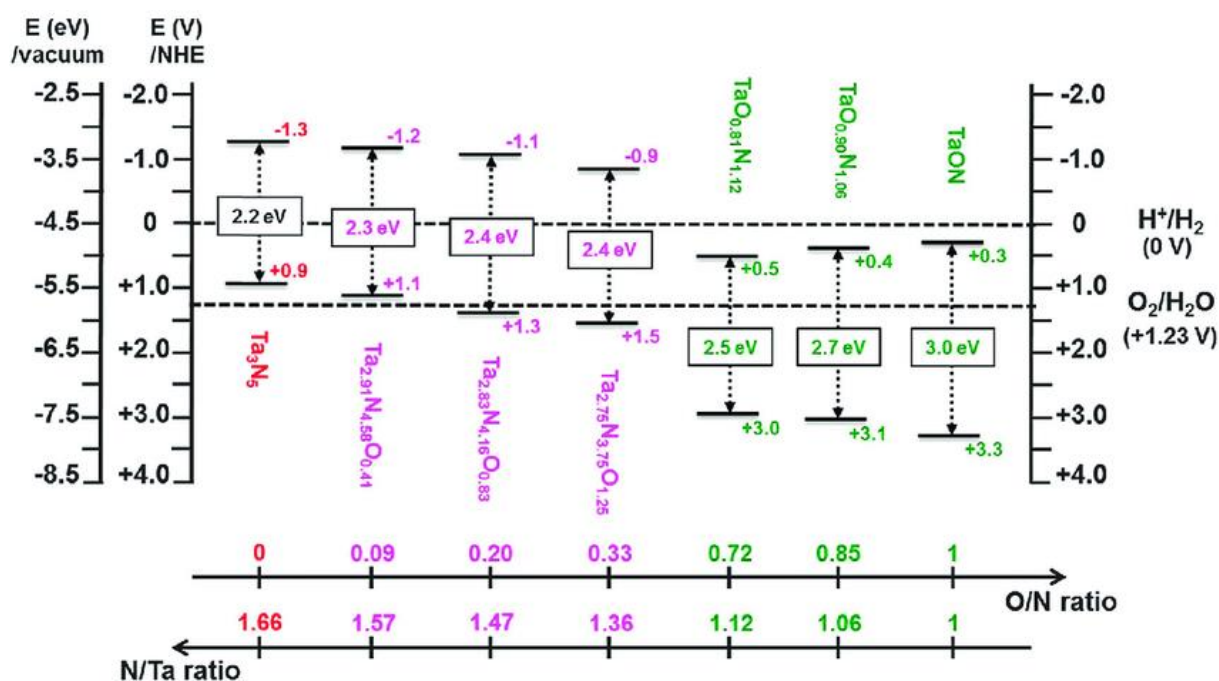


Figure 1.11 Representation of narrowing the band gap of a semiconductor by doping [43-Harb 2014]

The incorporation of nitrogen into metal oxides can be achieved by interstitial or substitutional doping. The position of the N-2p level in the band gap, in the case of anatase, depends on the site occupied by the nitrogen atom (interstitial or substitutional) (see figure 1.12). Studies have reported that interstitial N-doping of TiO₂ is better for narrowing the band gap compared to substitutional N-doping [44-Sushma 2017, 45-Boningari 2018]. Therefore, it might be more effective for achieving high visible-light absorption, while substitutional doping may be preferred for improving the stability and durability of the photoelectrode [46-Piatkowska 2021].

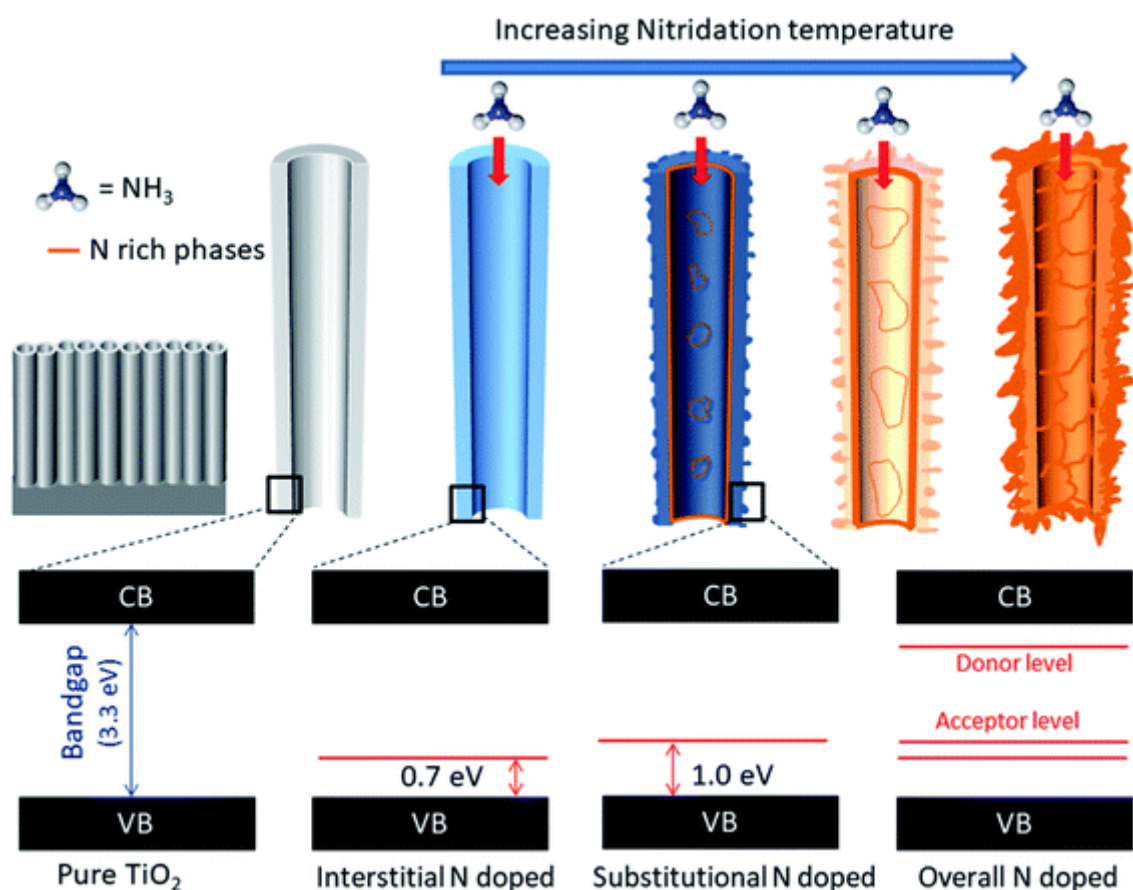


Figure 1.12: Schematic representation of N doping via increasing nitridation temperature and respective bandgaps and the presence of interband states related to interstitial and substitutional doping [47-Khan 2021].

For PEC application, it is not sufficient to have an efficient light absorption; it is also necessary to reduce the electron/hole recombination. The N-2p level situated in the gap can also be seen as a defect state or an impurity state in the bandgap, which can act as recombination centers for photo-generated charge carriers.

Nitrogen impurity states are typically located near the valence band (VB) edge, their exact position and nature may vary depending on the specific metal oxide and preparation conditions. In some cases, nitrogen impurity states can act as shallow acceptor states, meaning that they can accept electrons from the valence band and become negatively charged.

However, in other cases, nitrogen impurity states can instead act as recombination centers for photo-generated charge carriers, leading to a decrease in the photocurrent generation. The position of the N-2p state in the gap is believed to be controlled by adjusting the doping concentration and the annealing temperature. Optimizing these parameters is believed critical for achieving high-performance nitrogen-doped metal oxide photoanodes for visible-light-driven water splitting.

1.3.4 Oxygen vacancies effect

In 2001, Asahi *et al.* conducted first-principles calculations to investigate the effect of N doping on the bandgap of TiO₂ [31-Asachi 2001]. They found that N-2*p* state could hybridize with O-2*p* state, leading to a narrowed bandgap and improved photoactivity under visible light. However, since then, other experimental and theoretical studies have challenged this conclusion, suggesting that N doping may introduce impurity energy levels or defects such as V_o/Ti³⁺ instead of reducing the bandgap. N³⁻ and O²⁻ ions have different charge states, and the incorporation of N atoms into TiO₂ can create charge imbalances that promotes the formation of V_o. This results in the formation of Ti³⁺ ions and oxygen vacancies (V_o), which can act as electron traps and reduce the photocurrent efficiency of TiO₂.

For instance, in their study, Irie *et al.* found that the incorporation of nitrogen into TiO₂ resulted in a decrease in the band gap and a shift in the absorption edge towards the visible region, indicating the formation of midgap states. However, they observed that the quantum yield of the TiO_{2-x}N_x was lower under visible light illumination compared to UV light, regardless of the N concentration [32-Irie 2003]. The authors found that nitrogen doping increased the concentration of oxygen vacancies in the material and enhanced the visible-light absorption. The increase in oxygen vacancy concentration was attributed to the substitution of nitrogen for oxygen sites.

It is also worth noting that the efficiency of anionic non metal doping can be influenced by several factors, including the dopant concentration, the synthesis method, and the annealing conditions. Higher doping concentrations may lead to the formation of recombination centers and therefore, the reduction of the concentration of free charge carriers available for redox reactions. Low doping concentrations lead to vacancies and defects affecting the stability of the material. To mitigate the instability introduced by incorporating nitrogen into metal oxide photoanodes, the choice of synthesis method to control the distribution of dopants within the semiconductor lattice and their photoelectrochemical properties is crucial.

1.3.5 Epitaxial thin film photoanodes

While anionic doping by itself may not directly increase the specific surface area of the semiconductor, it can indirectly lead to these improvements through the changes in the crystal structure and morphology. For instance, doping with nitrogen, carbon, or sulfur can alter the crystal structure of TiO₂, resulting in the formation of different polymorphs or phases that may have different surface properties, such as higher specific surface area or pore volume [48- Lian 2022, 46- Piatkowska 2021 41-

Wang 2019]. Furthermore, anionic doping can also modify the surface chemistry of the semiconductor, leading to the creation of new active sites or changes in the electronic properties of existing active sites. These modifications can enhance the photocurrent efficiencies.

Various techniques can be used to introduce nitrogen into the semiconductor material, including solid state-reactions, sol-gel methods, and hydrothermal synthesis. The specific technique used depends on the material being doped and the desired doping concentration.

- *Solid-state reactions*: This doping technique involves mixing the host material and dopant in a solid-state and then heating the mixture to a high temperature to promote diffusion. This technique has as advantage to introduce a wide range of dopants. However, the difficulty in controlling the diffusion of the dopant, and the high temperatures results in solid-state reactions, in non-uniform doping and the formation of undesired phases.
- *Sol-gel methods*: This technique involves the preparation of a sol or a gel containing the host material and dopant, followed by drying and calcination to form the final product. it allows a good control over the composition and size of the nanoparticles produced. Although, the technique is time-consuming and the final product may contain residual solvents impurities.
- *Hydrothermal synthesis*: In this technique, the host material and dopant are mixed in an aqueous solution and subjected to high pressure and temperature. Hydrothermal synthesis can produce highly crystalline and uniform particles with a high surface area, and it is also relatively simple to scale up. However, this technique requires specialized equipment and can be challenging to control.

However, achieving water splitting using materials grown from these processes has been challenging due to charge recombination at crystal defects and grain boundaries. To avoid all these drawbacks, our strategy is to use molecular beam epitaxy (MBE) for (oxy)nitride synthesis. It allows a precise control over the composition of the thin film. The oxygen and nitrogen fluxes can be adjusted independently, to finally produce high-quality, epitaxial thin films with good crystallographic properties and low defect densities. The main advantage of MBE, is to be able to vary the different parameters important for PEC (structure, thickness, doping) independently. Although, this techniques is limited to small areas of substrates and is difficult to scale up for mass production. It is therefore, restricted to fundamental studies.

1.3.6 Summary

Nitrogen doping of oxide materials holds promise for photoelectrochemical (PEC) applications. The introduction of nitrogen into oxide materials can result in a narrower band gap, which enhances their ability to absorb visible light. The positions of the energy bands can also be tuned by adjusting the amount of nitrogen doping, offering opportunities for optimizing their electronic properties.

However, nitrogen doping can introduce oxygen vacancies to maintain charge balance of the unit cell, and this introduces a competition between reducing the band gap and increasing recombination rates. The presence of nitrogen-induced electronic states within the band gap, as well as the presence of oxygen vacancies, raises questions about their impact on PEC performance.

1.4 References

- [1]. National Renewable Energy Laboratory (NREL). Hydrogen Basics. Available online: <https://www.nrel.gov/hydrogen/hydrogen-basics.html>
- [2]. D. Hart, J. Howes, B. Madden and E. Boyd. (2016). Hydrogen and Fuel Cells: Opportunities for Growth. A Roadmap for the UK, E4Tech and Element Energy.
- [3]. Cavendish H. Three papers, containing experiments on factitious air, by the Hon. Henry Cavendish, F.R.S., communicated by Dr. Priestley. (1766) Philos Trans R Soc Lond. 56:141-184.
- [4]. Nicholson, W. & Carlisle, A. (1800). Experiments and observations on the decomposition of water and of the bodies which it holds in solution by means of electricity. Philosophical Transactions of the Royal Society of London, 90, 1-32.
- [5]. Ritter, J. (1801). On the chemical effects of electrical currents. Annals of Philosophy, 2(6), 411-418.
- [6]. S.Y. Tee, K.Y. Win, W.S. Teo, L.-D. Koh, S. Liu, C.P. Teng, et al. (2017) Recent progress in energy-driven water splitting, Adv. Sci. 4, 1600337
- [7]. Hosseini, S.E.; Wahid, M.A. (2016). Hydrogen production from renewable and sustainable energy resources: Promising green energy carrier for clean development. Renew. Sustain. Energy Rev. 57, 850–866
- [8]. El-Emam, R. S., Zamfirescu, C., & Gabriel, K. S. (2023). Hydrogen production pathways for Generation-IV reactors. In Handbook of Generation IV Nuclear Reactors (pp. 665-680). Woodhead Publishing.
- [9]. Wang, L., Pérez-Fortes, M., Madi, H., Diethelm, S., & Maréchal, F. (2018). Optimal design of solid-oxide electrolyzer based power-to-methane systems: A comprehensive comparison between steam electrolysis and co-electrolysis. Applied Energy, 211, 1060-1079.
- [10]. Gallandat, Noris & Romanowicz, Krzysztof & Züttel, Andreas. (2017). An Analytical Model for the Electrolyser Performance Derived from Materials Parameters. Journal of Power and Energy Engineering. 05. 34-49.
- [11]. Grätzel, (2001). M. Photoelectrochemical cells. Nature 414, 338–344

- [12]. Lianos, P. (2011). Production of electricity and hydrogen by photocatalytic degradation of organic wastes in a photoelectrochemical cell: the concept of the photofuelcell: a review of a re-emerging research field. *Journal of Hazardous Materials*, 185(2-3), 575-590.
- [13]. Jeong, Sang Yun, Jaesun Song, and Sanghan Lee. (2018). Photoelectrochemical Device Designs toward Practical Solar Water Splitting: A Review on the Recent Progress of BiVO₄ and BiFeO₃ Photoanodes. *Applied Sciences* 8, no. 8: 1388.
- [14]. W. Shockley, (1957). Electrons and Holes in Semiconductors, in *Solid State Physics*, vol. 1, F. Seitz and D. Turnbull, Eds. New York: Academic Press, 1957, pp. 361-438.
- [15]. M. G. Walter, E. L. Warren, J. R. McKone, S. W. Boettcher, Q. Mi, E. A. Santori, and N. S. Lewis. (2010). Solar water splitting cells. *Chemical Reviews* 110, 6446
- [16]. Biswas, N. K., Srivastav, A., Saxena, S., Verma, A., Dutta, R., Srivastava, M., ... & Dass, S. (2023). The impact of electrolytic pH on photoelectrochemical water oxidation. *RSC advances*, 13(7), 4324-4330.
- [17]. Schmickler, W. and E. Santos. (2010). *The Semiconductor-Electrolyte Interface. Interfacial Electrochemistry*. Springer Berlin Heidelberg.117
- [18]. Xu, X. T., Pan, L., Zhang, X., Wang, L., & Zou, J. J. (2019). Rational design and construction of cocatalysts for semiconductor-based photo-electrochemical oxygen evolution: a comprehensive review. *Advanced Science*, 6(2), 1801505.
- [19]. S. M. Sze and K. K. Ng, (2006). *Physics and properties of semiconductors - a review*, in *Physics of Semiconductor Devices* .John Wiley & Sons, Inc.
- [20]. T. R. Cook, D. K. Dogutan, S. Y. Reece, Y. Surendranath, T. S. Teets and D. G. Nocera. (2010). Solar Energy Supply and Storage for the Legacy and Nonlegacy Worlds. *Chem. Rev.* 110, 6474-6502.
- [21]. Jiang, C., Moniz, S. J., Wang, A., Zhang, T., & Tang, J. (2017). Photoelectrochemical devices for solar water splitting—materials and challenges. *Chemical Society Reviews*, 46(15), 4645-4660
- [22]. Zhang, H.; Huang, H.; Ming, H.; Li, H.; Zhang, L.; Liu, Y.; Kang, Z. Carbon quantum dots/Ag₃PO₄ complex photocatalysts with enhanced photocatalytic activity and stability under visible light. *J. Mater. Chem.* (2012), 22, 10501–10506.

- [23]. B. A. Pinaud, J. D. Benck, L. C. Seitz, A. J. Forman, Z. Chen, T. G. Deutsch, B. D. James, K. N. Baum, G. N. Baum and S. Ardo. (2013). Technical and economic feasibility of centralized facilities for solar hydrogen production via photocatalysis and photoelectrochemistry. *Energy Environ. Sci.*, 6, 1983-2002
- [24]. Q. Meng. (2021). Surface Engineering of BiVO₄-based Photoelectrochemical Cells for Water Splitting. Ph.D. Thesis. kth royal institute of technology, Sweden.
- [25]. L. Vayssieres, (2010). On solar hydrogen and nanotechnology, John Wiley & Sons.
- [26]. R. van de Krol, Y. Liang, and J. Schoonman. (2008). Solar hydrogen production with nanostructured metal oxides. *Journal of Materials Chemistry* 18, 2311
- [27]. A. Zaleska. (2008). Doped-TiO₂: a review, *Recent Pat. Eng.* 2, 157–164
- [28]. Di Valentin, C., Pacchioni, G., & Selloni, A. (2004). Origin of the different photoactivity of N-doped anatase and rutile TiO₂. *Physical review B*, 70(8), 085116.
- [29]. Piątkowska, Aleksandra, Magdalena Janus, Kacper Szymański, and Sylwia Mozia. (2021). C-,N- and S-Doped TiO₂ Photocatalysts: A Review. *Catalysts* 11, no. 1: 144.
- [30]. S. Cho, J. W. Jang, K. J. Kong, E. S. Kim, K. H. Lee, and J. S. Lee. (2013). *Adv. Funct. Mater.* 23(19), 2348
- [31]. Asahi R, Morikawa T, Ohwaki T, Aoki K, Taga Y. (2001) .Visible-light photocatalysis in nitrogen-doped titanium dioxide. *Science*; 293: 269-271.
- [32]. Irie, H., Watanabe, Y., & Hashimoto, K. (2003). Nitrogen-concentration dependence on photocatalytic activity of TiO₂-x N x powders. *The Journal of Physical Chemistry B*, 107(23), 5483-5486.
- [33]. Ihara T, Miyoshi M, Triyama Y, Marsumato O, Sugihara S. (2003) Visible-light-active titanium oxide photocatalyst realized by an oxygen-deficient structure and by nitrogen doping. *Appl Catal B*; 42: 403-409.
- [34]. K. Sivula. (2013). Metal Oxide Photoelectrodes for Solar Fuel Production, Surface Traps, and Catalysis *Phys. Chem. Lett.* 4, 10, 1624–1633
- [35]. Xi, L., & Lange, K. M. (2018). Surface modification of hematite photoanodes for improvement of photoelectrochemical performance. *Catalysts*, 8(11), 497.
- [36]. A. Kay, I. Cesar, and M. Grätzel. (2006). New Benchmark for Water Photooxidation by Nanostructured α -Fe₂O₃ Films. *Journal of the American Chemical Society* 128, 15714.

- [37]. Wang, J., Cui, Y., & Wang, D. (2019). Design of hollow nanostructures for energy storage, conversion and production. *Advanced Materials*, 31(38), 1801993
- [38]. Chaves, A., Azadani, J. G., Alsalman, H., Da Costa, D. R., Frisenda, R., Chaves, A. J., ... & Low, T. (2020). Bandgap engineering of two-dimensional semiconductor materials. *npj 2D Materials and Applications*, 4(1), 29.
- [39]. Zhou, H., Qu, Y., Zeid, T., & Duan, X. (2012). Towards highly efficient photocatalysts using semiconductor nanoarchitectures. *Energy & Environmental Science*, 5(5), 6732-6743.
- [40]. Tan, J., & Liu, J. (2021). Electrolyte engineering toward high-voltage aqueous energy storage devices. *Energy & Environmental Materials*, 4(3), 302-306.
- [41]. Wang, Q., & Domen, K. (2019). Particulate photocatalysts for light-driven water splitting: mechanisms, challenges, and design strategies. *Chemical Reviews*, 120(2), 919-985.
- [42]. Aoki, Y., Sakurai, M., Coh, S., Chelikowsky, J. R., Louie, S. G., Cohen, M. L., & Saito, S. (2019). Insulating titanium oxynitride for visible light photocatalysis. *Physical Review B*, 99(7), 075203.
- [43]. Harb, M., Sautet, P., Nurlaela, E., Raybaud, P., Cavallo, L., Domen, K., ... & Takanabe, K. (2014). Tuning the properties of visible-light-responsive tantalum (oxy) nitride photocatalysts by non-stoichiometric compositions: a first-principles viewpoint. *Physical Chemistry Chemical Physics*, 16(38), 20548-20560.
- [44]. Sushma, C.; Kumar (2017). S.G. C–N–S Tridoping into TiO₂ matrix for Photocatalytic Applications: Observations, Speculations and Contradictions in the Codoping Process. *Inorg. Chem. Front.* 4, 1250–1267.
- [45]. Boningari, T.; Inturi, S.N.R.; Suidan, M.; Smirniotis, P.G. (2018). Novel One-Step Synthesis of Nitrogen-doped TiO₂ by Flame Aerosol Technique for Visible-Light Photocatalysis: Effect of Synthesis Parameters and Secondary Nitrogen (N) Source. *Chem. Eng. J.* 350, 324–334
- [46]. Piątkowska, A., Janus, M., Szymański, K., & Mozia, S. (2021). C-, N-and S-doped TiO₂ photocatalysts: A review. *Catalysts*, 11(1), 144.
- [47]. Khan, S., Ruwer, T. L., Khan, N., Köche, A., Lodge, R. W., Coelho-Júnior, H., ... & Fernandes, J. A. (2021). Revealing the true impact of interstitial and substitutional nitrogen

doping in TiO₂ on photoelectrochemical applications. *Journal of Materials Chemistry A*, 9(20), 12214-12224.

- [48]. Du, S., Lian, J. & Zhang, F. (2022). Visible Light-Responsive N-Doped TiO₂ Photocatalysis: Synthesis, Characterizations, and Applications. *Trans. Tianjin Univ.* 28, 33–52

Chapter II

Experimental details

***Summary:** This chapter discusses briefly the important aspects of epitaxy and epitaxial growth of thin films. Section 2.1 deals with fundamental aspects of epitaxy. Section 2.2 is a summary of past work on epitaxial thin films. Their main deposition methods used to prepare the samples during my Ph.D. work are introduced. Section 2.3 to 2.5 describe the characterization technics used to study the films.*

2.1 Epitaxy and epitaxial thin films

During the early 1960s, a significant breakthrough occurred in the field of growing metal films on surfaces using vacuum deposition techniques. Researchers at Bell Labs developed a technique called molecular beam epitaxy (MBE) allowing for the precise control of epitaxial growth thin films. [1-Cho, A. Y., & Arthur, J. R. 1976].

2.1.1 Epitaxy

2.1.1.1 Definition

The term "epitaxy" is derived from the greek words "epi" and "taxis," which mean "on top of" and "arrangement," respectively. In epitaxial thin film growth, a crystalline film is grown on top of a substrate such as to be highly ordered and aligned with the substrate [2-Sze 2007]. The orientation relationship is driven by the crystal systems and lattice parameters. Epitaxy can be classified into two types: *Homoepitaxy* and *Heteroepitaxy*. Homoepitaxy refers to the state when both, the film and the substrate, are made of the same material. Heteroepitaxy is the most common form in various applications such as semiconductors, ferroelectrics or optoelectronic devices, and is related to the situation where film and substrate are dissimilar.

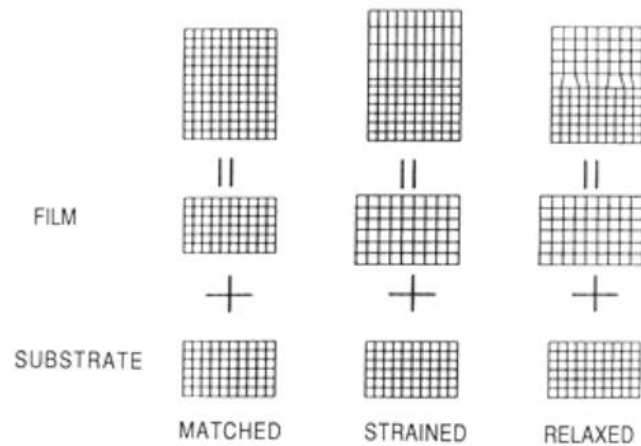


Figure 2.1: Schematic illustration of lattice matched, strained and relaxed epitaxy [3- Ohring 1992]

In epitaxial growth, matching the lattice between the substrate and the deposited material is important for achieving high-quality films with low defect densities. Depending on the lattice parameters, different regimes can occur (Figure 2.1) [3- Ohring 1992]:

- The matched regime: when the difference between the two lattice parameters is small
- The strained regime: when the two lattices strain to accommodate their crystallographic structure
- The relaxed regime: when edge dislocations form at the interface

2.1.1.2 Important parameters for epitaxial growth

The quality of the epitaxial layer depends on the nature of the substrate. The substrate material should be a single crystal with a high degree of structural perfection, and suitable crystallographic orientation to enable the epitaxial layer to grow uniformly and without defects. Moreover, low surface contamination is necessary to obtain pure epitaxial layer. The growth temperature is also an important parameter. Due to the thermal induced mobility, higher temperatures lead to better crystalline growth that can be detrimental to the 2D nature of the film.

The deposition rate is also an important parameter. If it is too high, the thin film may become non-uniform, rough, or contain defects.

2.2 Film deposition techniques of metal oxide films

Solid-state reaction are the typical techniques used to produce bulk oxide materials, which can result in polycrystalline or single-crystal structures. High temperatures and pressures, can often lead to

defects, impurities, or phase transitions that can significantly affect the properties of these bulk materials. It was after the key developments of thin film growth techniques in the 1980s and 1990s, that researchers began to apply these techniques to the growth of *multi-component complex oxide thin films*. The goal is to create materials with unique and tunable properties such as ferroelectricity, magnetism, and high dielectric constant, that found applications in fields such as electronics, optics, and energy storage (Figure 2.2).

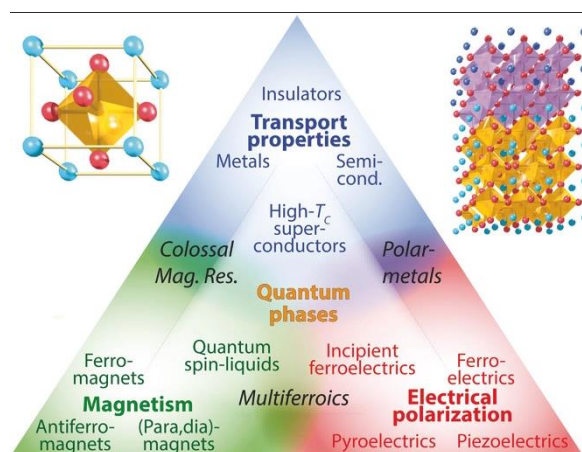


Figure 2.2: The ABO_3 perovskite family of complex oxides hosting a wide array of functional properties and electronic phases. The basic BO_6 octahedral unit is located at the center of the unit cell with A sites on the corner (top left). This simple building block enables a large configurational space for functional heterostructures of structurally similar films with diverse properties (top right) [6-Brahlek, M., Gupta, A. S., Lapano, 2018].

Over the years, various processes have been developed for the deposition of metal oxide thin films based mainly on physical vapor deposition processes (PVD) and chemical processes.

PVD includes, Pulsed Laser Deposition (PLD) that uses a high-power laser to ablate a target material, the ablated material then condenses onto a substrate to form a thin film. It also includes magnetron sputtering which involves bombarding a target material with high-energy ions in a vacuum chamber. The ion bombardment dislodges atoms from the target material, which then travel through the vacuum and condense onto a substrate, forming a thin film. Without forgetting to mention Molecular Beam Epitaxy (MBE), where solid materials are evaporated to form beams of atomic or molecular species. It is typically done at higher temperatures (around 600-800°C) as compared to hybrid vapor phase MBE (*h*MBE) where thin films are grown on substrates at relatively low temperatures (typically around 400-600°C) with a graded composition by combining two or more deposition techniques. *h*MBE uses both solid and metallic organic sources. For example, Egawa *et al.* described the growth

of AlGaIn/GaN heterostructures using *h*MBE, where the GaN layer was grown using plasma-assisted MBE and the AlGaIn layer was deposited using MOCVD [5-Egawa 2005].

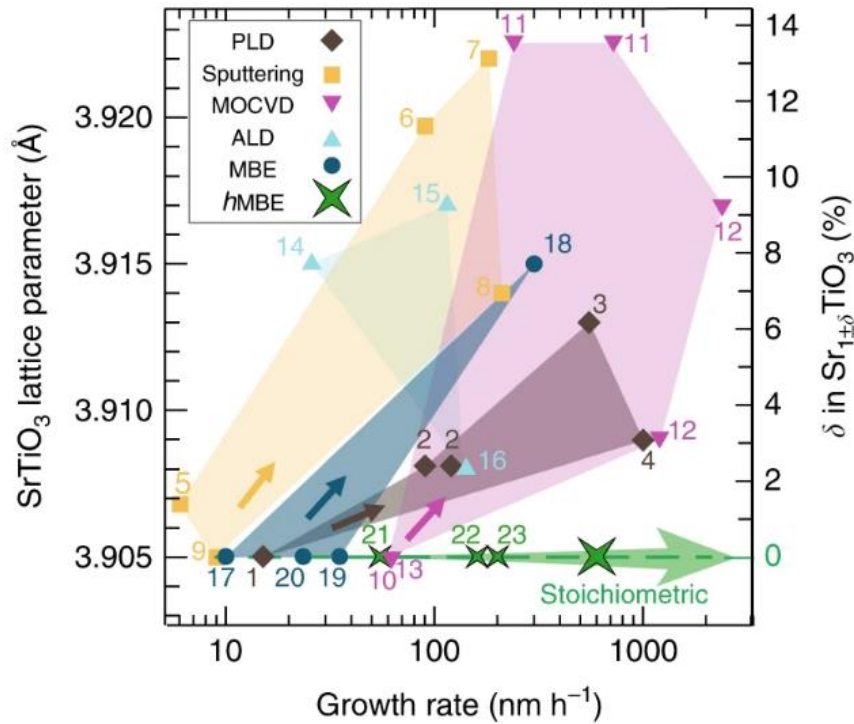


Figure 2.3: Intrinsic SrTiO₃ film lattice parameter reported for different growth rates using scalable oxide thin film growth techniques: Pulsed Laser Deposition (PLD), sputtering, Metal-Organic Chemical Vapor Deposition (MOCVD), Atomic Layer Deposition (ALD), Molecular Beam Epitaxy (MBE), and hybrid Molecular Beam Epitaxy (*h*MBE). The defect concentration δ due to nonstoichiometric growth condition was determined from the intrinsic film lattice parameter expansion [4-Lapano, 2019].

For chemical vapor deposition processes, we can cite MOCVD (Metal-Organic Chemical Vapor Deposition) and ALD (Atomic Layer Deposition). The first technique is based on vaporizing metal-organic precursors, while ALD uses two or more precursors that are introduced into a reaction chamber once at a time.

The choice of which technique to use depends on the specific material system and application requirements as well as the desired structure and needs. For example, Lapano *et al.* [4-Lapano, 2019] (Figure 2.3) compiled the lattice parameter of SrTiO₃ as a function of growth rate and growth method. They found that in this case MBE and *h*MBE methods can produce stoichiometric SrTiO₃.

2.2.1 Oxygen and Nitrogen Plasma Assisted Molecular Beam Epitaxy (O&NPA-MBE)

In 1970, the term molecular beam epitaxy (MBE) was firstly, used by Cho and his team [17-Cho 1970]. The development of the technique was driven by the need for a crystal growth technology that could prepare single crystalline films of few nanometers, in high quality and purity for use in electronic devices.

Oxygen and Nitrogen Plasma Assisted Molecular Beam Epitaxy (O&N PA-MBE) is an Ultra-High-Vacuum (UHV) based technique for producing homogenous epitaxial oxide or nitride films. The base pressure in the chamber (*ca.* 10^{-10} mbar) makes the environment free of polluting molecules (*e.g.* water, carbon) and oxygen, and allows for the elaboration of high-purity films.

A description of the growth apparatus, used in this thesis is given in figure 2.4; it is equipped with oxygen and nitrogen plasma source.

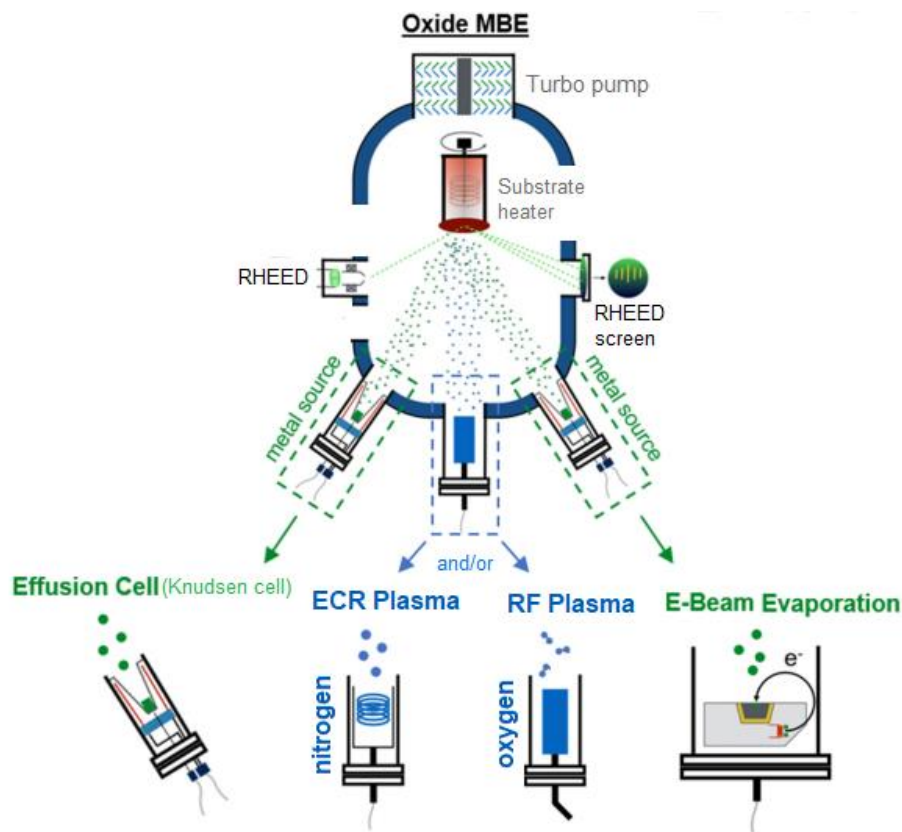


Figure 2.4: O&NPA-MBE deposition chamber: a schematic representation

The vacuum system consists in a stainless-steel growth chamber, which is connected to a preparation chamber under UHV (ultra-high vacuum) conditions and an airlock mechanism, ensuring the integrity

of the vacuum environment. Several sample manipulators allow for the transfer of samples from the growth chamber to - and back to the ambient air when needed. The components of the growth chamber must resist to temperatures up to 200°C for prolonged durations for bakeout in order to reduce out-gassing from internal walls.

Several pumping systems allow to reach a base pressure of about 10^{-10} mbar: turbo molecular pump, ion pumps, and Ti-sublimation, secure the quality of the vacuum.

In this apparatus, the metal oxide(nitride) is elaborated, using separated Knudsen sources for metals, or e-beam source for refractory materials, an RF plasma oxygen source, and an ECR nitrogen source.

A Knudsen cell typically consists of a crucible heated to high temperatures to evaporate the material to be deposited. For example, titanium is evaporated in a W crucible at around 1200 °C, and barium in a Ta crucible at around 430°C. The evaporated material then condenses onto the substrate to form an oxide or a nitride by reaction with the plasma. To control the metal flux, the temperature of the crucible is adjusted and calibrated using a quartz microbalance temporarily placed at the same location as the sample during calibration.

In addition to Knudsen cells, we used also an electron beam evaporator, for tantalum evaporation. In this evaporator, the material is placed in a crucible, and an electron beam is directed onto the material, causing it to heat up and evaporate. It is especially suitable for refractory materials.

During growth, the substrate is heated up to 600° C, and the sample holder can rotate around its normal to ensure an homogeneous growth.

In situ characterization tools allow to monitor the growth process in real-time and provide feedback for optimizing growth conditions such as reflection high-energy electron diffraction (RHEED). Post growth Auger and XPS spectroscopies provide information about the chemical composition of the samples.

2.2.1.1 Radio frequency oxygen plasma source (RF)

An oxygen plasma source is used to provide atomic oxygen to assist the growth process. The plasma is generated by a radio-frequency (RF) power source by exciting oxygen gas using radio frequency waves within a quartz cavity at 350W (Figure 2.5). The resulting plasma is composed of electrons, molecular oxygen, and monoatomic oxygen, with the latter comprising around 20% of the total composition.

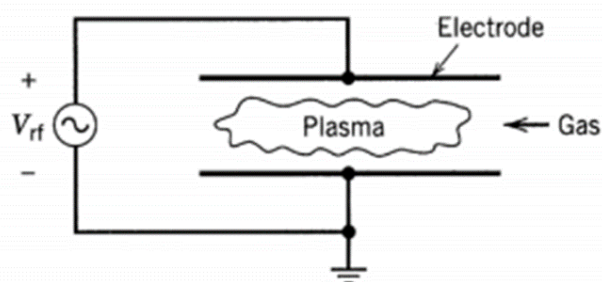


Figure 2.5: Schematic drawing of the principal of the RF source

Monoatomic oxygen makes it highly oxidant. A Baratron® pressure controller device manufactured by MKS controls the flow of oxygen into the quartz cavity. The gas is then introduced into the O&NPA-MBE chamber through a 200µm diameter hole, and the flux of monoatomic oxygen can be controlled by adjusting the Baratron® parameter in turns corresponding to a precise pressure in the cavity. Increasing the turns results in a higher oxygen partial pressure and a higher flux of monoatomic oxygen. For instance, the perfect oxidation of TiO₂ layers corresponds to 3.5 turns and a pressure in the 10⁻⁷mbar range in the MBE chamber.

2.2.1.2 Electron cyclotron resonance nitrogen plasma source (ECR)

The plasma source used to nitride the films, is an Electron Cyclotron Resonance (ECR) hybrid nitrogen plasma source from SPECS GmbH (Berlin, Germany). Fully compatible with ultra-high vacuum (UHV) conditions, the plasma source utilizes microwaves with a frequency of 2.45 GHz, which are generated by a microwave magnetron and coupled to the plasma chamber. In the chamber, the microwaves excite a plasma and are absorbed. The plasma density is enhanced by the magnetron cyclotron resonance effect, which is provided by an 86 mT magnetic quadrupole arranged around the plasma chamber [9-SPECS]. The electrons in the plasma undergo electron cyclotron resonance motion, which greatly increases their path length and the probability of collision with other molecules, leading to ionization. This effect enhances the ionization rate and improves the efficiency of the plasma source (Figure 2.6 for the principle and Figure 2.7 for the setup).

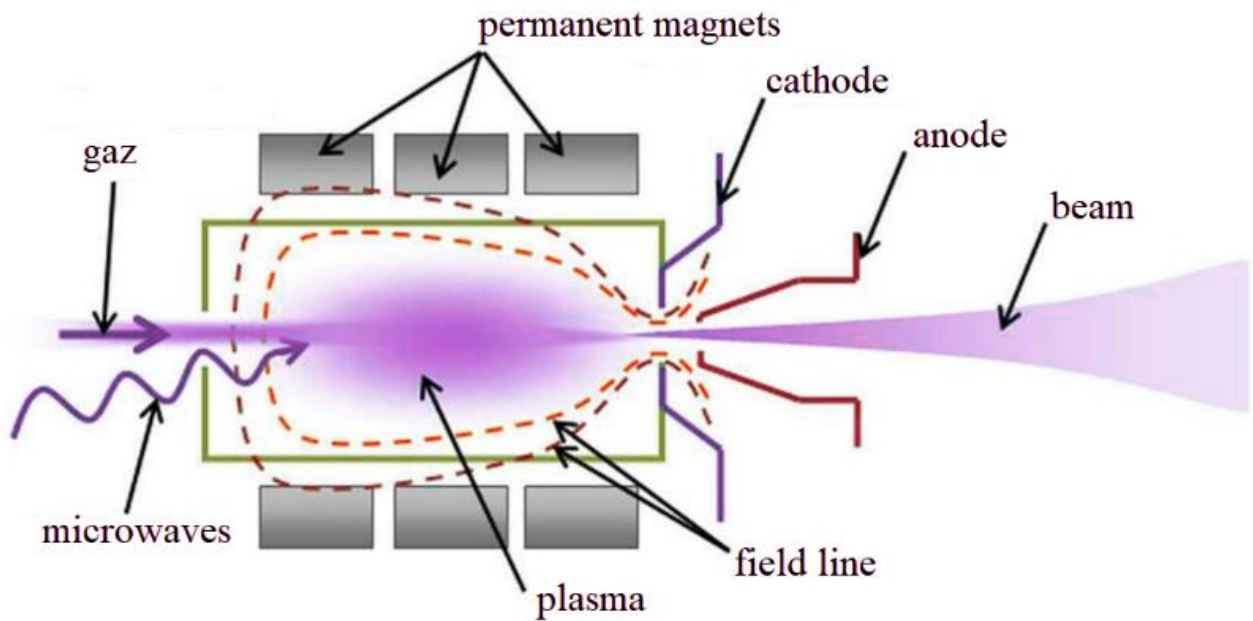


Figure 2.6: Schematic mechanism of an ECR nitrogen plasma source

The hybrid plasma source combines the characteristics of an atom source and an ion source to produce mixed gas fluxes, the ions can be extracted and accelerated thanks to additional grids. Before use, the source was carefully calibrated to find the conditions for nitriding as detailed in the next chapters.

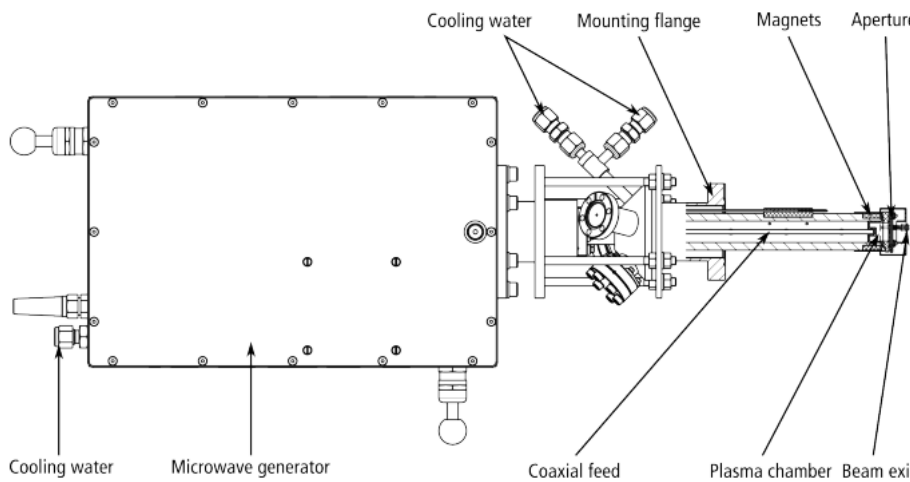


Figure 2.7: Features on the ECR source used during this study [9-SPECS 2013]

The plasma chamber closes with an aperture plate. The characteristics of the source output are determined by the configuration of this same aperture plate and by electrodes. The aperture plate at the front of the chamber has a hole of 200nm that allows plasma reactants to escape into the experimental chamber. Based on our needs, the source is composed of three aperture designs and operating modes. Figure 2.8 provides a comparison of the three different aperture configurations.

- *Atom mode:* In this mode, the plasma is confined inside the chamber enabling the thermalization of the atoms when they are in contact with the aperture (Figure 2.8). The outcome is a low-energy flux of atomic species emitted from the source. Moreover, the small size of the hole and the thickness of the insulator reduce the gas flow from the plasma chamber into the experimental chamber. The source will then, function at lower chamber pressures compared to ion mode apertures.
- *Ion mode:* In an ion source, there are two electrodes located at the end of the plasma chamber. The anode controls the beam energy of the ions produced by the source. The second extractor electrode, is used to optimize the beam current that reaches the sample (Figure 2.8). The beam current increases with this extractor voltage until it reaches a maximum point known as the knee point. Beyond this point, the beam current will be subject of a small or no variation, depending on factors such as anode voltage, gas flow, and magnetron power.
- *Hybrid mode:* The hybrid source combines features of both atom and ion sources. An insulator on the plasma chamber for thermalizing atoms and anode and extractor grids for controlling the ion current and the energy of the beam energy.

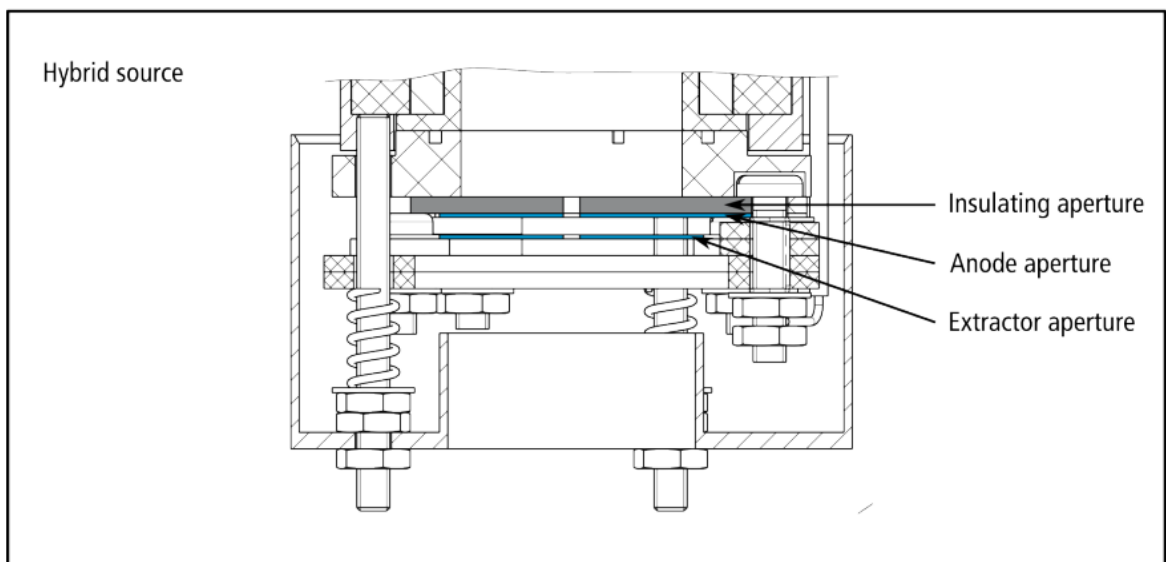


Figure 2.8 : Aperture producing Hybrid mode.

With nitrogen-plasma-based methods, the rate of reactive nitrogen supply in the growth chamber is

determined by plasma parameters and is independent of substrate temperature (in contrast to NH_3 -based methods). The substrate temperature is measured by a thermocouple directly behind the substrate mounting plate. It is necessary to conduct crystal growth at temperatures sufficient for high-quality growth. The main restriction is the formation of nitride in competition with oxides at high temperatures.

2.2.2 Substrate preparation

The quality of the substrate surface can affect the properties and therefore, requires careful attention to ensure a high-quality and uniform film deposition.

Substrates for photoelectrochemical measurements must be conductive in order to allow for the measurement the flow of electric current. They have also to be, suitable for epitaxial growth, their lattice parameter and structure should be adapted to promote 2D growth, and good epitaxy conditions.

2.2.2.1 Undoped and 1 at.% Niobium doped SrTiO_3 (001) in film

The research conducted in chapter 3 involves the growth of TiO_xN_y and nitrogen doped BaTiO_3 films on 1 at.% Nb-doped SrTiO_3 (001) single crystals, which had a square shape of $1 \times 1 \text{ cm}^2$ and a thickness of 1 mm. The Nb: SrTiO_3 substrate has a cubic perovskite structure and we use the (001) surface that has a square lattice, with a of 0.3905 nm lattice parameter. The Nb doping provides a good electrical conductivity, in contrast to fairly insulating undoped SrTiO_3 . Before each deposition, the substrates were annealed at 600°C using radiative heating and cleaned using high brilliance oxygen plasma to remove any chemisorbed surface contamination, such as water or carbon. The cleaning process takes 90min, and the Baratron was set to 1.3 turns, which corresponds to a pressure in the 10^{-8} mbar range in the O&NPA-MBE chamber. Such substrate cannot be repaired after deposition of a thin film.

2.2.2.2 Platinum (111)

Pt (111) single crystals with a diameter of 8 or 10 mm and a thickness of 1 mm were used as substrates for growing N-doped TiO_2 (studied in chapter 4). Pt has a face-centered cubic (FCC) crystal structure with a lattice parameter of 0.392 nm. For Pt (111), the surface lattice is hexagonal-like lattice with a surface parameter of $a = 0.277$ nm. The platinum substrates can be reused after reparation. The deposited oxide layer on Pt substrates can be removed by performing an Ar^+ ion beam etching at a pressure of 10^{-5} mbar with an energy beam of 4 kV, and a well ordered surface is obtained after a

high temperature electron beam annealing at 1000°C. These substrates present then, smooth and well-ordered surfaces.

Prior to each deposition, the substrates underwent a cleaning process at 600°C using oxygen plasma to eliminate contamination. The cleaning procedure lasted for one hour. During this process, the Baratron was adjusted to 1.5 turns, corresponding to a pressure range of approximately 10^{-7} mbar in the O&NPA-MBE chamber.

2.3 Characterization techniques *in situ* and in laboratory

In solid-state physics and materials science, characterization methods are usually based on the interaction of radiation with matter [10-Harris 1981]. It is important that the wavelength match the investigated property (Figure 2.9).

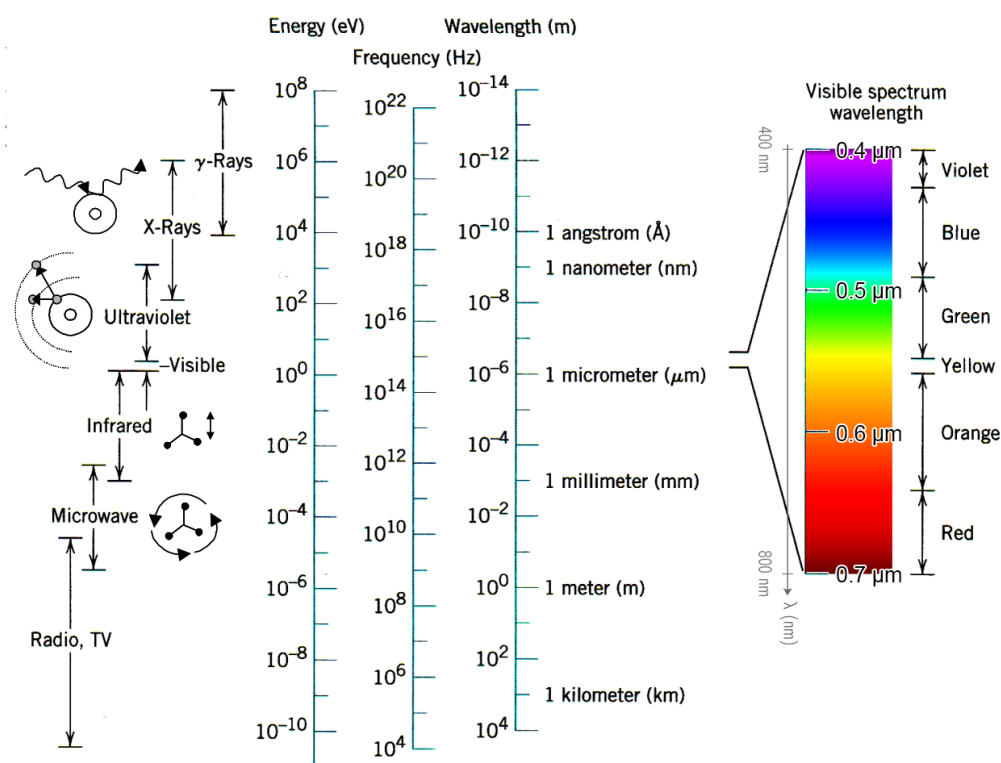


Figure 2.9: Classification of different electromagnetic waves.

2.3.1 Reflexion high energy electron diffraction (RHEED)

Reflexion high energy electron diffraction (RHEED) is the principal *real time* analytical tool used during molecular beam epitaxy (MBE).

In RHEED, a high energy monoenergetic electron beam (30 keV in our case) is directed towards the surface at a glancing angle θ_g about 1° to 4° (Figure 2.10a). Hence, the penetration depth is limited to the first atomic layers, and the electron beam is diffracted by the surface of the sample. A fluorescent screen placed diametrically opposite to the incident beam, records the surface diffraction pattern, and by turning the sample along its azimuth, one can record surface reciprocal pattern in different directions (Figure 2.10a).

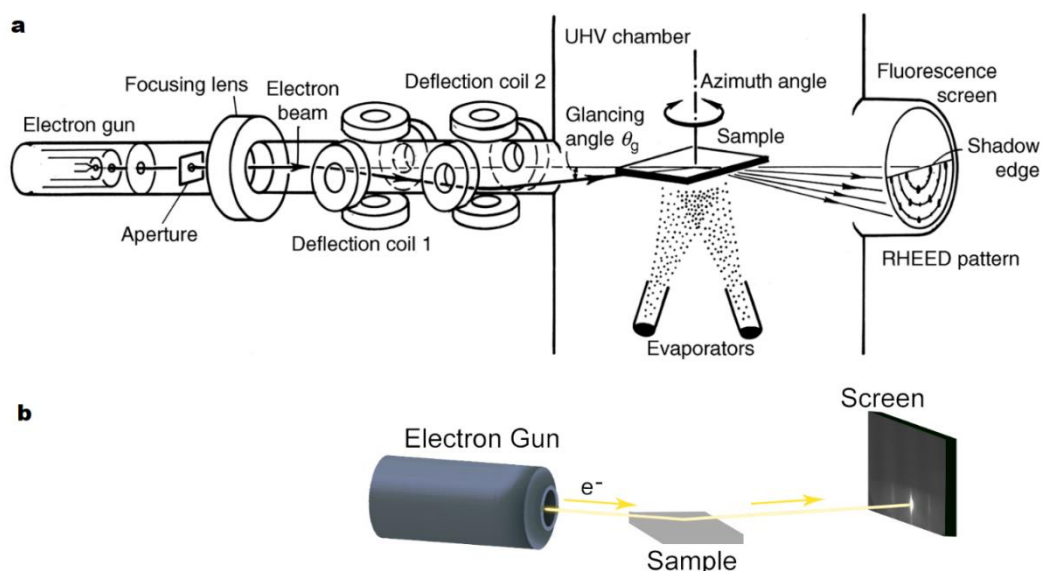


Figure 2.10: **a** Schematic diagram of RHEED apparatus [11-Hasegawa 2012] **b** The simplest RHEED set up includes an electron gun, a (here a plasma clean substrate of Pt (111)), and a fluorescence screen.

The reciprocal lattice of an ideal single crystalline 2D surface consists of vertical *rods* [11-Hasegawa 2012]. The *diffraction pattern* seen in RHEED corresponds to the intersection of the Ewald sphere and the reciprocal lattice. Examples of typical RHEED pattern are represented on figure 2.11, as a function of the morphology of the surface.

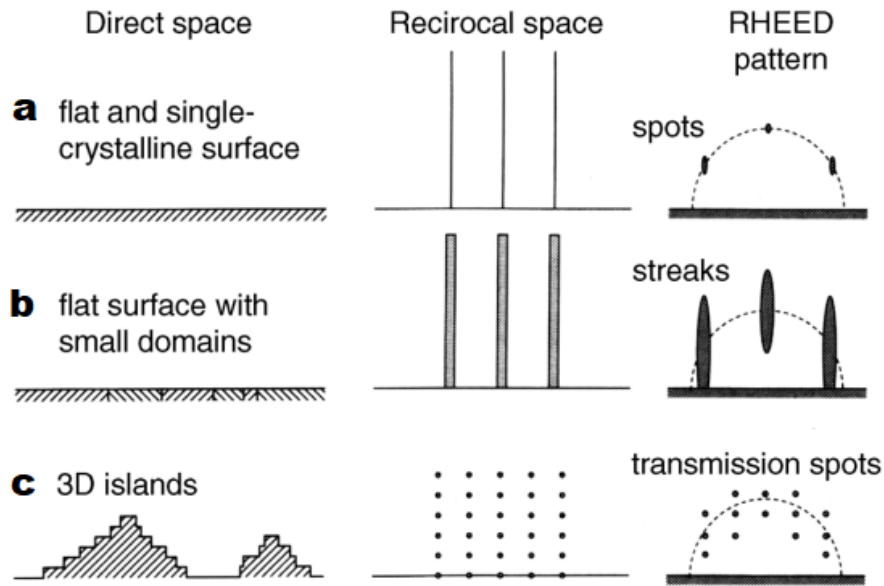
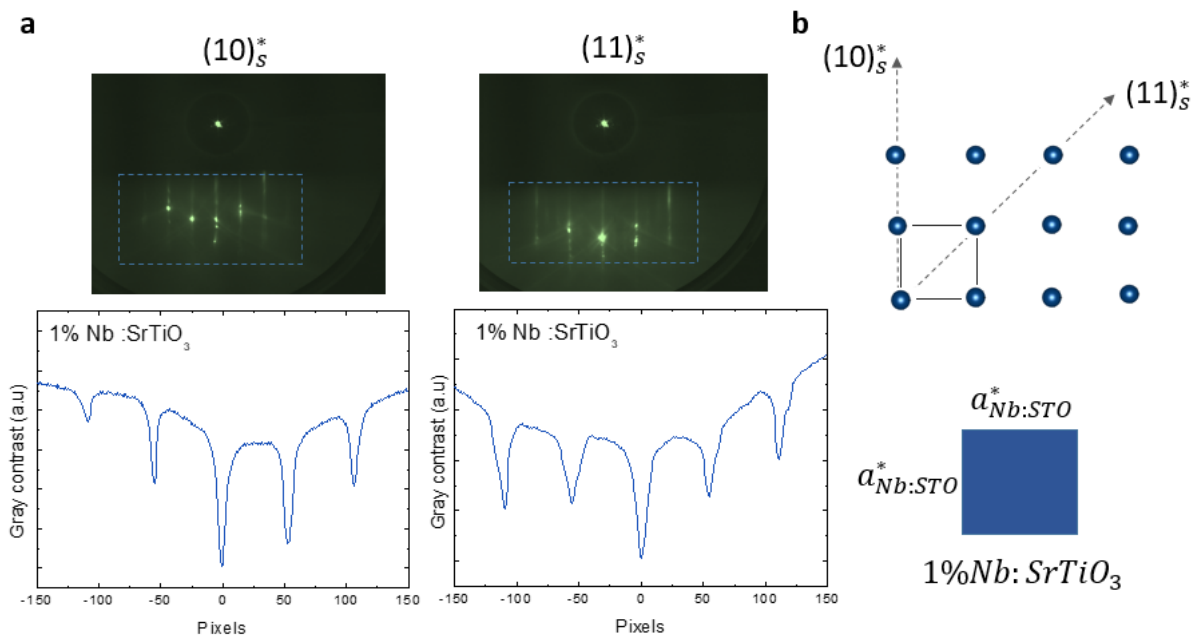


Figure 2.11: Different types of morphologies of single crystal surfaces: real-space morphology (left), associated, reciprocal space (middle), and corresponding RHEED patterns (right) [from 11-Hasegawa 2012]

Typical information that can be deduced from RHEED patterns are epitaxial relationships and the lattice parameters of the samples as well as the relaxation thickness of the growing layer [12-Barbier2005, 13-Derj 2022]. The examples of Nb:STO (and BTO/Nb:STO) are shown on figure 2.12, for two different azimuths direction $(10)_s^*$ and $(11)_s^*$.



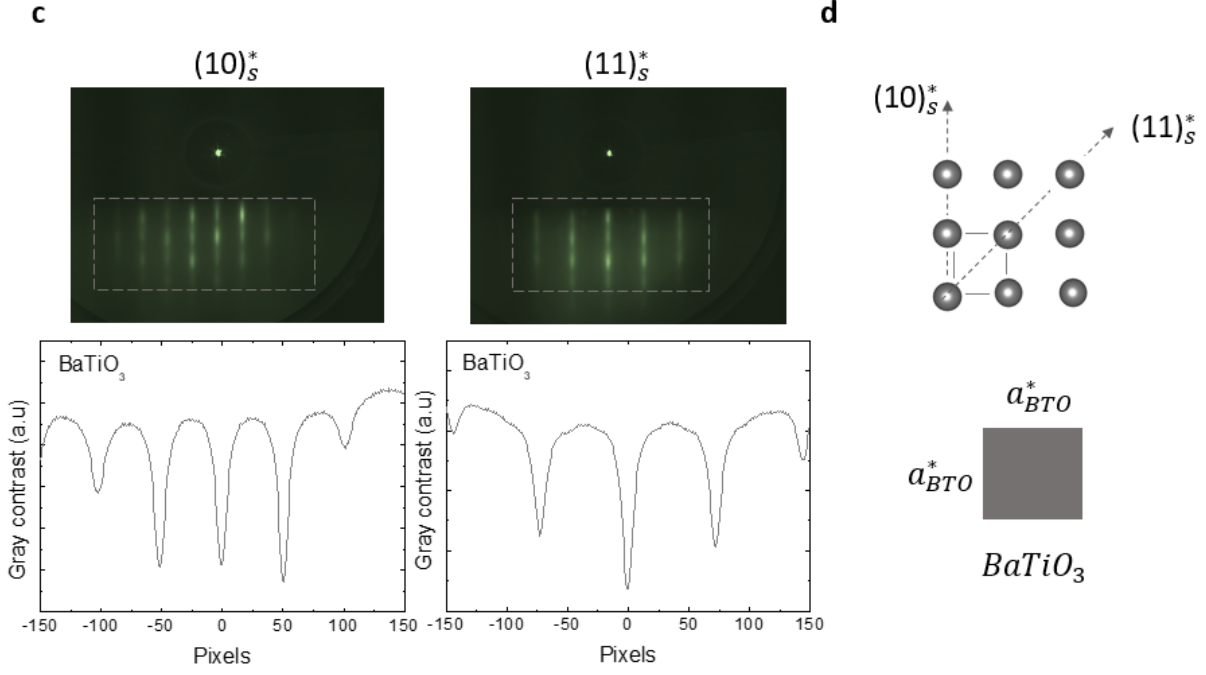


Figure 2.12: Principle of RHEED pattern analysis in order to calculate the surface lattice parameters in the case of **a** the 1% Nb doped SrTiO_3 (001) and **c** BaTiO_3 deposited on 1% Nb doped SrTiO_3 (001) surfaces, with their corresponding RHEED pattern (green contrast) with blue (gray) dashed rectangles highlighting the integration box used to obtain the curves of the integrated RHEED images. **b** and **d** the surface reciprocal geometry indicating two different azimuths for each sample surface reciprocal lattice $(10)_s^*$ and $(11)_s^*$.

The in-plane lattice parameter evolution can be determined using integrated line profiles extracted from the RHEED patterns. For example, figure 2.12 show the typical RHEED patterns and their integrated profiles, along $(11)_s^*$ azimuths, observed during the growth of BaTiO_3 (BTO) on 1% Nb doped SrTiO_3 (Nb:STO). The growth being performed at 450°C , the thermal expansion coefficients of the SrTiO_3 and BaTiO_3 were taken into account (*ca.* $7.4 \times 10^{-6} \text{ K}^{-1}$ and $1.3 \times 10^{-5} \text{ K}^{-1}$, respectively). Since we know the STO lattice constant, we can deduce for each pattern the BTO one from:

$$a_{\text{BTO}} = a_{\text{Nb:STO}} \left(\frac{d_{\text{Nb:STO}}}{d_{\text{BTO}}} \right)$$

With a_{BTO} (resp. $a_{\text{Nb:STO}}$) the lattice parameters of BTO (resp. Nb:STO) and d_{BTO} (resp. $d_{\text{Nb:STO}}$) the distances in pixels between two peaks of its integrated profile at 450°C .

2.3.2 X-ray Photoelectron Spectroscopy (XPS)

The photoelectric effect was first introduced by Hertz [14- Hertz 1887] and explained by Einstein [15- Einstein 1905]. The principle of X-Ray Photoelectron Spectroscopy (XPS) relies in the photoelectric effect or what is also known as the photoemission process (see figure 2.13), whereby photons can induce electron ejection from a solid.

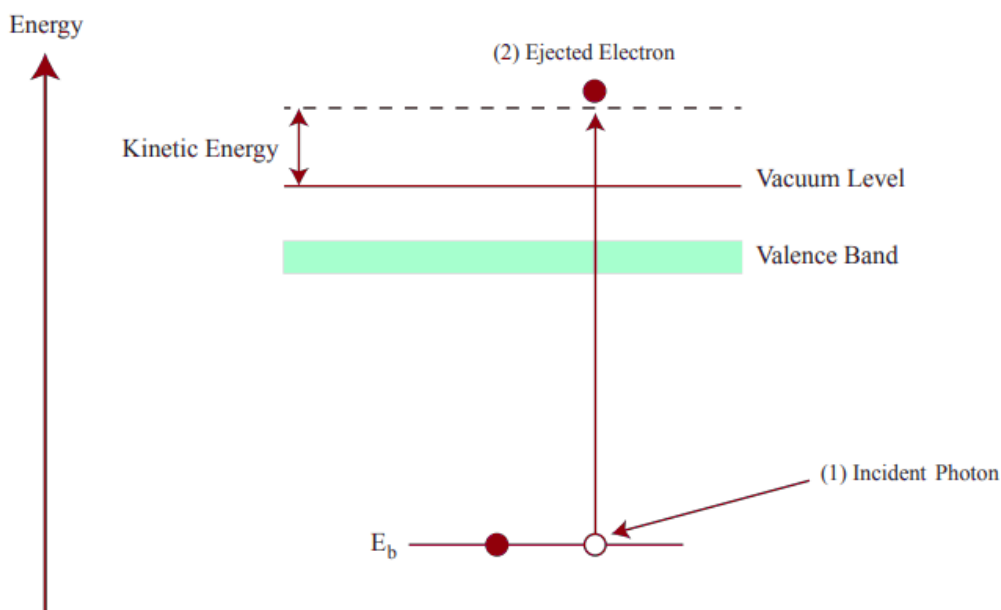


Figure 2.13: Energy level diagram depicting the photoelectric effect. An incoming photon is absorbed such to provide a sufficient energy to an electron to overcome the binding energy (E_b). Because of the quantification of the electronic levels, the kinetic energy of the emitted electron has elemental specificity and hence allows for surface chemical identification.

The X-ray photons source is an X-ray tube, where a metallic aluminum anode is irradiated by high energy electrons, resulting in the emission of X-ray photons. In our case, the energy used was thus, Al K_α radiation (1486.7 eV energy).

The surface sensitivity of XPS arises from electron mean free path of the ejected electron. It corresponds to a few atomic layers, depending on the kinetic energy. In a rough approximation the electron mean free path follows simple equation, given in figure 2.14.

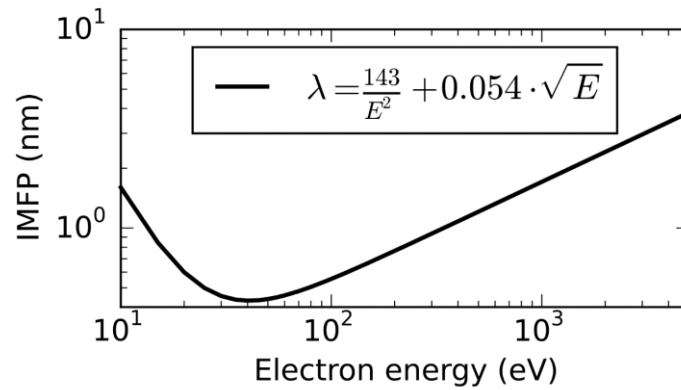


Figure 2.14: Simplified universal curve for the electron inelastic mean free path in elements based on the equation in the inset [16].

Under principle of energy conservation, the kinetic energy (E_{kin}) of the emitted photoelectron is given by the equation bellow, where ‘ $h\nu$ ’ is the photon energy, ‘ E_b ’ is the binding energy and ‘ Φ ’ is the work function of the electron energy analyzer.

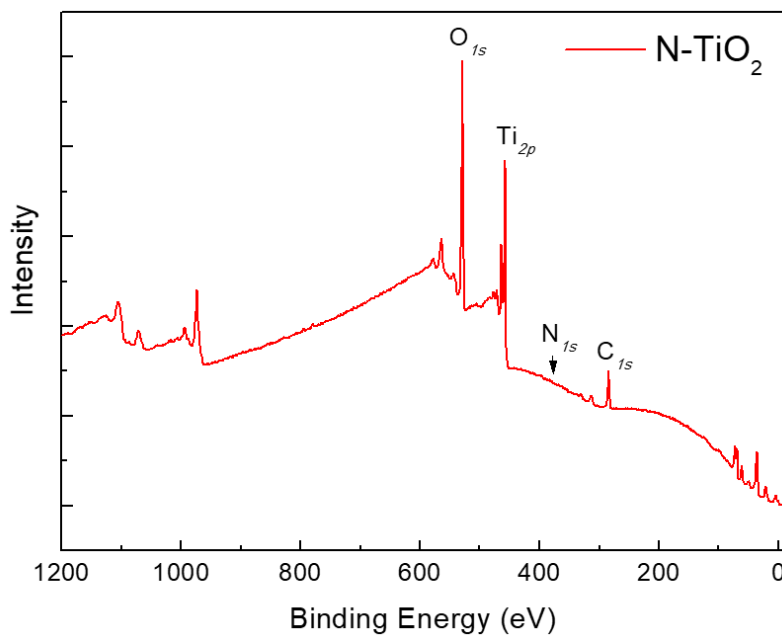


Figure 2.15: Ex situ widescan XPS spectrum taken for an N-doped TiO_2 film which highlights the presence of Ti, O and C at the surface. The N-1s peak is too low to be seen in the widescan.

$$E_{\text{kin}} = h\nu - E_b - \Phi$$

All XPS spectra were processed and interpreted using CasaXPS [18-Fairley 2021].

2.3.3 Auger Spectroscopy (AES)

Auger electron spectroscopy (AES) is a surface-sensitive analytical technique used to determine the elemental composition of materials.

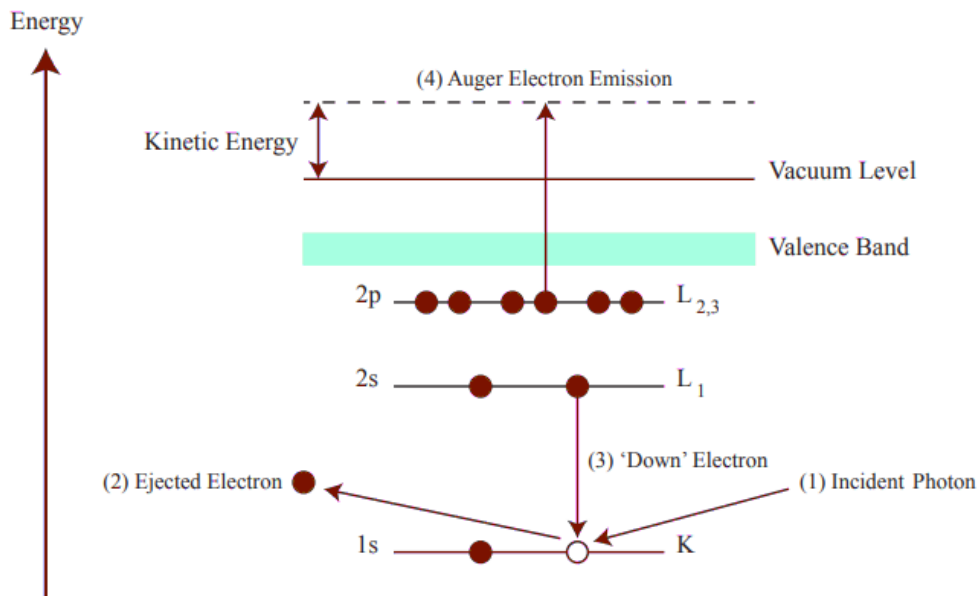


Figure 2.16: Energy level depicting the process by which an Auger electron is emitted.

In AES, a sample is bombarded with a beam of electrons, with an energy of a 3 keV. When an electron from the beam interacts with an atom on the surface of the sample, it can cause the ejection of an electron from one of the inner shells of the atom. The resulting hole is filled by an electron from a higher energy level, and the energy difference is released in the form of an Auger electron (Figure 2.16). The kinetic energy of the Auger electron are measured, which provide information about the atom from which it originated [19-Briggs 2003]. For the particular example of figure 2.16, the kinetic energy is then given by:

$$E_{\text{kin}} = E_k - E_{L1} - E_{L2,3}$$

AES can be used to analyze the composition of a wide range of materials. It is particularly useful for surface analysis and can provide information about the top few layers of atoms on the surface of a material [20-Hofmann 2008]. Figure 2.17 depicts an AES spectrum of N-doped BaTiO₃ film.

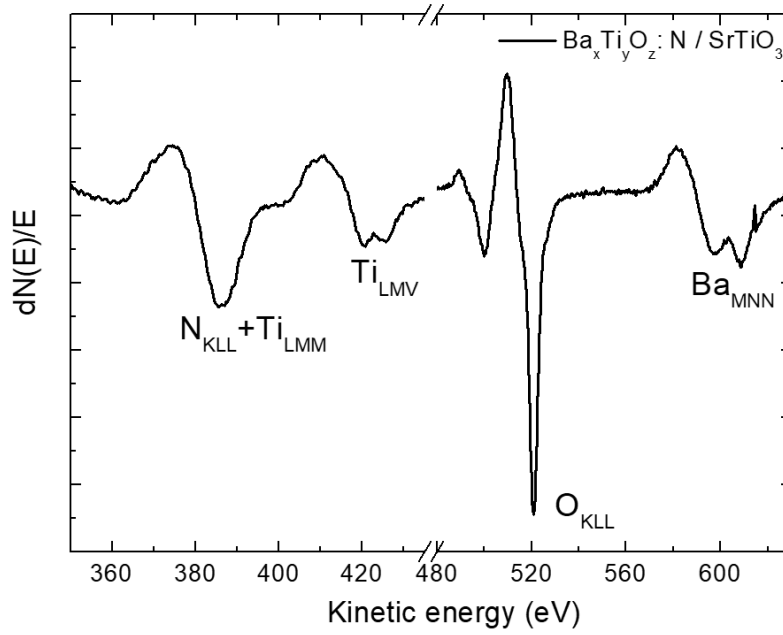


Figure 2.17: Auger scan for a N-doped BaTiO₃ layer deposited on 1% Nb: SrTiO₃ (001).

2.3.4 X-ray Reflectivity (XRR)

X-ray Reflectivity (XRR) was performed to investigate specific physical properties of epitaxial thin films such as film thickness, roughness and the electron-density profile.

For specular X-ray reflectivity, the exit angle and incident angle of the electron beam are equal (Figure 2.18), the wavevector transfer Q_z is perpendicular to the surface and is given by:

$$Q_z = \frac{4\pi \sin(\theta)}{\lambda}$$

Where θ is the incident angle and λ the photon wavelength.

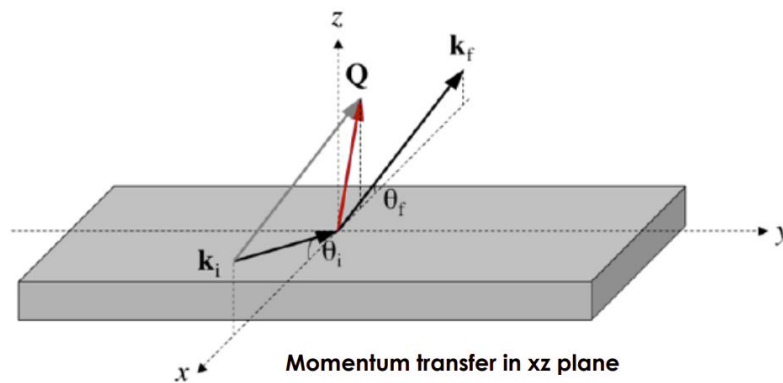


Figure 2.18: Schematic representation of the resulting momentum transfer Q_z in XRR

The reflectivity signal of a surface is normalized to the incident intensity $R = \frac{I_R}{I_0}$, measured as a function of the wavevector transfer. The particularity of the curve is that it decays rapidly (especially for rough surfaces) and it is composed of an interference pattern (Kiessig fringes) from the scattering of different layers (for example, in a thin film or multilayer). Thus, from XRR curves, we can deduce important parameters such as the critical angle for total external reflexion, the roughness and the film thickness (Figure 2.19).

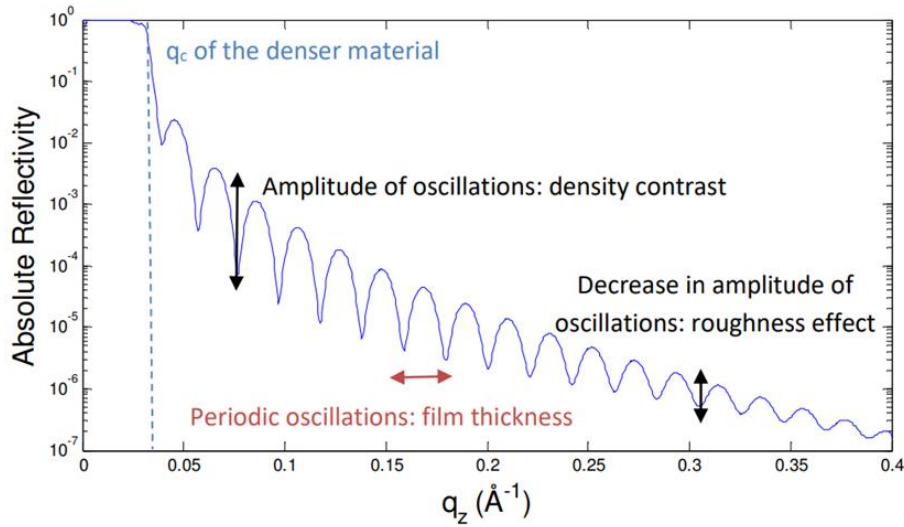


Figure 2.19: Typical features of a reflectivity curve [21-Gibaud 2009]

The goal of X-ray reflectivity measurements is to infer an electron density profile perpendicular to the surface. Layer models are used to fit the data and we used the *REFLEX* software [21-Gibaud 2009]. The χ^2 is used to describe the quality of the agreement between the model and the experiment data and is given by:

$$\chi^2 = \frac{1}{n} \sum_{i=1}^n \left(\frac{y_{data_i} - y_{calc_i}}{y_{data_i}} \right)^2$$

Where on n measured y_{data_i} , each one corresponds to a modeled value, y_{calc_i} .

Moreover, to reach a high Q_z a high incident intensity is required. Therefore, our measurements were done using synchrotron radiation (Diffabs beamline at synchrotron SOLEIL).

2.4 Photoelectrochemical characterization

2.4.1 Experimental setup

To mimic the artificial photosynthetic process, we set-up in our laboratory the following PEC configuration (Figure 2.20):

-As a light source, we used an ozone-free Newport 1000 W *Xe* Arc Lamp. It is completed with output water filters to avoid inconvenient heating of the set-up by the infrared radiations (IR). The intensity of the light on the sample was evaluated to amount to around 300 mW cm^{-2} .

-The electrodes of our PEC system are immersed in an aqueous electrolyte (NaOH with $c_{\text{NaOH}}=0.1\text{M}$ *i.e.* pH = 13). The reactor is transparent to light allowing for the irradiation to reach the photoanode (the working electrode : our sample). The sample is sealed on the sample holder allowing the contact between the sample surface and the electrolyte. The electrical contact with the external circuit is taken at the back of the sample; a good conductor as substrate is required (here Pt and Nb:SrTiO₃). The cathode or counter electrode (CE) is a platinum wire. The reference electrode (RE), is an Ag/AgCl reference electrode where the potential reference is $V_{\text{Ag/AgCl}} = +0.197 \text{ V vs. NHE}$.

Our system contains a reference electrode to observe half reactions in the cell and provide, a reference potential. *“However, it should be stressed that efficiencies measured in this way are photoelectrode efficiencies and not cell efficiencies.”*[22- Minggu 2012]

In a cylindrical vessel, with a quartz window as a flat optical window to allow most of the light spectrum including UV to pass through and illuminate our epitaxial thin film. This same film is used as the photoanode or working electrode (WE). All electrochemical measurements were performed at room temperature to respect environmental purposes.

The potentiostat, connected to the computer, is a Princeton Applied Research (PAR) 263A. Using Power Suite software (dedicated to electrochemistry) and by home-made LabView programs, we can control the applied potential and the current acquisition between the three electrodes.

The monochromator (Cornerstone 130 model 74004 monochromator (Newport)) is used to measure the photocurrent as a function of the wavelength. The wavelength was varied between 200 and 600 nm, with 5 nm steps.

We used a PAR 5210 lock-in amplifier and an optical chopper (MC-2000 from Thorlabs) at a reference frequency of 20 Hz to modulate the light and increase the signal to noise ratio.

Finally, the computer collects all the data and control the instruments.

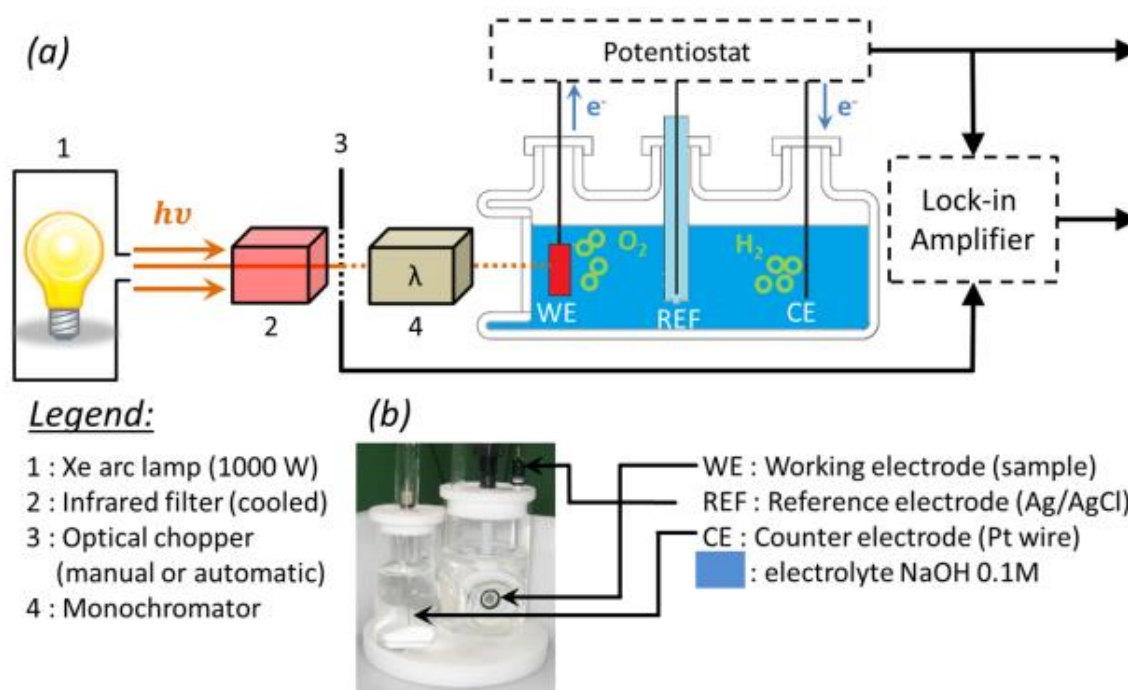


Figure 2.20: (a) Photoelectrochemistry setup, and (b) details of the mounting within the cell [from 22-Rioult 2015].

2.4.2 I-V voltammetry

I-V voltammetry, also known as photocurrent-voltage (I-V) curve analysis, is a technique used in photoelectrochemistry to study the behavior of a photoelectrode at different potentials. A voltage is applied to the working electrode with respect to the reference electrode and the current flowing through the counting electrode is measured as a function of the swept applied voltage (Figure 2.21) [23-Bard 2000- 25 Compton].

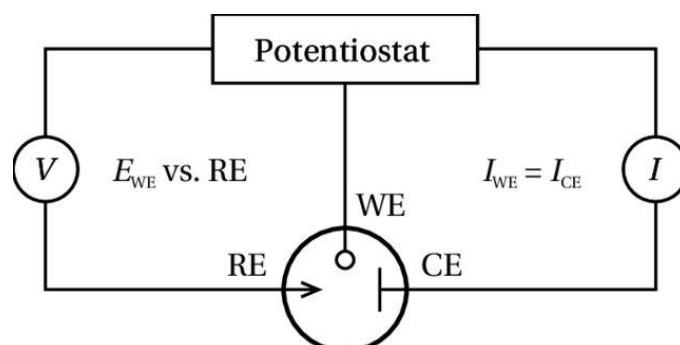


Figure 2.21: Schematic representation of the measurement system

The I-V curve obtained from this experiment can thus, provide information about the electrochemical reaction occurring at the electrode surface. To increase the signal/noise ratio, several I(V) curves are acquired and averaged. The measures are done under illumination (*i.e.* with light, L) and without illumination (*i.e.* in dark conditions, D). In order to take account for the illuminated surface, the current I is converted in current density J in mA/cm². The photocurrent is then, defined as the difference between the current recorded under light and without light (dark), and it is given by :

$$J_{ph} = J_L - J_D$$

To compare the efficiencies of our samples, we usually select a particular potential (at 0 or 0.4V vs. Ag/AgCl for instance) and compare their photocurrent at this same voltage. Further and for the purpose of spotlighting the illumination effect on the current, we measured J(V) curves with an ON/OFF chopped light obtained with a manual optical shutter (model 71445 from Newport).

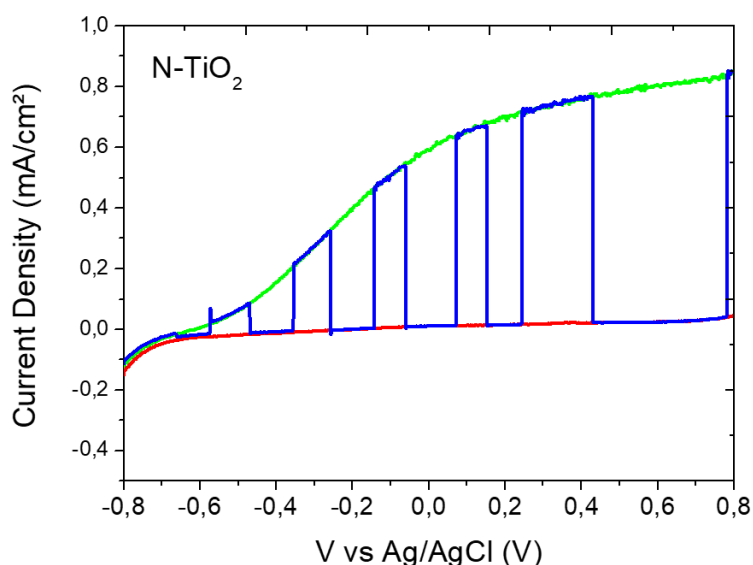


Figure 2.22: I(V) curves: $J_D(V)$ (red curve) and $J_L(V)$ (green curve) and ON/OFF chopped (blue curve).

Figure 2.22 displays an example of J_{ph} , J_L and J_D curves with permanent and chopped light, the effect of illumination is obvious. From this figure, we can approximately derive the onset potential (applied potential for which the water electrolysis starts) which is *ca.* -0.6 V vs. Ag/AgCl under illumination, and superior to 0.8V vs. Ag/AgCl in dark conditions. We notice a negative current density at -0.7 V vs. Ag/AgCl meaning that the sample has a cathode behavior at low potential.

For the I(V) voltammetry measurements performed in this thesis, the applied potential window varied from [-1;+0.7] to [-1; +0.8] (in V vs. Ag/AgCl), depending on the samples measured.

2.4.3 I- λ measurement

Photocurrent measurements as a function of the incident light wavelength (*i.e.* $I(\lambda)$ measurements) allow to get insight into the spectral response of our layers. The photocurrent density data are normalized to the corresponding incident light flux that is represented in figure 2.23.

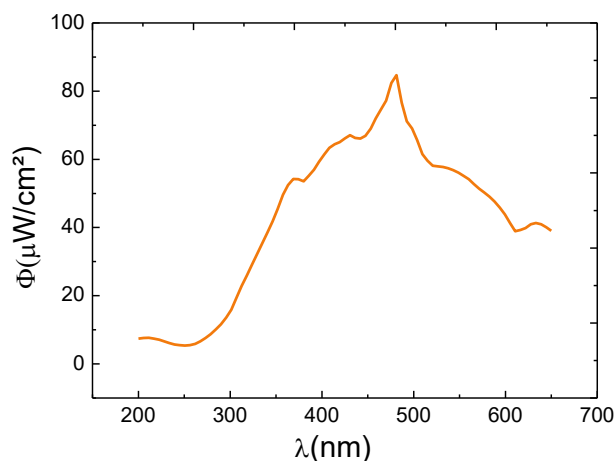


Figure 2.23: Light flux of the Xe arc lamp after the monochromator as a function of the wavelength

The wavelength was varied between 200 and 600 nm, with 5 nm steps. The obtained curve (see figure 2.24) is proportional to the ‘electrochemical absorption’ (α).

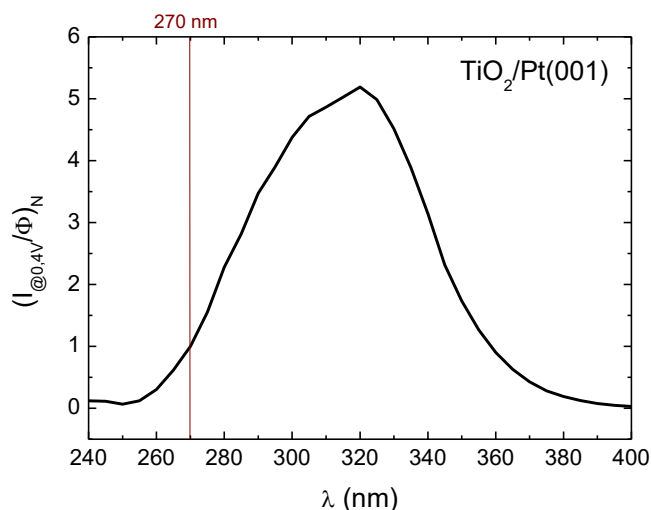


Figure 2.24: Electrochemical absorption as a function of the wavelength at 0.4 V vs. Ag/AgCl of TiO_2 deposited on (001) and normalized at 270 nm.

To compare our samples, we estimated the ‘photoelectrochemical band gaps’ of our samples through the ‘efficient Tauc plot’ method [26-Tauc 1968] by plotting $(\alpha h\nu)^2$ vs. $h\nu$ ($h\nu$ being the photon energy and α the absorption coefficient of the material).

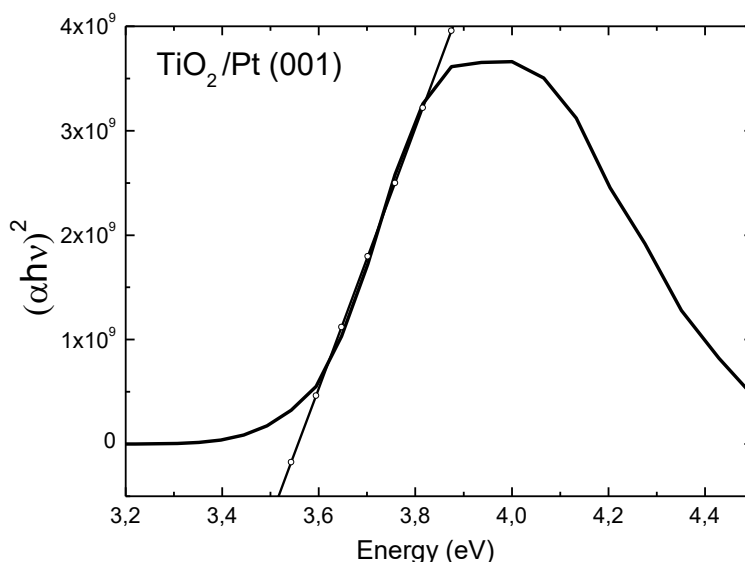


Figure 2.25: Direct band gaps determined using the ‘efficient Tauc plot method’, for TiO_2 deposited on Pt (111).

The efficient Tauc plot method involves fitting a straight line to the linear portion of the Tauc plot and extrapolating it to the x-axis to determine the direct photoelectrochemical bandgap energy, by fitting $(\alpha h\nu)^2$ vs. $h\nu$, (see, Figure 2.25) and the indirect photoelectrochemical bandgap energy, by fitting $(\alpha h\nu)^{0.5}$ vs. $h\nu$ (E_g).

2.4.4 Electrochemical impedance spectroscopy

In electrochemical impedance spectroscopy (EIS) a small, sinusoidal voltage is applied to a sample and we measure the resulting current response. The resulting measure give the impedance of an electrochemical systems over a range of frequencies. The impedance represents then, the overall opposition of a circuit to the flow of the electric current the system. As a complex quantity, both real (resistance) and imaginary (reactance) parts compose it. The reactance can be further splitted into capacitive reactance and inductive reactance, depending on the type of electrical circuit [27-Macdonald 2018].

EIS that is a non-destructive, non-invasive technique used to provide valuable information about the properties of these systems, such as their resistance, capacitance, and inductance, as well as the kinetics of the electrochemical reactions taking place [28-Lasia 2014].

In a circuit or system, the impedance can be expressed by:

$$Z = V(\omega)/I(\omega)$$

Where $V(\omega)$ is the voltage and $I(\omega)$ the current flowing across at a given frequency ω . Herein, EIS measurements were performed in dark conditions. A dynamic signal of 10 mV amplitude with frequencies from 100 kHz down to 10 Hz was superimposed to a direct current bias ranging from -1 to $+0.9$ V vs Ag/AgCl, with 0.1 V steps, using the potentiostat and the lock-in amplifier to generate the alternative signal $V(\omega)$ and to measure the generated current $I(\omega)$.

Usually, the semiconductor electrolyte interface is simulated by a combination of ideal capacitors. However, unlike an ideal capacitor, which has a constant impedance that decreases with increasing frequency, a non-ideal capacitor may exhibit behaviors such as frequency-dependent capacitance, dielectric loss, or electrode polarization. The commonly employed approximation in EIS is the introduction of a constant phase element (CPE) in the replacement of ideal capacitance [29-Morrison 2007]. For this purpose, we modeled our system with a RS-RCPE circuit (see figure 2.26), and the impedance of a CPE is then, given by the following equation:

$$Z = R_S + (i\omega^n Q + R^{-1})^{-1}$$

Where R_S and R are the series and space charge layer resistances respectively and $i\omega^n Q$ the admittance of CPE, where n is between 0.9 and 1 ($n = 1$ for perfect capacitance). The CPE can also be used to model the behavior of materials that are not perfectly conductive, such as semiconductors or insulators. In these cases, the CPE can represent the capacitance that arises due to the formation of a space charge layer or the presence of localized states within the material.

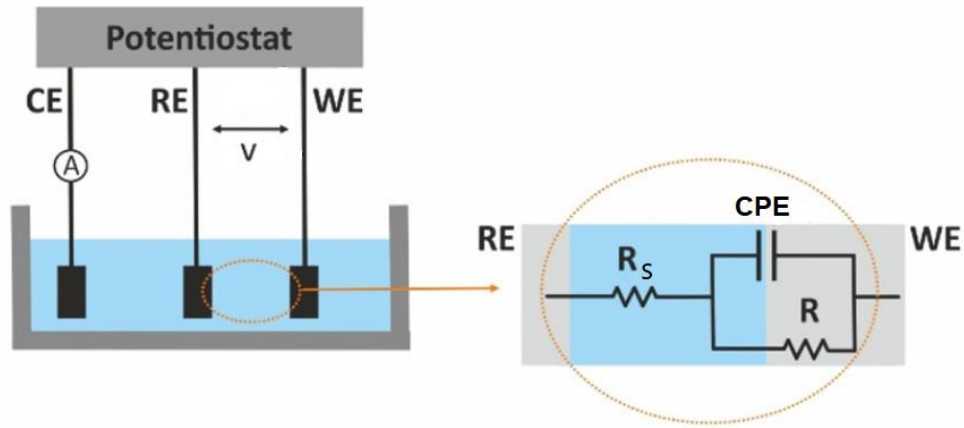


Figure 2.26: Photoelectrochemical cells of 3 electrodes with the working (WE), counter (CE), and reference (RE) electrodes and its equivalent RS -RCPE circuit model [30-Lazanas2023].

Then, we estimated the capacitance value of the CPE using the formula [31- Brug 1984]

$$C = Q^{1/n} (R_S^{-1} + R^{-1})^{(n-1)/n}$$

The Mott-Schottky plot is a graph of the inverse square capacitance (A^2/C^2) versus the applied voltage (V) for a semiconductor material in contact with an electrolyte solution. The plot is named after Nevill Mott [32- Mott 1938], who independently developed the theory behind this plot in the early 20th century.

The Mott-Schottky plot is typically used to determine the carrier concentration (N_D) and the flat-band potential (V_{fb}) of a semiconductor material. The carrier concentration is related to the slope of the plot, while the flat-band potential is related to the intercept of the plot with the x-axis.

The equation for the Mott-Schottky plot is given by:

$$\frac{A^2}{C^2} = \frac{2}{eN_D\epsilon_0\epsilon_r} \left(V - V_{fb} - \frac{k_B T}{e} \right)$$

where A is the illuminated surface area, ϵ_0 the dielectric constant of vacuum (8.85×10^{-12} F/m), ϵ_r is the dielectric constant equal to 31 for anatase [33- Matsumoto 1938], to 173 for rutile [34- Juliao 1980], between 7 and 11 for corundum titanium dioxide and around 1000-4000 for BaTiO₃ [35- Kumar 2008]. V is the potential applied to the photoelectrochemical cell, k_B is the Boltzmann constant (1.38×10^{-23} J/K), and e is the elementary charge (1.6×10^{-19} C). The flat-band potential corresponds to the voltage where the capacitance is infinite, *i.e.* the voltage where the band bending is vanishing. Overall, the use of CPEs in EIS allows for a more accurate and comprehensive modeling of complex electrochemical systems.

2.5 Further characterization methods

Over the last decade, researchers have explored many sophisticated *ex situ* and *in situ* techniques using high brilliance synchrotron radiation measurements. Among the small quantities of matter that a thin film represents. These large experimental systems provide powerful tools to probe the undisclosed underlying mechanisms of their promising properties. In this section, we present a comprehensive overview of synchrotron X-ray techniques we managed to use during this thesis.

2.5.1 Synchrotron X-ray Diffraction (XRD)

For oxide MBE growth, X-ray diffraction has been used as a major probe for film growth and surface structures analysis. X-ray diffraction (XRD) is a method based on the analysis of the diffraction patterns of X-rays that were scattered at a specific angle known as the Bragg angle, by the atoms in the material in order to study its atomic and molecular structure [36-Bragg 1913]. The spacing of the atomic planes in the crystal lattice and the wavelength of the X-ray beam determine the Bragg angle. The Bragg law illustrated in figure 2.27, which states that $n\lambda = 2d \sin\theta$, relates these parameters, where n is an integer, λ is the wavelength of the X-rays, d is the spacing of the atomic planes, and θ is the Bragg angle [37-Cullity 2001, 38-Shih 2013].

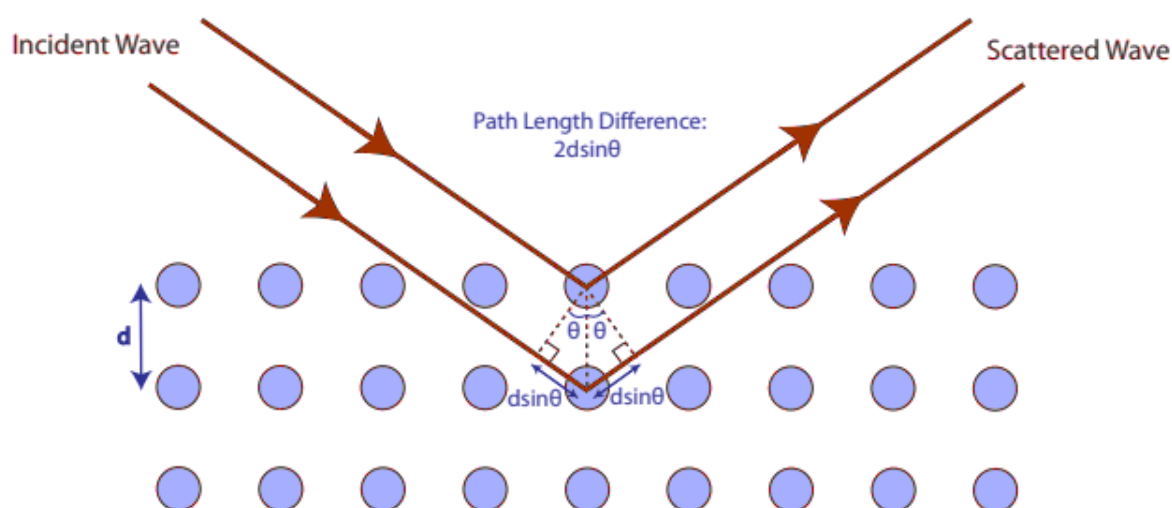


Figure 2.27: Schematic illustration of Bragg's law.

The diffraction pattern consists of a series of peaks or lines that correspond to the different planes of atoms in the crystal. The position, intensity, and width of these peaks provide information about the crystal structure, such as the unit cell dimensions, atomic positions, and symmetry of the crystal. XRD

is a non-destructive, highly sensitive, and precise analytical technique. For typical X-ray wavelengths, the refractive index is slightly smaller than one. The direction of the refracted beam does not deviate much from the incident one and total external reflection occurs on the surface side. Therefore, the X-rays are reflected strongly from the surface at the critical angle of incidence, which allows the structure of the uppermost layers of a material to be probed. In surface XRD (SXRD), a beam of synchrotron radiation is directed onto a sample, to glancing incidence and the resulting diffraction pattern is analyzed to determine the crystal structure of the material. During this thesis, we run SXRD measurements at the Diffabs beamline at Synchrotron SOLEIL in France.

The Diffabs beamline is equipped with state-of-the-art XRD and XRR instrumentation, including a 2D detector for high-resolution diffraction imaging, a diffractometer for in-plane and out-of-plane XRD measurements.

The study was done at room temperature and at a photon energy of 9 keV. The significant digits of lattice parameters, 0.002 Å, were determined from the maximal deviation from the average value (over all accessible orders) of the substrate fitted (Lorentzian peak shape) Bragg peak positions. All XRD peak positions were derived from the Lorentzian shape fits to the experimental data after χ^2 convergence.

2.5.2 Resonant Photoemission (RPE)

Resonant Photoemission Spectroscopy (RPES) is a technique that involves using excitation photons with energies close to the absorption (*i.e.* X-ray Absorption Spectroscopy (XAS)) threshold of a core level. This technique provides chemically selective photoemission, allowing for example the investigation of valence band features in solids.

By using photons with energies near the absorption edge, two mechanisms can extract an electron from the valence band:

-Direct Photoemission: This is the photoemission process where a photon is absorbed, promoting an electron from the valence band to the empty state. The emitted photoelectron carries information about the valence band region.

-Auger Relaxation: This process occurs when the incident photons have an energy exactly at the absorption edge. In this case, a core electron is excited to an empty state, and then the system undergoes an Auger relaxation process where the excited electron fills the core hole and another electron is

emitted from the valence band. This electron has the same kinetic energy as the direct photoemission electron. This auto-ionization process contributes to the resonant photoemission spectra.

The resonant photoemission spectra are then, obtained due to the final-state coherent interference between the two corresponding electron waves involved in the direct photoemission and the Auger relaxation processes. This interference produces characteristic features in the spectra. The processes are depicted in figure 2.28.

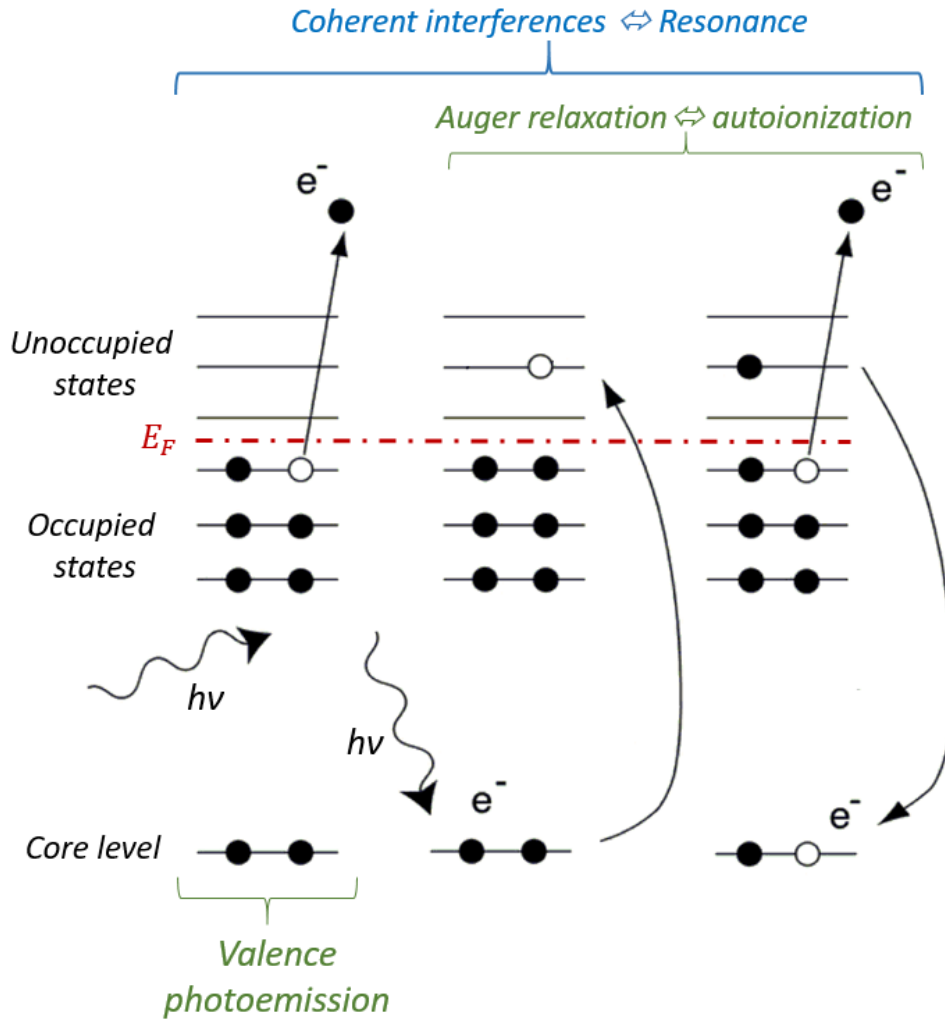


Figure 2.28: Schematic diagram of the resonant phenomena when investigating the valence band in RPES: interference between the photoemission from the valence band and the Auger relaxation. E_F stands for the Fermi level of the sample.

In this thesis, RPES have been used to study valence band of BTO at L_2 , L_3 edge of titanium.

By working at the L_3 edge of Ti, only states corresponding to Ti atoms will resonate in the valence band.

The RPES experiments were done at CASSIOPEE beamline at the Synchrotron SOLEIL. This beamline is dedicated to angle-resolved photoemission spectroscopy in the energy range of 50-1600 eV. RPES experiments are typically performed using a hemispherical analyzer (here a Scienta R4000 electron analyzer) and a high-energy-resolution monochromator to obtain high-resolution and high-throughput measurements.

2.3.3 X-ray absorption spectroscopy (XAS) and Extended X-ray absorption fine structure (EXAFS)

X-ray absorption spectroscopy (XAS) involves photoionization. The XAS spectrum is usually obtained by measuring the intensity of the X-rays transmitted through the sample as a function of energy or current generated in the sample. The spectrum contains information about the electronic structure of the absorbing atoms in the sample, such as the energy levels of the inner shells, the number of unoccupied states in the conduction band, and the bonding and coordination environment of the absorbing atoms.

XAS can be performed in a variety of modes of measurement, including transmission, fluorescence, and total electron yield, and can be applied to a wide range of materials, including solids, liquids, and gases. Practically for our EXAFS experiments the XAS at the Ti-K edge was recorded by measuring the X-ray fluorescence of the samples at SAMBA beamline at synchrotron SOLEIL. The beamline covers the energy range from 4.8 eV to 40 keV, making it suitable for studying the electronic structure of a wide range of materials [41].

The XAS spectrum typically consists of two main features: the edge and the extended X-ray absorption fine structure (EXAFS). The edge corresponds to the energy required to excite a core electron to an unoccupied state, and its shape and position depend on the energy levels and environment of the absorbing atom. The EXAFS region contains information about the local atomic structure surrounding the absorbing atom (see figure 2.29) [42-Bianconi 1988].

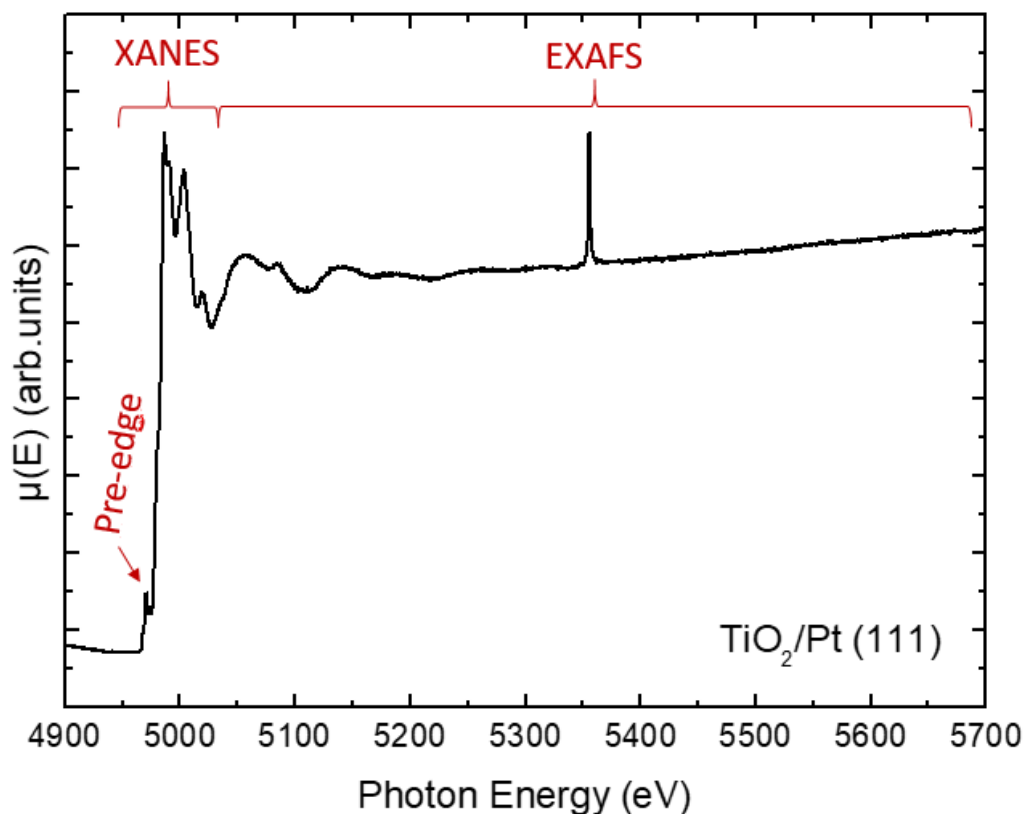


Figure 2.29: Ti-K edge absorption spectra for a $\text{TiO}_2/\text{Pt}(111)$ film. The different remarkable regions are highlighted in red.

EXAFS oscillations result from the interference of the emitted photoelectron waves, which arise due to the wave-like nature of the photoelectron emitted by the absorbing atom. The photoelectron can be viewed as a spherical wave emanating from the excited atom, and its wave vector changes as a function of the energy (E) of the incident photons:

$$k(E) = \sqrt{\frac{2m}{h^2}} (E - E_0)$$

Where, k is a wave vector of photoelectron, m is the electron mass (9.11×10^{-31} kg), E_0 the absorption edge energy.

The EXAFS oscillations are directly related to the absorbing atom's environment, including the number, type, and distance of neighboring atoms. EXAFS provides thus, valuable insights into the chemical environment of specific atoms. For example, in the case of N doped TiO_2 , the EXAFS signal measured immediately after the Ti-K edge can provide information about the environment of Ti atom.

To conduct the analysis of a EXAFS spectrum (Figure 2.30):

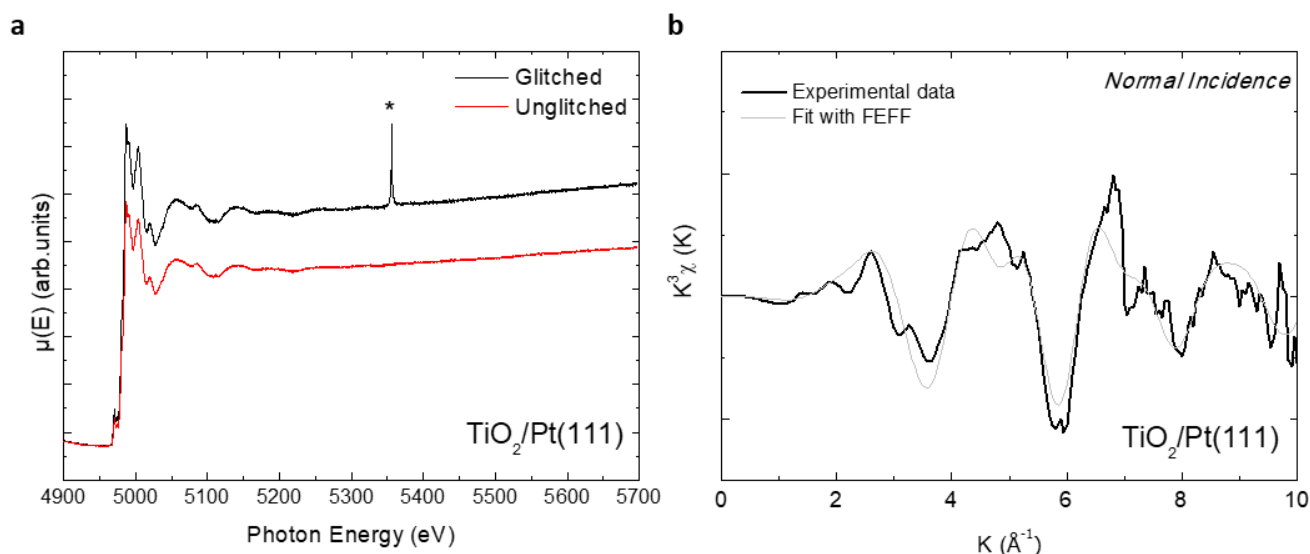


Figure 2.30: Ti-K edge EXAFS data post-processing illustration: (a) raw absorption spectra recorded in normal incidence with glitches (black line, glitches are indicated by asterisks) and glitch-free (red line), (b) corresponding experimental EXAFS oscillations obtained by the Athena software (black thick line) and the fitted data by FEFF calculations assuming a rutile crystallographic structure (grey thin line) using the Artemis software. Sample: $\text{TiO}_2 / \text{Pt} (111)$.

First, we need to preprocess the raw data to correct for background noise and any other experimental artifacts, this step is known as *deglitching*. Second, this may involve subtracting a background spectrum, normalizing the data, and/or applying a Fourier transform. We start converting $\mu(E)$ data (raw absorption spectra) into $\chi(k)$ data (EXAFS oscillations)

The EXAFS oscillations $\chi(k)$ in this approach can be expressed by [43-Magnan 1990]:

$$k\chi(k) = \sum_i \frac{N_i}{r_i^2} \times e^{-2\sigma_i^2 k^2} \times e^{-2r_i/\lambda(k)} \times F_i(k) \times \sin(2kr_i + \phi_i(k))$$

Where, k is the wavevector of the photoelectron, i is the index of shell of neighbours (N_i the number of neighbours in this shell, r_i their distance from the absorbing atom, σ_i^2 their Debye –Waller factor), λ is the mean free path of the photoelectron and F and ϕ are the amplitude and the photoelectron phase shift. σ^2 , the Debye Waller factor is related to the mean square displacement (MSD) of atoms from their equilibrium positions.

The EXAFS signal corresponding to a particular bond in a material is maximized when the linear polarization vector of the incident X-ray beam is parallel to the bond, and is minimized when it is

perpendicular to the bond. On the SAMBA beamline, the sample can be rotated so the polarization vector of the incident X-rays is either parallel or perpendicular to the surface of the sample. In normal incidence (*i.e.* when the X-ray beam is perpendicular to the surface), the polarization vector of the X-rays will then, be parallel to the basal plane of the sample. This will result in a preferential probing of the in-plane atomic structure of the sample. In contrast, in grazing incidence (*i.e.* when the X-ray beam is almost parallel to the sample surface), the polarization vector of the X-rays will be almost perpendicular to the basal plane of the sample. This will result in a preferential probing of the out-of-plane atomic structure of the sample.

EXAFS oscillations simulation are done using the Artemis software and FEFF calculations (with HORAE and FEFF 6 codes [44-Ankudinov 1998, 45-Ravel 2005]). FEFF6 files are used in the Artemis software to simulate the EXAFS oscillations observed in experimental data. The FEFF6 program calculates the possible single and multiple scattering paths from the absorbing atom to the neighboring atoms, taking into account the crystallographic structure of the material, the absorption edge type, temperature, and incident beam polarization. It then determines the contribution of these paths to the EXAFS signal. In Artemis, the user selects the paths to be used in simulating the experimental data. The fitting parameters for each path correspond to the amplitude, distance between the neighbor and absorbing atom, and the Debye-Waller factor.

2.5 References

- [1]. Cho, A. Y., & Arthur, J. R. (1975). Molecular beam epitaxy. *Journal of Vacuum Science and Technology*, 13(3), 747-753
- [2]. Sze, S. M. (1969). *Semiconductor devices: physics and technology*. Wiley.
- [3]. Ohring, M. (1992). The materials science of thin films. *Appl. Opt.*, 31(34), 7162.
- [4]. Lapano, J., Brahlek, M., Zhang, L. et al. (2019). Scaling growth rates for perovskite oxide virtual substrates on silicon. *Nat Commun* 10, 2464.
- [5]. Egawa, T., Mino, T., & Jimbo, T. (2005). Hetero-Epitaxy and Material-Bonding for 3Integrated Multi-Wavelength Photonic Devices. *Journal of Vacuum Science & Technology B*, 23(4), 1473-1476.
- [6]. Brahlek, M., Gupta, A. S., Lapano, J., Roth, J., Zhang, H.-T., Zhang, L., Haislmaier, R., Engel-Herbert, R. (2018). *Adv. Funct. Mater.* 28, 1702772.
- [7]. Cho, A. Y., Panish, M. B., & Hayashi, I. (1970). 3rd Int. Symp. On Gallium Arsenide and Related Compounds, The Institute of Physics, Conference Series Number 9, pp. 18-29.
- [8]. Cho, A. Y. (1999). How molecular beam epitaxy (MBE) began and its projection into the future. *Journal of Crystal Growth*, 201(202), 1-7.
- [9]. SPECS Surface Nano Analysis GmbH. (n.d.). MPS ECR HO. <https://www.specs-group.com/nc/specs/products/detail/mps-ecr-ho/>
- [10]. Harris, J. J., Joyce, B. A., & Dobson, P. J. (1981). Oscillations in the surface structure of Sn-doped GaAs during growth by MBE. *Surface Science Letters*, 103(1), L90-L96.
- [11]. S. Hasegawa. (2012) *Characterization of Materials (Second Edition)*, chapter Reflection High-Energy Electron Diffraction, pages 1925–1938
- [12]. Barbier, A., Belkhou, R., Ohresser, P., Gautier-Soyer, M., Bezencenet, O., Mulazzi, M., Guittet, M.-J., & Moussy, J.-B. (2005). Electronic and crystalline structure, morphology and magnetism of nanometric Fe₂O₃ layers deposited on Pt(111) by atomic oxygen assisted molecular beam epitaxy. *Physical Review B*, 72, 245423.
- [13]. Derj, A., Magnan, H., Mocuta, C., Le Fèvre, P., & Leroy, J. (2022). Properties of self-oxidized single crystalline perovskite N : BaTiO₃ oxynitride epitaxial thin films. *Materials Advances*, 3, 3135-3142
- [14]. Hertz, H. (1887). Über die Berührung fester elastischer Körper (On the contact of elastic solids). *Annalen der Physik*, 267(7), 983-1000.

- [15]. Einstein, A. (1905). Über einen die Erzeugung und Verwandlung des Lichtes betreffenden heuristischen Gesichtspunkt (On a heuristic point of view concerning the production and transformation of light). *Annalen Der Physik*, 17(6), 132-148.
- [16]. Hollander, J. M., & Shirley, D. A. (1970). Chemical information, from photoelectron and conversion- electron spectroscopy.
- [17]. Seah, M. P.; Dench, W. A. (1979), "Quantitative electron spectroscopy of surfaces: A standard data base for electron inelastic mean free paths in solids", *Surface and Interface Analysis*, 1: 2–11,
- [18]. Fairley, N., Fernandez, V., Richard-Plouet, M., Guillot Deudon, C., Walton, J., Smith, E., Fla-haut, D., Greiner, M., Biesinger, M., Tougaard, S., Morgan, D., & Baltrusaitis, J. (2021). Systematic and collaborative approach to problem solving using X-ray photoelectron spectroscopy
- [19]. Briggs, D., & Grant, J. T. (2003). *Surface Analysis by Auger and X-ray Photoelectron Spec-troscopy*. *Surf. Interface Anal.*2004;36: 1647
- [20]. Hofmann, S. (2012). *Auger-and X-ray photoelectron spectroscopy in materials science: a user-oriented guide* (Vol. 49). Springer Science & Business Media.
- [21]. Gibaud, A., & Vignaud, G. (2009). Specular reflectivity from smooth and rough surfaces. *X-ray and Neutron Reflectivity: Principles and Applications*, 85-131.
- [22]. Rioult, M. (2015). Hematite-based epitaxial thin films as photoanodes for solar water splitting (Doctoral dissertation, Ecole Polytechnique).
- [23]. Minggu, L. J., Daud, W. R. W., & Kassim, M. B. (2010). An overview of photocells and pho-toreactors for photoelectrochemical water splitting. *International journal of hydrogen energy*, 35(11), 5233-5244.
- [24]. Bard, A. J., & Faulkner, L. R. (2000). *Electrochemical methods: fundamentals and applications* (2nd ed.). Wiley.
- [25]. Compton, R. G., & Banks, C. E. (2018). *Understanding voltammetry*. World Scientific.
- [26]. J. Tauc, *Mater. Res. Bull.*, (1968), 3, 37.
- [27]. Macdonald, J. R., & Barsoukov, E. (Eds.). (2018). *Impedance spectroscopy: theory, experi-ment, and applications*. John Wiley & Sons.
- [28]. Lasia, A.(2014). Instrumental Limitations. *Electrochemical Impedance Spectroscopy and its Applications*, 333-339.
- [29]. Morrison, F. D., Jung, D. J., & Scott, J. F. (2007). Constant-Phase Element (CPE) Modeling of Ferroelectric Random-Access Memory Lead Zirconate-Titanate (PZT) Capacitors. *J. Appl. Phys.* 101, No. 094112.

- [30]. Lazanas, A. C., & Prodromidis, M. I. (2023). Electrochemical Impedance Spectroscopy— A Tutorial. ACS Measurement Science Au.
- [31]. Brug, G. J.; van den Eeden, A. L. G.; Sluyters-Rehbach, M.; Sluyters, J. H. (1984). The Analysis of Electrode Impedances Complicated by the Presence of a Constant Phase Element. *J. Electroanal. Chem. Interfacial Electrochem.* 176, 275–295
- [32]. Mott, N. F. & Gurney, R. W., (1938). The theory of the photolysis of silver bromide and the photographic latent image. *Proceedings of the Royal Society of London. Series A-Mathematical and Physical Sciences*, 164(917), 151-167.
- [33]. Matsumoto, Y.; Miura, Y.; Takata, S. (2016). Thickness-Dependent Flat Band Potential of Anatase TiO₂(001) Epitaxial Films on Nb:SrTiO₃(001) Investigated by UHV Electrochemistry Approach. *J. Phys. Chem. C* . 120, 1472–1477.
- [34]. Juliao, J. F.; Decker, F.; Abramovich, M. Photoelectrolysis of Water with Natural Mineral TiO₂ Rutile Electrodes. *J. Electrochem. Soc.* 1980, 67, 2264
- [35]. Kumar, P., Singh, S., Spah, M., Juneja, J. K., Prakash, C., & Raina, K. K. (2010). Synthesis and dielectric properties of substituted barium titanate ceramics. *Journal of alloys and compounds*, 489(1), 59-63.
- [36]. Bragg, W.H. and Bragg, W.L. (1913). The reflection of X-rays by crystals. *Proceedings of the Royal Society of London A: Mathematical, Physical and Engineering Sciences*, 88(605), 428-438.
- [37]. Cullity, B.D., and Stock, S.R. (2001). *Elements of X-ray Diffraction*, 3rd Ed. Prentice Hall, New Jersey, USA.
- [38]. Shih, K. (2013). *X-ray diffraction: Structure, principles and applications*. Nova Science Publishers, Inc..
- [39]. Hofmann, P., Schindler, K. M., Bao, S., Bradshaw, A. M., & Woodruff, D. P. (1994). Direct identification of atomic and molecular adsorption sites using photoelectron diffraction. *Nature*, 368(6467), 131-132.
- [40]. Zharnikov, M., Weinelt, M., Zebisch, P., Stichler, M., & Steinrück, H. P. (1994). First experimental determination of an adsorption site using multiple wave number photoelectron diffraction patterns. *Physical review letters*, 73(26), 3548..
- [41]. <http://www.synchrotronsoleil.fr/Recherche/LignesLumiere/SAMBA>.
- [42]. Bianconi, A. (1980). Surface X-ray absorption spectroscopy: Surface EXAFS and surface XANES. *Applications of surface science*, 6(3-4), 392-418.

- [43]. H. Magnan, (1990) Etude par EXAFS de l'ordre local dans des films minces métastables de fer et de cobalt, Ph.D. thesis, Université de Paris-Sud, Orsay, France
- [44]. Ankudinov, A. L., Ravel, B., Rehr, J. J., & Conradson, S. D. (1998). Real-space multiple-scattering calculation and interpretation of x-ray-absorption near-edge structure. *Physical Review B*, 58(12), 7565.
- [45]. B. Ravel and M. Newville (2005). *Journal of Synchrotron Radiation* 12, 537

Chapter III

Self-oxidized single crystalline N-doped oxide layers

Summary: In this chapter, we discuss the potential of nitrogen doped oxides as promising candidate due to their low cost, high electrochemical stability, and flexibility in composition and structure. The chapter summarizes the progress we made in the design, development, and application of Ti+N deposited on SrTiO₃ (001) and Ba+Ti+N deposited on SrTiO₃ (001) as electrodes for water splitting with an emphasis on innovative synthesis strategies and a deeper understanding of structure-activity relationships through systematic characterization. The chapter concludes by discussing the main challenges and prospects for the further development of more efficient photoelectrodes based on perovskite oxides, with the aim of guiding the development of novel metal oxides for photoelectrochemical water splitting.

3.1. Photoelectrochemical properties of perovskite oxides layers

Perovskite oxides have great potential as photoelectrodes for water splitting due to their tunable structural and compositional properties, adjustable electronic structure, and chemical durability [1-Wang 2020, 2-Zong 2021]. While they have demonstrated excellent OER (Oxygen evolution reaction) activity, their HER (Hydrogen evolution reaction) performance is still unsatisfactory due to their low intrinsic electrical conductivity [3-Si 2022]. Here, we focus on improving the OER activity for hydrogen production. To address this issue, various strategies such as doping and defect engineering, surface modification, and crystallographic structure control have been utilized to optimize their photochemistry behavior. Moreover, the internal electronic structure of perovskite oxides also strongly influences their photoactivity.

3.1.1 Structure of perovskite oxides

In an ideal cubic cell without oxygen vacancies, the prototypical perovskite oxide (ABO₃ ex: SrTiO₃) has a high symmetry of *Pmm3*, which is constructed from chains of corner-sharing [BO₆ ex: TiO₆] octahedra, with the larger A-site occupying the 12-fold coordinated sites (Figure 3.1a). In a ABO₃ perovskite A is a rare earth element or an alkaline earth element, and B is a transition metal.

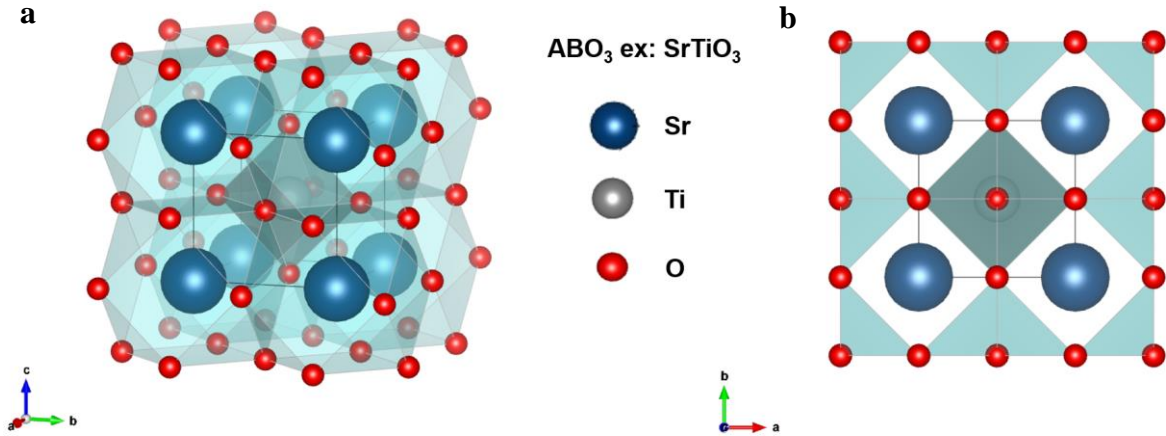


Figure 3.1: **a** Example of the representation of a perovskite crystallographic structure (SrTiO₃ used as substrate in this study) **b** (001) orientation of SrTiO₃.

3.1.2 BaTiO₃ a perovskite material

Barium titanate, BaTiO₃ (BTO), is a perovskite material. The A-site is occupied by Ba and the B-site is occupied by Ti. It is a well-known perovskite material studied for its excellent physicochemical properties such as dielectric and piezoelectric structures [4-Buscaglia 2021], biocompatibility [5-Vijatovic 2008], and optical characteristics [6-Mishra 2017].

During its synthesis, a non-stoichiometry of BaTiO₃ can occur due to several reasons, including oxygen vacancies, Ti or Ba vacancies and/or substitution of Ti or Ba atoms with impurities. These variations in composition can lead to changes in the electronic and structural properties of BaTiO₃. For example, oxygen vacancies (V_o) can lead to the creation of Ti³⁺ ions in the lattice, which can act as electron traps and affect the charge transport properties of BaTiO₃ [7-Donnerberg-2000] More precisely, two Ti⁴⁺ ions can be reduced to Ti³⁺ ions for each V_o [8-Cai 2009]. The chemical formula of the thin films is then given by $Ba^{2+}Ti_{1-2x}^{4+}Ti_{2x}^{3+}O_{3-x}^{2-}$.

For this reason, non-stoichiometry in BaTiO₃ can affect its electronic as well as its structural properties, beginning by its lattice parameters to the overall crystallographic structure caused by strain or simple distortions [9-Barbier 2012,10-Tyunina 2020]. Considering, PEC performances, the control and investigation of the surface/interface composition is crucial mostly during the synthesis process. One approach is to grow thin films of BTO by individual dosing of the metal ions and avoid defects. [9-Barbier 2012].

3.1.3 BaTiO₃ ferroelectric material

Major property of bulk BTO is that exhibits a spontaneous polarization, meaning that the material

has a permanent electric dipole moment even in the absence of an external electric field. This property known as ferroelectricity, arises due to the displacement of positively charged Ti atoms and negatively charged O atoms relative to each other in the crystal structure of BTO. BaTiO₃ is thus, a perovskite-type ferroelectric material that exhibits low-temperature ferroelectricity due to structural frustration of the cubic structure, caused by a misfit of B/A ions within the ABO₃ unit cell (Figure 3.2).

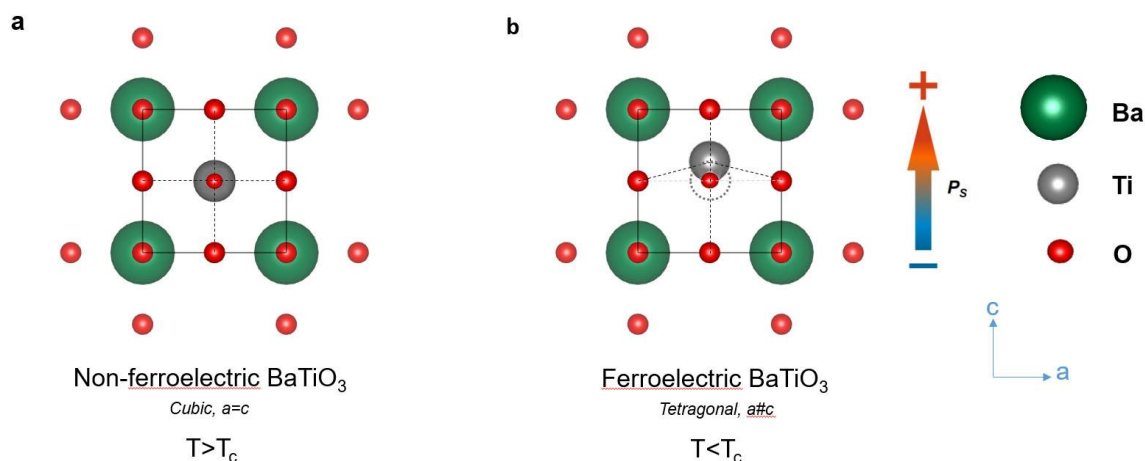


Figure 3.2: Behavior of the BaTiO₃ perovskite below and above the ferroelectric ordering temperature.

BTO has a large polarization value of $26 \mu\text{C cm}^{-2}$ along the c -axis, and a wide bandgap of ~ 3.2 eV, it is an n-type semiconductor (largely due to the presence of oxygen vacancies) so that it can just absorb photons in near-ultraviolet spectrum. The absorption of photons with energies greater than or equal to, the band gap, results in charge transfer predominantly between the O-2p states at the valence band maximum, to the Ti-3d states at the conduction band minimum.

The valence band minimum and conduction band maximum of BaTiO₃ are approximately 2.9 and -0.3 V vs NHE, respectively. The bands are located at similar energies to those in TiO₂ (-0.5 and 2.7 V vs NHE, respectively), which is potentially suitable for water oxidation and proton reduction, making it a promising candidate for water splitting. In 1976, Nasby and Quinn investigated photoelectrochemical water splitting on BaTiO₃ single crystals and observed photoinduced currents of approximately $10.1 \mu\text{A}$ (for a device area of 0.18 cm^2) under UV light [10-Nasby1976]. They also found that BTO electrodes were stable under applied bias and could produce small photocurrents without an applied bias. Although the effect of ferroelectricity was not directly explored in this study, subsequent studies on ferroelectric surfaces were limited. Recently, in a study involving epitaxially

grown thin films of ferroelectric BTO, the authors were able to increase the photocurrent by a factor 2 by poling downward the polarization of the film and promote the OER [11- Rioult 2015].

In summary, the spontaneous polarization in ferroelectric materials creates an internal electric field that can lead to a separation of charge carriers and a higher concentration of reactive species at the surface. This can enhance photochemistry and improve the efficiency of chemical reactions driven by light absorption occurring at the surface of the ferroelectric.

BaTiO₃ is an excellent material for fundamental studies, on the effect of internal electric fields and on charge carrier dynamics, due to, a low temperature para-to-ferro-electric phase transition ($T_c \sim 130^\circ\text{C}$), which makes the non-ferroelectric phase easily accessible.

3.2 Growth and epitaxial single crystalline film of Ba+Ti+N on 1 at.% Nb :SrTiO₃(001)

Nitrogen doping in BaTiO₃ (N:BTO) involves the substitution of oxygen atoms with nitrogen atoms in the crystal lattice of the material. We present in this section results concerning the growth of Ba+Ti+N film compared with the growth of BTO thin film of same thickness (~14nm). The Ba+Ti+N was elaborated with an ECR nitrogen plasma source and the BTO with RF oxygen plasma source. The crystallographic, the electronic structure and the chemical composition were analysed afterwards and before measuring their photocurrent.

3.2.1 Nitride materials by Molecular Beam Epitaxy

In order to determine the growth parameters, two calibration routines were used. The first calibration routine involved determining the effusion cell flux for titanium and barium. To maintain consistency with our model systems, we specifically chose structures that could be grown epitaxially. Therefore, the well-established conditions to grow epitaxial BTO film with a 1:1 stoichiometry for Ti:Ba is kept the same with respect of the conditions found by Barbier et al. in 2012 [9-Barbier 2012]. Effusion cells fluxes were determined using a quartz microbalance. The measure starts at the evaporation temperature of the metal ions. Once the temperature is reached, the effusion cell shutter is opened and the quantity of deposited matter is read on the microbalance over a period of time, and the deposition rate is then, deduced. Multiple effusion cell temperatures for both species were measured, in order to select the deposition rates relative to the epitaxial growth condition. To check the stoichiometry after growth, the derivative peak to peak amplitude from Ti_{LMM}/Ba_{MNN} is calculated from the AES spectrum of the films.

The second calibration routine utilized was determining the nitrogen incorporation concentration for

nitriding using ECR plasma source. The choice of nitrogen source (ECR, RF nitrogen or ammonia [12-Kamp 1997]) has a significant impact on the optical and structural properties of the resulting films [13-Yun2002]. For example, Yun *et al.* observed that films grown using RF nitrogen exhibited higher optical bandgap energies and better crystal quality as compared to those grown using ammonia. The difference is likely due to differences in the reactivity and adsorption kinetics of the nitrogen sources on the surface during growth (Cf chapter 2).

3.2.2 ECR nitrogen source calibration: Atomic Nitrogen

To calibrate the atomic nitrogen flux of the plasma source, an investigation was conducted to explore the potential nitriding of a polished Al foil.

The cleaning process for the Al substrate involved the following sequential steps. Initially, the substrate was polished using a rough paper for the removal of surface contaminants. Subsequently, the substrate was immersed in ultrasonic baths of Ethanol to eliminate soluble residues. Following the ultrasonic cleaning, the substrate underwent a rinse with Ethanol and the substrates were dried using nitrogen blowers. Finally, the dried substrates were mounted onto a molybdenum block and transferred to the MBE system.

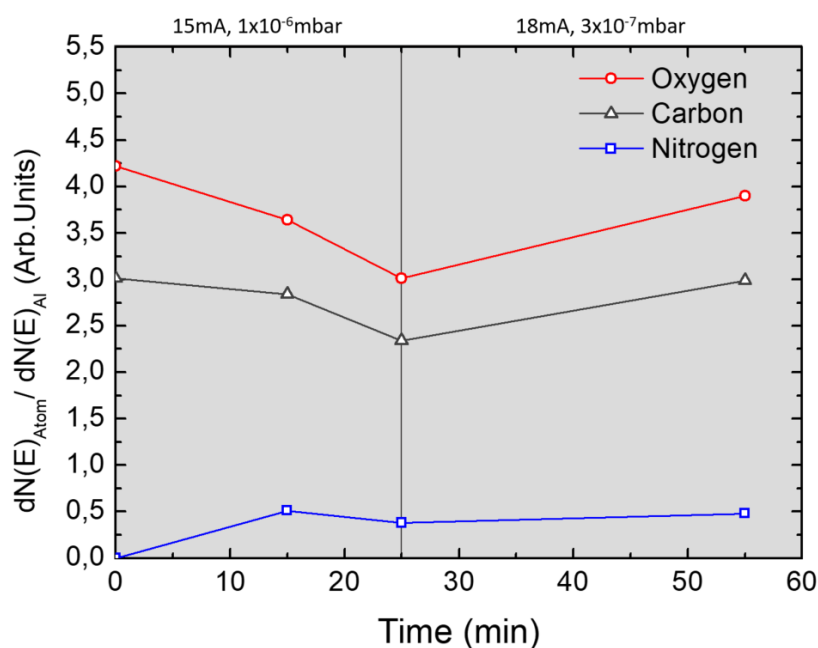


Figure 3.3: Evolution of the concentration of each species; O, N, and C during nitridation of Al using the ECR source with a single hole aperture. The solid lines are guides to the eyes.

After the substrate preparation, the nitridation of Al is performed at 450°C for 55 minutes with the magnetron current of the ECR and nitrogen pressure were set to 15mA and 1×10^{-6} mbar, respectively,

for the first 15 min. Afterwards for a duration of 30 min, we increased the current and reduced the pressure to the minimum of operating conditions we obtained experimentally (18mA, 3×10^{-7} mbar, respectively). At different steps (at 0 min, 15 min, 25 min and 50 min), we performed AES spectra in order to measure the amount of carbon, oxygen and nitrogen (Figure 3.3). The nitrogen amount increases at 15 minutes but for further deposition the amount of nitrogen remained constant while C and O amounts do not decrease, showing that the nitridation of Al in these conditions is not very efficient. However, nitrogen is present on the substrate.

In order to find the best parameters for the pressure and the magnetron current, we measured the sample current which is due to the ECR plasma and is expected to be higher at low pressure and with high magnetron current. The sample current measured at 18 mA as a function of pressure is represented in figure 3.4a and the sample current at 4×10^{-7} mbar as a function of magnetron current is represented on figure 3.4b. The optimum current is obtained for 18 mA and 3×10^{-7} mbar corresponding to the area with a constant current.

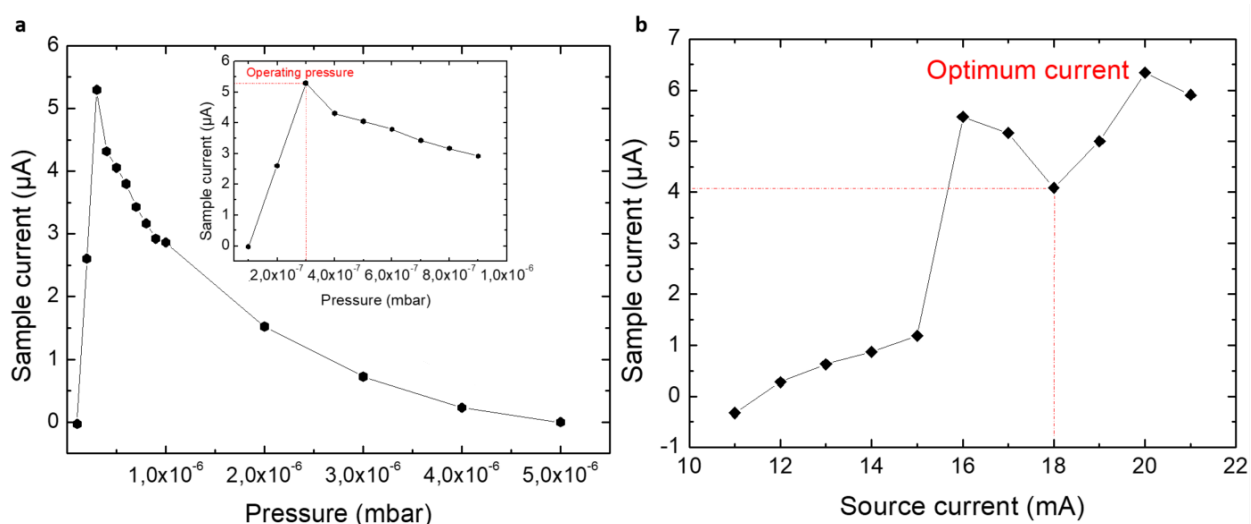


Figure 3.4: Calibration of the **a** operating pressure and **b** the source current for nitriding.

Under high temperature conditions and an active nitrogen flux, the oxygen and carbon atoms in the very top layer of Al can be replaced by nitrogen which creates a very thin AlN layer. This process is referred to as nitridation of the substrate. During this initial stage, both the C and O Auger signals reduced in proportion, consistently with the N overlayer coverage. Surprisingly, the N signal slightly decreased while the O and C signals continued to decrease. One possible explanation for this phenomenon is that atomic nitrogen becomes weakly adsorbed on the surface as the nitridation process proceeds.

3.2.2 Deposition of Ti+N on SrTiO₃ (001) and 1% Nb:SrTiO₃ (001)

Ti is known to readily form Ti nitride through various elaboration methods. It is thus a suitable method

to setup our N source to produce nitrides or oxynitrides. However, bulk TiN has a large band gap which may be unfavorable for PEC applications.

3.2.2.1 Crystal growth of TiN: Synthesis of our first nitride.

As a second step in the nitriding study, the focus was on the fabrication of the first nitride layer. The chosen material, titanium nitride (TiN), possesses a rock salt crystal structure typically formed under extremely high pressures. TiN adopts a face-centered cubic (FCC) rock-salt structure with a space group $Fm\bar{3}m$ (225) with a lattice parameter $a_{\text{theory}} = 0.424$ nm [19-Pierson 1996] (Figure. 3.5d). The lattice mismatch between the (001) crystal planes of TiN and SrTiO₃ is about 8%. The Ti + N film was grown on SrTiO₃ substrates at 450°C after the usual cleaning process for 1 hour and half under oxygen plasma. The Ti flux was the same as the one used to grow BaTiO₃. The nitrogen flux parameters were 18mA and 4×10^{-7} mbar, a condition under slightly lower nitrogen pressure than in the AlN experiment, in order to work a bit away from the threshold. For both low index azimuths, the *in situ* RHEED patterns (Figure 3.5a) are consistent with a cube/cube epitaxy. The streak-like pattern is characteristic of two-dimensional scattering, indicating that the TiN film is smooth. On figure 3.6, we compare the deposition to another film that was grown under the same conditions by doubling the deposition duration (360 min) and on 1%Nb: SrTiO₃ (001) for electrical conductivity and solar water splitting purposes. When the deposition was performed on Nb-doped substrates. The diffraction spots of the patterns and their integrated profiles at 360 minutes exhibited significantly sharper and more elongated features (Figure 3.6a). This observation suggests that the Ti+N film grown on the Nb-doped substrate achieved improved crystallinity.

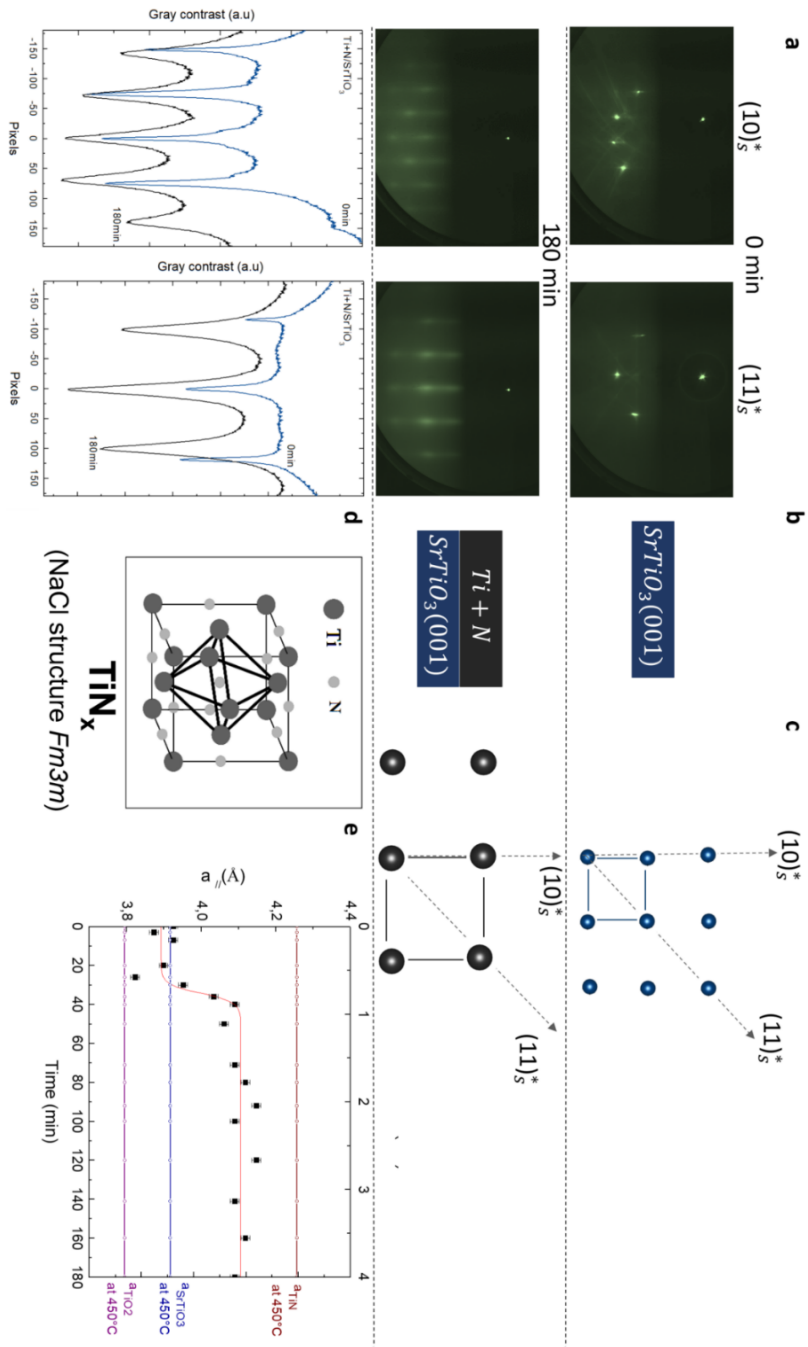


Figure 3.5: **a** the observed RHEED patterns along the $(10)_s^*$ and $(11)_s^*$ azimuths during growth for a 4 nm thick film and their corresponding integrated profiles along the streak directions, at 0 and 180 min. **b** The upper (resp. bottom) line shows the data for the SrTiO₃ (001) substrate (resp. Ti+N/SrTiO₃ (001) film). **c** the corresponding surface reciprocal lattice is represented, making explicit the diffraction directions, the elementary cell (in the reciprocal space) is also shown. **d** TiN Rocksalt structure. **e** Evolution of the TiN in-plane lattice parameter ($a_{//}$) derived from the $(10)_s^*$ direction RHEED pattern assuming rocksalt structure as a function of the film thickness compared with of the lattice parameter of bulk TiN (dark red), SrTiO₃ (dark blue) and TiO₂ rutile (purple) at the deposition temperature (450°C) (taking into account the thermal expansion).

During the first 20 minutes of deposition, the initial sharpness of the RHEED pattern of SrTiO₃(001) degrades slightly. From each RHEED pattern, we extracted line profiles to determine the in-plane lattice parameter evolution (Figure 3.5e and Figure 3.6d) assuming a rocksalt structure of the film. Optimal crystal growth and the crystal relaxation is achieved after 50 minutes growth. Taking into account the coefficient thermal expansion (approx. $7.4 \times 10^{-6} \text{ K}^{-1}$ and $9.0 \times 10^{-6} \text{ K}^{-1}$) the lattice parameters for SrTiO₃ and TiN at 450°C are 0.391 nm and 0.426 nm, respectively. However, the measured in-plane lattice parameters are found to be 0.411 nm for a deposition time of 180 minutes and 0.416 nm for 360 minutes deposition (Figure. 3.5e and Figure 3.6d). These results conform a cubic epitaxial growth with a slightly lower lattice parameter than bulk TiN.

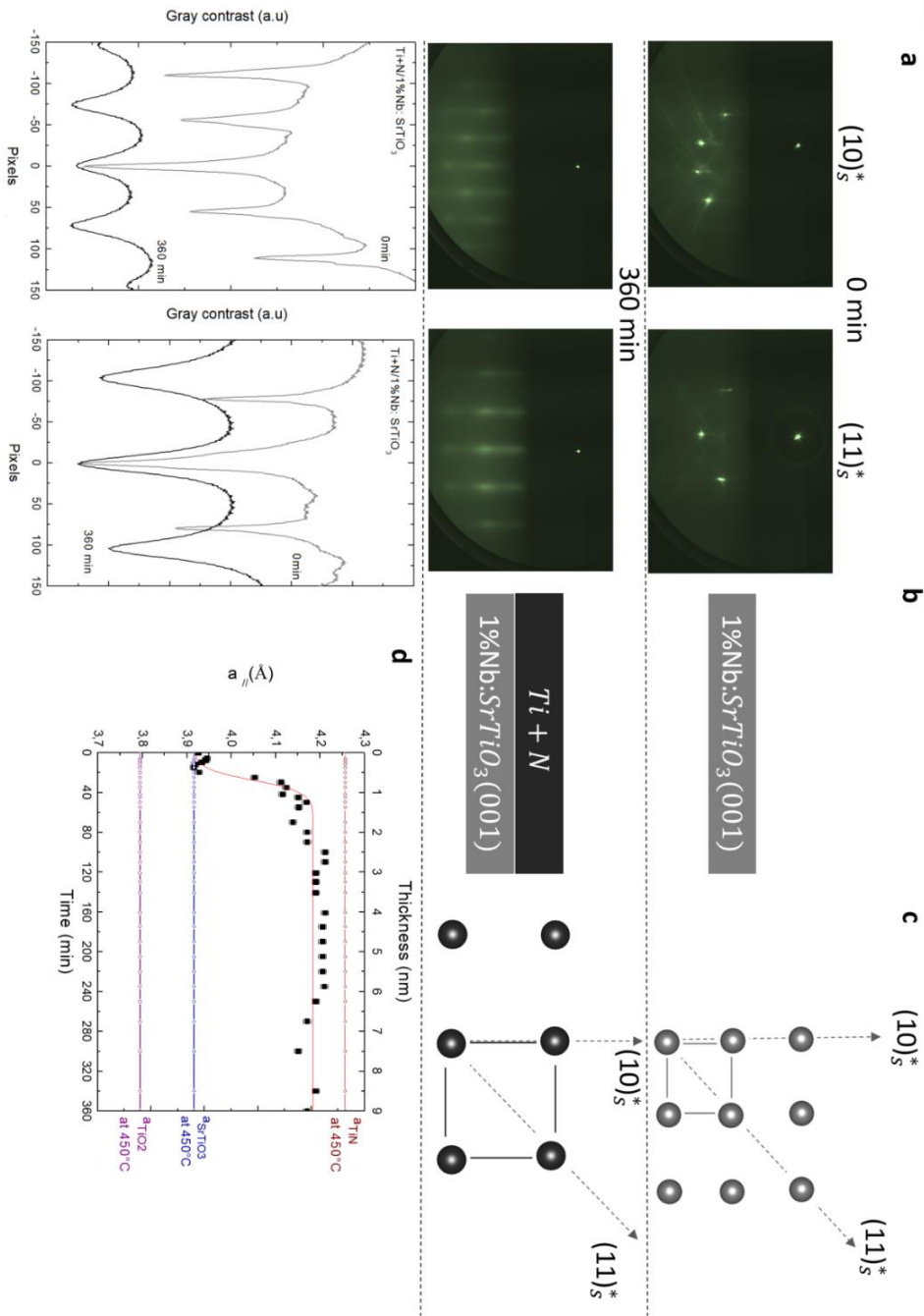


Figure 3.6: **a** The observed RHEED patterns along the $(10)_s^*$ and $(11)_s^*$ azimuths during growth for a 9 nm thick film and their corresponding integrated profiles along the streak directions, at 0 and 360 min. **b** The upper (resp. bottom) line shows the data for the 1%Nb:SrTiO₃ (001) substrate (resp. Ti+N/ 1%Nb:SrTiO₃ (001) film). **c** The corresponding surface reciprocal lattice is represented, making explicit the diffraction directions, the elementary cell (in the reciprocal space) is also shown. **d** Evolution of the TiN in-plane lattice parameter ($a_{//}$) as a function of the film thickness deduced from the $(10)_s^*$ direction RHEED pattern. Dashed lines stand for the in-plane lattice parameter of bulk TiN (dark red), SrTiO₃ (dark bleu) and TiO₂ (purple) at the deposition temperature (450°C) (taking into account the thermal expansion).

3.2.2.2 Chemical composition of Ti+N on SrTiO₃(001) and 1% Nb:SrTiO₃ (001).

Figure 3.7 displays the *in situ* AES results for TiN films with two different thicknesses. Interestingly, both films exhibit an O_{KLL} peak in the spectra, despite no intentional introduction of oxygen into the growth chamber. The results confirm a clear oxide content after growth i.e. TiO_xN_{1-x}. It is worth noting that AES was performed *in situ* within the same chamber after the film growth. The presence of oxygen in the film is likely attributed to the diffusion of oxygen from the SrTiO₃ substrate. To quantify the amount of oxygen in the film, the $\frac{O_{KLL}}{Ti_{LMV}}$ ratio is calculated. The Ti_{LMV} peak is chosen instead of the Ti_{LMM} one since the Ti_{LMM} peak overlaps with the N_{KLL} peak.

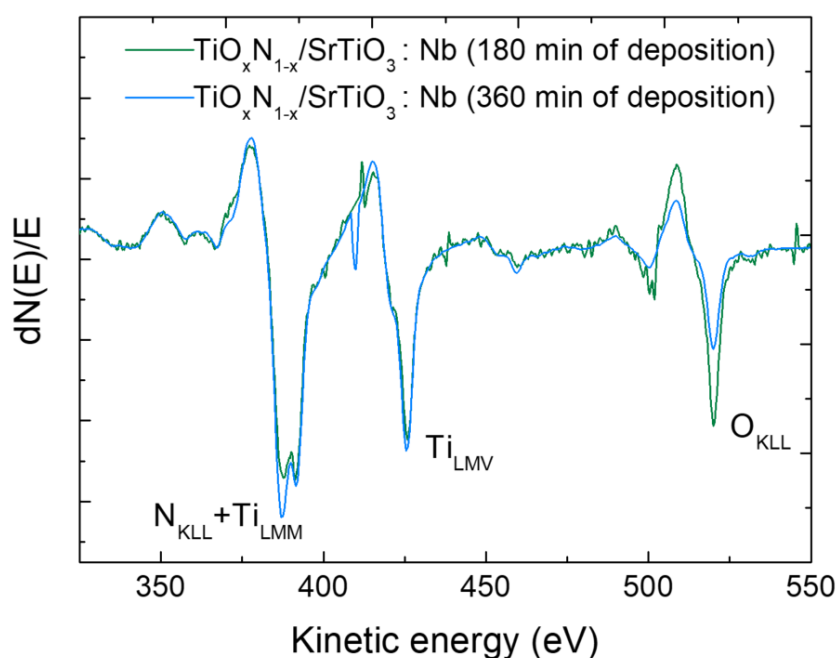


Figure 3.7: *In situ*, AES spectra of the thin Ti+N film (180min deposition) deposited on SrTiO₃(001) and the thick Ti+N film (360min deposition) deposited on 1%Nb:SrTiO₃. The spectra are normalized at 418 eV.

For the thicker (respectively thinner) film, the $\frac{O_{KLL}}{Ti_{LMV}}$ ratio is 0.51 (respectively 0.99). This means that the thinner film contains a higher proportion of oxygen as compared to the Ti content.

Interestingly, doubling the deposition time nearly halved the oxygen amount diffusing from the substrate to the film surface. Thus, a longer deposition time allows for a more efficient incorporation of nitrogen into the film.

The quantification of N content by AES is however difficult since the main N_{KLL} peak overlapped with the Ti_{LMM} peak at ~390eV (Figure 3.7). Direct quantification of Ti:N ratio using the main peaks

will lead to overestimating the N content. We thus, realized complementary experiments to determine the N content by *ex situ* XPS.

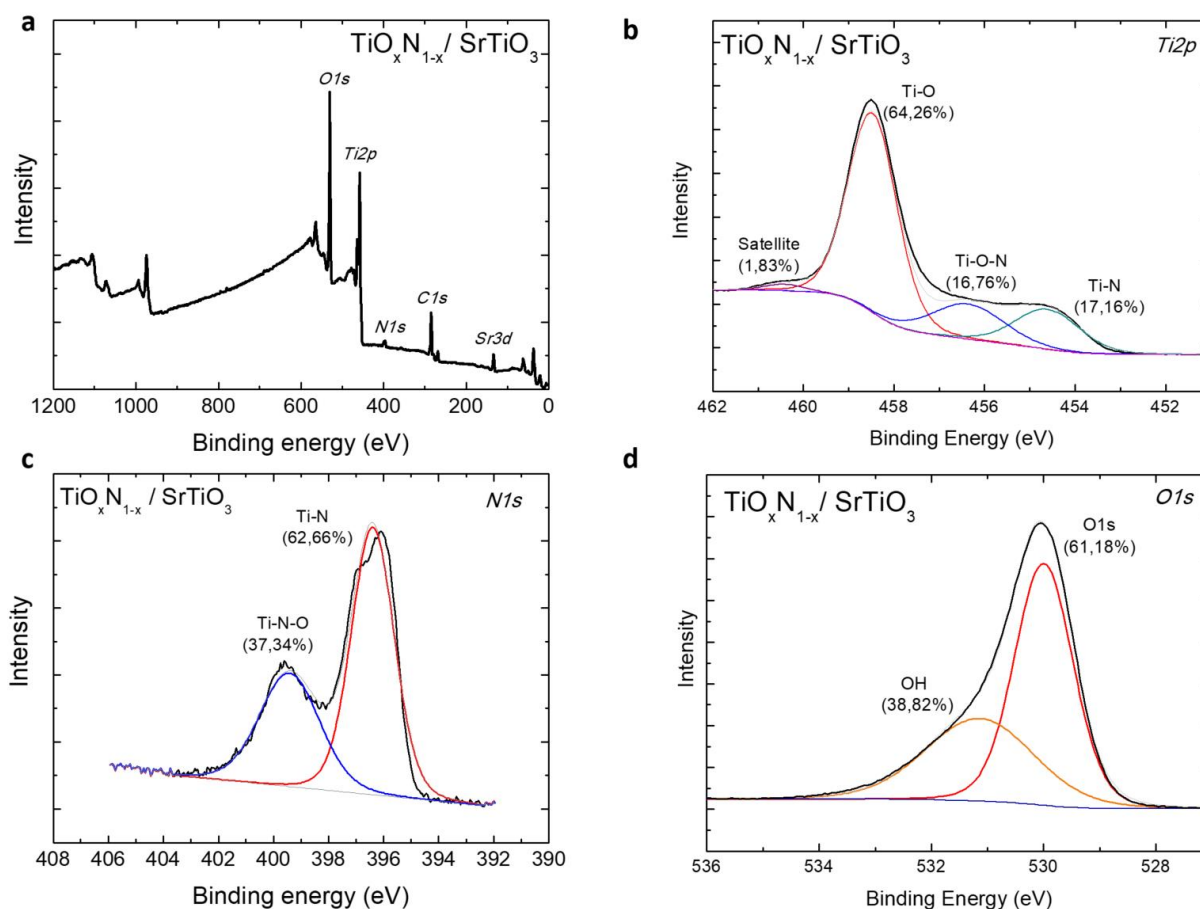


Figure 3.8: X-ray photoemission spectra of thin Ti+N (180min deposition) deposited on SrTiO₃(001). **a** Wide scan **b** Ti-2p core level, **c** N-1s core level and **d** O-1s core level.

Firstly, a survey spectrum is acquired to determine the elements present in the TiN film (Figure 3.8a). The C 1s XPS peak, due to surface contaminants at 284.8 eV, was used as a reference for the detected peak positions. For quantification, the area under the peak is evaluated using Ti-2p and N-1s peaks we obtain a $\frac{N}{Ti} = 15.2\%$ ratio (Figure 3.8c). Considering that the measurement is realized *ex situ*, the oxygen quantification is here irrelevant due to air contamination, which also explains the presence of hydroxyl groups (OH) on the surface (Figure 3.8d). Nonetheless, nitrogen species existing in the bulk means that the ECR plasma source is functioning well and allows doping oxide layers as expected.

3.2.2.3 The crystal structure of Ti+N on SrTiO₃(001) and 1% Nb:SrTiO₃(001).

Before adding barium flux to scheme, we studied more profoundly the film intrinsic properties raised

from this method of growth.

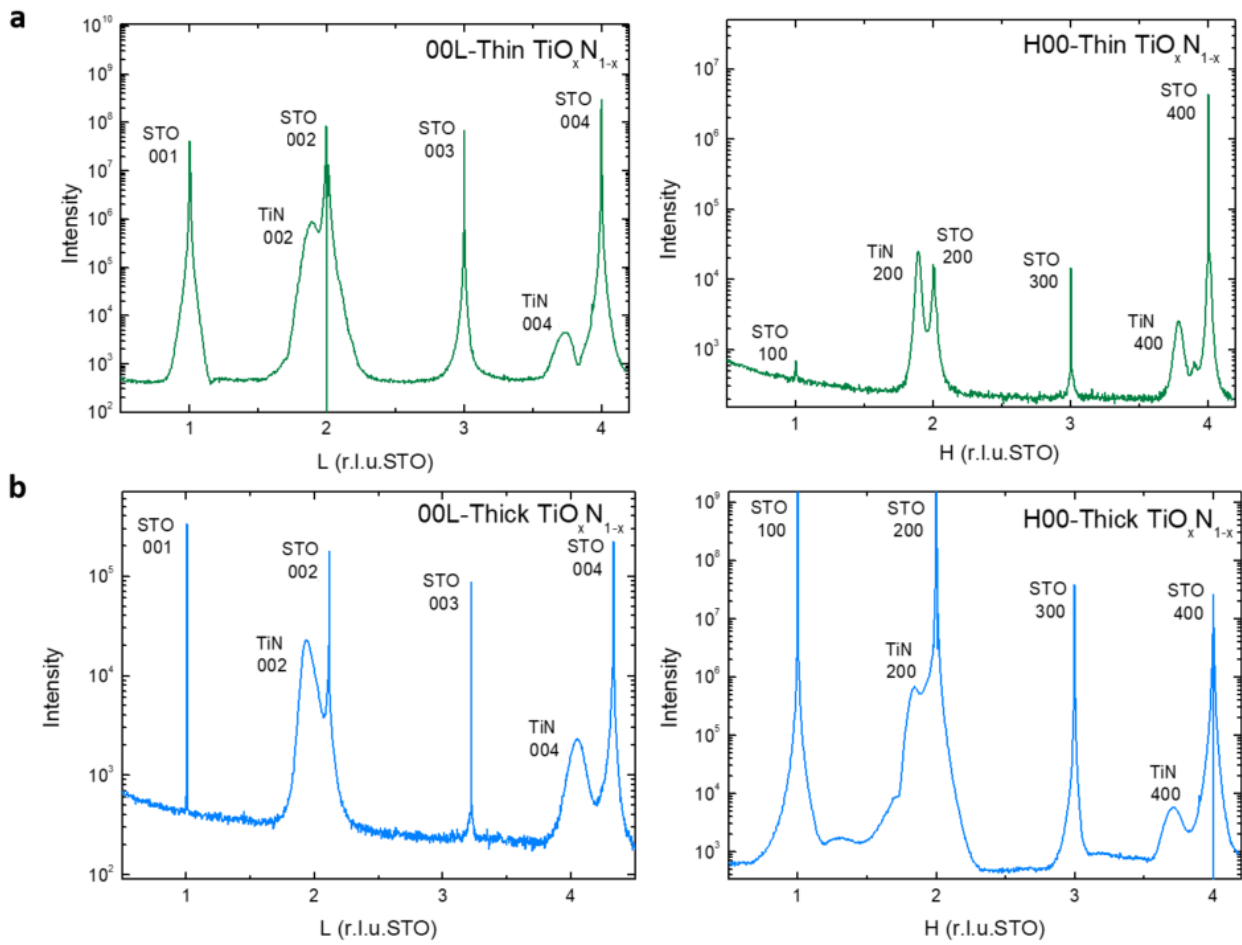


Figure 3.9: Wide angle X-ray diffraction along specular directions for **a** thin $\text{TiO}_x\text{N}_{1-x}$ (180min deposition) sample and for **b** thick $\text{TiO}_x\text{N}_{1-x}$ (360min deposition) sample.

The crystallographic structure was studied by X-ray diffraction on the DIFFABS beamline at synchrotron SOLEIL the results are reported in figure 3.9. The out of plane specular scans (00L) and in-plane diffraction (H00) are given for the thin and thick samples. The Bragg peaks were well fitted using Lorentzian shaped peaks, and the sharp peaks of SrTiO₃ (001) indicated the high crystalline quality of the single crystalline substrate. The TiN 002 and TiN 004 Bragg peaks appear in the form of a bump on the low L side of the SrTiO₃. From specular XRD measurements, we can derive the out-of-plane lattice parameter c , and the in-plane parameter a from grazing incidence measurements. We obtained $c = 4.13 \pm 0.10 \text{ \AA}$ for the thin film and $4.20 \pm 0.10 \text{ \AA}$ for the thick film. The a values are in good agreement with the RHEED diffraction data (Table 1). Hence, the thicker layer ($c/a = 0.997$) is slightly more cubic than the thinner one ($c/a = 1.005$) which might be due to the concentration imbalance between oxygen and nitrogen in the lattices. It might also be suggested that incorporating defects in the TiN lattice such as vacancies at Ti sublattice sites, allows the cell to shrink in order to

release the internal stress. This behavior happens often in TiN oxidized films produced by physical vapor deposition techniques [21-Greene 1995, 22-Perry 1992]. Epitaxial TiO_xN_{1-x} films can thus, easily be grown with either tensile ($c/a < 1$) or compressive ($c/a > 1$) strain.

Sample	RHEED		XRD	
	a _{//} (Å)	a (Å)	c (Å)	$\frac{c}{a}$
Thin-TiO _x N _{1-x}	4.11	4.13	4.15	1.005
Thick-TiO _x N _{1-x}	4.16	4.20	4.21	0.997

Table 1: Summary of significant sample growth parameters deduced from the in-plane RHEED measurements and both in-plane and out-of-plane parameters deduced from XRD measurements for each sample.

3.2.2.4 Influence of nitriding on photoelectrolysis

The band gap energy of TiN is around 3.35-3.45 eV, which makes it potentially suitable material for absorbing UV. The photoelectrochemical properties of the oxidized TiN were studied and compared to a film about the same thickness of TiO₂ (360min deposition). The TiO₂ film was also grown on Nb doped STO during 360min in the same conditions as the ones used by Magnan *et al.* in 2019 [20-Magnan 2019]. Photoelectrochemical measurements demonstrated visible light photoresponse for both photoelectrodes (Figure 3.10a).

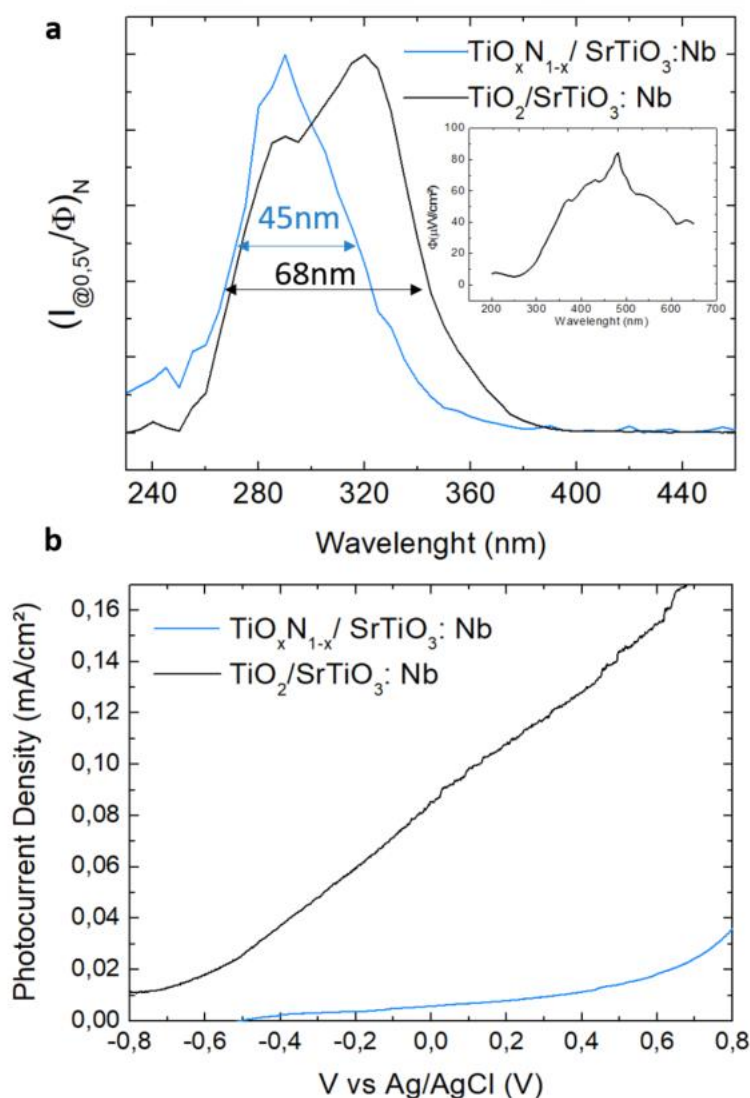


Figure 3.10: **a** Efficient absorption photocurrent density as a function of the wavelength at 0.5 V vs. Ag/AgCl normalized at 320nm, (inset) light flux of the Xe arc lamp as a function of the wavelength, **d** Photocurrent density versus the applied voltage (vs. Ag/AgCl), for thick $\text{TiO}_x\text{N}_{1-x}$ (360min deposition) (blue) and (black) thick TiO_2 (360min deposition) layers.

Figure 3.10a presents data on the photocurrent density normalized to the incident light flux at 0.5V. The spectral absorption of $\text{TiO}_x\text{N}_{1-x}$ and TiO_2 have a Full Width at Half Maximum (FWHM) of 45 nm and 68 nm, respectively (see figure 3.10a). The TiN oxidized sample exhibits a narrower window of efficient absorption with a slightly shifted maximum towards the Ultra-Violet (UV) light range. It is found that the synthesized $\text{TiO}_x\text{N}_{1-x}$ electrode shows lower photopotential under visible light illumination than a pure TiO_2 electrode for solar water splitting as expected considering the larger band gap of TiN (Table 2). However, we demonstrated that from using effusion cells and an ECR nitrogen plasma source, epitaxial (oxy)nitride layers can be produced by exploiting the diffusion of

oxygen from the substrate. This leads however, for films with very high N content to an unfavorable evolution of the band gap and thus to reduced PEC performance as compared to TiO₂.

Sample	FWHM (nm)	Photoelectrochemical band gap (eV)	J _{ph@0,5V}
TiO ₂ /SrTiO ₃ :Nb	68	3.12	0,14
TiO _x N _{1-x} /SrTiO ₃ :Nb	45	3.31	0,01

Table 2: Summary of significant sample photoelectrochemical properties investigated in the present work. The FWHM and the photoelectrochemical band gap deduced from the efficient Tauc plot and the photocurrent measured at 0.5V for thick TiO_xN_{1-x} (360min deposition) and thick TiO₂ (360min deposition) layers deposited on 1%Nb doped SrTiO₃.

3.2.2.5 Conclusion on the firsts experiments on nitriding

TiO_xN_{1-x} films were elaborated using an ECR microwave plasma source in an atomic nitrogen flux. The precise control over growth parameters ensures the production of epitaxial 2D films with precise layer thicknesses.

The presence of oxygen in the film can be attributed to two main sources. Firstly, oxygen diffuses from the SrTiO₃ substrate through self-diffusion. Secondly, oxidation can occur on the film surface when it is exposed to air. The amount of oxygen present in the film depends on its thickness, and it is uncertain if the distribution of oxygen is homogeneous throughout the film.

Titanium is indeed known to easily form nitrides, such as titanium nitride, through various fabrication methods. This property makes it a suitable candidate for setting up our nitrogen plasma source to produce nitrides and/or oxynitrides. Although, when it comes to using TiN for photoelectrochemical (PEC) applications, there is a potential concern due to its large band gap (typically 3.4 eV). When nitrogen is introduced into the TiO₂ films to form oxynitrides (TiO_xN_{1-x}), it can increase the band gap compared to pure TiO₂. Oxidized TiN or heavy N doping are thus obviously not a good option here. However, by carefully controlling the composition and concentration of nitrogen, for low doping levels, it is possible to tailor the electronic properties of the resulting oxynitride making it more favorable for PEC applications (Cf. chapter 4).

The next part of the chapter will focus on using the same oxidation method (diffusion from the substrate) but with films that have the same crystallographic structure as the substrate, *i.e.*, a

perovskite structure and expected lower band gap for the oxynitride. This approach aims to address the limitations encountered with TiN we will thus, explore the synthesis of oxynitride perovskites using the investigated atomic nitrogen flux for nitriding.

3.3 Growth of epitaxial single crystalline film of Ba+Ti+N on 1 at.% Nb :SrTiO₃(001)

The objective of the study was to elaborate an oxynitride thin film using only the atomic nitrogen plasma source without the presence of any other oxygen source. The ECR plasma source was set at 18 mA for a regulated pressure of 4×10^{-7} mbar in the main chamber. Further, the oxynitride film was compared to an undoped BaTiO₃ film grown with the assistance of a high brilliance atomic oxygen plasma source (RF 350 W, pressure 1×10^{-7} mbar for Baratron at 3.1 tours).

Table 3 summarizes the two deposition conditions used in the study, which we deemed significant for investigating the available parameters. The chosen results samples reported here were derived from multiple deposits on undoped SrTiO₃ substrates for calibration purpose.

Sample	O	N
BaTiO ₃	3.1trs/350W(RF)	--
BaTiO ₃ N _{3-y}	--	P _N = 4.0×10^{-7} mbar/ I=18mA

Table 3: Summary of significant sample growth conditions

3.3.1 *In situ* analysis of the samples

3.3.1.1 *In situ* RHEED

During the growth, the samples were kept at about 450 °C while the crystallographic structure was followed by *in situ* RHEED. Figure 3.11a presents the RHEED patterns of the Ba+Ti+N structures grown by NPA-MBE on Nb:SrTiO₃(001) substrates. Both samples showed RHEED patterns with straight lines, accounting for a 2D growth, at least up to 60 min. In the Frank-van der Merwe growth mode, the deposited atoms spread out evenly over the surface of the substrate, forming a continuous film. This mode is characterized by the complete wetting of SrTiO₃ by the growing material.

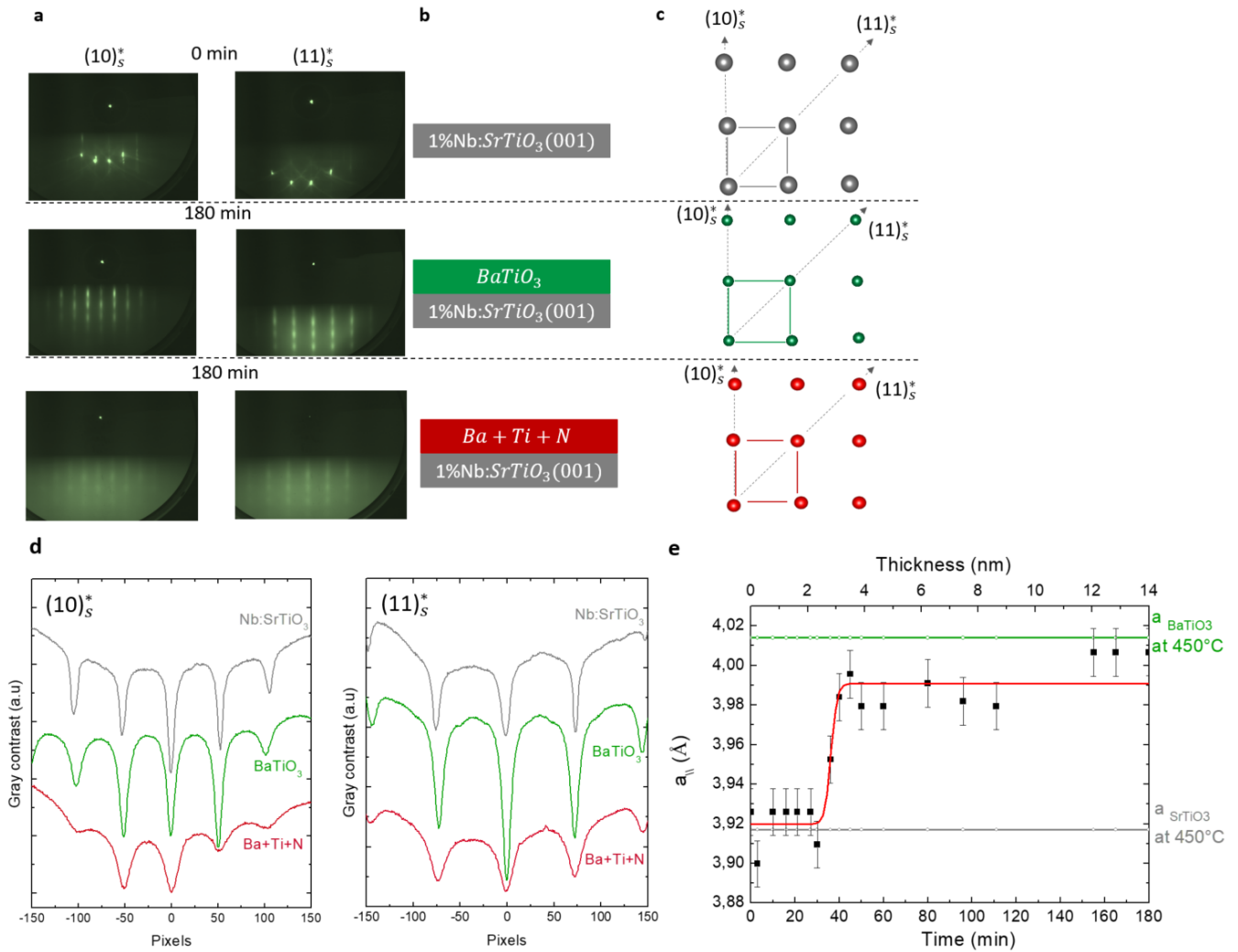


Figure 3.11: **a** RHEED patterns along $(10)_s^*$ and $(11)_s^*$ azimuths observed during the growth of BaTiO₃ and Ba+Ti+N on 1%Nb doped SrTiO₃. The total thickness is about 14 nm after 180 min of deposition. **b** growth steps. **c** The corresponding surface reciprocal lattice is represented, making explicit the diffraction directions, the elementary cell (in the reciprocal space) is also shown. **d** The corresponding integrated profiles of the RHEED patterns of Nb:SrTiO₃, plasma cleaned, and BaTiO₃ and Ba+Ti+N deposited on Nb:SrTiO₃ after 180min along the streak directions. **e** Evolution of the Ba+Ti+N/Nb:SrTiO₃ in-plane lattice parameter (denoted by $a_{||}$) derived from RHEED patterns recorded during growth at a sample temperature of 450 °C. Horizontal green and gray lines indicate the SrTiO₃ and BaTiO₃ bulk cubic lattice parameters at 450 °C, thermal expansion coefficients were taken into account.

3.3.1.2. *In situ* AES measurements

Directly after growth, AES measurements were performed in order to identify species in the sample. Figure 3.12 displays the AES spectra obtained after the growth of Ba+Ti+ N and on BTO films. Oxygen is present in both samples, even though no oxygen was intentionally introduced during the growth of the Ba + Ti + N film. Similar to the TiN film, the presence of oxygen is attributed to the diffusion of oxygen from the substrate. Since, the *in situ* AES results for both films are very similar, it can be concluded that the Ba + Ti + N film appears to be mainly a film of barium titanate (BTO).

Despite being similar, the uncorrected Ti_{LMM}/Ba_{MNN} ratio is ~1.3, which agrees with the expected 1:1 stoichiometry for Ti:Ba mentioned earlier and reported in the literature [9-Barbier 2012-23 Shimoyama 2001]. However, a closer examination of the Auger spectra reveals a small difference between BTO and Ba+ Ti+ N film around the Ti_{LMV} peak. This peak consists of two components with slightly different relative intensities (Figure 3.12b). These components are often used to determine changes in the stoichiometry of Ti compound surfaces and variations in the surface oxygen stoichiometry after metal deposition [24-le Fevre 2004].

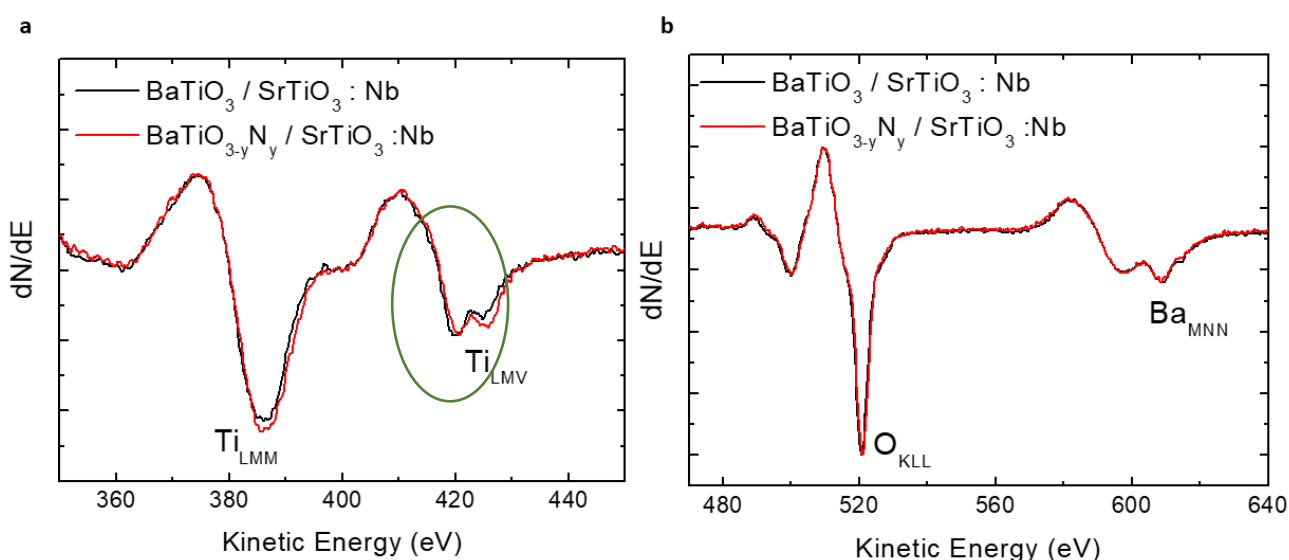


Figure 3.12: Auger scans for BTO and N:BTO layers deposited on Nb:STO From [25-Derj 2022].

Rao et al. conducted a study on the evolution of Ti_{L2,3M2,3V} Auger spectra in compounds with a gradual reduction of titanium ion from TiO₂ to metallic titanium [26-Rao 1982]. The spectra show a transition from a single line at 408 eV in TiO₂ to a single line at around 414 eV in metallic titanium. The low kinetic energy component is associated with an interatomic L₃MV(O) decay, while the other metallic component is associated with an intra-atomic L₃MV(Ti) process. V(O) and V(Ti) refer to O and Ti

contributions to the oxide valence band, respectively. In figure 3.12a, it is noticeable that the low kinetic energy component is reduced in the nitrated sample, indicating less oxidized Ti species in this sample. This modification of the electronic structure confirm either the incorporation of N atoms in the material lattice and/or the presence of oxygen vacancies.

In situ analysis provides initial insights into the film's composition and crystal structure during the deposition process. The *in situ* Ba + Ti + N film strongly resembles barium titanate in terms of composition and crystal structure. However, to determine the presence of nitrogen and to further investigate the exact crystal structure, additional characterization techniques are necessary.

3.3.2 *Ex situ* investigation of the samples

3.3.2.1 *Ex situ* XPS measurements

In order to determine the stoichiometry of the thin films, the primary photoemission peaks for both doped and undoped samples were studied by *ex situ* XPS. No *in situ* apparatus was available at the same time of the study.

The O-1s core level peak appears at a binding energy of ~529 eV in both samples (Figure 3.13a). Although the line's quantitative interpretation is difficult due to air exposure, its shape is noteworthy as it indicates the existence of a two well-defined contribution. The lowest binding energy (BE) component of O-1s belongs to O incorporated in the oxide, while the highest BE peak is relative to hydroxyl which is favored in case of surface oxygen vacancies [27-Idriss 2021]. This hydroxyl peak is more pronounced in the Ba+ Ti+ N sample (Figure 3.13a). The intensity of the integrated O-1s XPS peak with respect the Ti-2p XPS peak was found to be 1.8% lower for the Ba+ Ti +N layer. This is consistent with a lower oxidation in the Ba+ Ti+ N film.

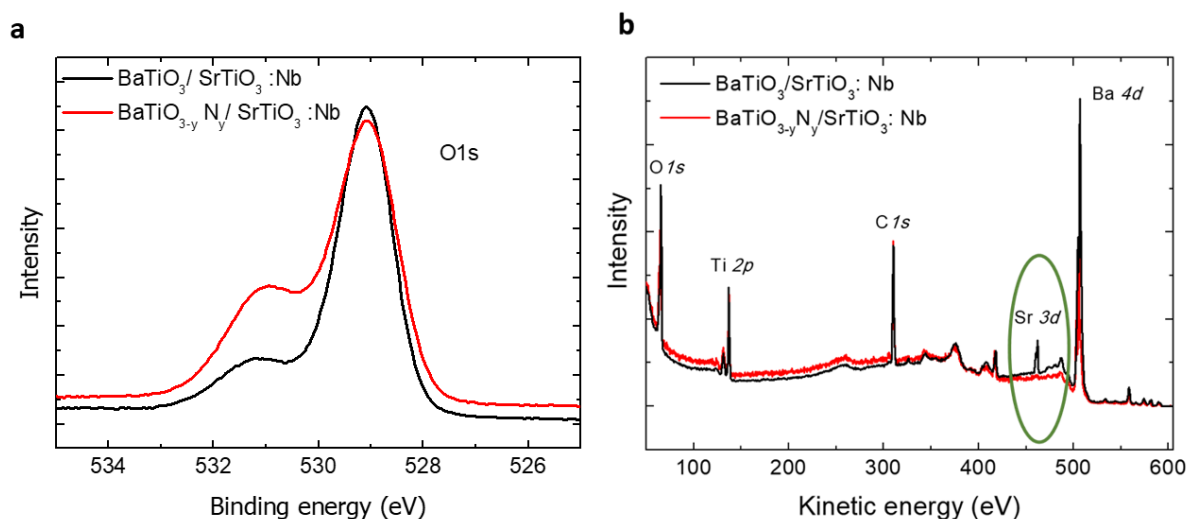


Figure 3.13: **a** Photoemission O-1s core levels of undoped (black) and N-doped (red) BaTiO₃ layers. **b** Wide photoemission scans of undoped (black) and N-doped (red) BaTiO₃ layers. From [25-Derj 2022]

The sample can be considered as a N-doped BaTiO₃ (BaTiO_{3-y}N_y, N:BTO).

The presence of the N-1s peak in the XPS spectrum indicates the incorporation of nitrogen in the film. The N-1s peak can be deconvoluted into two distinct components standing for different nitrogen species or chemical environments within the film. The peak at 398.3 eV binding energy was attributed to Ti-O-N bonds or surface-adsorbed nitrogen, while the peak at 395.5 eV was assigned to Ti-N bonds [28- Trenczek-Zajac 2009]. The composition of the sample was determined using CasaXPS software, which provides N/Ti and N/Ba ratios of 3.8% and 2.9%, respectively. These ratios correspond to a N/O ratio of approximately 1%, which is a significantly high value for a perovskite lattice grown without charge-compensating cations.

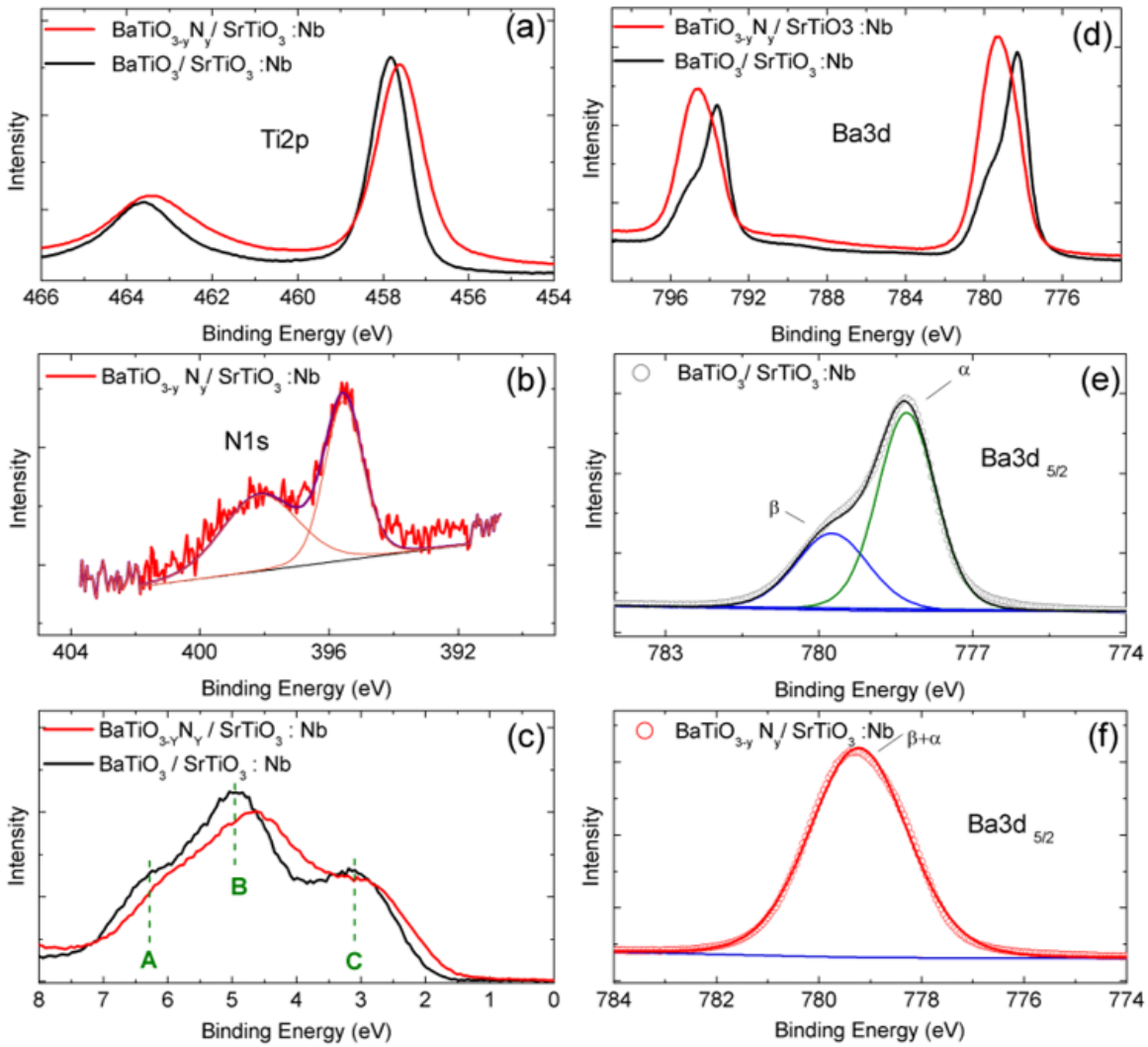


Figure 3.14: Photoemission spectra of undoped (black) and N-doped (red) BaTiO₃ layers for (a) Ti-2p, (b) N-1s core levels, (c) the valence band region, (d) Ba-3d, (e) Ba-3d_{5/2} (undoped), the green contribution corresponds to the α component and the blue one to the β component, and (f) Ba-3d_{5/2} (doped). For (e, f) symbols stand for experimental data. For (b, e, f) thin bottom lines correspond to Shirley type backgrounds and thick straight lines to best fits. The best-fit parameters are reported in Table 4. From [25-Derj 2022]

The Ti-2p_{3/2} XPS line of the BTO sample displayed a single, narrow feature at 457.8 eV binding energy. Upon nitriding, this feature shifted slightly to 457.6 eV (as shown in figure 3.14a), which is consistent with a similar shift about 0.2 eV observed by Wang et al. in a N-doped SrTiO₃ [29-Wang 2012]. This shift can be explained by an increase in electron density on Ti after the incorporation of nitrogen in the lattice, which has a lower electronegativity than oxygen. Further, the Ti-2p XPS line for the Ba+Ti+N sample could not be deconvoluted into multiple components, indicating that the Ti

atoms maintained a well-defined oxidation state in a homogeneous material.

Peak	Ba 3d _{3/2}			Ba3d _{5/2}		
	E _B (eV)	Δ(eV)	ρ(%)	E _B (eV)	Δ(eV)	ρ(%)
BTO						
α	793.6	1.39	28.5	778.3	1.34	40.0
β	795.1	1.52	12.1	779.7	1.68	19.3
N:BTO						
α + β	794.5	2.23	39.78	779.2	2.25	59.2

Table 4: Best fit parameters for Ba-3d photo-emission lines deconvolution for undoped and N-doped BaTiO₃/SrTiO₃:Nb samples. E_B stands for binding energy, Δ for peak width (full width at half maximum values), ρ for the relative weight of each line.

The difference between the two samples appears through modifications in the valence band (VB) region, as depicted in figure 3.14d. The valence band of the nitrated sample is shifted by 0.2 eV towards lower binding energies, which is in agreement with the predictions made by Zou et al. regarding N-doped SrTiO₃ [30-Zou 2012]. This shift indicates the presence of vacancies in the film [31-Xing 2016]. The valence band of BaTiO₃ comprises three well-established contributions, labeled A, B, and C in Figure 3.14c, and its shape has been studied in previous reports. The low-energy part of the valence band consists of a pure O-2p π contribution, while the high-energy contributions result from hybridization between O-2p σ and Ti-3d levels. For this reason, the new shape of the valence band in the doped sample indicates changes in the hybridization between Ti and O orbitals.

Furthermore, the Ba-3d_{5/2} peak decomposition analysis of the undoped BaTiO₃ sample indicates the presence of two distinct components, labeled as α and β. These components were initially associated with different chemical states in early studies of BaTiO₃ surfaces, for example by Mukhopadhyay *et al.* The α component was attributed to the bulk perovskite phase, while the β component was thought to originate from a more surface-like environment [32-Mukhopadhyay 1995]. Recent studies suggested that the β component is likely associated with a surface Ba peroxide (BaO₂) layer, which was previously identified as a surface layer made of Ba oxides and can be removed through ethanol etching [9-Barbier 2012, 33-Chakrabarti 2017, 34-Droubay 2015]. The best fit parameters for the individual line decomposition are reported in table 4. The presence of nitrogen in the BaTiO₃ film

causes a significant modification in the chemical environment of barium, as evidenced by the broad single component observed at an intermediate position between α and β in the Ba-3d_{5/2} peak. This different behavior might be due to the different growth methods used for both fluxes, oxygen being provided either by an atomic oxygen plasma or by the diffusion for the substrate. Additionally, N doping prevents the segregation of Sr in the film, which is typically observed in thin films grown with atomic oxygen plasma due to the easy substitution between Ba and Sr in the perovskite lattice. This difference induced by N doping is visible in the overview XPS spectrum (Figure 3.13b).

3.3.2.2 XRD measurements

For further investigation, the crystalline structure was studied by *ex situ* X-ray diffraction (XRD) and X-ray reflectivity (XRR).

In Figure 3.15, the wide angle XRD patterns of the BaTiO₃N_{3-y} sample are presented out of plane (along 00L) and in plane (along 220) (inset). The specular Bragg peaks of BaTiO_{3-y}N_y appears as broad peaks on the low L side of the Nb:SrTiO₃ Bragg peaks, providing information about the film thickness and strain [35-Tsurumi 1999-36-Zhao 2020]. The film exhibits also well defined in-plane Bragg peaks, also situated near the Nb:SrTiO₃ Bragg peak. These patterns confirm the perovskite structure of the BaTiO₃N_{3-y} film.

The lattice parameters were determined from the averaged Bragg peak positions. They were $a = (0.398 \pm 0.001)$ nm and $c = (0.408 \pm 0.003)$ nm and revealed that the doped layer is significantly more tetragonal ($c/a = 1.025$) than the undoped BaTiO₃ one ($c/a = 1.010$) [9-Barbier 2012] (Table 5). These results suggest that nitrogen has been incorporated into the lattice of the BaTiO_{3-y}N_y layer due to the presence of nitrogen and/or oxygen vacancies as detected by XPS.

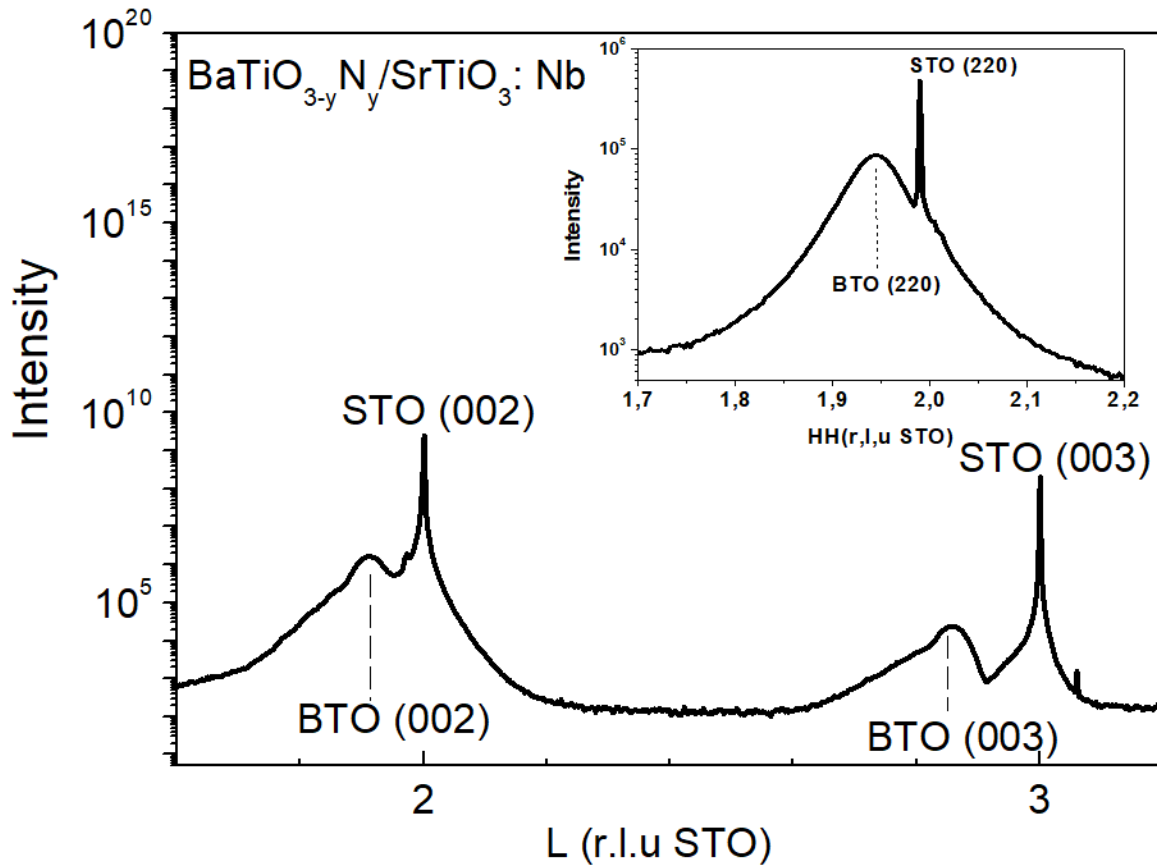


Figure 3.15: Wide angle X-ray diffraction along specular direction for BaTiO₃N_{3-y} sample. (inset) In surface plane scan along the [HH0] direction across the (110) Bragg peaks of BaTiO₃N_{3-y} and Nb : STO corresponding to the best fit. [25-Derj 2022]

To relate the peak broadening observed in the 00L X-ray diffraction pattern to the crystal size of the material we used the corresponding Scherrer plot. The Debye Scherrer equation, used to estimate the average size of the crystallites, or grains, in a material based on the width of the Bragg peaks is given by:

$$D = \frac{K\lambda}{\beta \cos \theta}$$

Where D is the average crystallite size, λ is the wavelength of the X-ray beam used, β is the full-width at half maximum of the Bragg peak, θ is the Bragg angle, and K is the Scherrer constant, *i.e.* a factor that depends on the crystal symmetry and shape of the particle, it is commonly taken as 0.9.

The FWHM, is measured for several Bragg peaks from the diffraction pattern of the material. Then $\cos \theta$ is plotted with respect to 1/FWHM. The slope of the resulting straight line can, therefore, be

used to estimate the average crystallite size of the material (Figure 3.16).

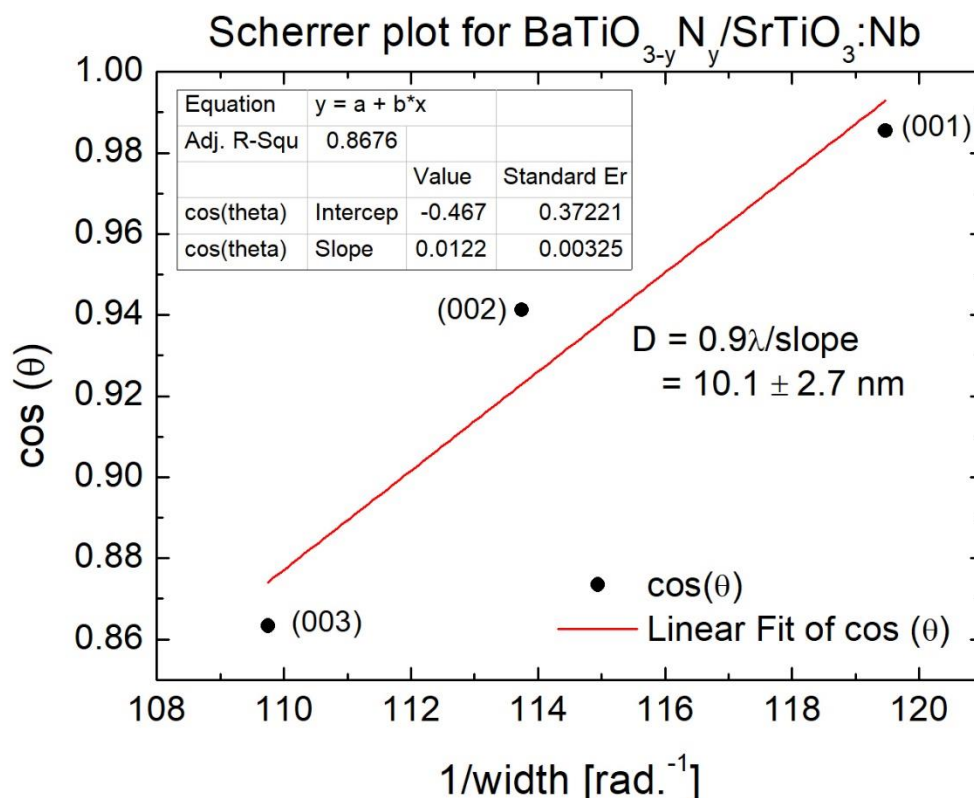


Figure 3.16: Scherrer plot for the N-doped BaTiO₃ layers. The measured data is represented by the solid squares and the linear fit by the red line. From [25-Derj 2022]

It is necessary to mention that epitaxial single crystalline films are grown with a particular orientation, such as along the [001] or [111] crystallographic directions, they can only exhibit a single family of Bragg peaks along the [00L] direction. This means that the number of peaks that can be considered in a structural size-strain analysis is limited to those belonging to this family of reflections [37-Nath 2020]. Therefore, our study was limited. However, since the characteristics from the sherrer plot equals roughly the film thickness it can be concluded the strain does not significantly affect our films. The obtained rocking scan results showed narrow peak widths, measuring only approximately 0.022°. The narrow peak widths observed in the rocking scans indicate the high crystallinity perpendicularly to the surface plane of the N-doped sample. Crystalline materials exhibit sharp, well-defined peaks in rocking scans, while broader peak widths are indicative of structural imperfections or disorder in the crystal lattice.

For the in-plane, behavior-rocking scans were performed at increasing in-surface-plane momentum transfers. The FWHM of these peaks, Δ , decreases with increasing momentum transfer, as described

by the equation $\Delta^2 = \Omega^2 + (2\pi/(Q \times D))^2$ (Figure 3.17). In this equation, Ω represents the in-plane mosaic spread, which is a constant angular width. D is the finite domain size, which leads to a constant broadening with respect to the momentum transfer Q . The relationship between D , Q and the angular width $\Delta\omega$ is then, given by $D = \frac{2\pi}{Q \times \Delta\omega}$. Eventually, the values of Q and D can be obtained from a linear fit to the $\Delta^2 = f(1/Q^2)$ plot [36-Barbier 2001]. The layer exhibited thus, a high crystalline quality and epitaxial single crystalline nature, with a mosaic spread as small as 1.271° and a domain size of 7 nm.

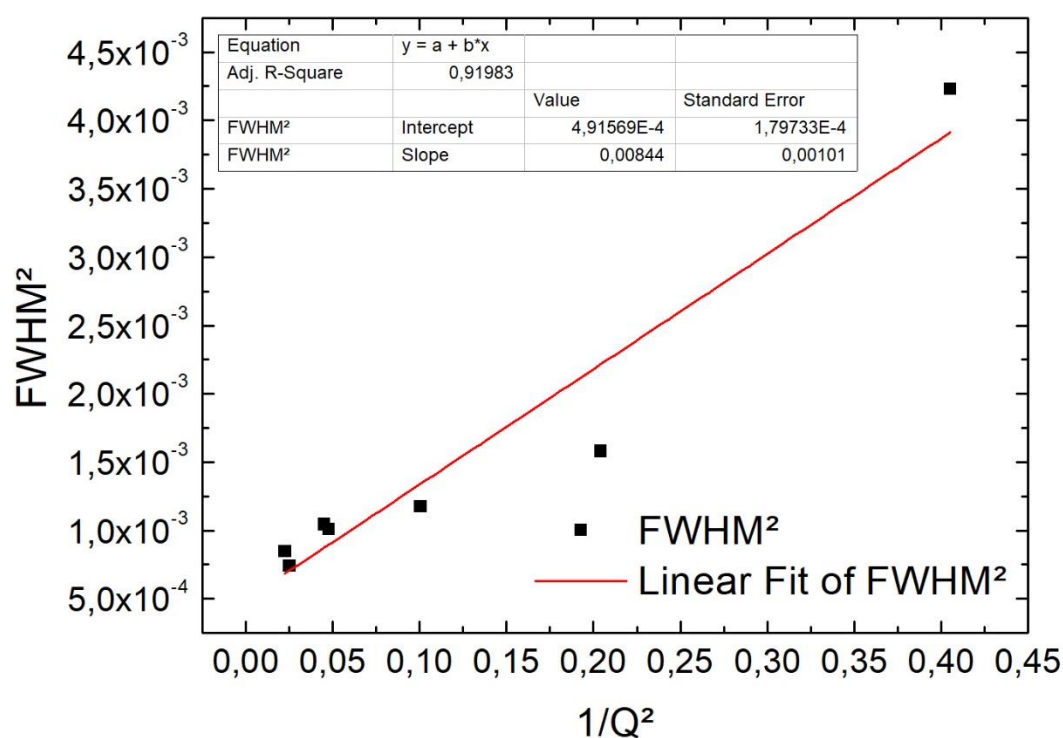


Figure 3.17: FWHM widths of all accessible in surface plane Bragg peaks of the N-doped BaTiO₃ layer as a function of 1/Q² (black) and best linear fit (red line). [25-Derj 2022]

Sample	O	N	a(nm)	c(nm)	c/a
BaTiO ₃	3.1trs/350W	--	0.399	0.403	1.01
BaTiO _{3-y} N _y	--	P _N =4.0×10 ⁻⁷ mbar/ I=18mA	0.398	0.408	1.025

Table 5: Summary of significant sample growth conditions and properties examined in the present

work. a (respectively c) are the in-plane (respectively out-of-plane) parameters deduced from XRD measurements.

3.3.2.3 XRR measurements

In figure 3.18, the reflectivity curve of the BaTiO_{3-y}N_y film is plotted with respect to the perpendicular momentum Q_z . The calculated reflectivity for the best fit model (straight line) is also plotted (which was refined using the REFLEX software [38-Gibaud 2009]). A single layer model was found to be inadequate in representing the data, but a simple 2-layer model was able to reproduce the experimental measurements very well with a χ^2 value of 0.007.

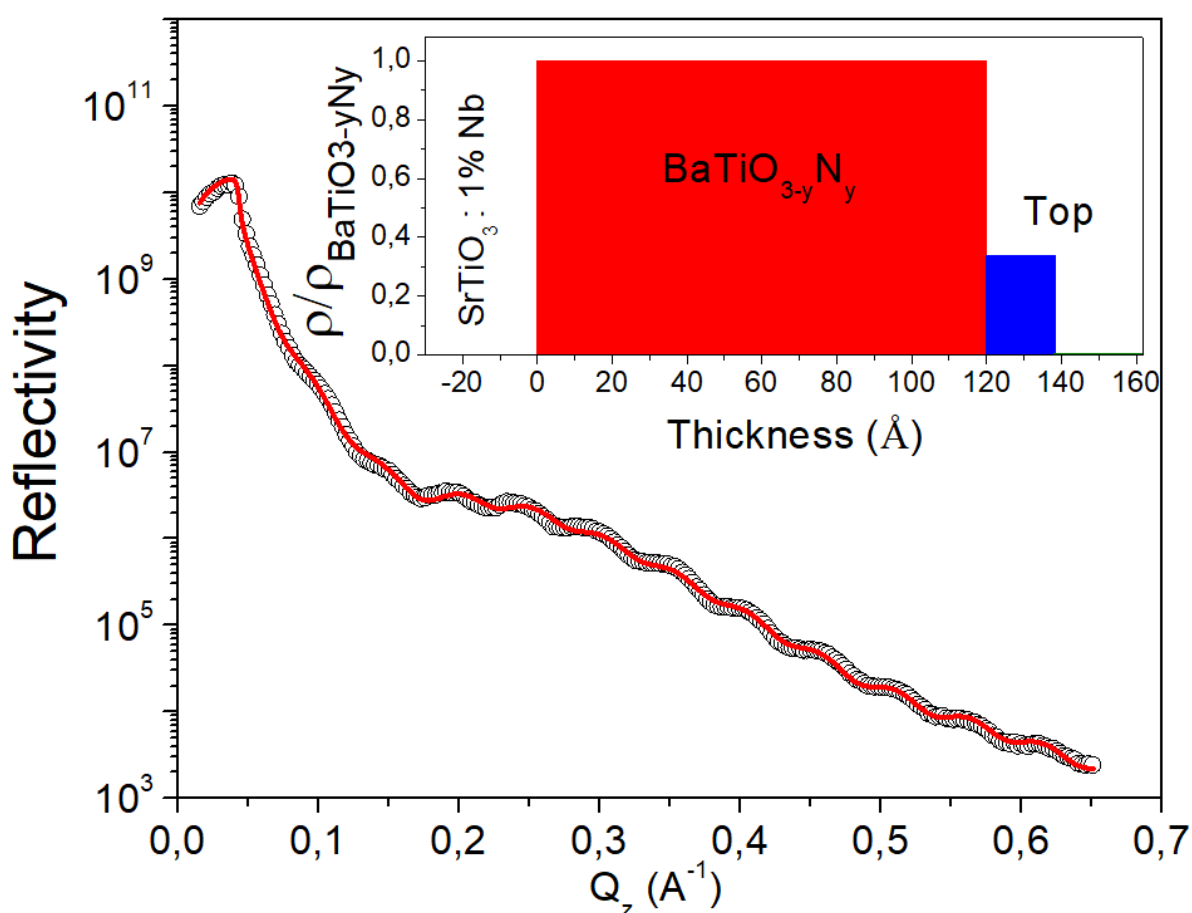


Figure 3.18: Specular reflectivity measurements (○) and best fit (—) for the N : BTO sample deposited on SrTiO₃ : 1% Nb. The inset shows the electronic density profile. From [25-Derj 2022].

The best fit model consisted of a homogeneous layer with a thickness of 12 nm covered by a surface layer of 2 nm with a lower density. While the measured substrate roughness was 0.27 nm r.m.s., the top layer roughness was approximately 0.33 nm r.m.s. The density profile of the best fit is displayed in the inset of figure 3.18. The sharpness of the layer model is a noteworthy feature, especially

considering the growth method.

3.3.2.4 Electronic structure investigation by XAS and RPES

Synchrotron radiation-based resonant photoelectron spectroscopy RPES and XAS were used to investigate the electronic structure of BaTiO₃ and related doped material.

Resonant photoelectron spectroscopy (RPES) is a technique that measure a photoemission peak using photon energy near an absorption edge. In the case of BaTiO₃, resonant valance band photoemission at the Ti-2*p* threshold provides a picture of the contribution of the Ti-3*d* states to the predominantly O-2*p* valence band (means that the oxygen 2*p* orbitals are the main contributor to the valence band energy levels), and thus provides information on the Ti-3*d*:O-2*p* hybridization. This studies illuminate the effects of changing crystal structure and band filling on Ti-O/N hybridization in N-doped and undoped BaTiO₃.

3.3.2.4.1 XAS at the Ti-L_{2,3} edges and O-K edge

RPES is usually combined with the XAS at the K, L, M edges of the corresponding material. Here, the absorption at the Ti-L_{2,3} edges and O_K edge are of interest. The Ti-L_{2,3} (respectively O-K), corresponds to an excitation of an electron from the Ti-2*p* (respectively O-1*s*) core-level to the Ti-3*d* (respectively O-2*p*) conduction band. In perovskite crystals, the Ti-3*d* is splitted in two components: Ti-3*d*_{eg} (high energy states) and Ti-3*d*_{t_{2g}} (low energy states) as shown in figure 3.19a. In this symmetric octahedral structure, when the octahedron is distorted, the e_g doublet is further split into d_{x²-y²} and d_{3z²-r²}, with d_{3z²-r²} pointing towards the vertex oxygen of the octahedron. This splitting of the e_g orbitals is therefore, expected to increase when the oxygen polyhedra surrounding the titanium atom are distorted [39-Wang 2021]. Meanwhile, the t_{2g} triplet consists of the d_{xy}, d_{xz}, and d_{zx} orbitals. Intensified cation shift leads to the generation of an oxygen pyramid structure, where the energy levels of d_{x²-y²} and d_{3z²-r²} become similar.

O-K edge XAS in figure 3.19b shows the partial density of O-2*p* orbitals, where the A and A' peaks correspond to the bonding states of Ti t_{2g} and e_g with O-2*p*, while the B peaks reflect the bonding state of Ba-5*p* and O-2*p* [40- Chassé 2011].

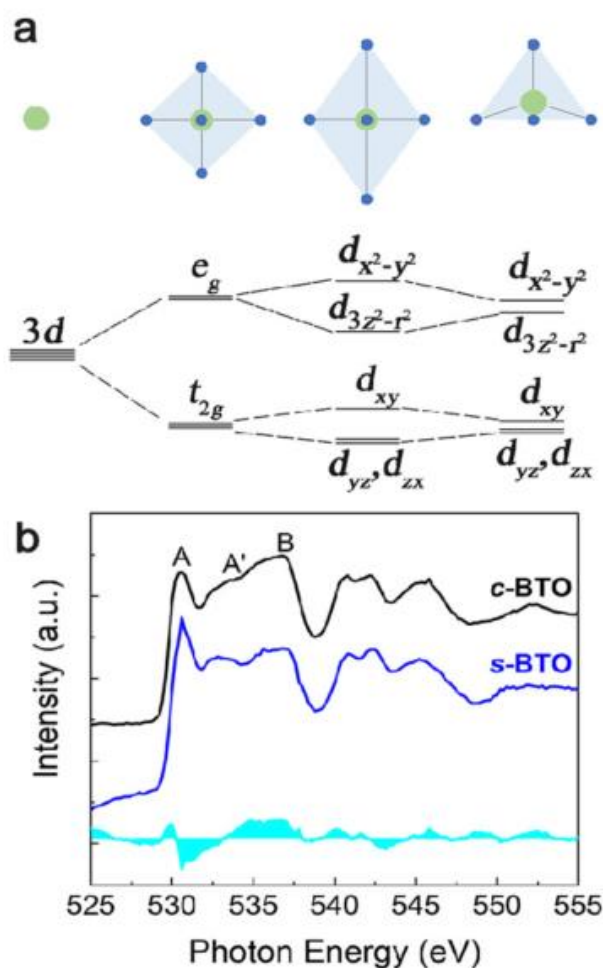


Figure 3.19: **a** Schematic of the splitting of the 3d orbital of Ti in the TiO₆ octahedron and TiO₅ pyramid; **b** O-K edge XAS of BaTiO₃:BaO composite thin film (c-BTO) and single-phase BaTiO₃ thin film (s-BTO), with the outlined area is obtained by subtracting the intensity of s-BTO from that of c-BTO [39-Wang 2021].

Figure 3.20a, shows the Ti-L_{2,3} edge X-ray absorption spectrum. It provides further insights into the electronic structure of the N-doped BaTiO₃ sample. The width of the Ti-3d_{eg} peak observed is higher in the BaTiO_{3-y}N_y sample as compared to the undoped sample. This broader width indicates a higher level of distortion in the oxygen polyhedra, confirming the results obtained from X-ray diffraction (XRD) experiments.

Let us compare the measured edge jump in BaTiO₃N_{3-y} to the undoped sample. It is proportional to the number of unoccupied states in the vicinity of the absorbing atom. As indicated by the black arrow and more clearly shown in the insets, the ~456.5 eV shoulder increases with nitrogen doping. According to Chen *et al*, the observed peak can be attributed to the Ti³⁺-L₃ edge indicating an increase of oxygen vacancies within the lattice [41-Chen 2015].

The XAS at the O-K edges are shown in figure 3.20b. The main features A (t_{2g}) and B (e_g) are due to hybridized states between O-2*p* and Ti-3*d*. We can also prove the increase of surface oxygen vacancies from the O-K edge XAS spectra. As shown clearly in figure 3.20b, the B peak increases dramatically for the doped sample as compared to peak A. This peak arises from the TiO:*pd*-hybridization with a σ -bonding character [42-Muller 2004].

At 537 eV a feature is reduced with nitrogen doping. The peak is due to 5d (e_g)(Ba)-2p(O) hybridization. The broadening of the peak suggests a partially covalent interaction between oxygen and metal ions. This result can be correlated with the modification of the chemical environment of barium demonstrated earlier with the XPS data. With the introduction of nitrogen and/or the method of oxygen incorporation, this feature disappears, indicating a disruption also on the Ba-O atomic interaction.

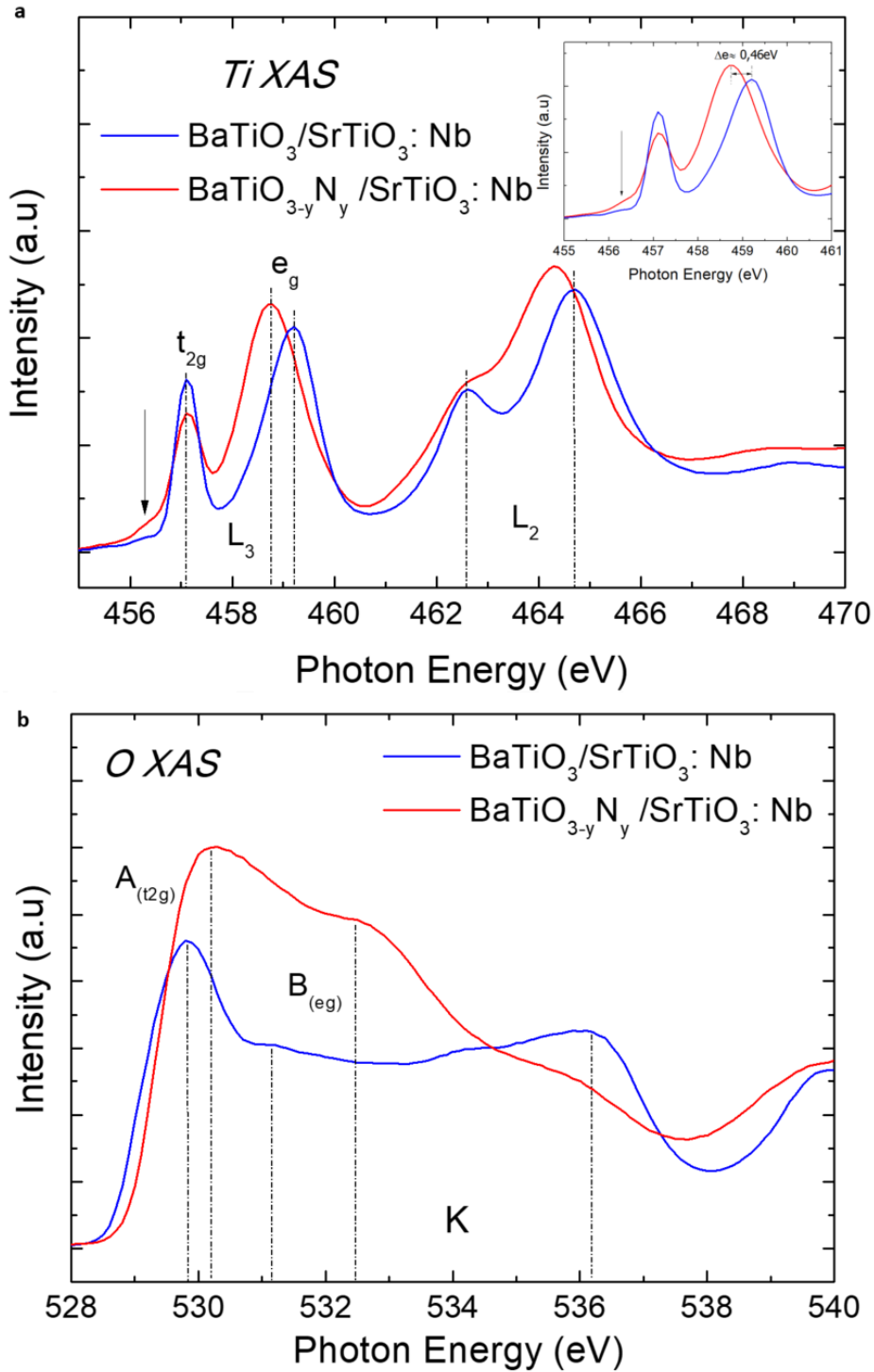


Figure 3.20: **a** Ti-L_{2,3} edge with a zoom on the Ti-L₃ edge on inset ($h\nu=375\text{eV}$) and **b** O-K edge XAS ($h\nu=520\text{eV}$) of undoped (blue) and N-doped (red) BaTiO₃ layers. Black arrows indicate the peak intensity coming from Ti³⁺.

3.3.2.4.2 Resonant photoelectron spectroscopy on doped and undoped BaTiO₃

Figure 3.21 shows a color contour plot for RPES VB spectra at the Ti-L_{3,2} absorption edge for doped and undoped BTO. The ordinate indicates the X-ray excitation energy and the abscissa shows the BE

of the initially formed excited valence state.

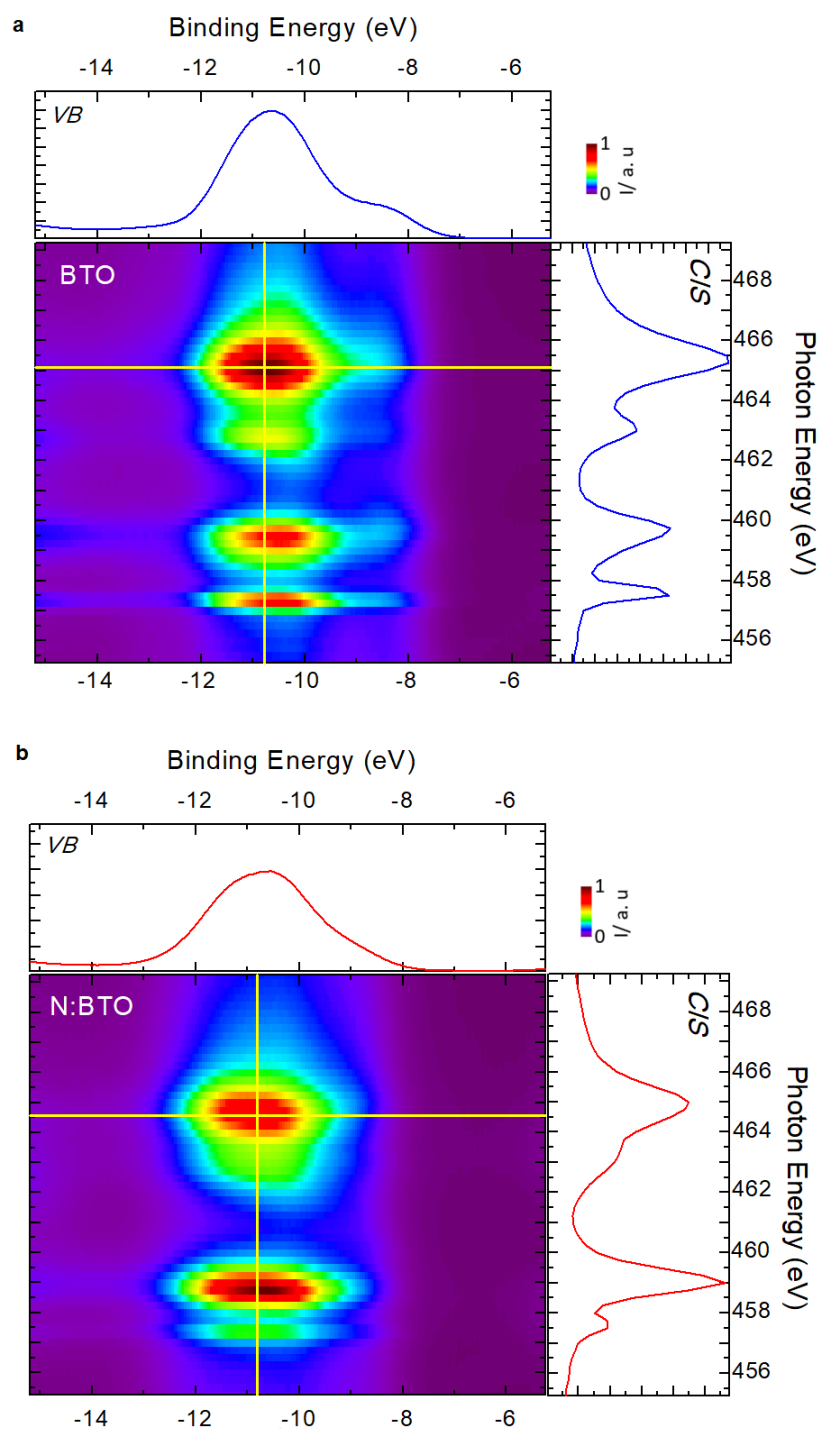


Figure 3.21: Resonant photoemission maps of VB at the Ti- $L_{3,2}$ edge for **a** undoped BTO and **b** N-doped BTO. The inset on top is the valence band (VB) recorded at the photon energy indicated by the yellow horizontal line, the inset on the right is the Constant Initial State (CIS), i.e the resonance of electron of binding energy indicated by the vertical yellow line.

Ti-L edge CIS (Figure 3.22) displays two regions, each split by crystal field into e_g and t_{2g} states. The splitting of d_{x²-y²} and d_{3z²-r²} is enlarged in the elongated N:BTO due to the distorted polyhedral crystal field. By comparing with XAS spectra (see figure 3.20), one sees that, in both samples, the t_{2g} orbitals exhibit weaker resonance compared to the e_g orbitals, and this effect is even more pronounced in the BaTiO_{3-y}N_y sample. This observation suggests that the t_{2g} orbitals are less hybridized with the titanium orbitals, as compared to the O-2p orbitals. The difference in resonance intensity between the t_{2g} and e_g orbitals indicates that the t_{2g} orbitals are less involved in the bonding interactions in comparison to the e_g orbitals.

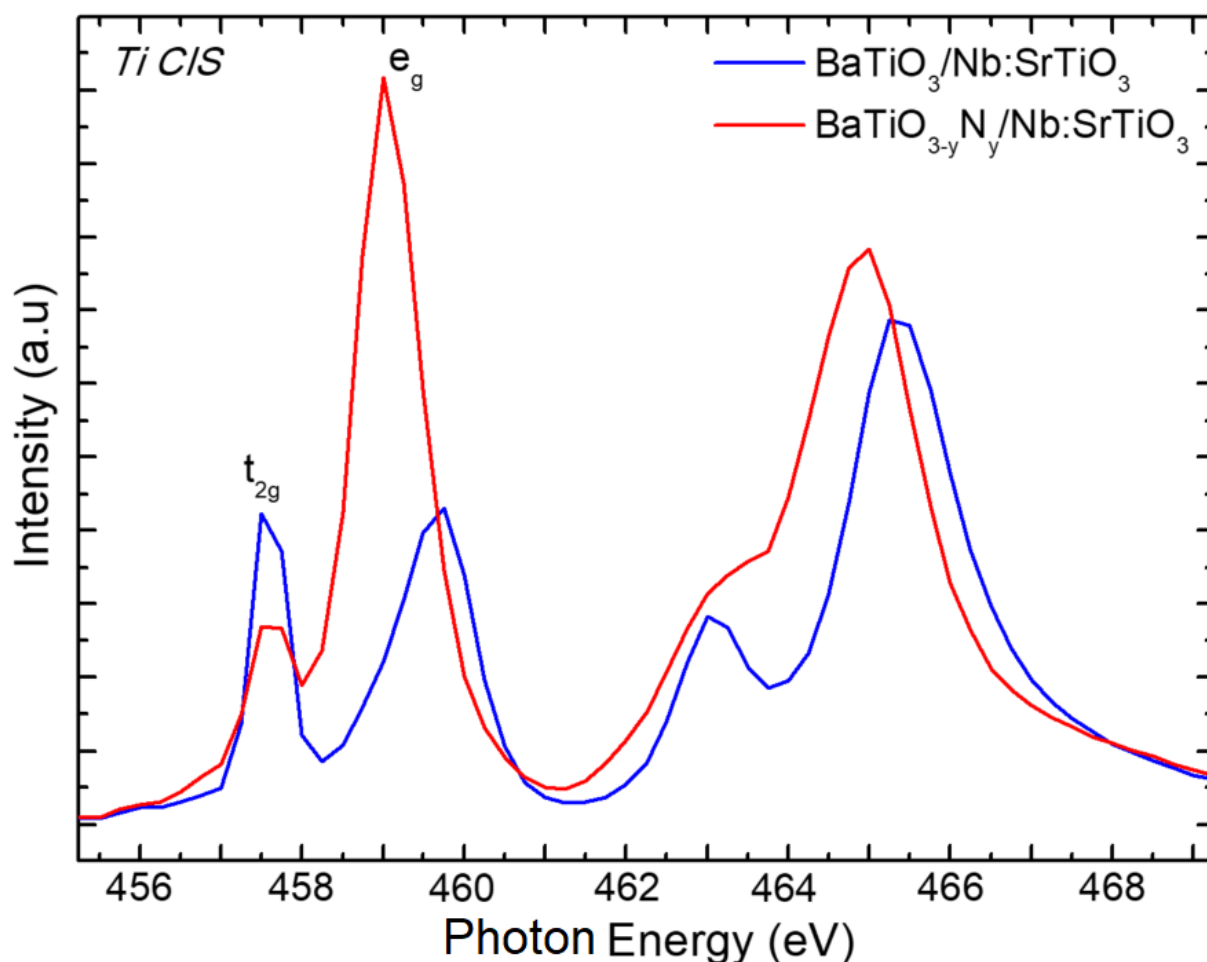


Figure 3.22: the Constant Initial State (CIS) for undoped (bleu) and N-doped BTO (red).

3.3.3 Photoelectrochemical properties analysis

In order to assess the potential for N doped BaTiO₃ to be used as a photoanode in visible-light water splitting, we carried out a study of the photoelectrochemical properties of each sample.

3.3.3.1 Photocurrent measurements

It is important to note that 1%Nb doped SrTiO₃, used here as a substrate, has been previously reported in literature as a photoanode material. However, the data presented in figure 3.23 indicates that there are distinct differences in the photocurrent measurements between the BTO and N:BTO samples, as was compared to the bare Nb:SrTiO₃ substrate [25-Derj 2022]. The signal from the layers is much lower than the one from the substrate. This suggests that for thick enough films the measured response of the films is not influenced by signals emanating from the substrate, as supported by the differences in both the magnitude and shape of the photoresponse (Figure 3.23).

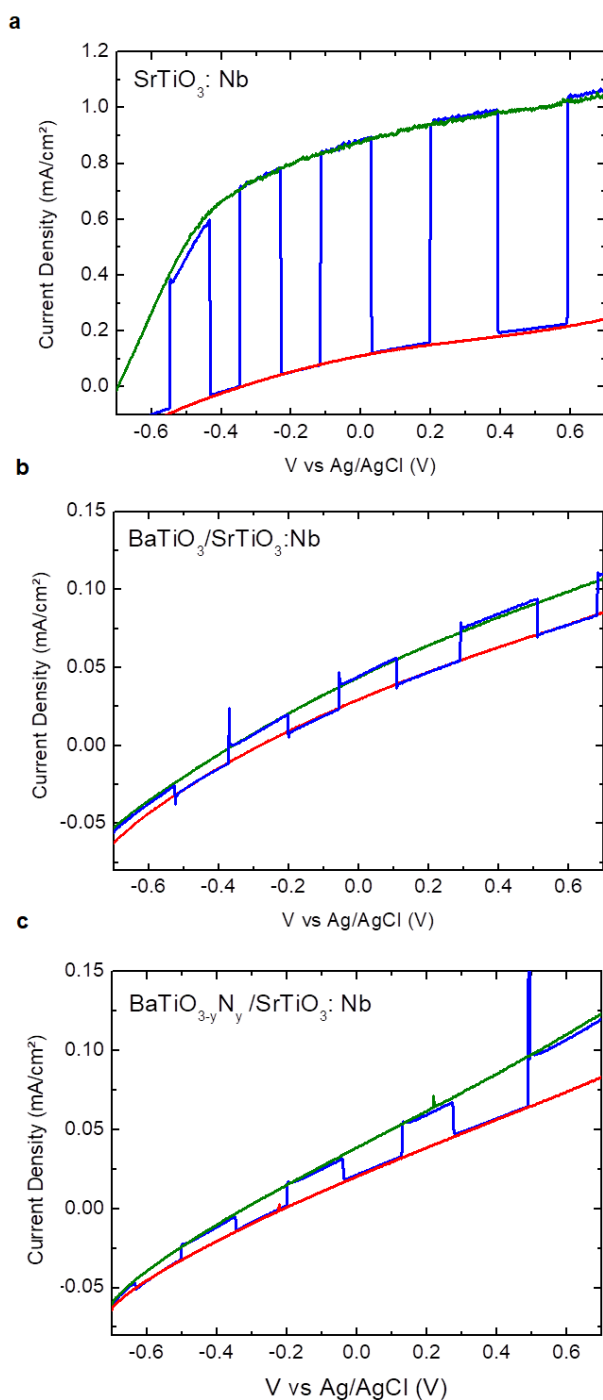


Figure 3.23: $I(V)$ voltammetry curves, light ON (green curves), light OFF (red curves), light switched between ON and OFF (blue curves) for **a** a bare SrTiO₃:Nb substrate, **b** a BaTiO₃ overlayer and **c** a N doped BaTiO₃ overlayer [25-Derj 2022].

The PEC properties show an improvement upon N-doping. For example, at 0 V vs. Ag/AgCl, the photocurrent density (J_{ph}) increases from 17 $\mu\text{A}\cdot\text{cm}^{-2}$ for the undoped sample to 19 $\mu\text{A}\cdot\text{cm}^{-2}$ for the doped one. The difference in J_{ph} increases with voltage, and at 0.7 V vs. Ag/AgCl, the photocurrent generated in the doped sample is 63% larger than the one of the undoped sample (see figure 3.24).

These findings are consistent with those reported by Xing *et al*, who observed an improvement in the PEC properties of hydrothermally prepared SrTiO₃ upon N doping [31-Xing 2016]. The authors found that nitrogen doping not only adjusts the visible light absorption feature but also enhances charge separation efficiency, leading to an increase in photocatalytic activity. However, it was difficult to draw a final conclusion about which factor - doping level, crystallinity, or nano-structuring - was the main contributor to the improvements in PEC properties.

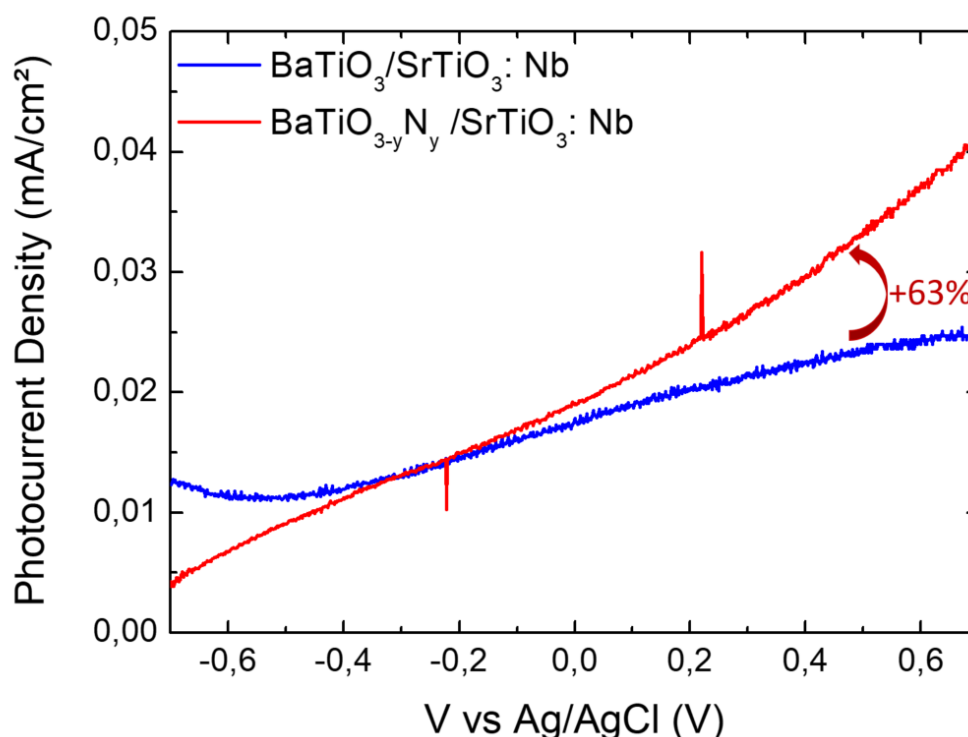


Figure 3.24: Photocurrent density versus the applied voltage (vs. Ag/AgCl) for undoped (blue) and N-doped (red) BaTiO₃ layers.

3.3.3.2 Absorption measurements

3.3.3.2.1 The spectral response

To gain a better understanding of the spectral response of our layers, we conducted photocurrent measurements while varying the incident light wavelength. The resulting photocurrent density data, normalized to the corresponding incident light flux, is presented in figure 3.25. FWHM of spectral absorption was found to be 51 nm and 56 nm for BTO and N:BTO, respectively.

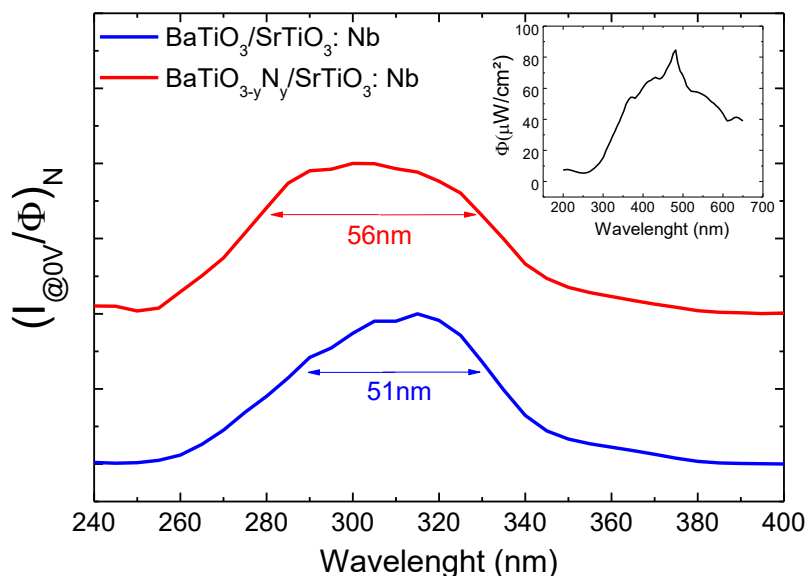


Figure 3.25: Efficient absorption photocurrent density as a function of the wavelength at 0 V vs. Ag/AgCl, (inset) light flux of the Xe arc lamp as a function of the wavelength for undoped (blue) and N-doped (red) BaTiO₃ layers.

Notably, the window of 'efficient absorption' is larger for the N-doped sample, with its maximum is slightly shifted towards the ultraviolet (UV) light range it exhibits a nearly symmetric shape as compared to the other condition.

3.3.3.2.2 The photoelectrochemical gap

The photoelectrochemical direct and indirect band gaps were determined using the "efficient Tauc plot" method [44-Tauc 1968]. It involved plotting $(\alpha h\nu)^2$ vs. $h\nu$ (photon energy) while taking into account α the absorption coefficient of the material, as shown in figure 3.26.

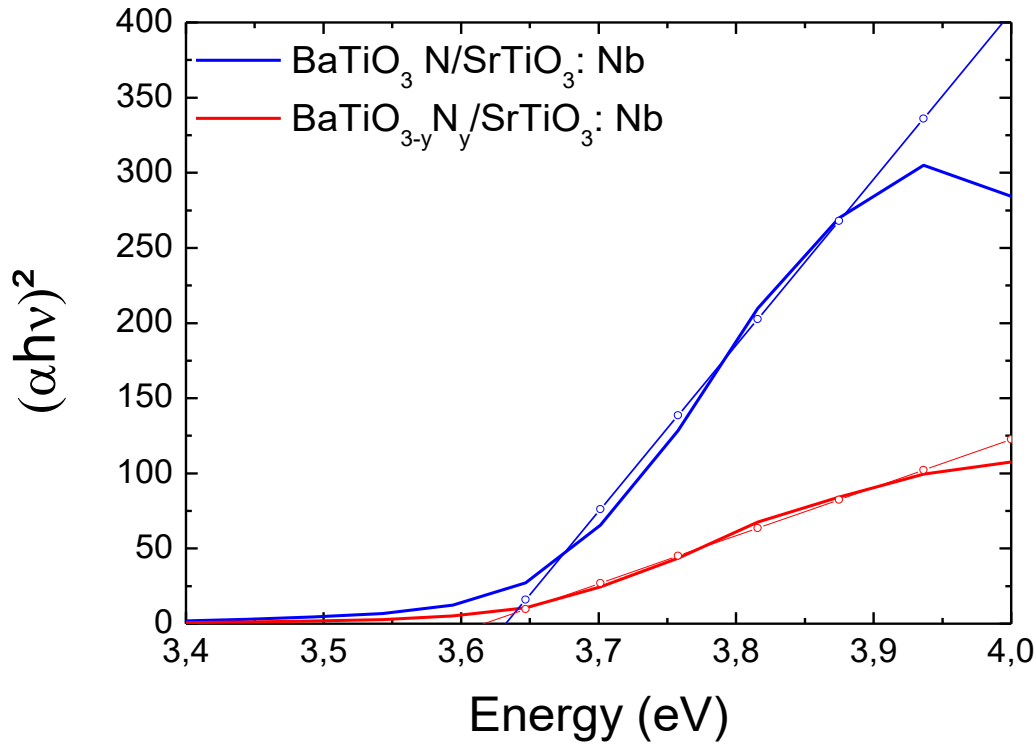


Figure 3.26: Direct band gaps determined using the “efficient Tauc plot method”, for undoped (blue) and N-doped (red) BaTiO₃ layers for undoped (blue) and N-doped (red) BaTiO₃ layers.

Using the "efficient Tauc plot" method, we determined the photoelectrochemical band gaps of the undoped and N-doped samples to be 3.62 eV and 3.61 eV, respectively. These values are very close to the literature value of 3.7 eV for BaTiO₃. When an n-type material is doped, the band gap may increase or decrease depending on the location of the Fermi level. In n-type semiconductors, doping with electron donor atoms can increase the charge carrier concentration if the Fermi level is near the conduction band edge. The apparent band gap can also increase due to the Burstein-Moss shift, where the Fermi level moves into the conduction band. This phenomenon has been observed in various materials, including non-oxide films [44-Polak 2017], oxide nanostructured films, non-oxide nanosheets films [46-Mariappan 2021], and oxide films [47-Tomeda 2018]. Otherwise, if electronic states are created just above the valence band, the apparent bandgap will decrease. In our study, the slight reduction in band gap and the increase in efficient absorption window observed in the N-doped sample are consistent with the findings reported by Xing et al. for N-doped SrTiO₃ [31-Xing 2016]. They suggested that N-doping negatively shifts the valence band maximum while oxygen vacancies positively shift the conduction band minimum, resulting in a reduction of the band gap value.

3.3.4 Discussion and conclusions

In this study we successfully grew an epitaxial oxynitride thin film of N:BTO using an atomic N plasma source, by evaporating only Ba+Ti+N on a SrTiO₃ oxide substrate. The resulting film had a low N concentration of about 3.8% (*vs.* Ti), indicating a cooperative self-diffusion of O from the SrTiO₃ substrate and self-limitation of N content. The film exhibited homogeneous properties, was single crystalline and epitaxial, and had a simple cube/cube epitaxial relationship up to 8 nm. The lattice parameter relaxation occurred during the first few nanometers and was almost complete at 12 nm, resulting in a tetragonal perovskite structure (Table 3). This could be attributed to the larger ionic radius of N³⁺ (0.146 nm) over O²⁻ (0.138 nm), which leads to lattice expansion when nitrogen occupies the oxygen sites in the BaTiO₃ host lattice. The substitution of O by N in the BTO lattice significantly modified the electronic structure, leading to enhanced active spectral optical absorption and PEC performance up to 63% at 0.7 V *vs.* Ag/AgCl. This enhancement may be due to improved light absorption, better kinetics at the electrode/electrolyte interface, and/or a lower recombination rate. Furthermore, an increase of *c/a* is also observed for BTO layers when higher oxygen vacancies are present, which could be related to the recently reported oxygen diffusion in BaTiO₃ and SrTiO₃ with oxygen vacancies. [48-Li 20011, 49-Zhao 2000, 50-Chen 2013]. The activation energy of diffusion is found to be lower for SrTiO₃ than for BaTiO₃ and decreases further with increasing vacancies levels, thus facilitating migration of oxygen atoms from SrTiO₃ to BaTiO₃, especially in thin films already deficient in oxygen.

Although the N:BaTiO₃ film exhibited a slightly narrower band gap as compared to pure BaTiO₃, this difference alone cannot explain the observed 63% improvement in the photoelectrochemical (PEC) performance. Besides, the kinetics at the electrode/electrolyte interface remained unchanged during ON/OFF photocurrent measurements [25-Derj 2022]. However, the incorporation of oxygen vacancies and N doping increases the number of charge carriers in the film, leading to higher conductivity and likely to a reduction of the recombination rate. Additionally, the larger *c/a* ratio resulting from the N doping may also have an effect on the PEC performance by increasing the ferroelectric polarization, which can also influence the generated photocurrent depending on its orientation [51-Magnan 2020].

The nitrogen incorporation into the native oxide modifies the electronic properties making oxynitrides attractive as visible-light-driven photoelectrodes. However, the charge imbalance compromises the stability of the films. The next section presents our firsts effort to maintain charge neutrality by

codoping BaTiO₃ by nitrogen and Tantalum.

3.4 Stable photoanode oxynitride perovskite by lattice charge compensation: Preliminary results

Transition metal oxynitride perovskites or the d⁰-type transition metal (Ta, Ti, Nb, or W) oxynitride perovskites can be written as ABO_{3-x}N_x, where A is a larger alkali, alkaline earth, or rare earth metal cation, lanthanide and B is a smaller transition metal cation. These perovskites are expected to absorb higher light absorption across the visible range due to the higher potential energy of the N-2p orbital as compared to the O-2p orbital [52-Maeda and Domen, 2011, 53-Maeda and Domen, 2007], as illustrated in figure 3.27b.

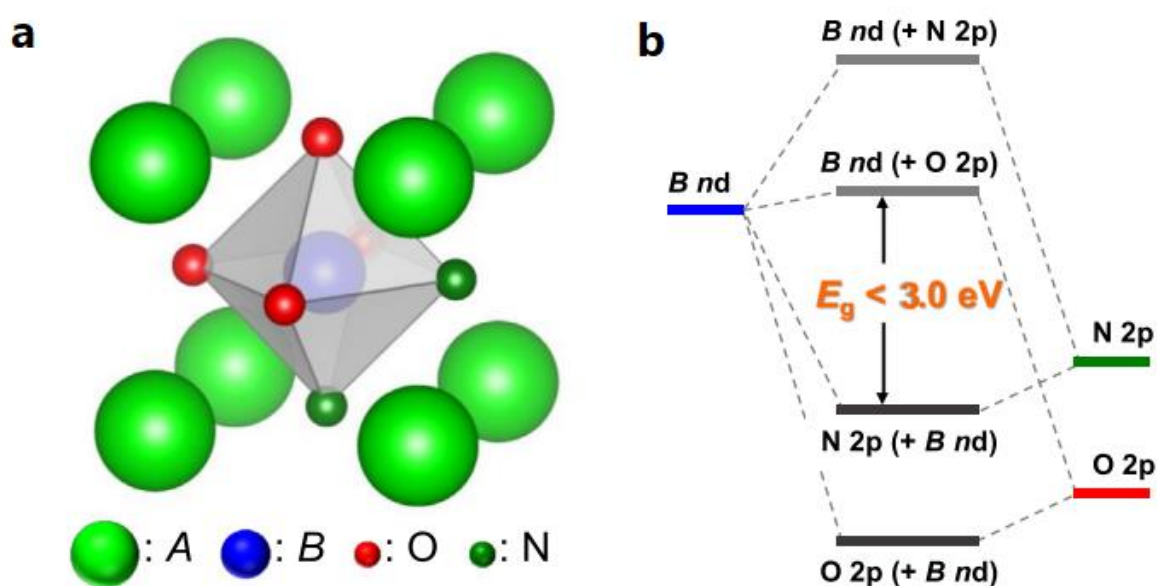


Figure 3.27: **a** Crystal structure and **b** band structure of typical d⁰-type transition metal oxynitride perovskite ABO_{3-x}N_x [53-Maeda 2007]

3.4.1 Stability of oxynitrides perovskite structure

Perovskite-type metal oxynitrides, ABO_{3-x}N_x, have been explored experimentally due to the flexibility of the perovskite structure, which allows physical and chemical properties to be well-tuned by substituting metal cations A or B.

Based on the theoretical calculations using density functional theory, Xu *et al.* found that the anion ordering in ABO₂N strongly depends on the size of the A (Ba, Sr, Ca), and B (Ta, Nb) cations, as well as the electronegativity difference between N and O. Specifically, they found that larger A cations tend to favor ordered anion arrangements, while smaller A cations tend to favor disordered or

random arrangements. Similarly, larger B cations tend to favor ordered arrangements, while smaller B cations favor disordered arrangements [54-Xu 2015, 55-Xu 2019].

For instance, while Ta and Nb atoms in perovskite oxynitrides tend to distort the octahedral structure, the rigidity of the Ba sublattice limits their ability to do so on a larger scale. The Ba sublattice acts as a sort of "constraint" on the distortion, preventing it from spreading and significantly altering the overall structure of the material.

3.4.2 Activating BaTaO₂N by Ti modification for water oxidation reactions

Based on the given information, BaTaO₂N is a semiconducting oxynitride with a bandgap energy of 1.8 eV, allowing it to absorb visible light up to 650 nm. However, perovskite oxynitrides strong absorption does not always correspond to efficient water splitting, and defects generated during synthesis can lead to fast charge recombination and poor photoelectrochemical performance.

In this study, Ta was introduced into N-doped BaTiO₃ to control defect levels and band gap as well as incorporating more nitrogen in the lattice, resulting in BaTa_xTi_{1-x}O_{3-x}N_x. This study highlights the potential for slight composition modifications in perovskite oxynitrides to design optical and photoelectrochemical properties as proposed by Wei *et al.* in BaTaO₂N with calcium modifications. They manage to improve the poor photoelectrochemical behavior of BaTaO₂N, initially attributed to its low band gap (1.8 eV), by incorporating Ca atoms in the lattice [56-Wei 2018]. Introducing Ta in BaTiO₃ appears thus as a promising method to improve the material performances for PEC application.

3.4.3 E-Beam evaporator for charge compensation

3.4.3.1 Charge compensation

When tantalum (Ta) replaces titanium (Ti) in the crystal lattice of N-doped BaTiO₃, charge compensation becomes possible. The additional positive charge of Ta may help to compensate for the extra negative charge from N. Defects in the crystal lattice, such as oxygen vacancies or nitrogen interstitials, are then less necessary.

3.4.3.2 Electron beam evaporation calibration

The BeamTrek® e-beam evaporator allows depositing refractory materials like Ta. The controller allows for precise control of the evaporation process, enabling accurate deposition of thin films. It provides control over parameters such as deposition rate and beam intensity (Cf chapter 2).

Calibrating the electron beam in the MBE chamber is realized in a similar way than for other effusion cells. The relevant evaporation parameter is how the e-beam intensity (high voltage being fixed at 8kV) and the quartz microbalance is used to determine the flux. To enhance the accuracy of the flux calibration, we monitored the evolution of the Ta auger line on a dummy substrate, such as a copper plate substrate measuring 1cm × 1cm (Figure 3.28). The actual deposition rate was then, cross checked during the deposition process for a given electron beam intensity.

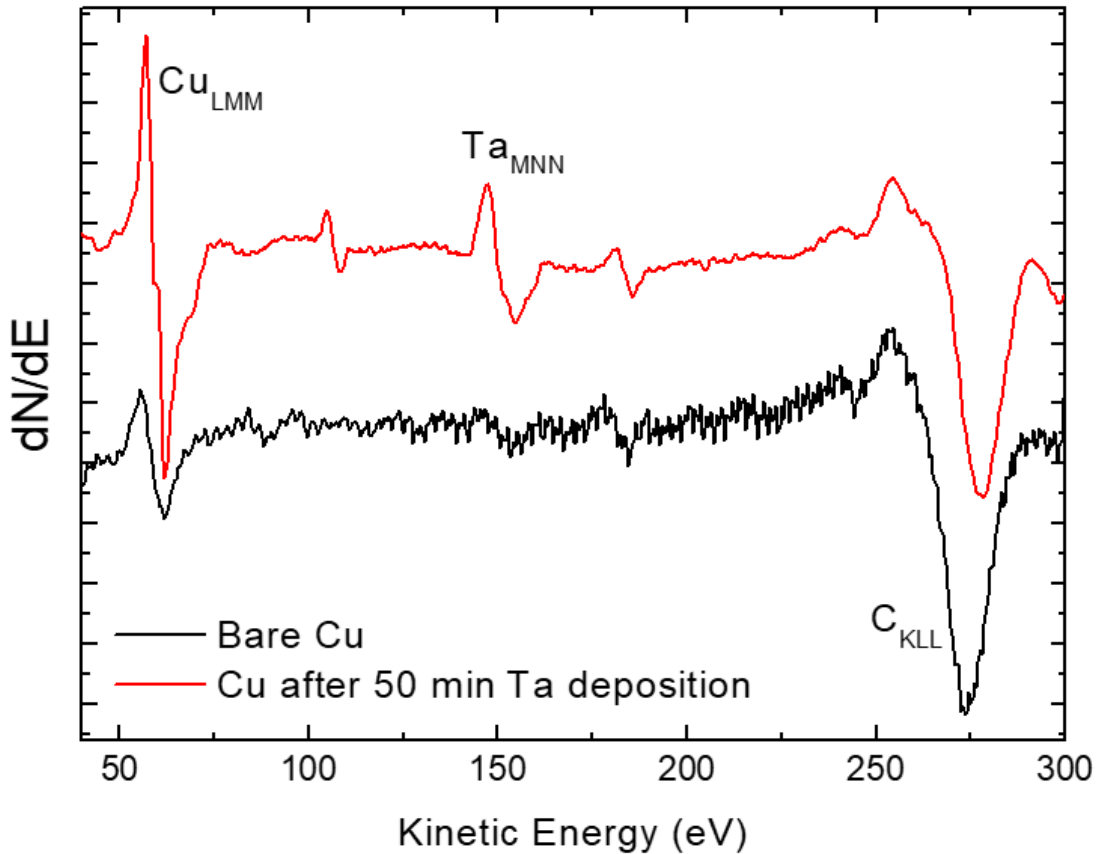


Figure 3.28: AES scans; before and after deposition of Ta on a polished and outgassed Cu substrate

3.4.4 Growth of BaTa_xTi_{1-x}O_{3-x}N_x on 1 at.% Nb :SrTiO₃(001)

BaTa_xTi_{1-x}O_{3-x}N_x (Ta-N: BTO) thin films deposited on 1 at.% Nb :SrTiO₃(001) (Nb:STO) substrates were grown by hybrid atomic/ion nitrogen plasma assisted MBE following a procedure inspired by the previously optimized growth of N-doped BaTiO₃ using atomic nitrogen plasma. Nitrogen plasma was set at a pressure of 4×10⁻⁷ mbar with low values for the voltages of the anode and the extractor (0.1kV and -0.2kV respectively). This condition represents the best condition obtained by Blaess *et*

al. and produces the highest level of N atoms with low kinetic energy ions for better incorporation [57-Blaess 2023]. The Ta current intensity of evaporation was held at 170mA to obtain a rate at 0.75Å/min with respect to the optimal deposition conditions of BaTiO₃.

3.4.4.1 Crystallographic structure investigation

RHEED patterns at various deposition times for a Ta-N:BTO film are shown on figure 3.29. The RHEED patterns slightly degrades during the first minutes of deposition until total disappearance. The epitaxial growth conditions are thus not reached for the chosen fluxes, and growth conditions.

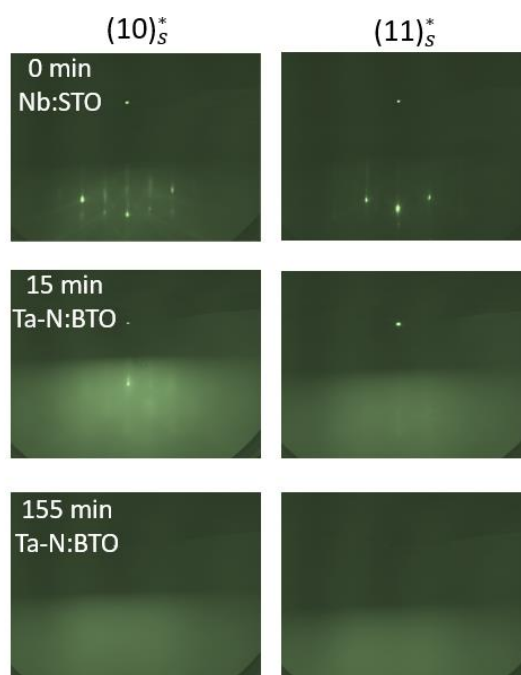


Figure 3.29: RHEED patterns, along $(10)_s^*$ and $(11)_s^*$ azimuths, observed during the growth of Ta-N:BTO on Nb:STO substrate.

3.4.4.2 *In situ* electronic structure study

3.4.4.2.1 Chemical composition

Figure 3.30 displays the Auger spectra obtained after growth for the reference layer, a nitrogen doped BaTiO₃ film, and the oxynitride films grown on niobium-doped SrTiO₃ (001) substrates. The spectra show remarkable similarity among all the samples. The expected elements, including Ta, Ti, Ba, and O, can be identified in these spectra. However, as seen earlier, AES alone is not sufficient to confirm the presence of nitrogen in these films. The Auger line for nitrogen overlaps with that of titanium (Ti_{LMM}), making it challenging to differentiate the signals.

Nevertheless, the AES measurements demonstrate that tantalum can be successfully incorporated into

the oxynitride layer without significantly affecting the initial chemical composition of the BaTiO₃ oxide. The AES spectra are similar for the other growth conditions not shown here.

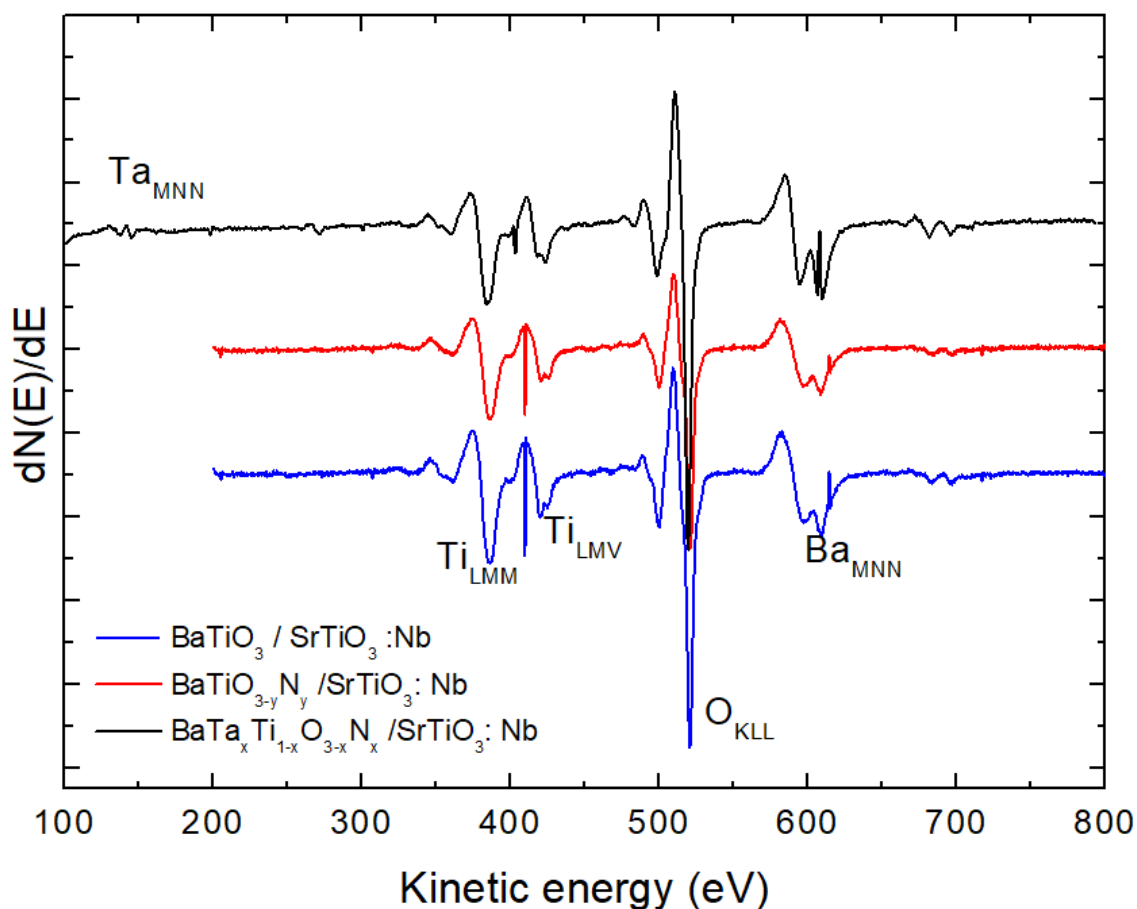


Figure 3.30: Auger spectra for Ta-N:BTO, N:BTO and a reference BaTiO₃ sample deposited on a Nb:STO(001)

3.4.4.2.2 Surface electronic environment

In situ XPS was employed to analyze the composition of the films. The collected spectra of the present species (Ta-4*f*, Ti-2*p*, Ba-3*d*, O-1*s* and N-1*s*) are presented in figure 3.31. Ta-4*f* state, figure 3.31a, for our samples can be fitted using two overlapping peaks centered at 28.1 eV and 26.3 eV, respectively. The two peaks can be assigned to Ta-4*f*_{5/2} and Ta-4*f*_{7/2} signals of Ta⁴⁺.

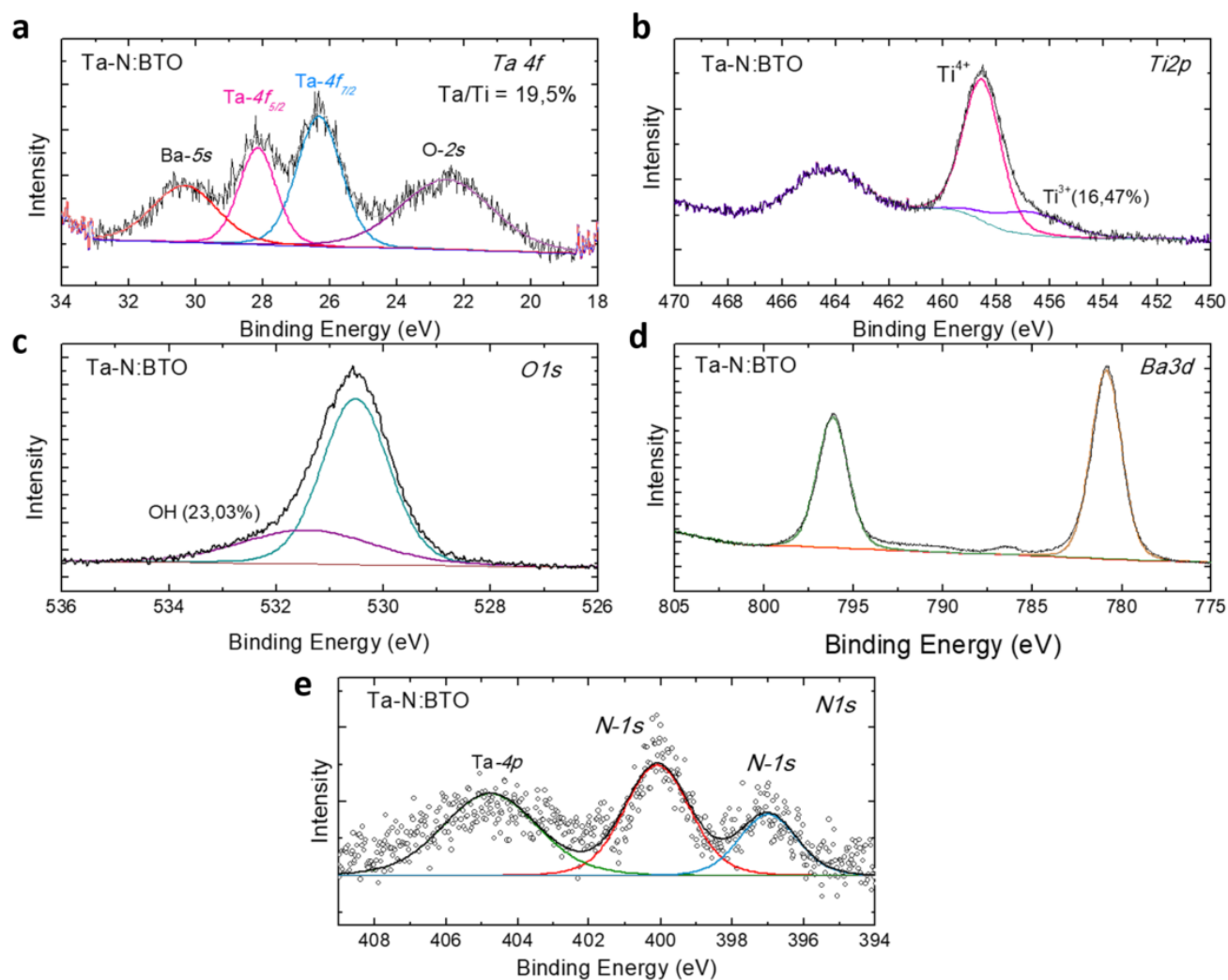


Figure 3.31: Photoemission spectra of a codoped BaTiO₃ layer with N and Ta atoms, for **a** Ta-4f, **b** Ti-2p, **c** O-1s **d** Ba-3d and **e** N-1s core levels

The Ta-N:BTO and N:BTO films not only show a different crystal structure but the compositional analysis revealed also the presence of Ti in both oxidation states (Ti⁴⁺ (458.5eV, 83.53%) and Ti³⁺ (456.7 eV, 16.47%) contents (Figure 3.31b)). The inhibition of Ti⁴⁺ species in the presence of Ta can be explained by the inductive effect of Ta on Ta-O/N bonds. Ta⁵⁺ is more electron-donating than Ti⁴⁺. Hence, when Ta partially substitutes Ti, it increases the covalence of neighboring Ta-O/N bonds. This higher covalence or stronger crystal field for Ta(O,N)₆ octahedrons stabilizes Ta in a higher oxidation state.

The O-1s state can be decomposed into two overlapping peaks centered at 530.5 eV and 531.4 eV. These two peaks are attributed to lattice oxygen (O²⁻) and surface hydroxyl group (OH⁻) [58-Lv 2017]. It is clear from figure 3.31c that the hydroxyl group peak increases Ta incorporation, indicating a more hydrophilic surface or additional oxygen vacancies for charge balance. However, both, the

Ba-3d peak positions and spectral shape are almost the same for Ta-N:BTO and N:BTO indicating very similar Ba-3d_{3/2} and Ba-3d_{5/2} contents (Figure 3.31d). The N-1s line contains two peaks as N:BTO, assignable to lattice N³⁻ species. The amount of nitrogen incorporated in the lattice with respect of Ti, is here estimated to 8.3% (twice higher than N:BTO) and 19.5% for Ta. Although, the results are preliminary and based on a limited number of samples.

The incorporation of Ta helped obviously to overcome the self-limitation seen in the N-doped BaTiO₃. Finally, the peak around 404.7eV attributed to the Ta-4p ascertains the presence of Ta in BaTa_xTi_{1-x}O_{3-x}N_x (Figure 3.31e). The codoping approach is thus a promising path.

3.4.5 Solar water splitting efficiency

Unfortunately, the absence of photocurrent and the resemblance of the photocurrent to that of the STO substrate suggest that the film's stability in the electrolyte was compromised. One possible reason for this instability could be attributed to the poor crystallographic structure of the film. A poor crystallographic structure can introduce defects, which can hinder electron transport and negatively affect the film's photoelectrochemical properties.

3.5 Summary

To summarize, we have achieved the successful growth of homogeneous epitaxial films of both TiO_xN_{1-x} and BaTiO_{3-y}N_y through atomic nitrogen assisted molecular beam epitaxy. Our approach involves the oxygen diffusion from the SrTiO₃ substrate, which enables the substitution of nitrogen for oxygen in the perovskite lattice. However, the self-doping of nitrogen is limited by the necessity to include vacancies for oxygen to maintain charge neutrality. Our growth method enables the production of high-quality oxynitride films that are otherwise difficult to obtain. Contrarily to Ti+N, for Ba+Ti+N, the N doping homogeneously modifies the electronic structure, and an enhances light absorption. For this reason, this novel material can potentially be used as an advanced light harvesting material.

The successful incorporation of Ta in the N-doped BaTiO₃ lattice results in the formation of BaTa_xTi_{1-x}O_{3-x}N_x, a new compound. However, this original method does not allow yet the growth of oxynitride films of very high crystalline quality. It is evident that further advancements and optimization of the growth conditions are still required to achieve the desired results.

3.6 References

- [1]. Wang, W., Xu, M., Xu, X., Zhou, W., & Shao, Z. (2020). Perovskite oxide based electrodes for high-performance photoelectrochemical water splitting. *Angewandte Chemie International Edition*, 59(1), 136-152.
- [2]. Zong, R., Fang, Y., Zhu, C., Zhang, X., Wu, L., Hou, X., ... & Shao, J. (2021). Surface defect engineering on perovskite oxides as efficient bifunctional electrocatalysts for water splitting. *ACS Applied Materials & Interfaces*, 13(36), 42852-42860.
- [3]. Si, C.; Zhang, W.; Lu, Q.; Guo, E.; Yang, Z.; Chen, J.; He, X.; Luo, J. (2022). Recent Advances in Perovskite Catalysts for Efficient Overall Water Splitting. *Catalysts*, 12, 601.
- [4]. V. Buscaglia, M. Buscaglia, G. Canu. (2021) . BaTiO₃-Based Ceramics: Fundamentals, Properties and Applications. *Encyclopedia of Materials: Technical Ceramics and Glasses*. Elsevier. Pages 311-344
- [5]. M. M. Vijatović, J. D. Bobić, and B. D. Stojanović (2008). History and challenges of barium titanate: II. *Sci. Sinter.* 40, 235–244.
- [6]. Mishra, V., Sagdeo, A., Kumar, V., Warshi, M. K., Rai, H. M., Saxena, S. K., ... & Sagdeo, P. R. (2017). Electronic and optical properties of BaTiO₃ across tetragonal to cubic phase transition: An experimental and theoretical investigation. *Journal of Applied Physics*, 122(6), 065105.
- [7]. Donnerberg, H & Birkholz, A. (2000). Ab initio study of oxygen vacancies in BaTiO₃. *Journal of Physics: Condensed Matter*. 12. 8239
- [8]. Cai, H. L., Wu, X. S., & Gao, J. (2009). Effect of oxygen content on structural and transport properties in SrTiO_{3-x} thin films. *Chemical Physics Letters*, 467(4-6), 313-317.
- [9]. Barbier, Antoine & Mocuta, Cristian & Stanescu, Dana & Jegou, P. & Jedrecy, Nathalie & Magnan, Helene. (2012). Surface composition of BaTiO₃/SrTiO₃(001) films grown by atomic oxygen plasma assisted molecular beam epitaxy. *Journal of Applied Physics*. 112..
- [10]. Nasby, R. D., & Quinn, R. K. (1976). Photoassisted electrolysis of water using a BaTiO₃ electrode. *Materials Research Bulletin*, 11(8), 985-992.
- [11]. Rioult, Maxime & Datta, Sukanya & Stanescu, Dana & Stanescu, Stefan & Belkhou, Rachid & Maccherozzi, Francesco & Magnan, Helene & Barbier, Antoine. (2015). Tailoring the photocurrent in BaTiO₃/Nb:SrTiO₃ photoanodes by controlled ferroelectric polarization. *Applied Physics Letters*. 107.

- [12]. Kamp, M., Mayer, M., Pelzmann, A., & Ebeling, K. J. (1997). Fundamentals, material properties and device performances in GaN MBE using on-surface cracking of ammonia. *Materials Research Society Internet Journal of Nitride Semiconductor Research*, 2.
- [13]. Yun, F., He, L., Xiu, F. et al. (2002). Optical and Structural Investigation of AlN Grown on Sapphire with Reactive MBE Using RF Nitrogen or Ammonia. *MRS Online Proceedings Library* 764, 323
- [14]. Kirchner, V., Heinke, H., Birkle, U., Einfeldt, S., Hommel, D., Selke, H., & Ryder, P. L. (1998). Ion-induced crystal damage during plasma-assisted MBE growth of GaN layers. *Physical Review B*, 58(23), 15749.
- [15]. Winters, H. F., & Kay, E. (1967). Gas incorporation into sputtered films. *Journal of Applied Physics*, 38(10), 3928-3934.
- [16]. SPECS User Manual. MPS-ECR—Plasma Cracker Source, Version 2.0 (2013)
- [17]. Molnar, R. J., Singh, R., & Moustakas, T. D. (1995). Operation of a compact electron cyclotron resonance source for the growth of gallium nitride by molecular beam epitaxy (ECR-MBE). *Journal of electronic materials*, 24, 275-281.
- [18]. R. Zhan ; Wang. C, Wen. W, Zhu. X . Study of ECR microwave plasma nitriding. Department of modern Physics. University of Science and Technology of China, Hefei, Anhui,230026, China
- [19]. Pierson . H.O, (1996). Handbook of refractory carbides and nitrides. Properties, Characteristics, Processing and Applications, Noyes Publications, New Jersey, USA,
- [20]. Magnan, H., Stanescu, D., Rioult, M., Fonda, E., & Barbier, A. (2019). Epitaxial TiO₂ thin film photoanodes: influence of crystallographic structure and substrate nature. *The Journal of Physical Chemistry C*, 123(9), 5240-5248.1
- [21]. J. E. Greene, J. E. Sundgren, L. Hultman, I. Petrov, and D. B. Bergstrom, (1995) *Appl. Phys. Lett.* 67, 2928 .27A.
- [22]. J. Perry, V. Valvoda, and D. Rafaja, (1992) *Thin Solid Films* 214, 169 28B
M. Marlo and V. Milman, (2000) *Phys. Rev. B* 62, 2899
- [23]. Shimoyama, K., Kubo, K., Maeda, T., & Yamabe, K. (2001). Epitaxial Growth of BaTiO₃ Thin Film on SrTiO₃ Substrate in Ultra High Vacuum without Introducing Oxidant. *Japanese Journal of Applied Physics*, 40(5A), L463.

- [24]. P. Le Fevre, J. Danger, H. Magnan, D. Chandesris, J. Jupille, S. Bourgeois, M. A. Arrio, R. Gotter, A. Verdini, A. Morgante, (2004). Stoichiometry-related Auger lineshapes in titanium oxides: influence of valence-band profile and of Coster-Kronig processes, *Physical Review B* 69, 155421
- [25]. Derj, A., Magnan, H., Mocuta, C., Le Fèvre, P., Leroy, J., & Barbier, A. (2022). Properties of self-oxidized single crystalline perovskite N: BaTiO₃ oxynitride epitaxial thin films. *Materials Advances*, 3(7), 3135-3142.
- [26]. C. N. R. Rao and D. D. Sarma . (1982). Interatomic Auger transitions in transition-metal oxides. *Phys. Rev. B* 25, 2927
- [27]. Idriss, H. (2021). On the wrong assignment of the XPS O1s signal at 531–532 eV attributed to oxygen vacancies in photo- and electro-catalysts for water splitting and other materials applications. *Surface Science*, 712, 121894.
- [28]. Trenczek-Zajac, A., Radecka, M., Zakrzewska, K., Brudnik, A., Kusior, E., Bourgeois, S., ... & Imhoff, L. (2009). Structural and electrical properties of magnetron sputtered Ti (ON) thin films: the case of TiN doped in situ with oxygen. *Journal of Power Sources*, 194(1), 93-103.
- [29]. Wang, D. H., Jia, L., Wu, X. L., Lu, L. Q., & Xu, A. W. (2012). One-step hydrothermal synthesis of N-doped TiO₂/C nanocomposites with high visible light photocatalytic activity. *Nanoscale*, 4(2), 576-584.
- [30]. Zou, F., Jiang, Z., Qin, X., Zhao, Y., Jiang, L., Zhi, J., ... & Edwards, P. P. (2012). Template-free synthesis of mesoporous N-doped SrTiO₃ perovskite with high visible-light-driven photocatalytic activity. *Chemical Communications*, 48(68), 8514-8516.
- [31]. Xing, G., Zhao, L., Sun, T., Su, Y., & Wang, X. (2016). Hydrothermal derived nitrogen doped SrTiO₃ for efficient visible light driven photocatalytic reduction of chromium (VI). *SpringerPlus*, 5(1), 1-13.
- [32]. Mukhopadhyay, S. M., & Chen, T. C. (1995). Surface chemical states of barium titanate: Influence of sample processing. *Journal of materials research*, 10(6), 1502-1507.
- [33]. Chakrabarti, S., Ginnaram, S., Jana, S., Wu, Z. Y., Singh, K., Roy, A., ... & Yang, J. R. (2017). Negative voltage modulated multi-level resistive switching by using a Cr/BaTiO_x/TiN structure and quantum conductance through evidence of H₂O₂ sensing mechanism. *Scientific Reports*, 7(1), 4735.
- [34]. T. C. Droubay, L. Kong, S. A. Chambers and H. P. Hess, (2015) . Work function reduction by BaO: Growth of crystalline barium oxide on Ag(001) and Ag(111) surfaces *Surf. Sci.* 632, 201.

- [35]. Tsurumi, T., Nishizawa, S., Ohashi, N., & Ohgaki, T. (1999). Electric properties of zinc oxide epitaxial films grown by ion-beam sputtering with oxygen-radical irradiation. *Japanese journal of applied physics*, 38(6R), 3682.
- [36]. Zhao, M. J., Sun, Z. T., Zhang, Z. X., Geng, X. P., Wu, W. Y., Lien, S. Y., & Zhu, W. Z. (2020). Suppression of oxygen vacancy defects in sALD-ZnO films annealed in different conditions. *Materials*, 13(18), 3910.
- [37]. Nath, D., Singh, F., & Das, R. (2020). X-ray diffraction analysis by Williamson-Hall, Halder-Wagner and size-strain plot methods of CdSe nanoparticles-a comparative study. *Materials Chemistry and Physics*, 239, 122021.
- [38]. A. Gibaud and G. Vignaud, (2009). Specular Reflectivity from Smooth and Rough Surfaces. In: Daillant J., Gibaud A. (eds) *X-ray and Neutron Reflectivity. Lecture Notes in Physics*, Published by Springer, Berlin, Heidelberg, vol. 770, ch.3, pp. 85-131.
- [39]. Wang, Y., Zhang, L., Wang, J., Li, Q., Wang, H., Gu, L., ... & Xing, X. (2021). Chemical-pressure-modulated BaTiO₃ thin films with large spontaneous polarization and high Curie temperature. *Journal of the American Chemical Society*, 143(17), 6491-6497.
- [40]. Chassé, A., Schindler, K. M., Trautmann, M., Huth, M., Steudel, F., Makhova, L., ... & De-necke, R. (2011). High-resolution x-ray absorption spectroscopy of BaTiO₃: Experiment and first-principles calculations. *Physical Review B*, 84(19), 195135.
- [41]. Chen C, Avila J, Frantzeskakis E, Levy A, Asensio MC. (2015). Observation of a two-dimensional liquid of Fröhlich polarons at the bare SrTiO₃ surface. *Nature Communications*.
- [42]. Muller D. A., Nakagawa N., Ohtomo A., Grazul J. L. & Hwang H. Y. (2004). Atomic-scale imaging of nanoengineered oxygen vacancy profiles in SrTiO₃. *Nature* 430, 657–661
- [43]. Shi, J., Grinberg, I., Wang, X., & Rappe, A. M. (2014). Atomic sublattice decomposition of piezoelectric response in tetragonal Pb Ti O₃, Ba Ti O₃, and K Nb O₃. *Physical Review B*, 89(9), 094105.
- [44]. Tauc, J. (1968). Optical properties and electronic structure of amorphous Ge and Si. *Materials research bulletin*, 3(1), 37-46.
- [45]. Polak, M. P., Scharoch, P., & Kudrawiec, R. (2017). The electronic band structure of Ge_{1-x}Sn_x in the full composition range: indirect, direct, and inverted gaps regimes, band offsets, and the Burstein–Moss effect. *Journal of Physics D: Applied Physics*, 50(19), 195103.
- [46]. Mariappan, S. M., Shkir, M., Alshahrani, T., Elangovan, V., Algarni, H., & AlFaify, S. (2021). Insight on the optoelectronics and enhanced dielectric properties of strontium decorated

- PbI₂ nanosheets for hot carrier solar cell applications. *Journal of Alloys and Compounds*, 859, 157762.
- [47]. Tomeda, A., Ishibe, T., Taniguchi, T., Okuhata, R., Watanabe, K., & Nakamura, Y. (2018). Enhanced thermoelectric performance of Ga-doped ZnO film by controlling crystal quality for transparent thermoelectric films. *Thin Solid Films*, 666, 185-190.
- [48]. Li, C. L., Chen, Z. H., Zhou, Y. L., & Cui, D. F. (2001). Effect of oxygen content on the dielectric and ferroelectric properties of laser-deposited BaTiO₃ thin films. *Journal of Physics: Condensed Matter*, 13(22), 5261.
- [49]. Zhao, T., Chen, F., Lu, H., Yang, G., & Chen, Z. (2000). Thickness and oxygen pressure dependent structural characteristics of BaTiO₃ thin films grown by laser molecular beam epitaxy. *Journal of Applied Physics*, 87(10), 7442-7447.
- [50]. Chen, A. P., Khatkhatay, F., Zhang, W., Jacob, C., Jiao, L., & Wang, H. (2013). Strong oxygen pressure dependence of ferroelectricity in BaTiO₃/SrRuO₃/SrTiO₃ epitaxial heterostructures. *Journal of Applied Physics*, 114(12), 124101.
- [51]. Magnan, H., Deleuze, P. M., Brehin, J., Plays, T., Stanescu, D., Flavell, W. R., ... & Barbier, A. (2020). Tuning the charge carriers migration in epitaxial BaTiO₃ thin-film photoanodes. *The Journal of Physical Chemistry C*, 124(19), 10315-10323.
- [52]. Maeda, K., Domen, K. (2011). Oxynitride materials for solar water splitting. *MRS Bulletin* 36, 25–31 .
- [53]. Maeda, K., Domen, K. (2007). New Non-Oxide Photocatalysts Designed for Overall Water Splitting under Visible Light. *The Journal of Physical Chemistry C*. 111 (22), 7851-7861
- [54]. Xu, X., & Jiang, H. (2015). Anion order in perovskite oxynitrides AMO₂N (A = Ba, Sr, Ca; M = Ta, Nb): a first-principles based investigation. *Journal of Materials Chemistry A*, 3(18), 9741-9748.
- [55]. X. Xu and H. Jiang, (2019). First-principles investigation on anion order, electronic structure and dielectric properties of BaTaO₂N. *Journal of Materials Chemistry A*, 7, 14583–14591
- [56]. Wei, S., Zhang, G., & Xu, X. (2018). Activating BaTaO₂N by Ca modifications and cobalt oxide for visible light photocatalytic water oxidation reactions. *Applied Catalysis B: Environmental*, 236, 651-660
- [57]. Blaess. C; Matzen. S; Lin. H; Creutzer. G; Derj. A; Magnan. H; Moussy. J; Rountree. C; MOCUTA, C; Charra. F; Silly. M; Barbier. A. Nitrogen doping in epitaxial self-oxidized BaTiO₃ ferroelectric thin films: from chemical to optical properties. 2023. on review
- [58]. M.L. Lv, X.Q. Sun, S.H. Wei, C. Shen, Y.L. Mi, X.X. Xu, Ultrathin lanthanum tantalate

perovskite nanosheets modified by nitrogen doping for efficient photocatalytic water splitting,
ACS Nano 11 (2017) 11441–11448.

Chapter IV

Nitrogen incorporation into TiO₂ epitaxial thin films

***Summary:** In this chapter, we focus on the deposition of oxynitride films on a non-oxide substrate (platinum) to prevent oxygen self-diffusion. The deposition process utilizes an RF oxygen plasma source and an ECR nitrogen source. Our main objective was to introduce nitrogen into epitaxial rutile TiO₂ films and investigate their photoelectrochemical properties under different oxidation and nitriding conditions. By synthesizing TiO_xN_y hybrid materials and modifying the TiO₂ surface with nitrogen doping, we aimed to enhance the properties and performance of TiO₂-based devices, particularly photoelectrodes for solar water splitting. The samples were elaborated in a controlled UHV environment, along with the exploration of various synthesis conditions and the examination of the chemical and electronic structures influence on nitrogen doped TiO₂ properties.*

4.1 Properties of TiO₂

Further development of the preparation methods of oxynitrides and especially those that allow for controllable deposition of thin films from constituents such as titanium, oxygen, and nitrogen are here undertaken. Instead of the oxidation of TiN to build an oxynitride, the precursor will this time be TiO₂ in which nitrogen will be incorporated. The process involves utilizing an additional hybrid ECR nitrogen plasma source to grow the film on a platinum (Pt) substrate, enabling the introduction of nitrogen atoms and ions. This is achieved in addition to a controlled atmosphere of Ti and oxygen plasma. The aim is to fully comprehend how changes in the chemical composition and deviation from stoichiometry affects the properties of the resulting sample.

4.1.1. TiO₂ a popular semiconductor

Discovered in 1791 by the German chemist Martin Heinrich Klaproth, it was only until the early 20th century that the material revealed its potential as a pigment in the paint industry and became widespread. Due to its high refractive index, it is not only an excellent whitening agent but also, an UV blocker. Non-toxic, chemically inert, its application interests extended from the food and cosmetic industry to the organic contaminants degradation. For example, under light, TiO₂ can initiate a series of chemical reactions to break down organic compounds and pollutants in the environment (*i.e.* pho-

tocatalytic activity). This makes it an effective tool for cleaning water and air. Moreover, the development of a method using TiO₂ photoactivity to create energy combined with its capacity of degrading contaminants is a matter of growing interest. The use of TiO₂ as a semiconductor in solar cells has indeed, extensively been explored. However, it has been found that a combination of TiO₂ with other materials, such as organic dyes [2-Zhang 2017, 3-Wang 2004 and 4-Ahmad 2017] or perovskites [5-Lindblad 2014, 6-ke 2014, 7-Han 2015] is requisite to increase the efficiency of the cell. Even though, during this study, we focused on using it as the sole component tailoring its intrinsic properties by non-metal doping to eventually end up with an efficient cell.

4.1.2. TiO₂ rutile for solar water splitting

In nature, TiO₂ has eight different crystal structures, but only three of them, anatase, rutile, and brookite, have been extensively investigated for their applications due to their stability at atmospheric pressure (Figure 4.1). All three structures have titanium atoms that are sixfold coordinated, with oxygen atoms, forming a distorted TiO₆ octahedral structure. In spite of a similar structural unit, their physical and chemical properties differ from one another. Rutile TiO₂, for instance, is known to be the most thermodynamically stable phase, while anatase and brookite TiO₂ are metastable phases that can transform into the rutile phase after calcination. Rutile and anatase have a tetragonal structure, whereas brookite has an orthorhombic structure, as shown in table 1. The differences in the lattice parameters of TiO₂ with different crystal phases can lead to variations in their electronic structures and physicochemical properties and potential applications. The lowest gap is obtained for the rutile structure.

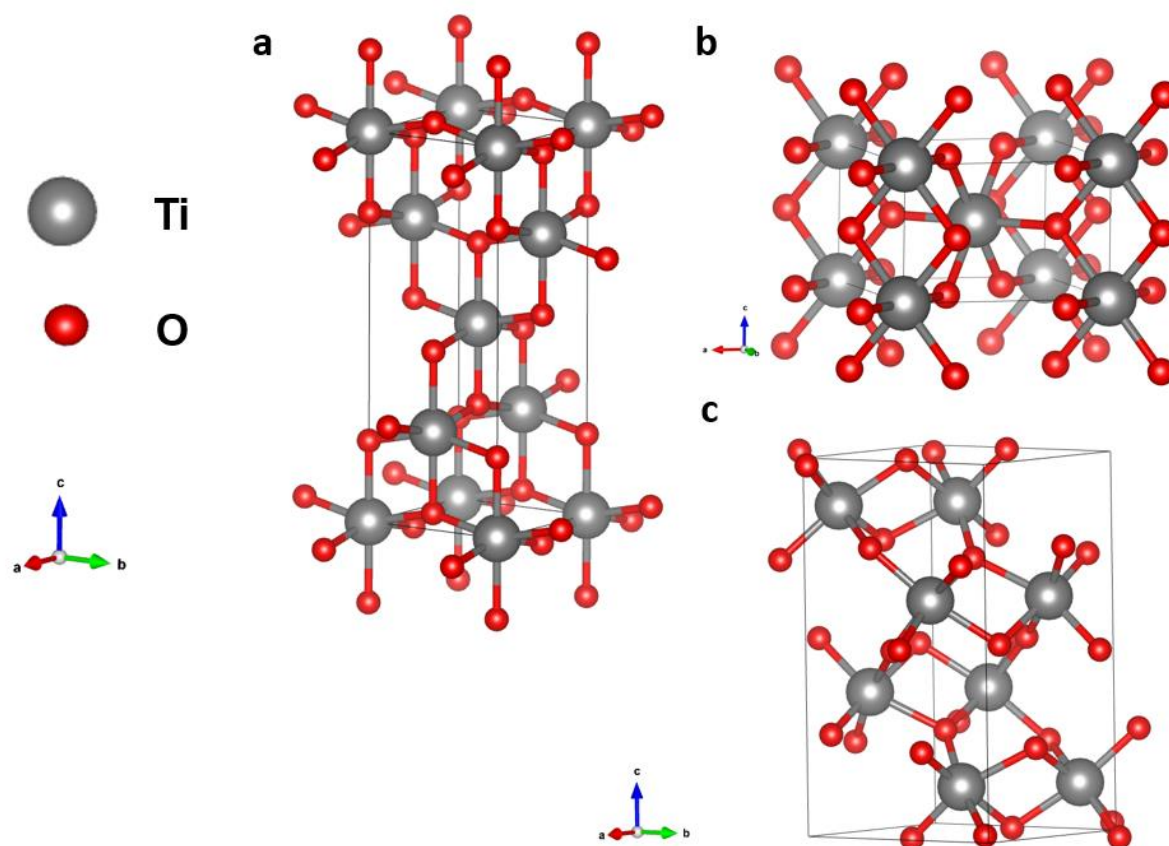


Figure 4.1: Crystal configurations of **a** anatase, **b** rutile, and **c** brookite TiO_2 . The small red sphere and large grey sphere represent the O and Ti atoms, respectively.

Anatase is the most commonly studied phase of TiO_2 for use in solar cells. It has a high surface area and high electron mobility, which makes it an excellent material for photocatalytic activities [8-Yamakata 2019]. Rutile, on the other hand, has a lower surface area and lower electron mobility than anatase, but it has better thermal stability and is more resistant to corrosion. Fortunately, rutile demonstrates higher activity than anatase for water oxidation [8-Yamakata 2019, 9-Ohno 1997, 10-Abe 2001, 11- Maeda 2013], due to higher lifetime of hole. Moreover, Magnan *et al.* showed that the crystal structure of the TiO_2 films on Pt (111) is rutile (100). Moreover, they have a higher photocurrent than anatase (001) for solar water splitting [1-Magnan 2019]. The electronic structure of the films dispose of a higher conduction band minimum position for the rutile films compared to anatase films.

In some cases, brookite has also been explored for its photocatalytic properties, despite its relatively low conductivity, which can limit the flow of charge carriers and decrease overall efficiency [12-Ohtani 1985, 13-Ohno 2015]. However, brookite is a relatively rare and expensive mineral, which may makes it less attractive for large-scale commercial production of solar cells.

Several studies suggest two reasons for these differences in photoactivity. Firstly, regardless of the TiO_2 phase used, the exposed crystal face plays a crucial role in improving photoactivity by controlling the reaction sites [14-Ohno 2002, 15-Bae 2009, 16-Murakami 2009]. Secondly, the depth of traps, which depends on the crystal phase, also plays a role. It has been estimated that the trap depths are <0.1 eV, ~ 0.4 eV, and ~ 0.9 eV for anatase, brookite, and rutile, respectively, in powders [8-Yamakata 2019]. Electron-trapping processes at sample defects limit the probability of electrons and holes recombining, effectively increasing the lifetime of holes. This results in a preference for hole generation over electron generation. However, in steady-state reactions, both electrons and holes need to be consumed. Therefore, the balance between the positive and negative effects of defects determines the distinctive photoactivities of anatase, rutile, and brookite TiO_2 phases.

Structure	Crystal system	Cell parameters (\AA)			Optical gap (eV)
		<i>a</i>	<i>b</i>	<i>c</i>	
Rutile	Tetragonal	3.758	3.758	9.514	~ 3.0 eV
Anatase	Tetragonal	4.584	4.584	2.953	~ 3.2 eV
Brookite	orthorhombic	9.166	5.436	5.135	~ 3.3 eV

Table 1: Structural data and optical gap for anatase, rutile, and brookite TiO_2

Based on the structural data provided in table 1, for photoelectrochemical (PEC) applications, TiO_2 in the rutile phase appears to be the most promising material as it meets almost all the necessary conditions. However, practical utilization of this semiconductor for PEC purposes requires significant efforts to increase its photoactivity while preserving its other important properties during photoelectrolysis.

4.1.3. TiO_2 limitations and improvements for PEC water splitting

Despite of its known potential since 1972 [17-Fujishima 1972], TiO_2 struggles to reach an appropriate efficiency for the photoconversion process within the visible range of the light spectrum. In fact, its relatively wide bandgap whatever the phase (Table 1), constitutes a major obstacle. Moreover, TiO_2 has a large band gap for water oxidation, which means that an energy input is required to drive the reaction.

Different ways have been tested to improve TiO_2 for solar water splitting: introducing oxygen vacancies [18-Hu 2019], sensitizing with dyes [19-Lang 2018, 20-Lang 2016], utilizing the surface

plasmon resonance effect on metals [21-Dahlam 2020], and tuning the bandgap by heteroatom doping [22-Geroge 2011, 23-Biswas 2018]. Until now, the substitution of the host in the TiO₂ crystal lattice with various heteroatoms (anion and/or cation) has been proven to be one of the most effective routes. However, the foreign elements may disrupt the local structure (ionic radii), electronic environment and charge balance in the TiO₂ matrix [24-Kapilashrami 2014]. Therefore, ascertaining the most suitable impurity elements is not an easy matter. Cation dopants (such as transition metals) [25-Sadanandam 2013, 26-Peres larios 2016, 27-Huang 2018], inner transition metals [28-Kočí 2018, 29-Singh 2018], and noble metals [30-Ribao 2019, 31-Ida 2018]), anion dopants (such as boron [32-Wang 2016], carbon [33-Shao 2017, 34-Jia 2018], nitrogen [35-Boningari 2018, 36-Calisir 2020], fluorine [37-Gao 2019, 38-Xie 2020], sulfur [39-Yuan 2018], and chlorine [40-Xu 2008, 41-Wang 2012]), cation/anion co-dopants [42-Li 2016, 43-Kim 2013, 44-Shaban 2019], and anion/anion co-dopants [45-Li 2008, 46-Khalilian 2015, 47-Divya 2019] have already been used. Jibao et al. have calculated the position of the anatase band with different dopants (see figure 4.2) [48-Jibao 2012]. It appears that the most efficient way to reduce the gap, while having a conduction band (CB) minimum and the dopant states above H₂/H₂O level, with non-metal doping, in anatase phase is N-doping.

4.1.4. Nitrogen doped TiO₂

The incorporation of nitrogen into TiO₂, is named in the literature as nitrogen-doped titanium oxide (N-doped TiO₂) or titanium oxynitride (TiO_xN_y).

Wong et al. and Okato et al. have suggested that the optimal dopant concentration for N doped anatase is around 1-2 at.% [49-Wong 2006, 50-Okato 2005]. At higher doping levels of Nitrogen, it is detrimental for photoactivity properties, due to distortion in the lattice structure and formation of deep-level states. While DFT calculation of Lee et al. [51-lee 2005] propose that localized nitrogen states just above the valence band maximum (VBM) are responsible for visible light photoactivity, experimental studies on single crystals by Batzill *et al.* evidenced that oxygen vacancies are also needed to stabilize substitutional nitrogen (N_O) in the TiO₂ lattice. In other words, nitrogen substitutional doping introduces N-2*p* states within the band gap close to the valence band maximum, which suppresses the Ti-3*d* band gap states and removes trapping centers for photogenerated holes. The accompanying formation of oxygen vacancies due to N doping causes a restructuring of the surface structure, indicating that compensation of charges may be achieved over long distances [52-Bratzill 2006, 51-lee 2005]. In a study by Diwald et al. nitrogen-doped rutile TiO₂ (110) single crystals, exhibited photoactivity at photon energies below the band-gap energy for rutile TiO₂. It was concluded that the active

dopant state of nitrogen was as an interstitial element bound to hydrogen in TiO_2 (110) rutile when treated with NH_3 [53-Diwald 2004]. This particular speciation has a higher N-1s binding energy than the substitutional nitride state, and as N_O , leads to an increase of the optical absorption in the visible light range.

As we experimented in the earlier section and was calculated by Di Valentin *et al.*, the shift in optical absorption has a different sign in rutile and anatase; a reduction of the gap in case of anatase and an increase in case of rutile [54-Di Valentin 2004]. This is due to the difference in hybridization between O-2p and Ti-3d orbitals in the two structures. While anatase exhibits a valence band with more pronounced O-2p character and a conduction band with more pronounced Ti-3d character, the rutile phase is more a covalent mixing [55-Asashi 2000]. For this reason, an electron generated in anatase by ultraviolet (UV) excitation is less mobile compared to rutile. [54-Di Valentin 2004]

The main cited drawbacks of pure titanium oxide for water photoelectrolysis applications are its sluggish responsiveness to visible light due to a large band gap, and the inefficient separation of photoinduced electron-hole pairs. The reduction of the bandgap of TiO_2 to enhance visible light absorption, particularly for applications like photoelectrolysis, has garnered significant interest. However, many previous studies have utilized materials with high defect densities, which obscure the understanding of how defects influence the interaction between the N dopant and the host lattice. To investigate the properties of intrinsic N-doped TiO_2 , it is crucial to minimize or eliminate defect densities in the material. One approach is to grow the material atom by atom, precisely monitoring the atomic fluxes to generate structurally perfect crystalline layers with controlled stoichiometry.

In this context, studies proposed to grow N-doped TiO_2 films homoepitaxially on TiO_2 (110) rutile substrates using plasma-assisted molecular beam epitaxy (PAMBE) [56-chambers 2007]. The use of rutile substrates leads to rutile film growth due to interface stabilization. This study revealed that considerably less N can be incorporated into the rutile lattice when defects are absent compared to when defects are present. In the absence of oxygen vacancy (V_O) defects, the N incorporation is limited to approximately 2 ± 1 at.% within the anion sublattice. This limitation arises from the stronger thermodynamic driving force to form Ti-O bonds rather than Ti-N bonds.

Other, structurally near-perfect films were used to investigate the properties of N-doped TiO_2 rutile. N atoms substitute for O atoms in the lattice (N_O), and itinerant electrons originating from interstitial Ti (III) formed during rutile homoepitaxy to compensate for their presence. As a result, N_O exhibited a formal charge of -3. Even at a N concentration of approximately 2 at.%, significant oscillator

strength is observed in the bandgap region around 2.5-3.0 eV, indicating bandgap reduction [57-Cheung 2007].

Ohsawa *et al.* investigated the visible-light photoactivity of nitrogen-doped TiO₂ materials and highlighted the qualitative difference in their activities between anatase (001) and rutile (110) polymorphs. Epitaxial films of TiO_{2-x}N_x with controlled structures and compositions are used to investigate this difference [58-Ohsawa 2009].

For anatase (001), holes generated by visible light at nitrogen sites readily diffuse to the surface and participate in oxidation reactions with adsorbed trimethyl acetate. This suggests that the holes are mobile and can effectively move towards the surface for surface reactions. To the contrary, in rutile (110), the holes remain trapped in the bulk of the material and do not readily participate in surface oxidation reactions. This indicates a lower hole mobility along the [110] direction in N-doped rutile compared to the [001] direction in N-doped anatase. The exact mechanism behind the observed difference in hole mobility between the two polymorphs is not yet fully understood.

Crystalline defects occupying during synthesis concern any material used in photoelectrodes, defects such as vacancies, interstitials, and impurities can introduce energy levels within the bandgap of the material affecting the carrier diffusion length and the charge collection efficiency. All these defects may limit the performances of the device.

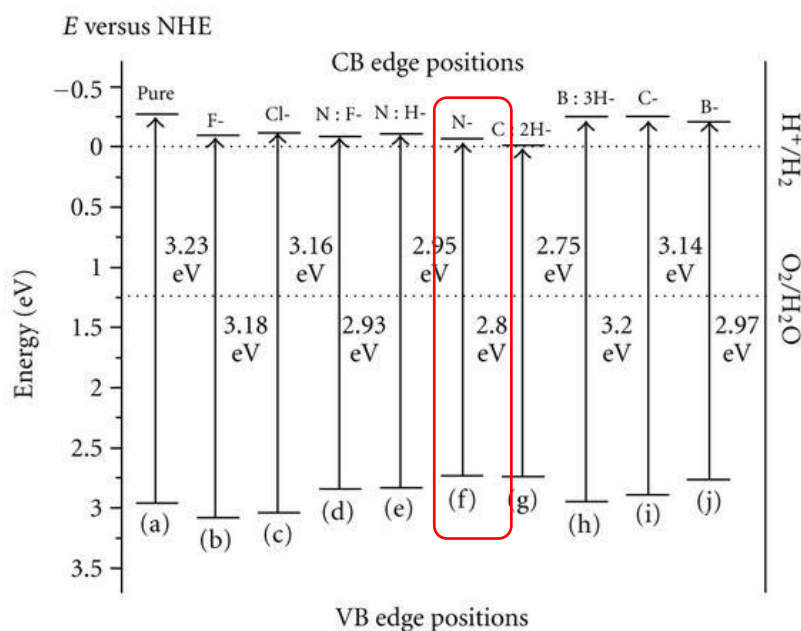


Figure 4.2: Calculated edge positions of conduction band and valence band for pure and non-metal doped anatase TiO₂ at pH=0 [48-Jibao 2012].

The specific types and concentrations of defects can be mitigated through careful material design and processing. Figure 4.2 demonstrates, that the most efficient way to reduce the gap while having a conduction band (CB) minimum and the dopant states above H₂/H₂O level, with non-metal doping in anatase phase, is N-doping. Closer to the water oxidation potential, it promotes the transfer of photoinduced electrons to the water molecules, leading to efficient water splitting. This higher position of the conduction band is attributed to the oxygen vacancies present in the rutile structure, which are known to facilitate charge transfer processes in PEC water splitting. Hence, during this study, we explored different recipes to optimize the crystal quality and minimize defects in epitaxial TiO₂ rutile films, as well as nitrogen doped TiO₂ rutile films, to improve the performance of our photoelectrochemical cells.

4.2 Growth and epitaxial single crystalline TiO₂ layer

4.2.1 Single-crystalline growth on Pt (111)

The contributions to PEC of crystallite quality, surface roughness, and surface orientation are usually entangled. To address this issue, single-crystalline samples can be used. However, single crystal growth may be influenced by various factors such as temperature, deposition rate, surface preparation and even the final thickness of the film [59-Rioutl 2014]. For instance, TiO₂ films on Pt(111) above 3 nm have been found with a rutile-like (100) structure [60- Atiglia 2012]. Below the ultra-thin film regime an hexagonal phase, lepidocrocite and TiO₂(B) is formed [61- Barcaro 2012, 62-Zhang 2007].

4.2.2 Nitrogen doping of TiO₂ thin films

4.2.2.1. Nitriding using hybrid ECR plasma Source

After working with the atomic mode of the ECR plasma source, we used here the hybride mode to enhance the nitridation. The two additional electrodes placed at the end of the plasma cavity of the growth chamber are used to extract ions (Cf. chapter 2). The anode and extractor voltages are adjusted to determine the amount of extracted ions and their respective energies, which can be monitored through the induced sample current. Meanwhile, a piezo valve connected to the software Prodigy regulates the pressure in the growth chamber.

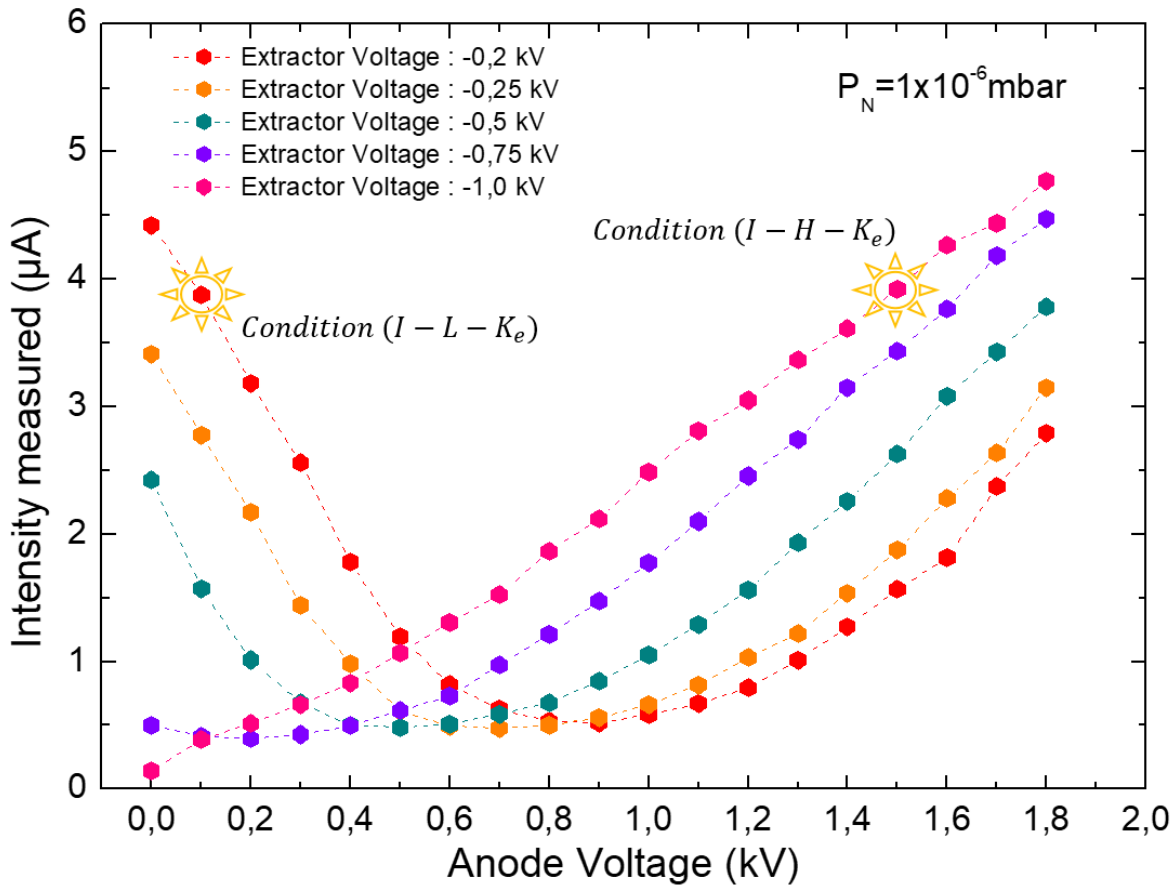


Figure 4.3: Nitrogen source calibration curves for $P_N = 1.10^{-6}$ mbar.

The nitrogen plasma working conditions are thus, selected from the plasma source calibration curve shown figure 4.3, for a nitrogen pressure $P_N = 1.10^{-6}$ mbar. The highest sample current conditions for low and high values for the voltages of the anode and the extractor were chosen. In atomic condition (Atomic, (A)), at low pressure atoms are favorable over ions while at high-pressure ions are promoted with low (I-L- K_e) and high kinetic energies (I-H- K_e). Figure 4.4 summarizes the used conditions for nitriding.

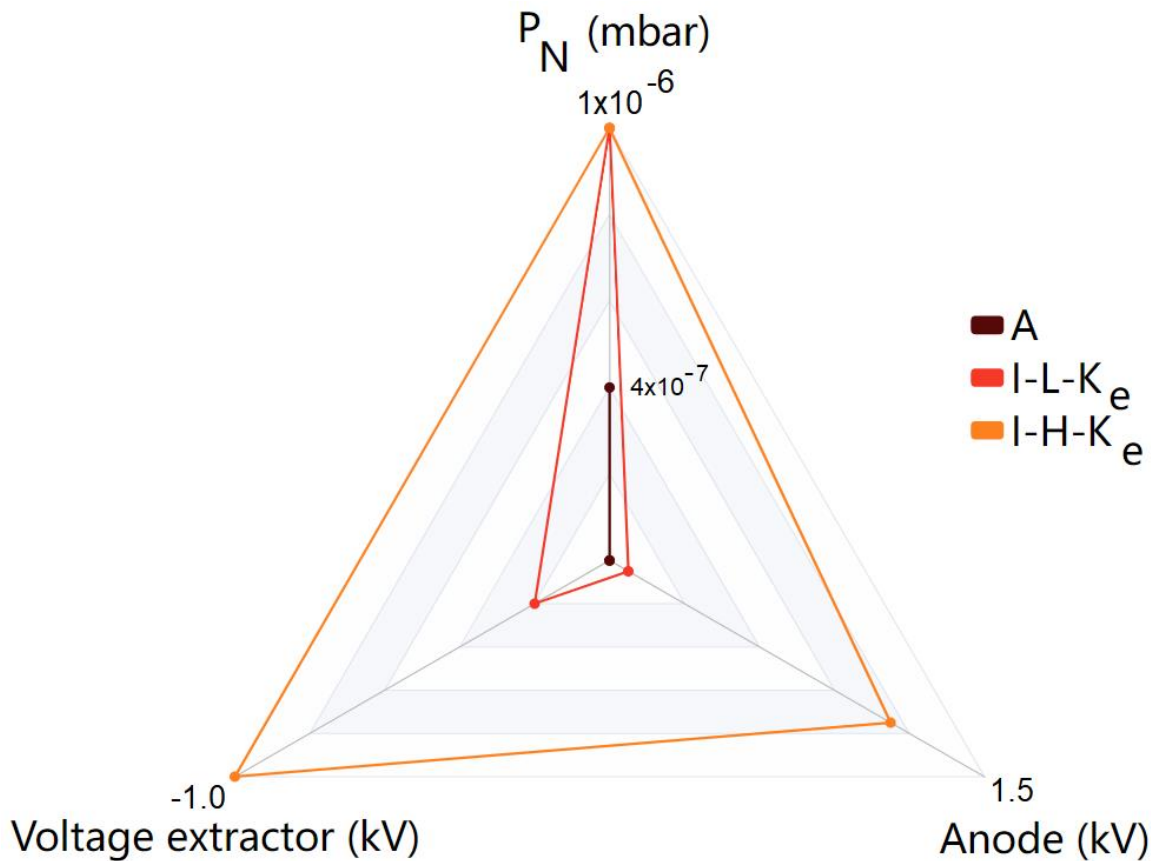


Figure 4.4: Nitrogen source condition parameters.

4.2.2.2 Growth conditions

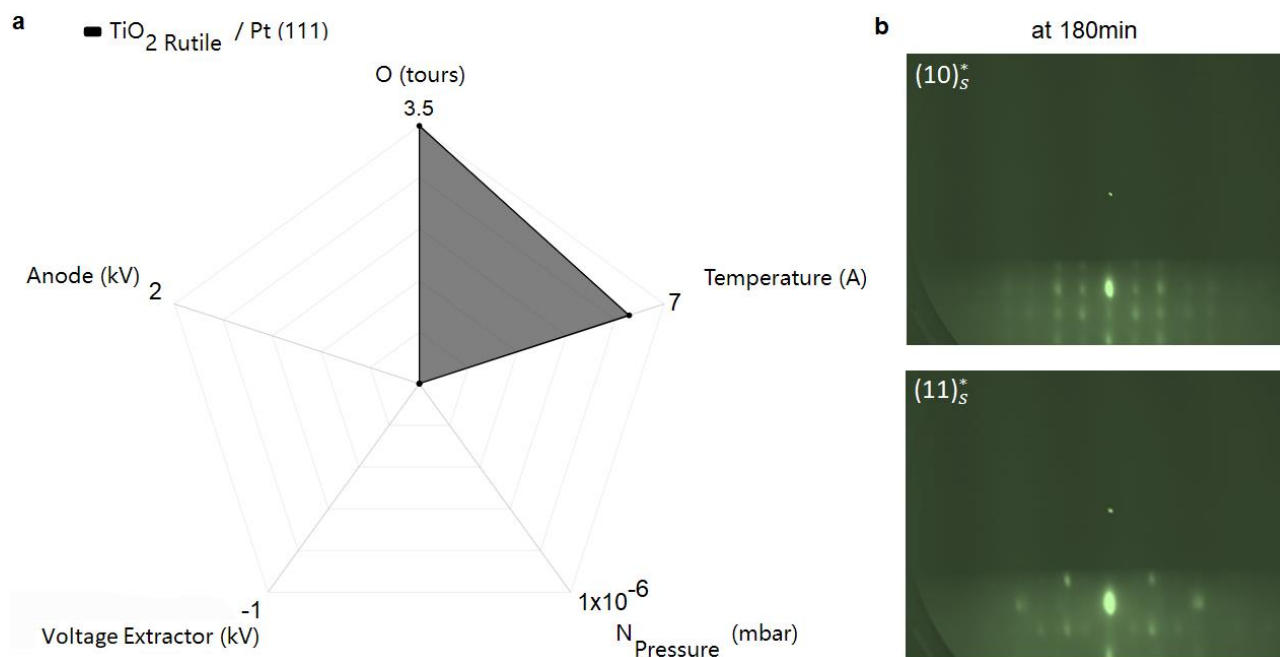
About 10 nm thick films were deposited using atomic oxygen and nitrogen plasma-assisted molecular beam epitaxy (O&NPA-MBE) on Pt (111) single-crystalline substrates. By using these model samples, we can explore the impact of nitrogen dopant, oxygen vacancies and crystallographic structure and orientation on the intrinsic photoelectrochemical properties of N- TiO_2 , while keeping the thickness constant.

The present study does not investigate the deposition of N- TiO_2 on Nb: SrTiO_3 (001) and Pt (001). Since previous research have demonstrated that on Nb:STO, TiO_2 tends to favor the anatase phase, and the resulting film has the lowest photocurrent [1-Magnan 2019].

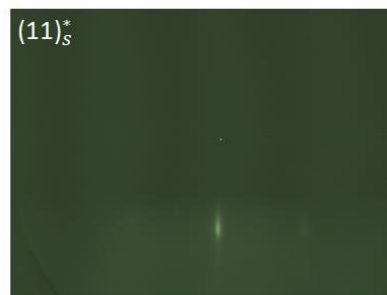
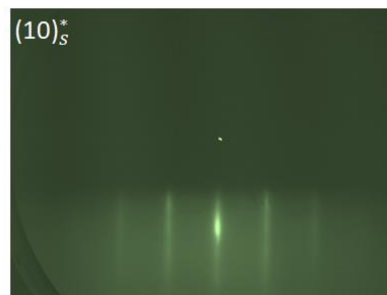
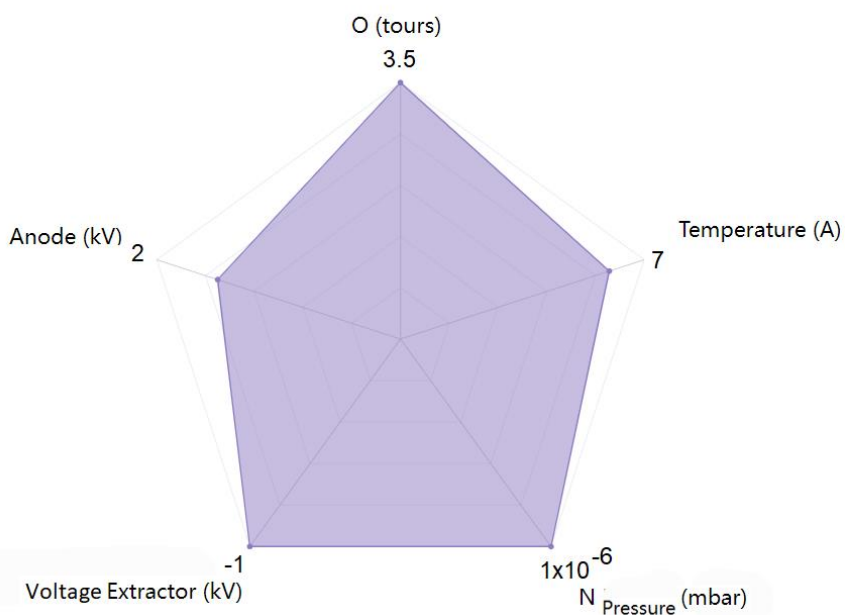
4.3 N-doped TiO_2 single layers on Pt (111)

The key questions that need to be addressed in the study of N- TiO_2 include determining whether nitrogen is incorporated into the TiO_2 lattice through substitutional or interstitial sites, understanding the nature of nitrogen speciation, identifying the maximum permissible concentration of nitrogen dopants, and investigating the impact of dopant concentration on the photoelectrochemical activity of N- TiO_2 .

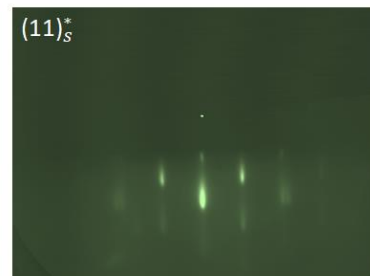
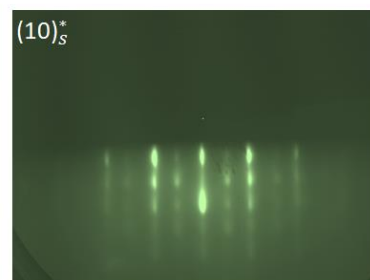
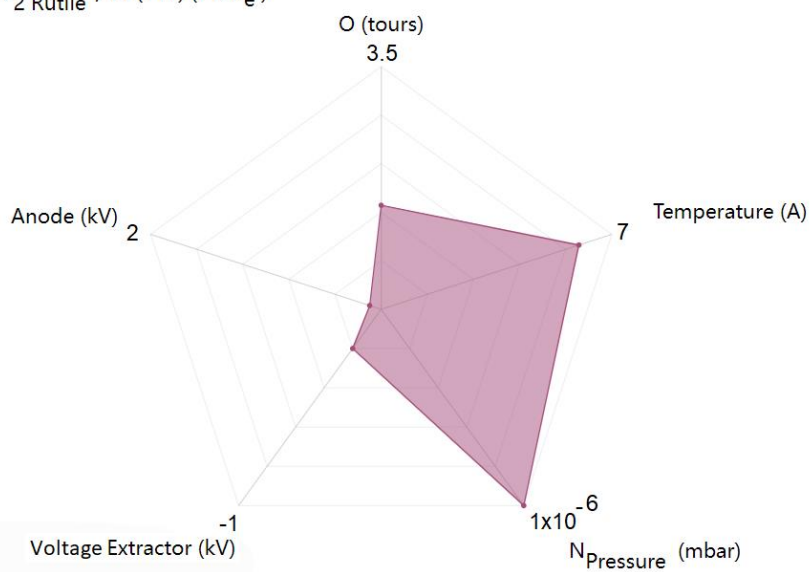
Figure 4.5 and table 2 summarize the main parameters of the five sets of growth conditions that were studied, for Pt (111) substrate. These conditions ranged from oxygen-rich ($f_N < f_O$) to more nitrogen-rich. Oxygen-rich conditions were achieved using high brilliance atomic oxygen plasma (3.5 tours, 350W) well-established conditions to obtain epitaxial TiO_2 films. For this first condition, the typical oxide deposition rate was of about 0.05 nm/min. The deposition time was the same for all samples and the nominal thickness of our films was always about 10 nm. To achieve excess nitrogen conditions, a mixed N atomic and/or N ionic flux (f_N) and an oxygen plasma of at least a (f_O) at $1.5tr(f_O)$ was required. Overall, the composition of the different samples were designed to promote nitrogen-rich conditions and/or oxygen vacancies during the growth of the samples.



■ N-TiO_2 Rutile / Pt (111) (I-H- K_e -O)



■ N-TiO_2 Rutile / Pt (111) (I-L- K_e)



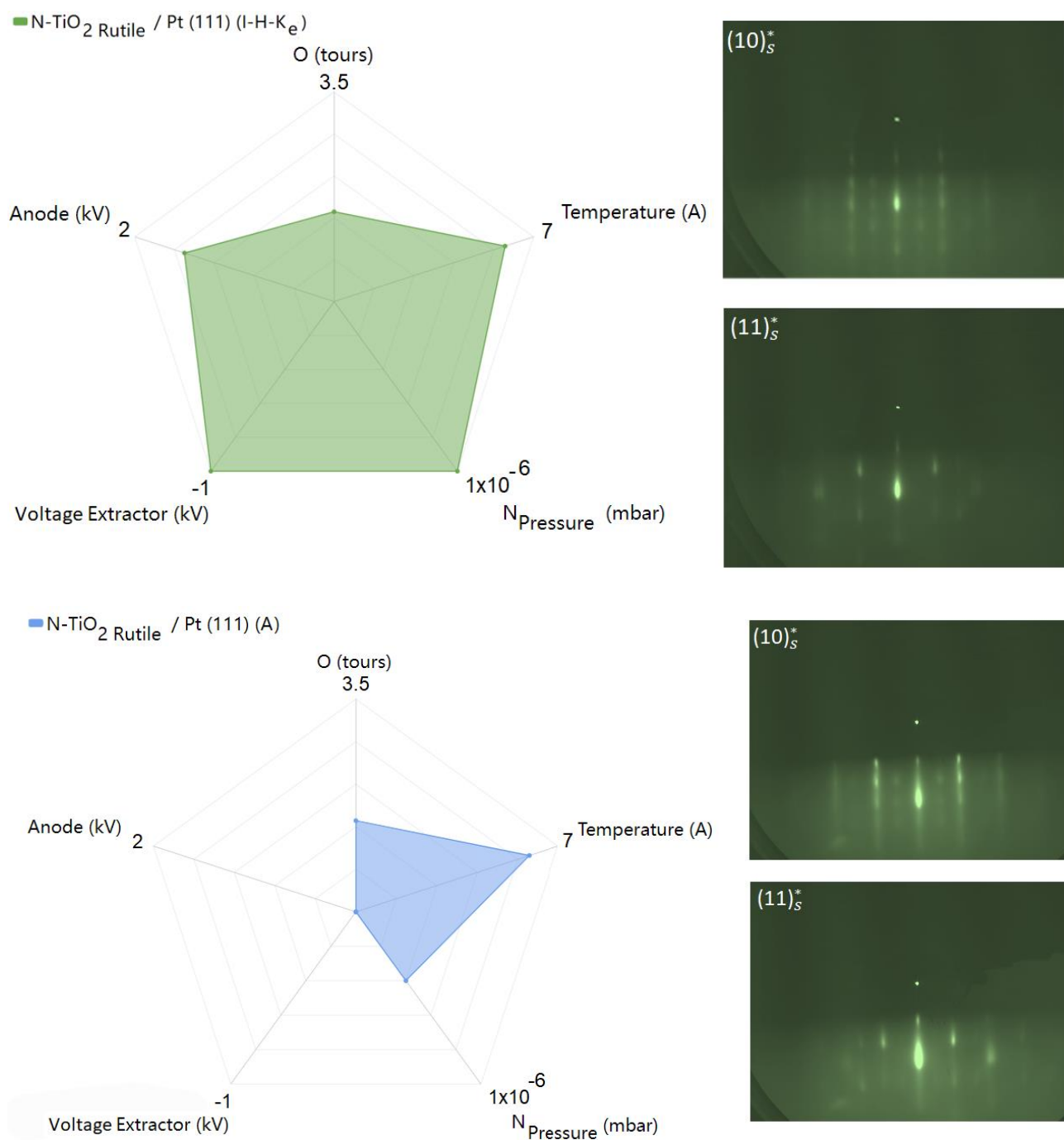


Figure 4.5: **a** Parameters for the synthesis of N-doped and undoped TiO_2 on Pt(111) **b** the corresponding RHEED patterns obtained along the $(10)^*_s$ and $(11)^*_s$ at 180 min of deposition. (i.e. end of deposition)

Samples	O (tours)	P _N (mbar)	V _N		T (A/°C)
			V _{Anode} (kV)	V _{Extractor} (kV)	
TiO ₂ Rutile	3.5	--	--	--	6 /450
N-TiO ₂ Rutile (I-H-Ke-O)	3.5	1.10 ⁻⁶	1.5	-1	6 /450
N-TiO ₂ Rutile (I-L-Ke)	1.5	1.10 ⁻⁶	0.1	-0.2	6 /450
N-TiO ₂ Rutile (I-H-Ke)	1.5	1.10 ⁻⁶	1.5	-1	6 /450
N-TiO ₂ Rutile (A)	1.5	4.10 ⁻⁷	--	--	6 /450
N-TiO ₂ Corundum (I-L-Ke)	1.5	1.10 ⁻⁶	0.1	-0.2	6.8 /550

Table 2: Condition parameters for the synthesis of N-doped and undoped TiO₂ deposited on Pt(111) for 180 min.

4.3.1. Crystallographic structure investigated by *in situ* RHEED

In situ RHEED patterns allow to monitor the growth, any qualitative change in the diffraction pattern evolution reveals immediately changes in the surface morphology and structure of the growing film. RHEED patterns of TiO₂/Pt (111) films at different N doping levels and/or oxygen vacancies are shown in figure 4.5. All the N-TiO₂ films were of very high crystalline quality with well contrasted patterns exhibiting 2D streaks. Figure 4.6 a,b,c shows in details the RHEED interpretation in the case of pure rutile, r-TiO₂ (100). The comparison of the integrated profiles of the RHEED pattern in the (10)*_s and (11)*_s directions for the different samples are reported in figure 4.7. All samples present similar profiles and seems to be in the rutile (100) structure except for N-TiO₂ at I-H-Ke-O nitriding conditions. Indeed, these extreme conditions put the flows of oxygen and nitrogen in competition so to make it difficult to form an ordered structure like for the others.

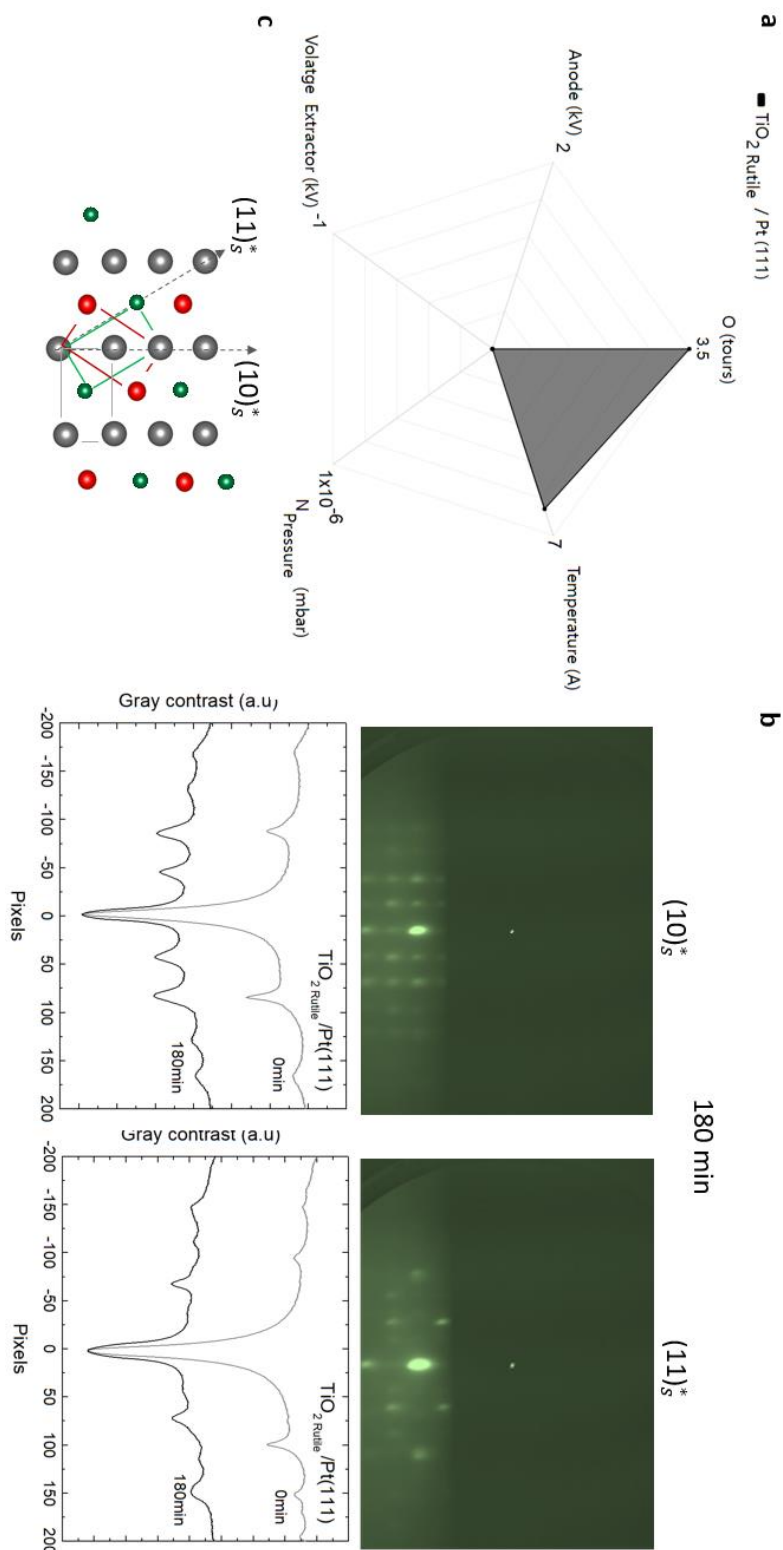


Figure 4.6: **a** Growth condition parameters for the synthesis of rutile $\text{TiO}_2/\text{Pt}(111)$ **b** RHEED pattern obtained along the $(10)_s^*$ with the corresponding integrated profiles at 0 and 180 min of $r\text{-TiO}_2$, **c** corresponding surface reciprocal lattices for the N-TiO_2 on Pt (111) samples. On **c**, the transparent red, green and grey rectangles highlight the elementary unit cell for $r\text{-TiO}_2$.

We can see that the transition between the bare substrate structures occurs by the appearance of typical peaks relative to the $r\text{-TiO}_2$ (100) structure on Pt (111). The presence of intensity modulations along the diffraction streaks indicates some surface roughening and/or 3D growth.

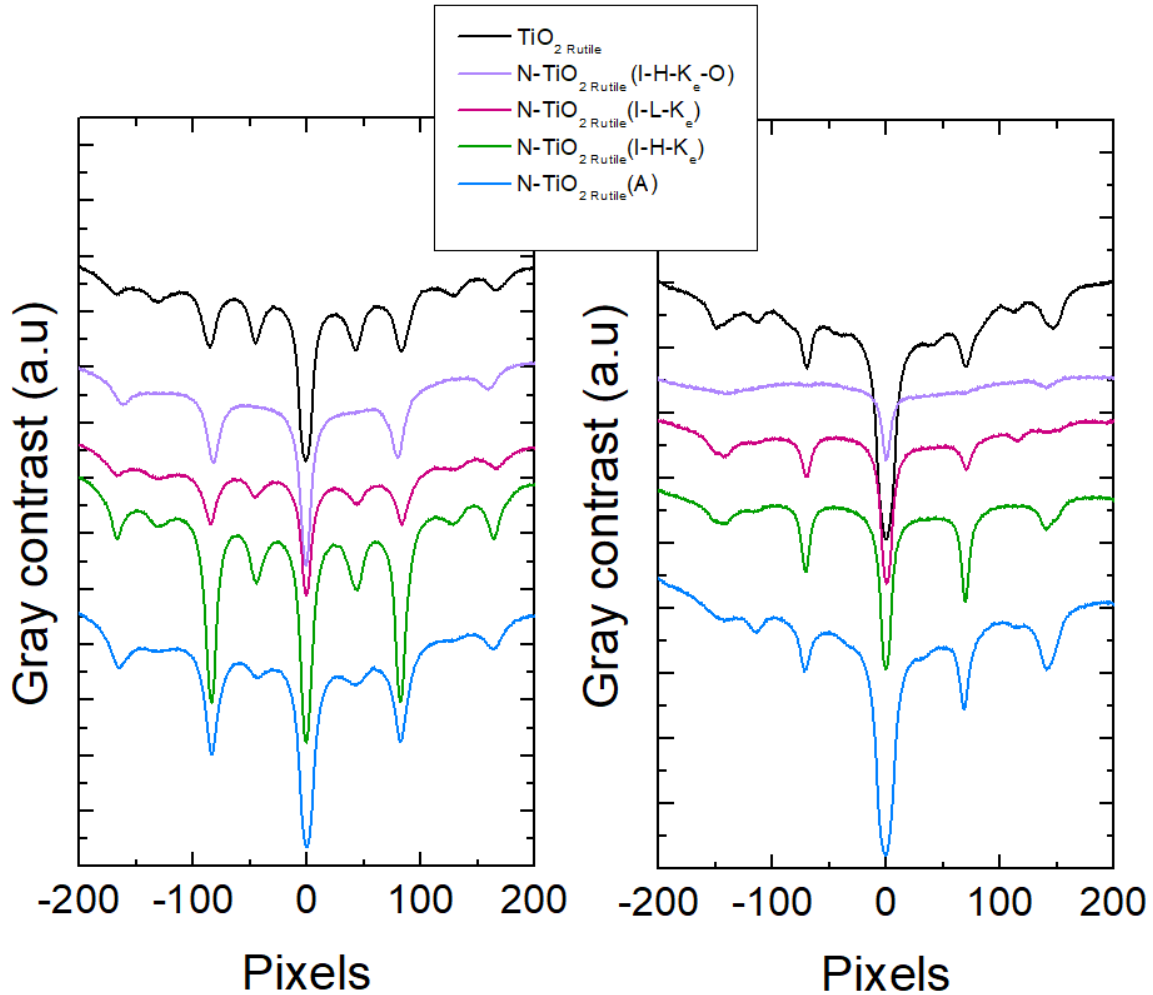


Figure 4.7: Integrated profiles of the RHEED patterns obtained along the $(10)_s^*$ and the $(11)_s^*$ directions at 180 min for undoped (black), N-doped at I-H- K_e -O (purple), N-doped at I-L- K_e (pink), N-doped at I-H- K_e (green) and N-doped at A (blue) growth conditions of TiO_2 layers deposited on Pt(111).

From the RHEED patterns obtained during the growth, we derived the in-plane lattice parameter evolution by measuring the spacing between streaks in the RHEED patterns obtained over the particular diffraction directions $(10)_s^*$ and $(11)_s^*$ of the Pt (111) surface reciprocal lattice.

The presence of intensity modulations along the diffraction streaks indicates some surface roughening, likely due to the relatively low substrate temperature during growth ($\sim 450^\circ\text{C}$). However, the morphology difference between low and high temperature can also be due to the incorporation of

nitrogen into the material. Nitrogen incorporation typically requires sufficient thermal energy for the nitrogen atoms to be incorporated into the crystal lattice. At a low substrate temperature of ~450°C in contrast with ~550°C, the thermal energy may not be sufficient for effective nitrogen incorporation, resulting in negligible levels of nitrogen in the material, this point will be discussed more in detail later (section 4.4.6).

4.3.2 Electronic structure analyzed by *ex situ* XPS measurements

The N-1s, Ti-2p, and O-1s core-level spectra were recorded using mono-chromatic Al K_α X-rays and are shown figure 4.8, 4.9 and 4.10 in normal emission geometry for all five growth conditions presented in table 2. Since the measurements were made *ex situ* the quantification of N is given with respect to the Ti.

The N-1s XPS spectra exhibits two distinct peaks, for the N-doped samples (Figure 4.8). For all the N-doped samples, there is a peak at ~399eV and an additional peak at ~396eV. Nitrogen can be located in the lattice of TiO₂ interstitially or/and substitutionally. Following Fujishima *et al.*, [72-Fujishima 2008] the N-1s peak at ~399eV is typically assigned to the interstitial nitrogen dopant, meaning the Ti–O–N or Ti–N–O oxynitride [73-Okato, 74-Wang 2009, 75-chen 2007]. While the peak at ~396 eV is ascribed to the substitutional nitrogen dopant (N_O), characteristic then, of N³⁻ that corresponds to TiN [75-chen 2007, 76-Esaka 1997, 77-Moulder 1992]. This peak cannot be assigned to the NO_x molecules, because the N-1s binding energy for NO_x is typically larger than 403 eV [77-Moulder 1992]. The measured binding energy (BE) is, however, lower than that of titanium nitride. In fact, the bonding of Ti and N in TiN is a mixture of covalent, metallic and ionic contributions. When oxygen atoms are present and form Ti-O bonds, the ionic character of the Ti-N bonding increases, meaning a charge transfer occur from Ti to N (negatively charged N atom interacts more strongly with the positively charged Ti ion). This phenomenon causes a redistribution of electron density and a shift in the electron energy levels, leading eventually, to a lower binding energy for the N-1s [76-Esaka 1997]. Therefore, such a BE shift is consistent with the formation of substitutional N³⁻ dopants in a TiO₂ matrix.

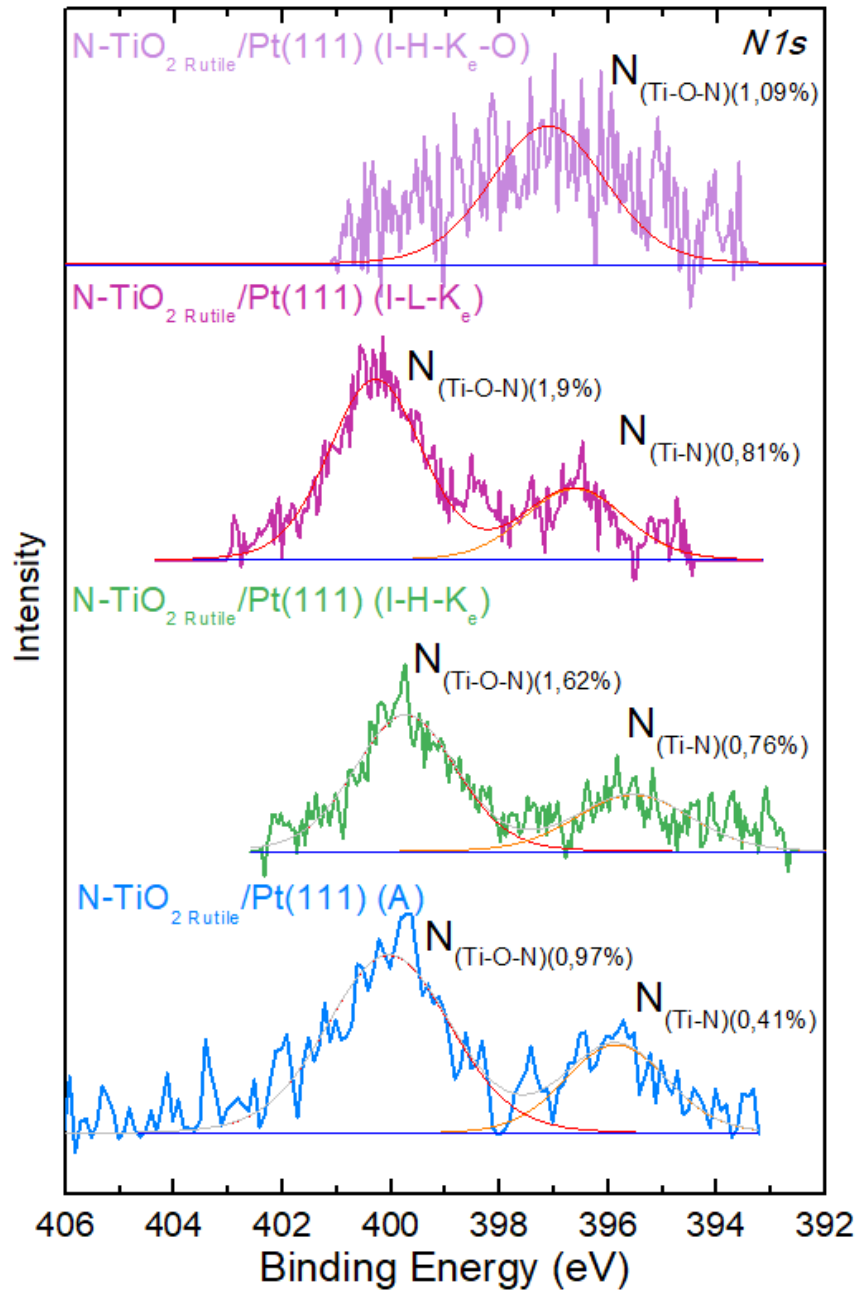


Figure 4.8: $\text{N}1s$ photoemission spectra of N -doped at I-H- K_e -O (purple), N -doped at I-L- K_e (pink), N -doped at I-H- K_e (green) and N -doped at A (blue) conditions of TiO_2 layers deposited on $\text{Pt}(111)$. The red contribution corresponds to the $\text{N}_{(\text{Ti-O-N})}$ component and the orange one to the $\text{N}_{(\text{Ti-N})}$ component, thin bottom lines correspond to linear type backgrounds and thick straight lines to best fits. The best-fit parameters are reported in Table 3.

The spectra of Ti-2*p* are shown in figure 4.9. The spin-orbit splitting leads to two contributions of the Ti-2*p*_{1/2} and Ti-2*p*_{3/2} located near 464.7 and 459.1 eV binding energies. These features are consistent with Ti⁴⁺ in the TiO₂ lattice. For the undoped TiO₂, these features are all assigned to Ti⁴⁺, indicating no Ti³⁺ species exist on the surface at all. However, for the other samples (Figure 4.15). The Ti-2*p*_{3/2} peak gradually shows a shoulder peak at lower binding energy with increasing N concentration. This corresponds to the presence of small contribution of Ti³⁺ species located around 456.9 eV. This peak is a direct consequence of the reduction of Ti⁴⁺ into Ti³⁺ because of the doping or/and oxygen vacancies.

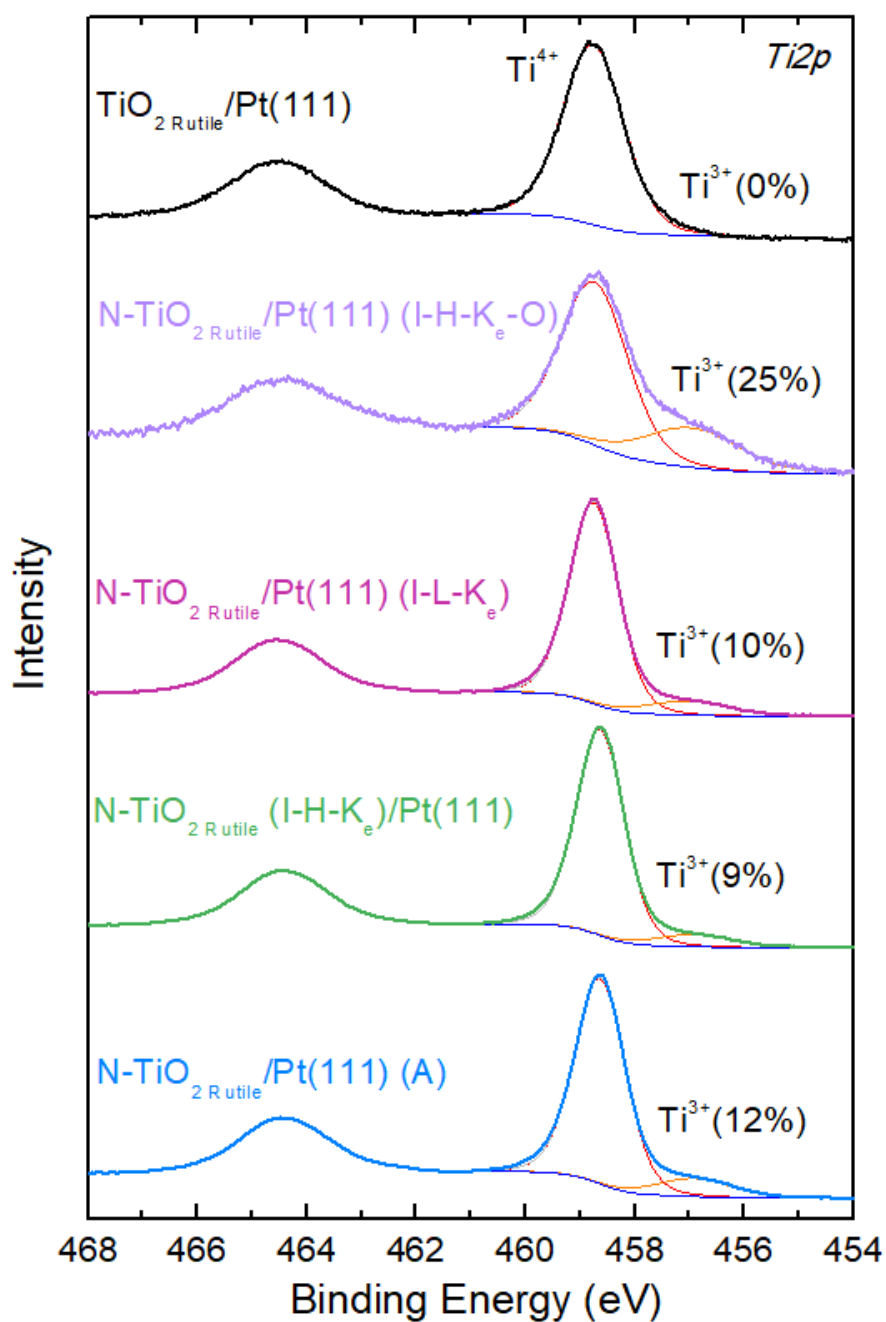


Figure 4.9: Ti-2p photoemission spectra of undoped (black), N-doped at I-H- K_e -O (purple), N-doped at I-L- K_e (pink), N-doped at I-H- K_e (green) and N-doped at A (blue) conditions of TiO_2 layers deposited on Pt(111). The red contribution corresponds to the Ti^{4+} component and the orange one to the Ti^{3+} component, thin bottom lines correspond to Shirley type backgrounds and thick straight lines to best fits. The best-fit parameters are reported in Table 3.

In all cases, the O-1s peak consists of a peak at ~ 530 eV, characteristic of lattice oxygen in TiO_2 (see figure 4.10). Surface adsorbed species such as OH, which are chemically shifted by +1.5 eV from

lattice oxygen (peak at ~ 531.5 eV) were also detected, it is known that this peak is favored by oxygen vacancies. Upon doping, the peaks shifted from a singlet to a doublet relative to those obtained in undoped TiO_2 Rutile. One observe that the intensity of the OH peak is higher for the sample subjected to I-H- K_e -O nitriding conditions, which also has a highest content of Ti^{3+} .

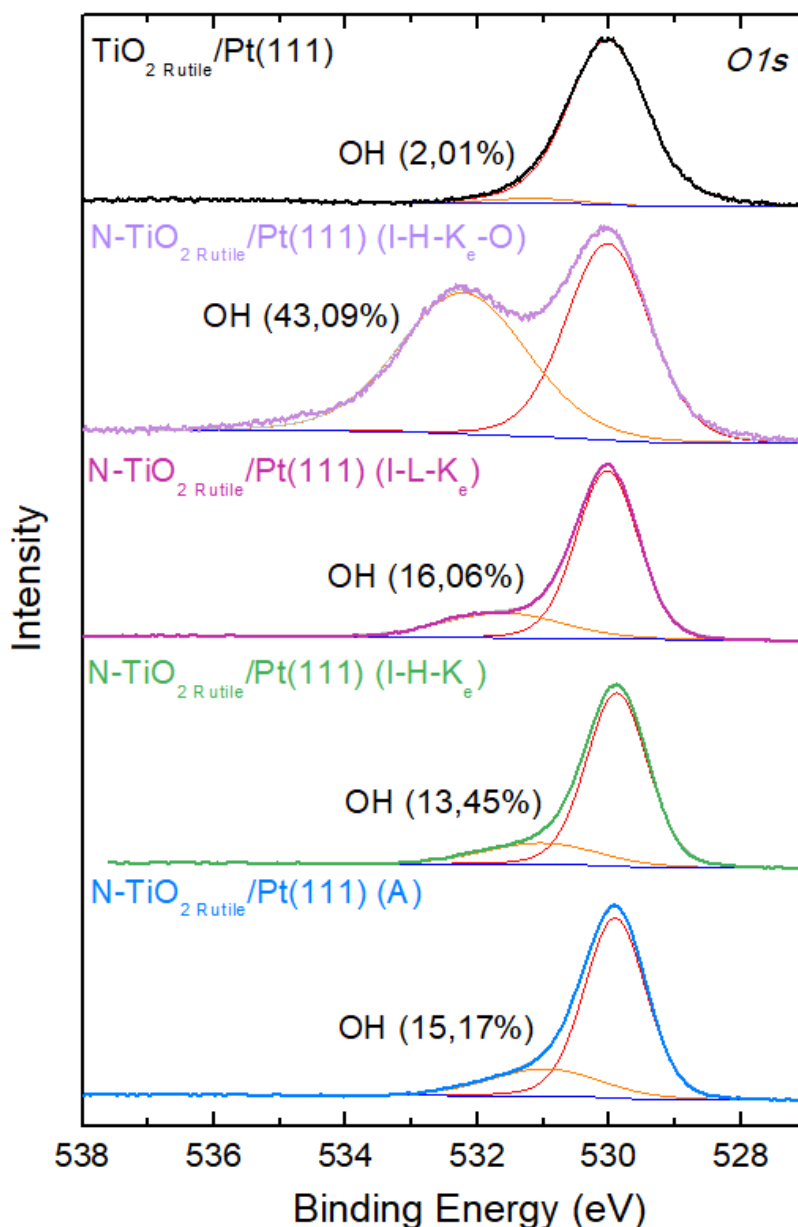


Figure 4.10: O-1s photoemission spectra of undoped (black), N-doped at I-H- K_e -O (purple), N-doped at I-L- K_e (pink), N-doped at I-H- K_e (green) and N-doped at A (bleu) conditions of TiO_2 layers deposited on Pt(111). The red contribution corresponds to the oxygen bulk component and the orange one to the hydroxyl component, thin bottom lines correspond to Shirley type backgrounds and thick straight lines to best fits. The best-fit parameters are reported in Table 3.

The study of the valence band (VB) allows to understand the modifications that result from N doping (see figure 4.11). In order to evaluate the value of the valence band edge (VBE) we extrapolate the slope near the maximum of valence band (Figure 4.11). These values are summarized in table 5. Due to the small thickness of the films, all the spectra exhibit the valence states of the film but also the valence state of Pt. The shape of O-2*p* derived valence band maximum appeared unchanged after N incorporation (a and b). However, except for the I-H-K_e-O condition, where an uniform shift of the VBE to higher binding energies is observed as compared to the undoped sample.

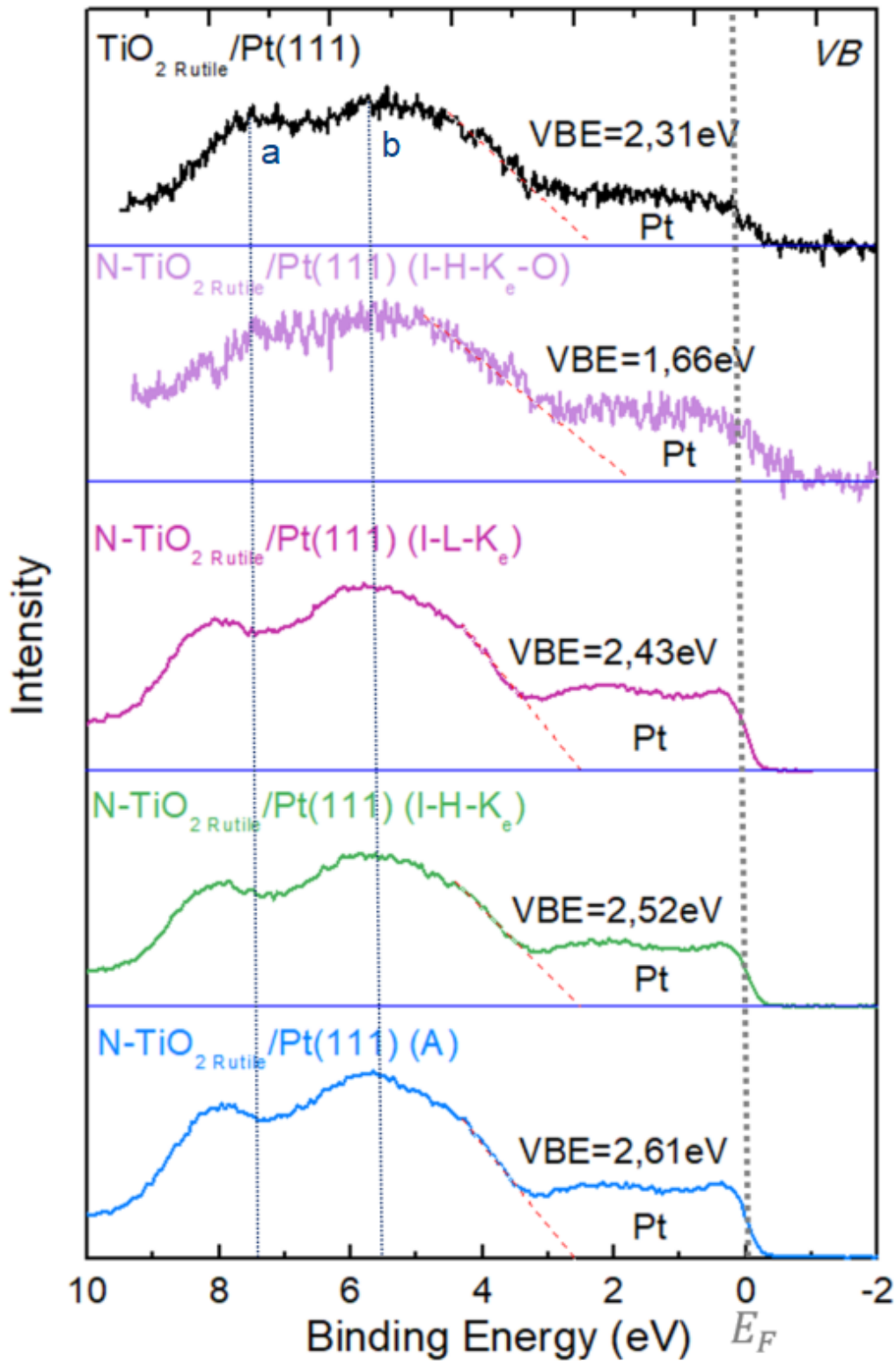


Figure 4.11: Valence band of undoped (black), N-doped at I-H-Ke-O (purple), N-doped at I-L-Ke (pink), N-doped at I-H-Ke (green) and N-doped at A (blue) conditions of TiO_2 layers deposited on Pt(111). Thick red dot lines correspond to the valence band edge (VBE) fits. NB: O-2p bonding state (a) and non-bonding state (b).

Sample	Ti ³⁺ /Ti ⁴⁺ (%)	N/Ti (%)	N /Ti (at%)		O _(OH) /Ti(%)	VBE (eV)
			$N_{(Ti-O)}$ $N_{Ti}(\%)$	$N_{(Ti)}$ $N_{Ti}(\%)$		
TiO ₂ /Pt (111)	0	0	0	0	2.01	2.63
N-TiO ₂ Rutile /Pt (111) (I-H-K _e -O)	25	1.09	1.09	0	43.09	1.66
N-TiO ₂ Rutile /Pt (111) (I-L-K _e)	10	2.71	1.90	0.81	16.06	2.43
N-TiO ₂ Rutile /Pt (111) (I-H-K _e)	9	2.38	1.62	0.76	13.45	2.52
N-TiO ₂ Rutile /Pt (111) (A)	12	1.38	0.97	0.41	15.17	2.61

Table 3: Concentrations (at. %) of the components in layers of nitrogen doped and undoped TiO₂ on Pt (111) and their VBE.

4.3.3 PEC measurements

4.3.3.1 I-V measurements

This section describes the photoelectrochemical behaviors of our samples. The results of I-voltammetry (IV) experiments conducted on N doped TiO₂ thin films compared to pure r-TiO₂ sample. According to the results shown in figure 4.12, the best sample for the photocurrent is the sample I-H-K_e (green curve). The onset potential (the potential at which a significant current begins to flow) for this N-TiO₂ sample is the same as compared to the pure r-TiO₂ sample (-0.7 V vs Ag/AgCl). However, depending on the N doping level, the other N-TiO₂ samples require a higher potential to initiate a significant current flow compared to the pure r-TiO₂ sample.

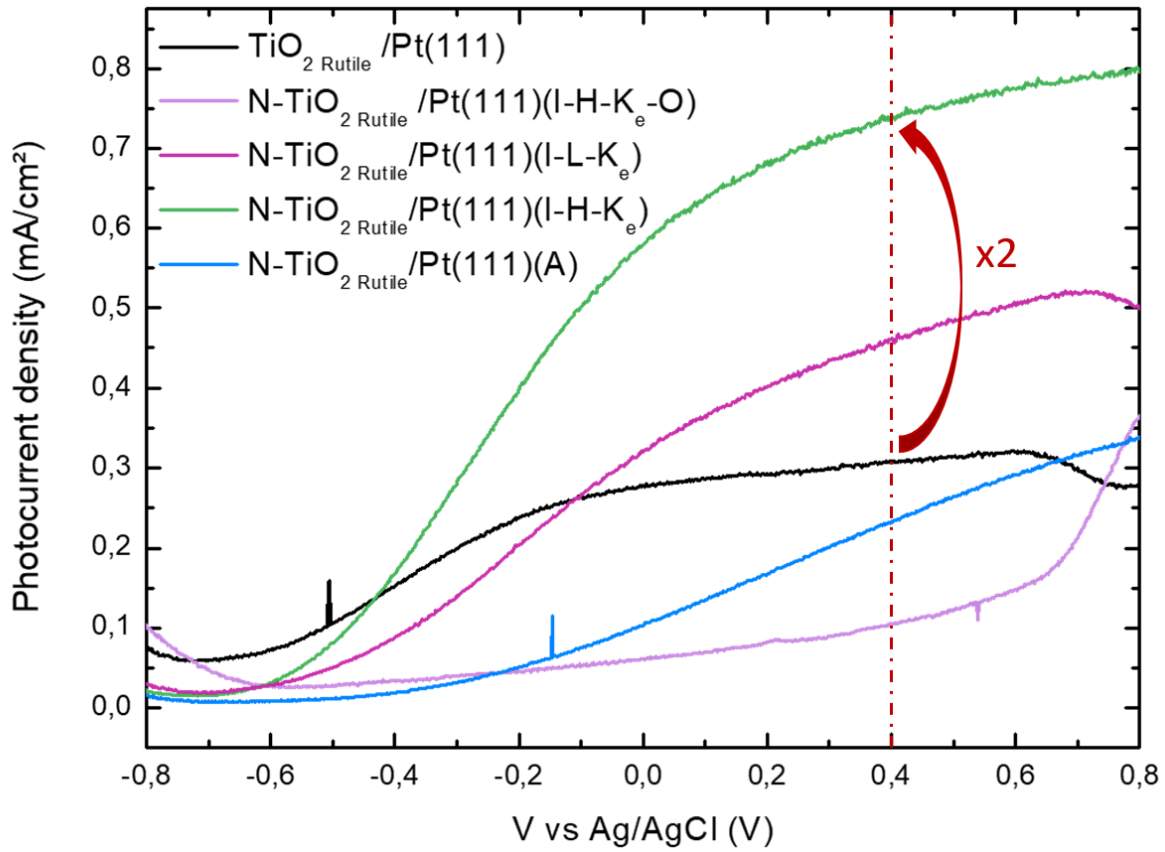


Figure 4.12: Photocurrent density curves undoped (black), N-doped at I-H-Ke-O (purple), N-doped at I-L-Ke (pink), N-doped at I-H-Ke (green) and N-doped at A (bleu) conditions of TiO₂ layers deposited on Pt(111).

The photocurrent of the N-TiO₂ at I-H-Ke conditions reaches 0.72 mA/cm² at 0.4 V, two times the photocurrent of undoped r-TiO₂ (~0.34 mA/cm²). This result shows the usefulness of N doping to improve TiO₂ for PEC applications.

4.3.3.2 The spectral response

Figure 4.13 illustrates the efficient absorption of the samples, represented as photocurrent density normalized to light flux and normalized at 270 nm. The FWHM of the absorption window varies based on the specific nitriding condition used during the synthesis.

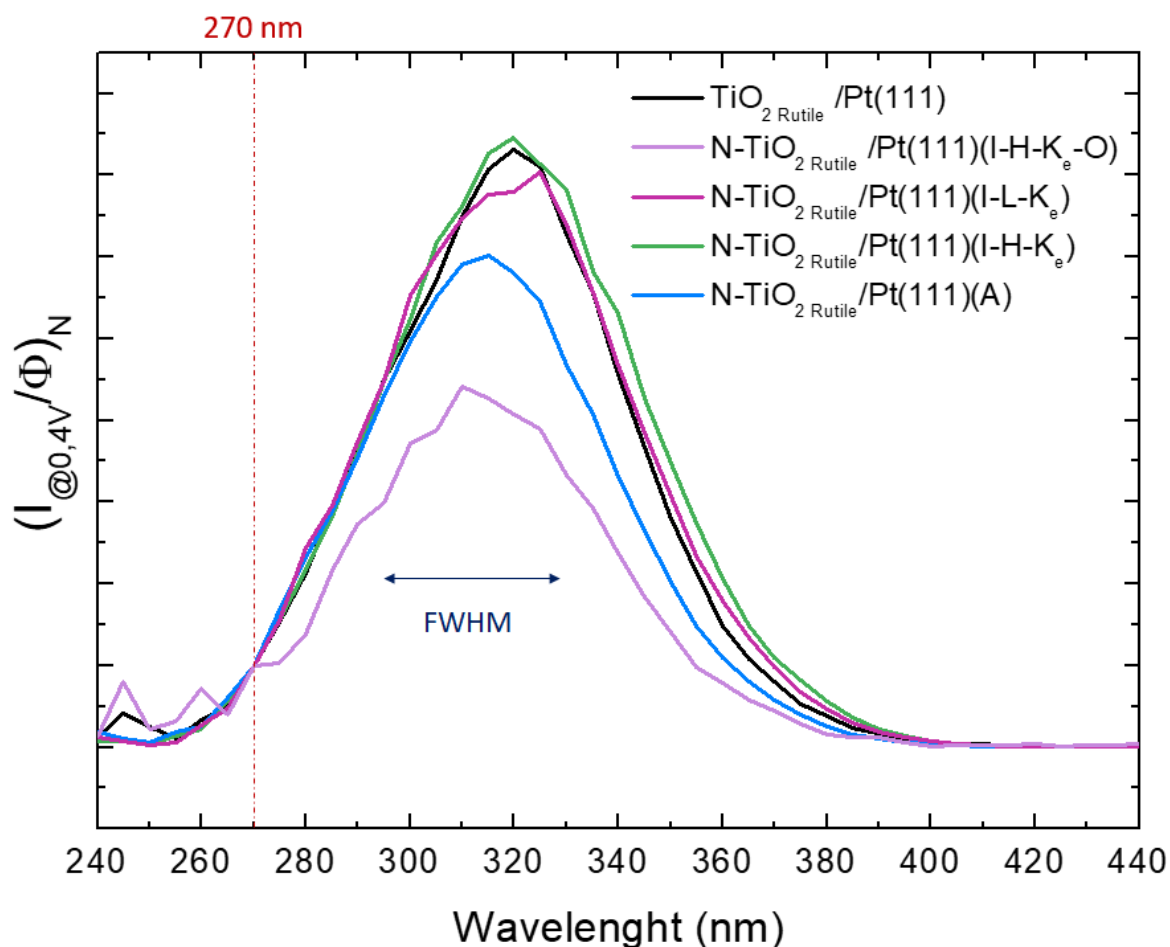


Figure 4.13: Efficient absorption spectra of undoped (black), N-doped at I-H- K_e -O (purple), N-doped at I-L- K_e (pink), N-doped at I-H- K_e (green) and N-doped at A (blue) conditions of TiO_2 layers deposited on Pt(111), as a function of the wavelength at 0.4 V vs. Ag/AgCl. For comparison between samples, the curves are normalized with the light flux of the Xe arc lamp used during the experiment at 270 nm.

Remarkably, the sample prepared using the I-H- K_e nitriding condition, which exhibits the highest photocurrent density, demonstrates a shift in its absorption edge by approximately 10 nm towards longer wavelengths when compared to the undoped TiO_2 film. Additionally, this particular sample displays the widest absorption window among all the samples studied.

These findings lead us to a reasonable assumption that effective photocurrent density is associated with superior visible light absorption.

4.3.3.3 The photoelectrochemical gap

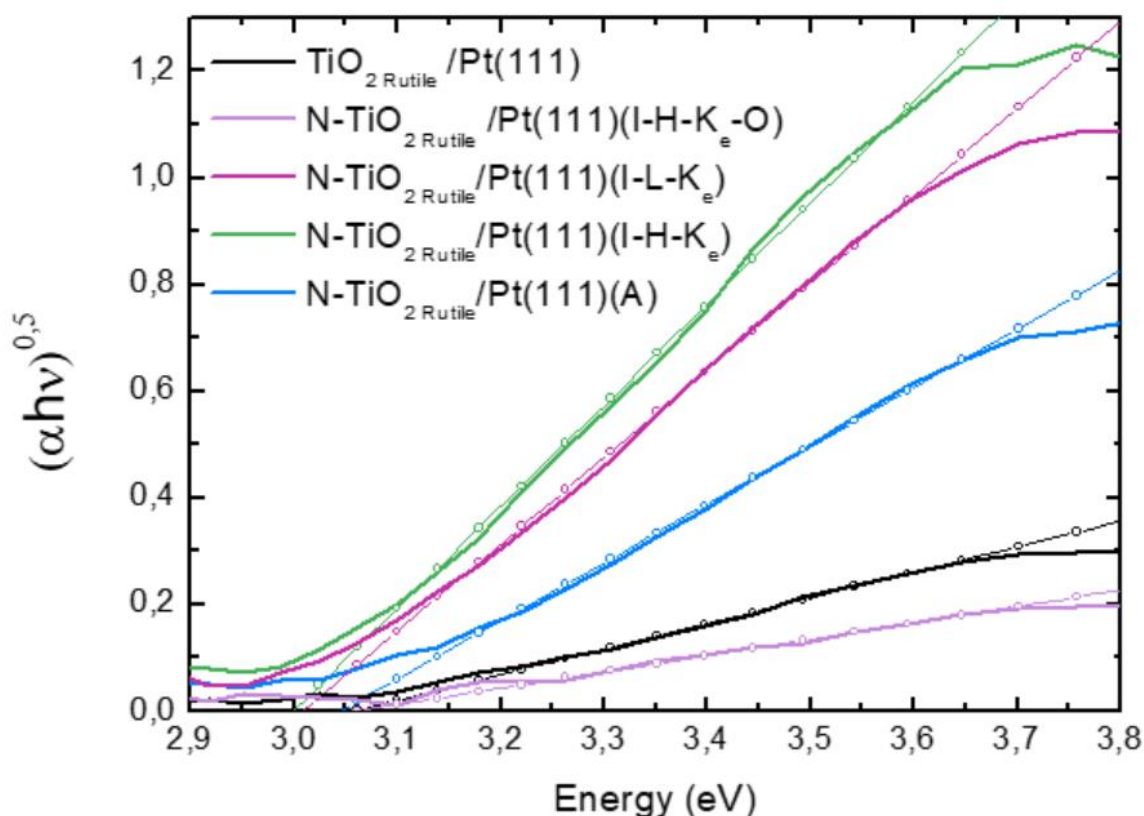


Figure 4.14 : Efficient Tauc plot deduced from curves of Figure 4.19 of undoped (black), N-doped at I-H- K_e -O (purple), N-doped at I-L- K_e (pink), N-doped at I-H- K_e (green) and N-doped at A (blue) conditions of TiO_2 layers deposited on Pt(111), as a function of the energy. The straight lines with open circles give an indication of the indirect efficient gap for different thin films.

From the efficient absorption curves one can calculate the efficient Tauc plot in order to deduce “efficient band gaps”. The efficient band gaps are respectively around 2.99 eV, and 3.06 eV (Table 4). These values are found to be very close to the band gap values from the literature for rutile (3.0 eV). As noticed earlier, these results show that the best visible light absorption occurs for N- TiO_2 Rutile / Pt(111) (I-H- K_e) (*i.e.*, the smallest band gap) which also yields the best photocurrent.

Sample	J _{Ph} (mA/cm ²)	FWHM (nm)	Indirect band gap (eV)
TiO ₂ /Pt (111)	0.34	58	3,05
N-TiO ₂ Rutile /Pt (111) (I-H-K _e -O)	0.11	57	3.06
N-TiO ₂ Rutile /Pt (111) (I-L-K _e)	0.46	62	3.01
N-TiO ₂ Rutile /Pt (111) (I-H-K _e)	0.72	63	2.99
N-TiO ₂ Rutile /Pt (111) (A)	0.23	58	3,04

Table 4: Photoelectrochemical parameters of N-doped and undoped TiO₂ deposited on Pt (111)

4.3.3.4 Electrochemical impedance spectroscopy

The Mott-Schottky plots ($1/C^2 = f(V)$), where C represents the capacitance are represented figure 4.15. The flat-band potential (V_{fb}) and carrier concentration (N_D) were obtained through Mott-Schottky curve fitting. The obtained values are indicated in table 5. The values of the flat-band potential showed slight variations for the different samples. However, the carrier concentration (N_D) values present stronger variations. For example, undoped TiO₂ had a carrier concentration almost 30 times higher than N-TiO₂ (I-H-K_e) the sample with the highest photocurrent.

The doped films displayed fluctuating N_D values, similar to the other photoelectrochemical parameters. Nitriding can have both positive and negative effects on charge carrier concentration. On the positive side, the incorporation of nitrogen atoms into the material's lattice can introduce additional charge carriers' concentration, which can enhance the photocurrent generation, leading to improved photoelectrochemical performance. However, on the negative side, nitriding may also have adverse effects on the charge carrier concentration. It could create defects or traps in the material, which can act as recombination centers for charge carriers and negatively affecting the photocurrent output.

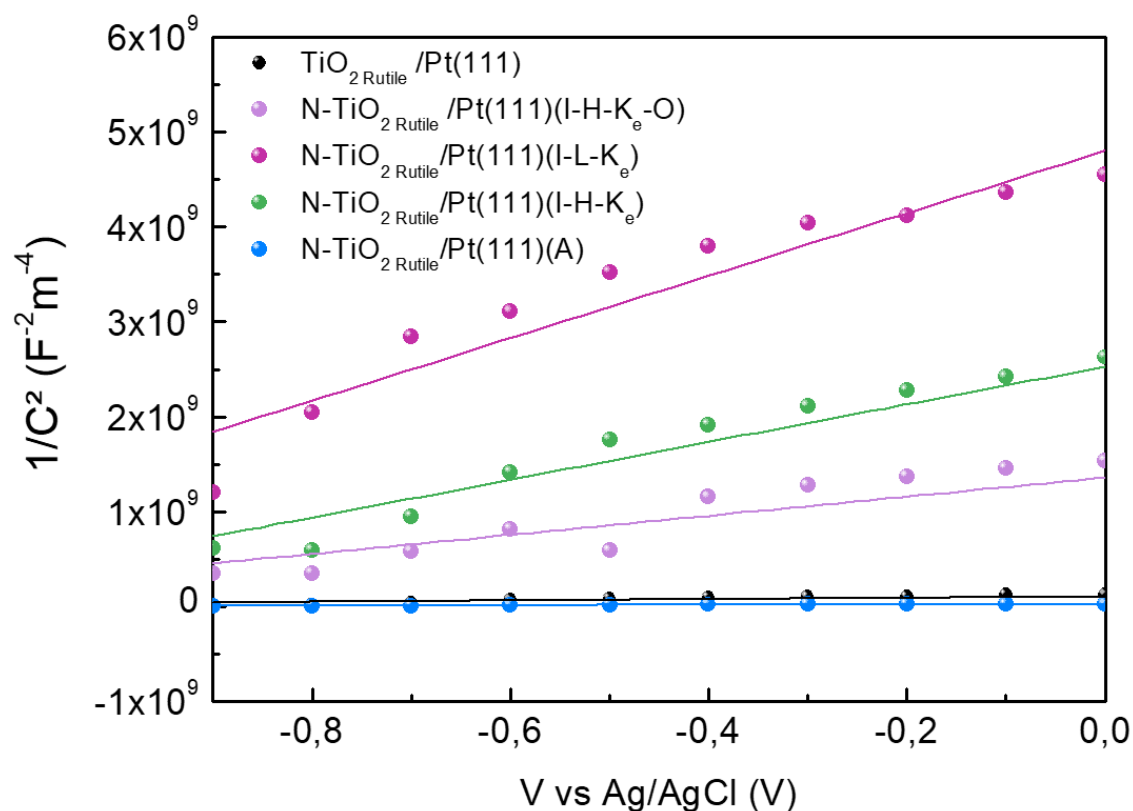


Figure 4.15: Mott–Schottky plots for undoped (black), N-doped at I-H-Ke-O (purple), N-doped at I-L-Ke (pink), N-doped at I-H-Ke (green) and N-doped at A (blue) growth conditions of TiO₂ layers deposited on Pt(111). Straight lines indicate the linear fit of each curve.

Sample	N _D (m ⁻³)	V _{fb} (V)
TiO ₂ /Pt (111)	4.89×10 ²⁸	-1.68
N-TiO _{2 Rutile} /Pt (111) (I-H-Ke-O)	3.21×10 ²⁷	-1.36
N-TiO _{2 Rutile} /Pt (111) (I-L-Ke)	1.07×10 ²⁷	-1.58
N-TiO _{2 Rutile} /Pt (111) (I-H-Ke)	1.64×10 ²⁷	-1.27
N-TiO _{2 Rutile} /Pt (111) (A)	1.05×10 ²⁹	-1.01

Table 5: Electrochemical impedance parameters deduced from the fit of $1/C^2 = f(V)$ of N-doped and undoped TiO₂ deposited on Pt (111)

4.3.4 Crystal structure: EXAFS measurements analysis

The EXAFS spectra of N-doped TiO₂ films were recorded at the Ti_K edge using normal incidence (linear photon polarization parallel to the film surface) and grazing incidence (linear photon polarization perpendicular to the film surface) (Figure 4.16). The EXAFS oscillations ($k^3\chi(k)$ data) are presented in figure 4.16 and the fit parameters in table 6. There is no significant change with N doping, and the spectra obtained in normal incidence differ from those obtained in grazing incidence, indicating an anisotropic structure for all doping levels.

The EXAFS data were analyzed using the HORAE and FEFF 8.4 codes, in the single scattering model assuming a TiO₂ rutile structure. The fitting parameters are the distances between Ti atoms and the octahedral shell of oxygen (O equatorial, and O axial), and two dilatation factors with respect to bulk rutile α parallel the surface and β perpendicular to the surface [1-Magnan 2019]. The fitting results at the Ti_K edge, are shown in figure 4.16a and 4.16b for undoped and from 9 at.% to 25 at.% of Ti³⁺ content in N-doped TiO₂ films. The corresponding interatomic distances, the positions of O_{equatorial} and O_{axial} and Ti, the first shell of Ti neighbor in the case of rutile (100), are reported in table 6. The parameters of bulk rutile are also provided.

The fitting parameters are close to the values of the bulk, indicating that the assumption of a rutile structure is accurate.

For the undoped defected octahedron, the axial distances and the equatorial distances are reduced compared to the bulk (see table 6).

The introduction of N results in notable changes in the equatorial and axial distances within the crystal structure, as observed table 6. Even if the rutile structure is conserved upon N-doping, the oxygen octahedron undergoes a significant distortion due to the presence of point defects that can include oxygen vacancies and/or substitutional/interstitial nitrogen atoms [78-Ceotto 2012].

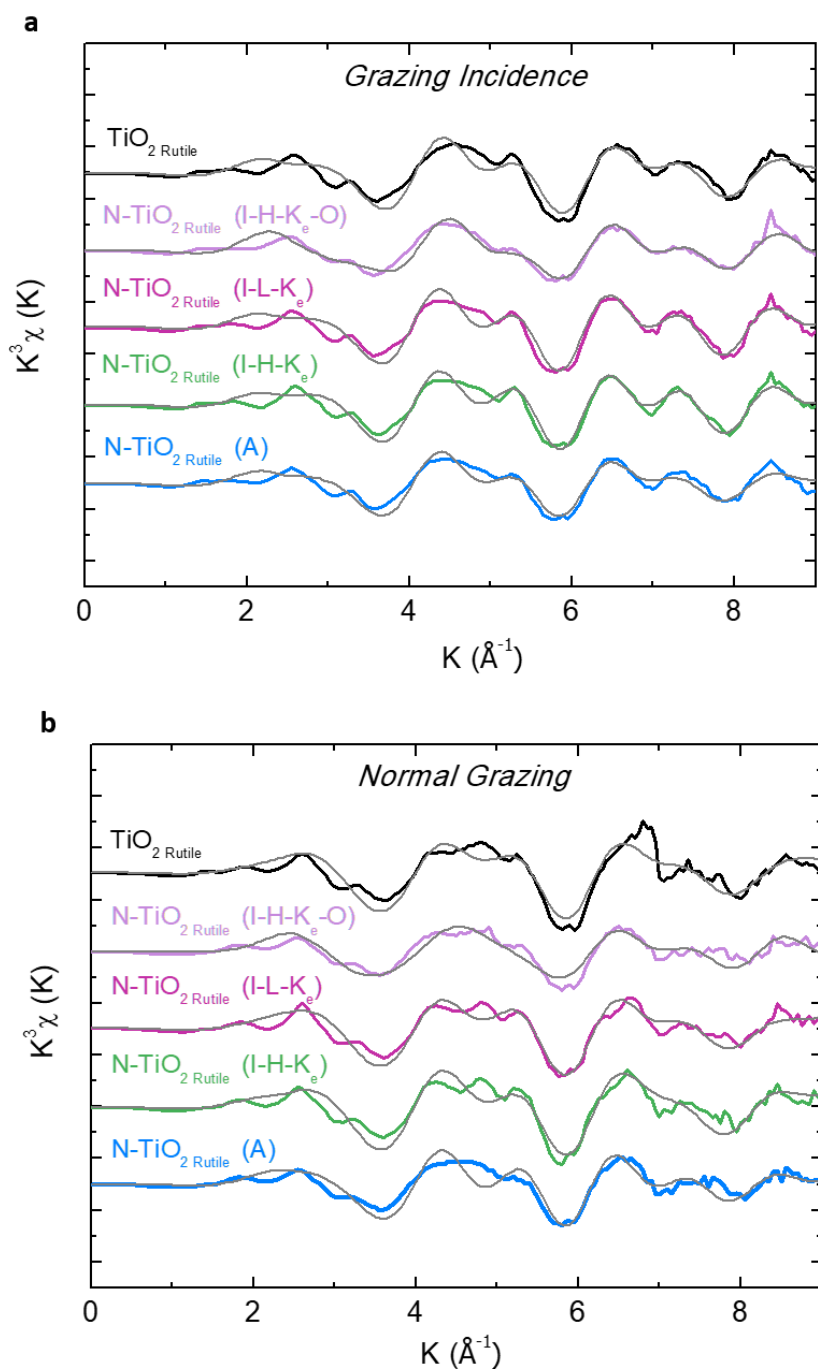


Figure 4.16: Experimental (colored thick lines) $k^3\chi(k)$ EXAFS oscillations and fit (gray thin line) by FEFF calculations (assuming a rutile structure) obtained in **a** grazing and **b** normal. Sample : undoped (black), N-doped at I-H- K_e -O (purple), N-doped at I-L- K_e (pink), N-doped at I-H- K_e (green) and N-doped at A (bleu) conditions of TiO_2 layers deposited on Pt(111).

Moreover, considering that the distance between Ti and O atoms in the octahedral shell can vary in two direction, two dilatation factors (α parallel to the surface and β perpendicular to the surface) are taken into account because of the strain imposed by the substrate. The structure of our most effective

photoanode (N/Ti 2.38% and Ti³⁺ at 9%), is more in-plane contracted and more out-of-plane contracted compared to pure r-TiO₂ (Table 6 and figure 4.17).

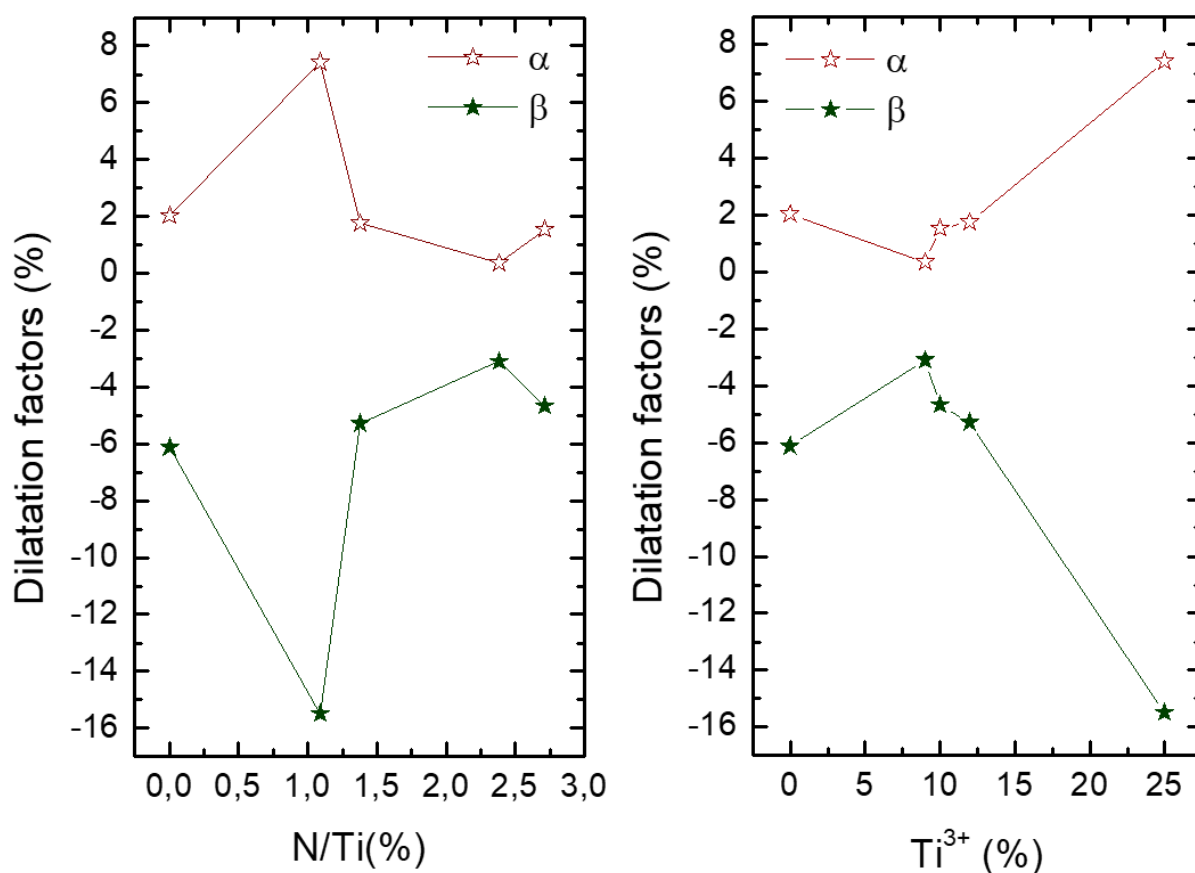


Figure 4.17: Evolution of the dilatation parameters; α parameter parallel to the surface (dark red unfilled stars) and β parameter perpendicular to the surface (dark green filled stars) as a function of the N/Ti ratios and the Ti³⁺ content.

The evolution of strain in the film, represented by the factors α and β obtained from EXAFS, is shown in figure 4.17 as a function of the N/Ti and Ti³⁺ ratios. All films exhibit an asymmetric evolution in both directions, confirming the anisotropy of the materials. The sample with lower crystallinity under I-H-K_c-O nitriding conditions exhibits a higher dilatation. Furthermore, as the quantity of oxygen vacancies increases, the anisotropy of the strain in the films becomes more pronounced.

Furthermore, since rutile (100) is compatible with the observed RHEED patterns ($c_{\text{in plane}}$ estimated by RHEED are close to the values deduced from the EXAFS measurements), we investigated the last $c_{\text{in plane}}$ determined from RHEED experiment as a function of the nitrogen content and of the Ti³⁺ content. The figure 4.18 shows that again the evolution of the $c_{\text{in plane}}$ parameter has an opposite trend. Depending on the preparation method, the disorder can vary significantly. The most efficient case

corresponds to an N-doping level at 2.38% with a Ti^{3+} content of 9% due to a smaller in plane parameter compared to the undoped sample. This result is therefore, consistent with the previous RHEED observation.

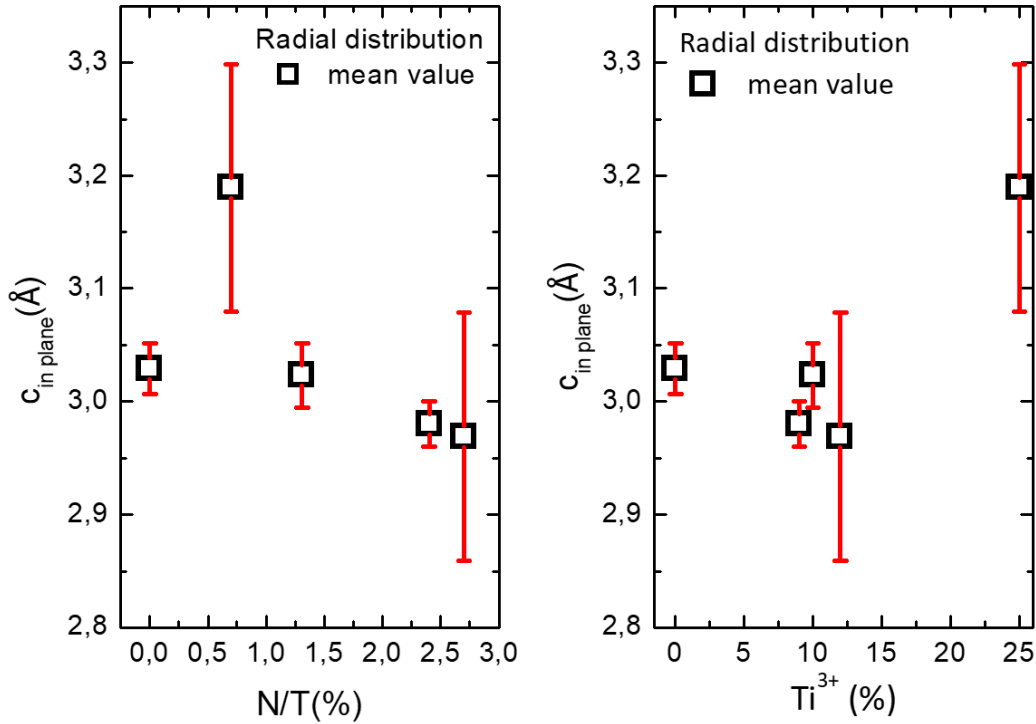


Figure 4.18: Evolution of $c_{\text{in plane}}$ lattice parameter as a function of the N/Ti(%) and the Ti^{3+} ratio and content in the films. In red, their corresponding error bars.

Sample	R_{factor}	$O_{\text{equatorial}}$	O_{axial}	Ti	α (%)	β (%)
Bulk rutile	--	1.98	1.95	2.96	--	--
TiO_2	0.188	1.943	1.941	3.029	2.03	-6.13
N- TiO_2 Rutile (I-H- K_e -O)	0.212	1.971	1.975	3.189	7.42	-15.5
N- TiO_2 Rutile (I-L- K_e)	0.165	1.975	1.940	3.023	1.53	-4.68
N- TiO_2 Rutile (I-H- K_e)	0.151	1.935	1.959	2.980	0.36	-3.1
N- TiO_2 Rutile (A)	0.1645	2.004	1.964	2.969	1.76	-5.28

Table 6: Structural parameters deduced from EXAFS experiment.

The incorporation of nitrogen in TiO_2 results in the creation of Ti^{3+} impurities and/or oxygen vacancies, which introduce lattice distortion in the material. This lattice distortion can have thus, significant implications for the optical absorption capability of the materials.

4.3.5 Influence of Ti^{3+} species, oxygen vacancies and nitrogen content on the crystal structure

The charge neutrality and the protection of N- TiO_2 rutile structure resulting from the substitution of divalent oxygen ions with trivalent N ions induce formation of oxygen vacancies, and further formation of Ti^{3+} centers. Furthermore, due to the preparation method, we also have samples with an amount of Ti^{3+} exceeding the amount of N doping (as shown in table 4). In order to gain further insights into the effects of N doping and the Ti^{3+} content, we decided to plot various relevant parameters (such as structural parameters, photocurrent, and the width of the depletion region) as a function of these two parameters.

The surface in plane parameters ($c_{\text{in-plane}}$, $a_{\text{in-plane}}$) have been deduced from the RHEED patterns and their evolution with N/Ti ratio and Ti^{3+} are represented in figure 4.19. The surface in plane parameters does not seem to be correlated with the N content, however the evolution with Ti^{3+} is almost monotoneous (i.e. increase of $a_{\text{in-plane}}$ and decrease of $c_{\text{in-plane}}$).

The figure following the evolution of the lattice in-plane parameters with the N/Ti ratio illustrates that the lattice approaches gradually a saturation at around 2 at.%, *i.e.* the lattice tends to a cubic structure, probably the TiN oxidized structure. On the other hand, the obtained curves as a function of the Ti^{3+} content shows that the lattice in-plane parameters when the Ti^{3+} content increases the lattice undergoes an in-plane dilatation with the $a_{\text{in-plane}}$ parameter and conversely a contraction on the $c_{\text{in-plane}}$.

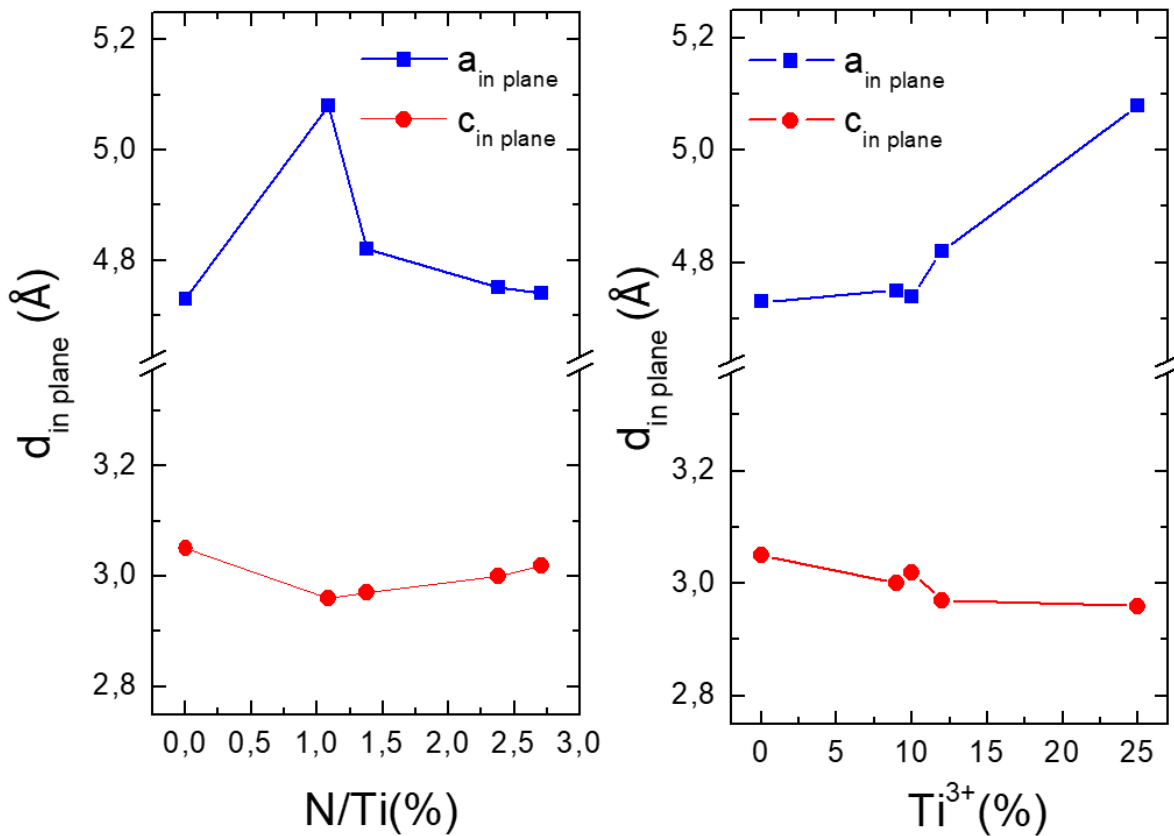


Figure 4.19: Evolution of the $a_{\text{in-plane}}$ (blue squares) the $c_{\text{in-plane}}$ (red circles) lattice parameters of TiO_2 as a function of the N-doping extent and Ti^{3+} ratio.

4.3.5.1 The photocurrent as a function of the N/Ti ratio and the Ti^{3+} content

Based on our experimental data, we have observed an intriguing behavior regarding the influence of the nitrogen content and the Ti^{3+} ratio in nitrogen-doped TiO_2 layers, for solar water splitting performance. In order to explain the high photocurrent we compared the efficiency of the different samples with pure rutile TiO_2 . Interestingly, we found that the photocurrent shows a clear correlation with both N content and Ti^{3+} content (Figure 4.20).

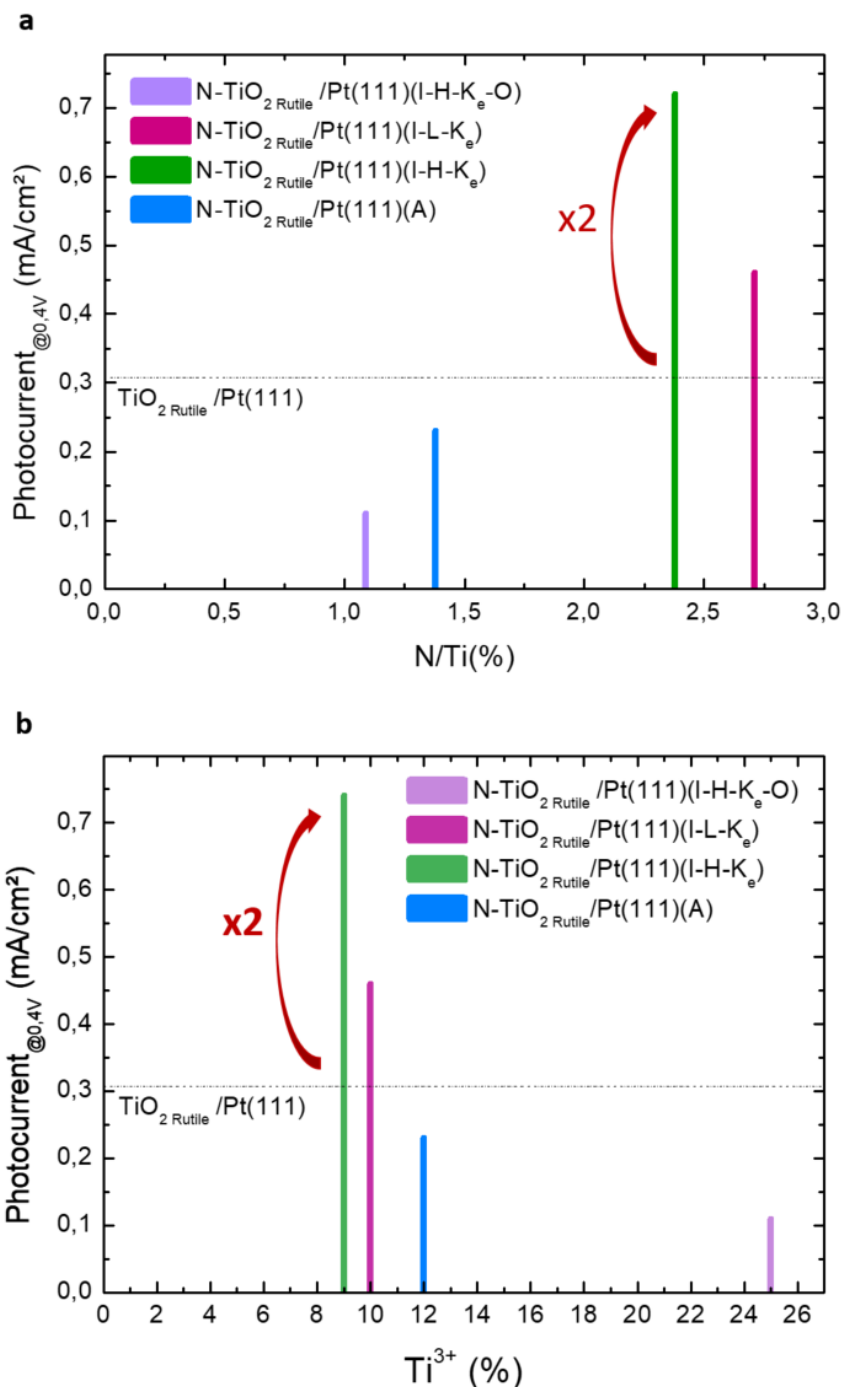


Figure 4.20: Comparison between the photocurrent of undoped (black), N-doped at I-H-Ke-O (purple), N-doped at I-L-Ke (pink), N-doped at I-H-Ke (green) and N-doped at A (blue) conditions of TiO_2 layers deposited on Pt(111) at 0.4V and their respective **a** N/Ti ratio and **b** Ti^{3+} content.

We discovered that to double the efficiency, an optimum N over Ti ratio of 2.38% and a Ti^{3+} content of 9% in the lattice are required. When these values exceed or fall below these optimal values, the photocurrent is reduced. As a matter of fact, the I(V) measurements align well with the absorption

spectra. The trend followed by the photoelectrochemical parameters confirms that this species contributes to the photoactivity of the samples. The photoelectrochemical band gaps showed a distinct pattern when Ti³⁺ content was varied. Below 9% Ti³⁺ content, the band gaps exhibited a narrowing effect, reaching a minimum value of 2.99 eV (see table 6). However, as Ti³⁺ content continued to increase beyond this point, the band gaps started to widen again.

This change in band gap behavior is also noticeable in the films spectral responses. At lower Ti³⁺ concentrations, the narrower band gaps allowed the material to absorb a broader range of wavelengths, resulting in more efficient light absorption. This widening of the range of 'efficient absorption' contributed to improved photoelectrochemical performance.

4.3.5.2 The width of the depletion zone

At the semiconductor/electrolyte interface, a depletion region is formed (see chapter 2). The shape of this depletion zone (W) depends on carrier concentration (N_D), flat band (V_{fb}), and applied potential (V) via the formula:

$$W(V) = \sqrt{\frac{2\epsilon_r\epsilon_0}{eN_D}}(V - V_{fb})$$

In our samples, nitrogen doping and Ti³⁺ doping in TiO₂ can affect the distribution and concentration of charge carriers that influences the width of the depletion zone with Ti³⁺ content.

Figure 4.21 displays the results of the study examining the relationship between the width of the depletion zone, the photocurrent, and the content of nitrogen and Ti³⁺ species in the film at a specific potential of 0.4 V vs Ag/AgCl.

Except for the peculiar data point at 1.38% nitrogen and 10% Ti³⁺ content, the width of the depletion zone reaches its maximum value at 11% Ti³⁺ content equivalent to 2.58% in nitrogen doping level. At this Ti³⁺ concentration, the width of the depletion zone is 6 nm, which corresponds to 60% of the film's thickness. Interestingly, for undoped TiO₂, the width of the depletion zone is only 1 nm, representing 10% of the sample's thickness.

The width of the depletion zone in the N-TiO₂ film plays a crucial role in the photocurrent generation and overall efficiency of charge carrier collection. A wider depletion zone provides a larger region

for the separation and collection of electron-hole pairs generated under illumination, leading to an increased photocurrent.

Moreover, the presence of vacancies in the material can contribute to an increased rate of carrier recombination near the edges of the depletion region. When a charge carrier is created outside the depletion layer, there is no electrical field to induce separation, leading to an increased likelihood of recombination. This recombination process further diminishes the number of carriers available for collection, ultimately reducing the photocurrent.

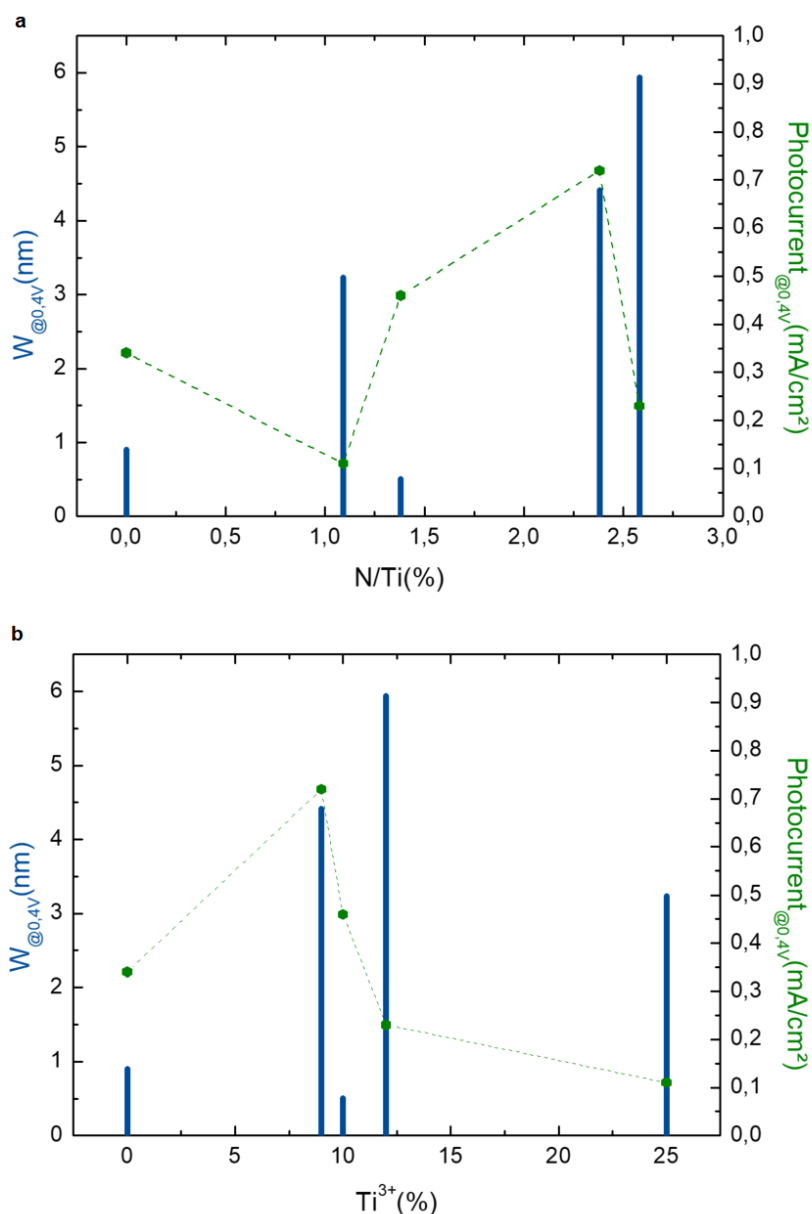


Figure 4.21: Evolution of the depletion width and the photocurrent both at 0.4 V vs Ag/AgCl as a function of the N/Ti ratio and Ti^{3+} contents on the films.

In the case of our films, the flat-band varies with the nitriding conditions, indicating a significant potential energy difference between the bulk of the material and its surface. It suggests an accumulation of electrons near the semiconductor surface. The presence of an electric field, can affect the transport and collection of photo-generated charge carriers. This, in turn, can influence the overall photocurrent of the photoelectrode. Figure 4.22 shows that there is an optimal range for the flat-band potential, between -1.2 eV and -1.5 eV.

The width of the depletion zone, the charge concentration, the flat band, and the photocurrent in a photoanode are correlated. Balancing the effects of nitrogen doping and oxygen vacancies is necessary for optimizing the performance of the material (Figure 4.22).

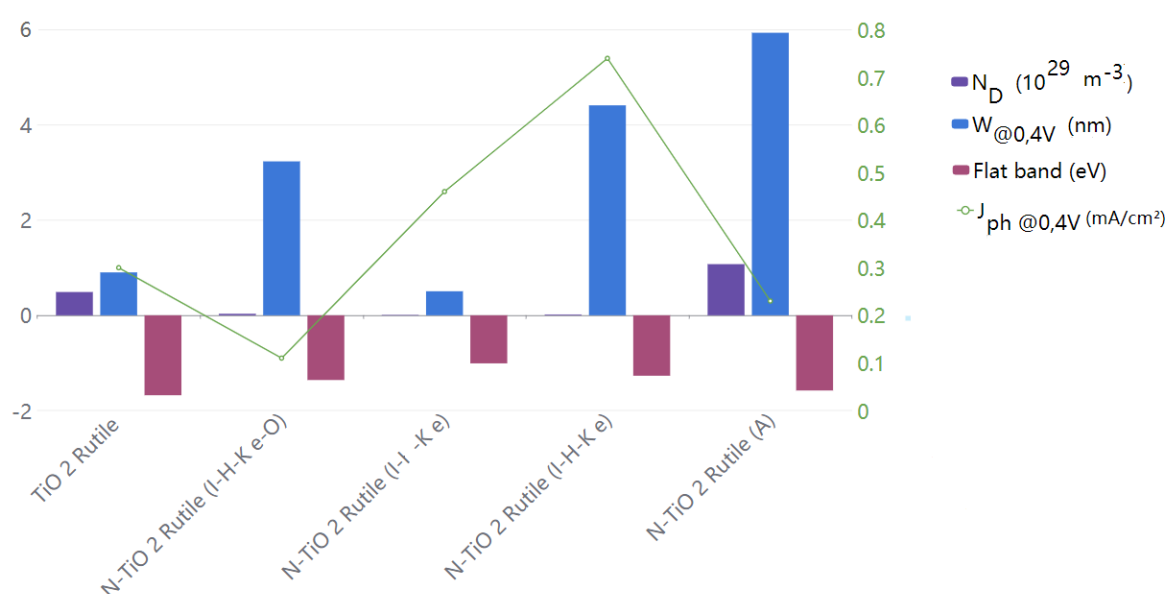


Figure 4.22: Electronic parameters of each sample and their resulted photocurrent.

4.3.5.3 Discussion and conclusions

The highest photocurrent is obtained for the sample grown under high kinetic energies (I-H-K_e) nitriding conditions, with a Ti³⁺ concentration of 9% (~2.38% N/Ti). Compared to undoped TiO₂, the photocurrent is multiplied by 2, and the effective bandgap is reduced from 3.05 eV to 2.99 eV, indicating better absorption of visible light. This significant photocurrent enhancement is attributed to the presence of Ti³⁺ rather than to the nitrogen concentration, with an optimum of Ti³⁺ content of around 9%. The presence of Ti³⁺ allows an increase of the depletion zone thickness, up to 50% of the total film thickness. However, excessively high Ti³⁺ concentrations have detrimental effects and will

ultimately induce a phase change. Somehow, the modifications occurring in the sample due to N doping appear as more important than the band gap reduction effect due to the N doping.

Extension of the light absorption from the ultraviolet (UV) region to the visible-light region may arise from the N-2*p* levels near the valence band and from the active sites induced by the oxygen vacancies and thus, the Ti³⁺ species.

Interestingly, we find that there is a maximum amount of nitrogen that can be incorporated into a sample. It may be determined by the presence of oxygen vacancies and Ti³⁺ content. Therefore, the presence and control of oxygen vacancies are crucial factors in determining the optimal nitrogen doping conditions for achieving best properties in TiO₂-based materials [50-Okato 2005].

Eventually, to compare the samples, it is more appropriate to focus on the concentration of Ti³⁺ rather than the doping N level.

4.4.6 Influence of the growth temperature: N-doped TiO₂ single layer on Pt (111)

4.4.6.1 Crystalline characterization

To investigate the effect of the temperature, we studied the growth, by O&NPA-MBE, of a film synthesized under I-L-K_e conditions with a substrate held at 550°C rather than 450°C. The growth process was monitored in situ by RHEED (see figure 4.23).

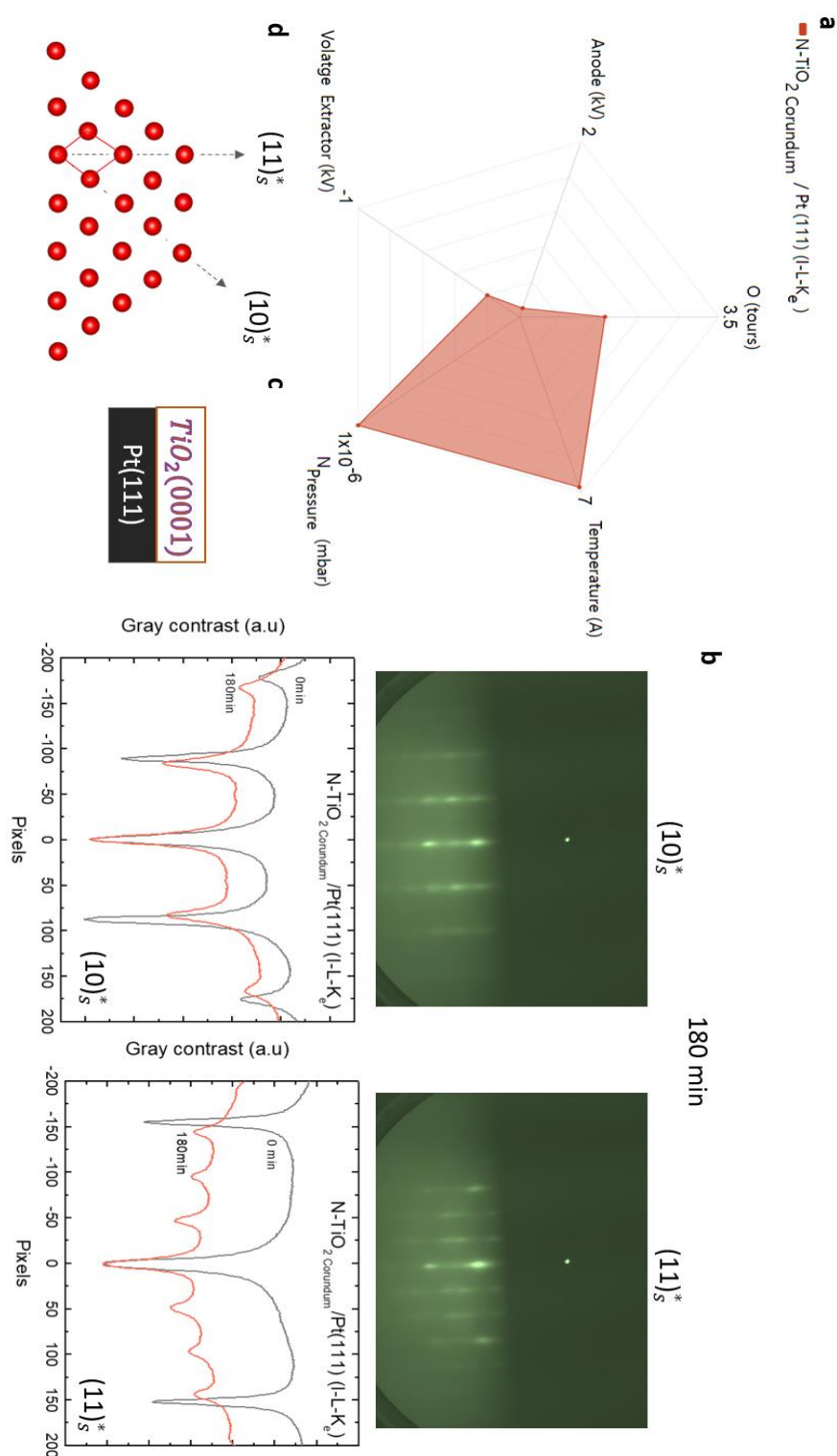


Figure 4.23: **a** Growth condition parameters for the synthesis of corundum $\text{N-TiO}_2/\text{Pt}(111)$ **b** RHEED patterns along two particular azimuths the $(10)_s^*$ and the $(11)_s^*$ with the corresponding integrated profiles at 0 and 180 min. **c** a scheme of the film deposited Pt (111). **d** corresponding surface reciprocal lattices, the elementary cell (in the reciprocal space) is also shown red square.

By comparing figures 4.23b and 4.6, it is clear that the crystallographic structure of TiO₂ is different. This is even clearer on the integrated profiles of the RHEED patterns (figure 4.23b). The disappearance of the lines specific to rutile TiO₂ and the appearance of a different integrated profile instead of the expected rutile phase suggest that the film undergoes a transition to a different crystal structure, which is identified as corundum Ti₂O₃. It is similar to Fe₂O₃/Pt(111) reported earlier [80-Magnan 2012]. Corundum refers to a crystal structure characterized by a hexagonal close-packed arrangement of oxygen ions with metal ions occupying the interstitial sites.

4.3.6.2 Investigation of the right crystallographic structure: EXAFS measurement

To support this observation EXAFS spectra were recorded in normal and grazing incidences at room temperature, on the SAMBA beamline at synchrotron SOLEIL. EXAFS data were analyzed according to the approach detailed in 3.3.2. Figure 4.24 gives the experimental $k^3\chi(k)$ EXAFS oscillations spectra for N-TiO₂ corundum. In an attempt to analyze the EXAFS spectra of our TiO₂ film, two models were employed: a corundum structure and a rutile structure. The fitting results, depicted in figure 4.28 and the parameter of fit indicated in table 7, reveal that the quality of fit was not satisfactory. However, both models could adequately describe the observed structure.

Although, RHEED patterns clearly indicate the presence of a corundum-like structure strengthening this interpretation.

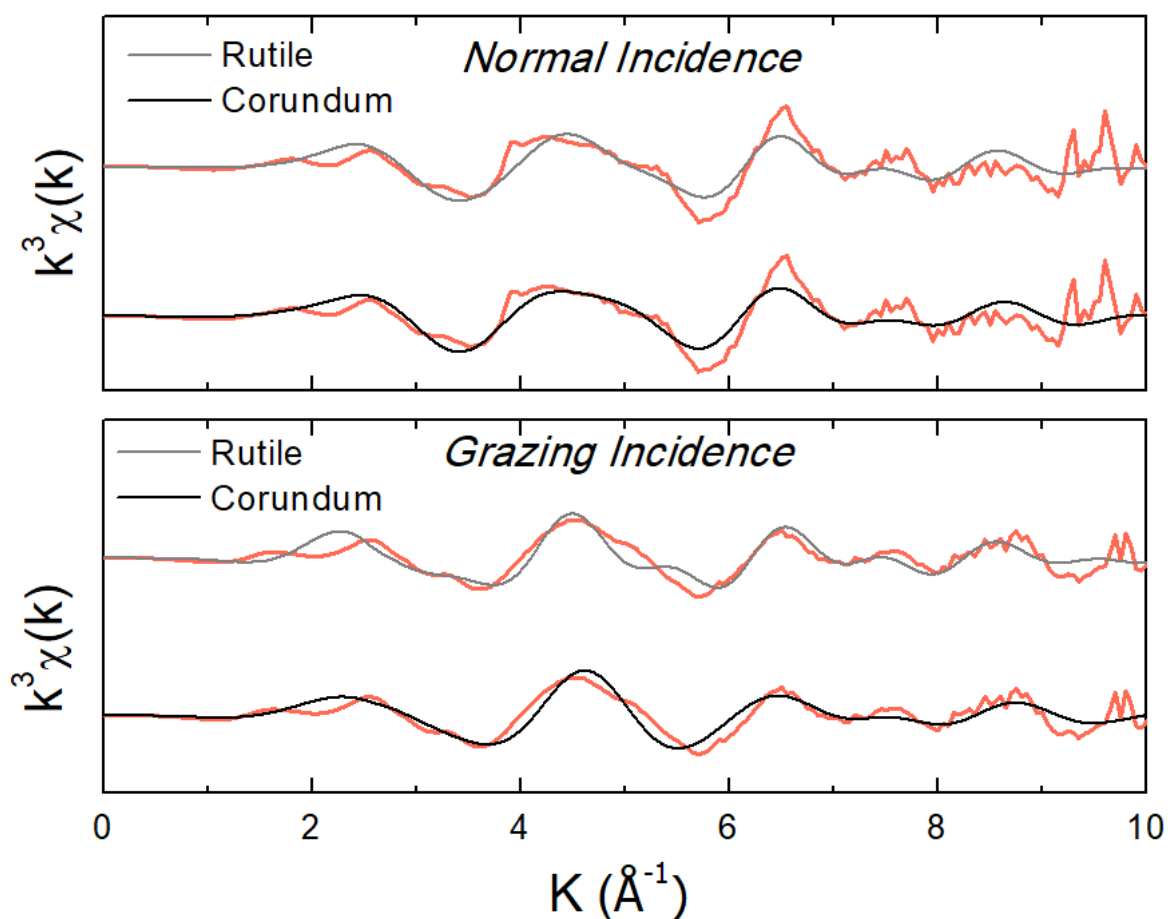


Figure 4.24: Raw (salmon lines) Ti K-edge $k^3\chi(k)$ EXAFS data N-TiO_2 Corundum/ $\text{Pt}(111)$ (I-L- K_e) in normal incidence (upper panel) and in grazing incidence (bottom panel) and fit of the data by FEFF calculation assuming the rutile (100) structure with the bulk lattice parameter (gray lines) and corundum (0001) with the bulk lattice parameter (black lines), with parameters indicated in Table 7 (best fit, black line).

The XANES and the pre-edge regions for the N-TiO_2 Corundum (I-L- K_e), are compared with undoped TiO_2 and N-TiO_2 rutile (I-H- K_e) on figure 4.25. The overall XANES shapes are different, meaning that the synthesis at 550°C modifies the oxynitride structure and the overall titanium valence state.

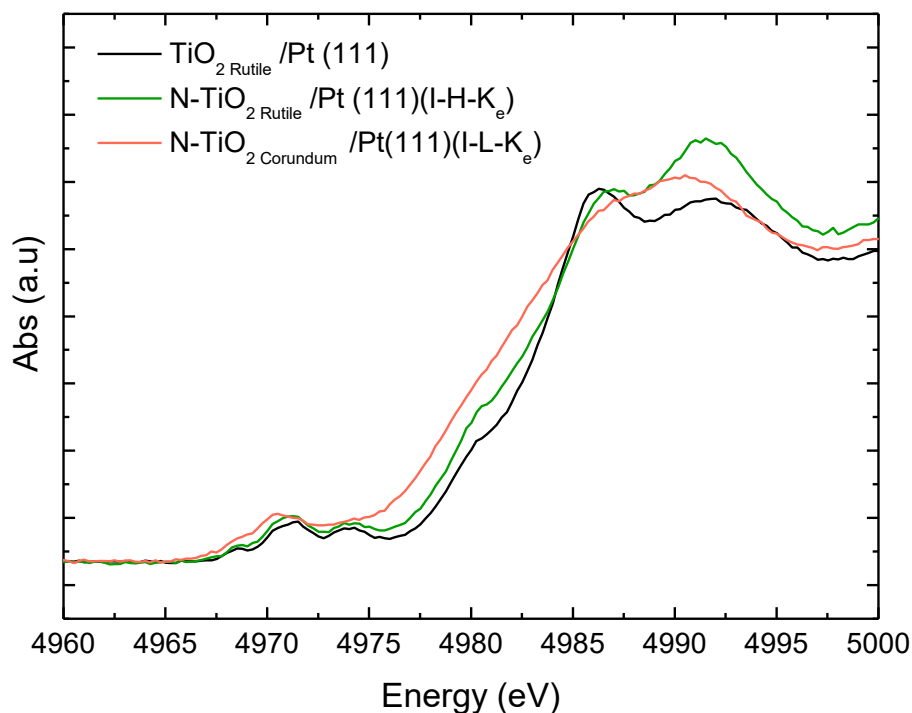


Figure 4.25: Experimental XANES spectra of three films; TiO_2 Rutile, N-TiO_2 at $I-H-K_e$ deposited at 450°C and N-TiO_2 at $I-L-K_e$ nitriding conditions deposited at 550°C , all samples are deposited on Pt (111).

As a comparison with the undoped TiO_2 film, we can see a shift of the XANES spectra toward lower photon energies of about 0.7eV for the N-TiO_2 Rutile and an even larger one for the N-TiO_2 Corundum (1.8eV). This result evidence that the valence state of titanium is not only Ti^{4+} , but also a mix of Ti^{4+} and Ti^{3+} , which is consistent with the XPS observations of the last section.

Sample	R_{factor}	$O_{\text{equatorial}}$	O_{axial}	Ti	α (%)	β (%)
Rutile	0.307	1.970	2.001	3.149	+0.3	-3.1
Corundum	0.324	1.977	2.013	2.705	+2	-6.1

Table 7: Structural Parameters (Distance, Dilatation Factors) obtained by EXAFS for N-TiO_2 at $I-L-K_e$ nitriding conditions deposited on Pt (111) at 550°C using rutile (100) and corundum (0001) structures.

4.3.6.3 Electronic environment

XPS spectra recorded on N- TiO_2 corundum are shown in figure 4.26. The Ti^{3+} feature, *i.e.* shoulder among the Ti^{4+} peak ($\sim 457\text{eV}$) is clearly more important in the N- TiO_2 corundum than in the N- TiO_2 rutile. We estimate at 28% the Ti^{3+} ratio content in the film. Moreover, a second shoulder peak appears at $\sim 455\text{eV}$ and is attributed to a Ti^{2+} contribution. From another side, the elevated temperature may enhance the desorption of nitrogen atoms from the film, resulting in a reduction in the nitrogen doping level at 2.46% and the XPS spectra, is now composed of only interstitial component (399eV). From the valence band spectrum, we can deduce the valence band edge: 2.14eV .

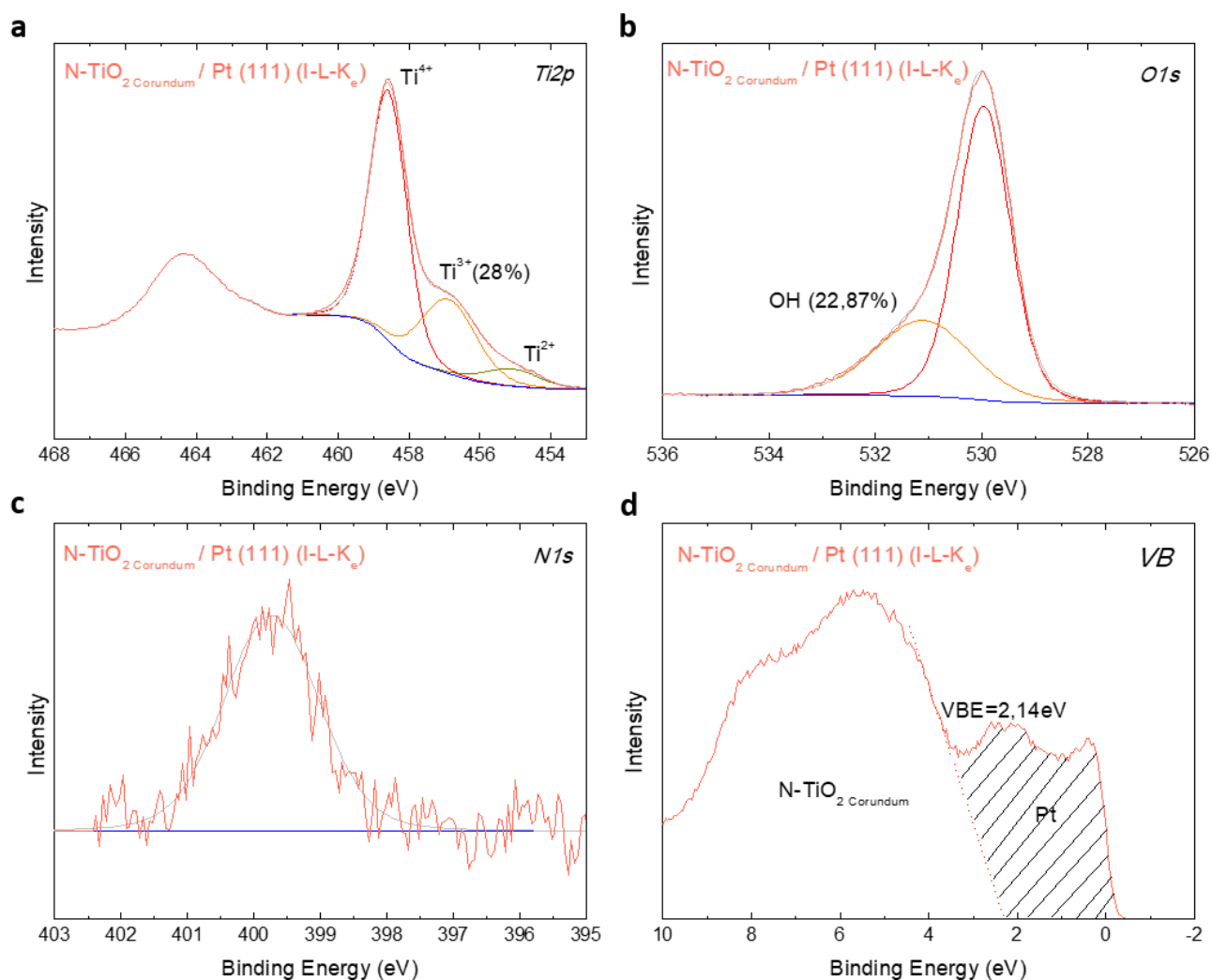


Figure 4.26: **a** $\text{Ti} 2p$, **b** $\text{O} 1s$, **c** $\text{N} 1s$, and **d** VB XPS spectra of nitrogen doped TiO_2 corundum phase deposited on Pt (111)

4.3.6.4 Photoelectrochemical properties

Photocurrent results are represented in figure 4.27 considering the concentration of Ti^{3+} centers in all synthesized samples. The optimal oxygen vacancies concentration (9%) from the photocurrent point of view is reached for a temperature of 450°C for which the photocurrent is almost multiplied by two with respect to the pure r- TiO_2 sample. For a higher growth temperature the photocurrent decreases, which can be explained by a too large Ti^{3+} concentration which lowers the photocurrent (in the same way than we noticed previously in 4.20) by introducing recombination centers in the structure.

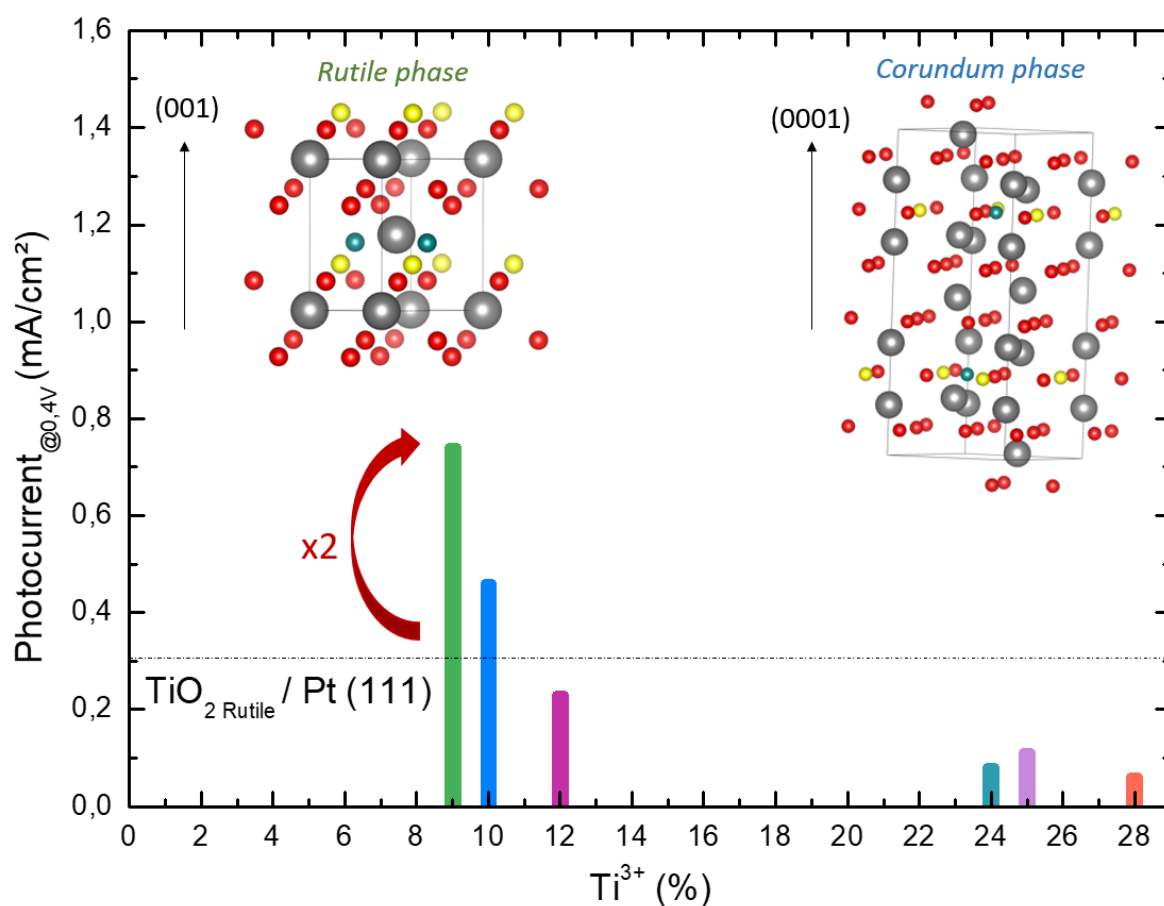


Figure 4.27: Photocurrent density at 0.4V for as a function of the content of Ti^{3+} in the lattice of studied samples

4.3.6.5 Discussion and conclusion

At high growth temperatures, a corundum-like Ti_2O_3 crystal phase is identified by RHEED suggesting the presence of the corundum Ti_2O_3 phase, which contain solely Ti^{3+} ions. However, XPS analysis shows that the majority of titanium ions have a valence state of Ti^{4+} (~69%). Additionally, the shift in the Ti_{2p} edge with respect to TiO_2 is 1.8eV, which is lower than the value observed for pure Ti_2O_3

(3eV) [81-Leitzke 2018]. Based on these findings, it is believed that the actual crystal structure is likely a combination or mixing of rutile and Ti_2O_3 rather than a pure corundum Ti_2O_3 phase.

However, for our specific purpose to improve solar water splitting the pure rutile phase is the more adequate. Moreover, operating at excessively high temperature of growth can lead to additional issues. The elevated temperatures may enhance the desorption of nitrogen atoms from the film, resulting in a reduction in the nitrogen doping level. This can negatively affect the desired properties and performance of the film.

Hence, to achieve the desired nitrogen doping level while maintaining the rutile phase, it is recommended to work at a temperature not higher than 450°C .

4.4.7 Influence of water reaction

In order to get insight in the role of the surface chemistry of our samples we exposed the three samples (undoped TiO_2 , N- TiO_2 rutile at I-H- K_e , and N- TiO_2 corundum at I-L- K_e) to a plasma oxygen cleaning treatment (60 minutes at 350°C under O plasma at 1.5tr), the photocurrent was measured once again in the PEC cell. After this oxidizing treatment, the results of the photocurrent measurements before and after the treatment are displayed in figure 4.28. For the three samples, a strong modification of the photocurrent compared to the initial experiment is obtained.

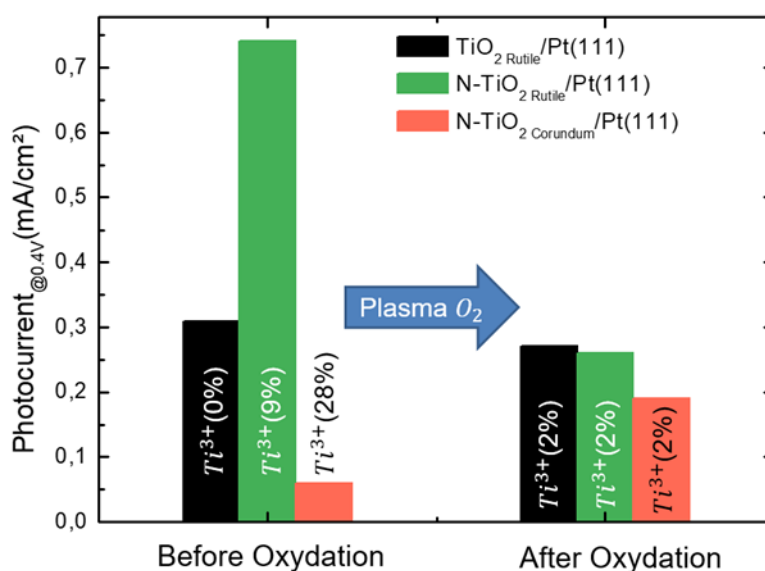


Figure 4.28: Evolution of the photocurrent at 0.4V vs Ag/AgCl before and after plasma O_2 cleaning process of doped and undoped films.

Furthermore, the concentration of Ti^{3+} species obtained from the Ti-2p core levels analysis for each sample has been evaluated and an equalization of this ratio (at 2%) is observed at the surface of each

film after the plasma treatment (as shown in figure 4.29). Therefore, the plasma treatment has reoxidized the reduced surfaces. The N doped surfaces now exhibit similar behavior to that of pure rutile TiO₂, which is the most stable film under the treatment conditions.

Additionally, our results demonstrate the importance of the surface state of the photoanode with respect to oxidation.

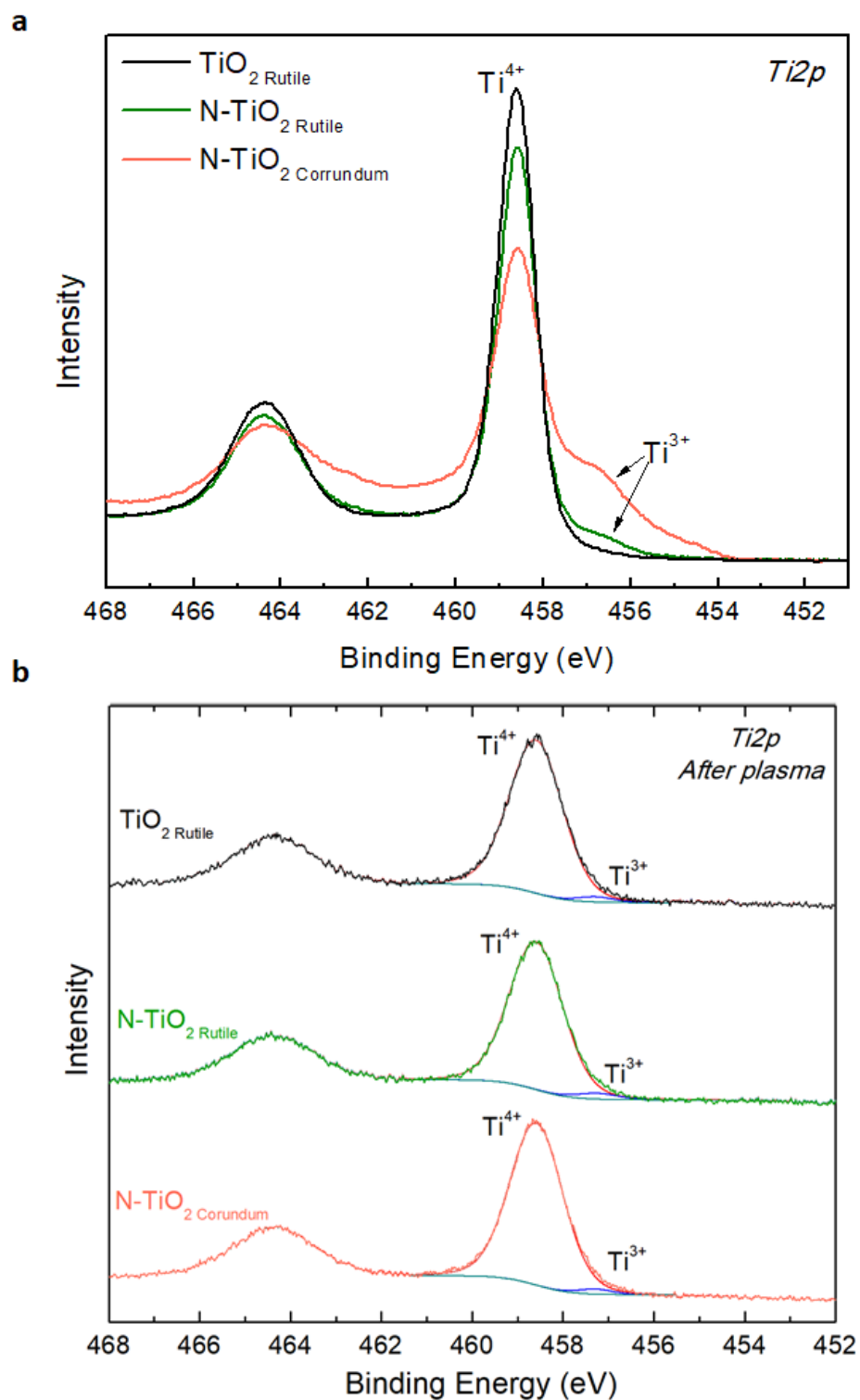


Figure 4.29: Comparison of the evolution of the Ti^{3+} contribution in the Ti-2p core levels before and after plasma O_2 cleaning process of doped and undoped films.

These findings highlight the significant impact of the plasma oxygen cleaning treatment on the surface properties and photocurrent behavior of the TiO_2 films. In order to further analyze these oxidized

samples, we choose to study their electronic structure after reaction with water (in dark and under light).

4.3.7.1 Experimental set-up of the reactor

Water plays an obvious and important role in the development and performance of photoanodes for solar water splitting. The stability and corrosion resistance of the photoanode material in the presence of water are crucial for long-term performance. Some materials may undergo corrosion or degradation in the presence of water, leading to reduced efficiency and durability of the photoanode. Therefore, in our lab we build up a reactor connected to the UHV set-up. In this reactor, it is possible to deposit a pure liquid water drop on the sample surface, in dark or under a light source (a 405 nm LED) (as shown figure 4.30). The drop is then evaporated (in dark or under light), and when no water is seen anymore on the surface, the sample is transferred *in situ* in the XPS chamber to investigate the electronic structure. Therefore, this set-up allows to study the *post mortem* surface after water deposition

The experimental protocol consists of the following steps, repeated for each sample: After completing each step, an XPS measurement is conducted.

- Cleaning with plasma: The sample is subjected to a cleaning process using plasma.
- Deposition of one pure drop of water: A single pure drop of water is deposited onto the sample surface.
- Cleaning with plasma: Following the water deposition, another round of cleaning with plasma is performed.
- Deposition of one pure drop of water under light: After the second plasma cleaning, a fresh pure drop of water is deposited on the sample surface, but this time it is done under the presence of light.
- Deposition of one pure drop of water under light (without cleaning): This step is performed on only one sample.

4.3.7.2 Model used for *post mortem* surface

XPS is used to measure the adsorption of both molecular water (H_2O) and dissociated water (OH) on the *post mortem* surfaces, by analyzing the changes in the O-1s spectra. We took example of the Anderson *et al.* model developed to calculate changes in the thickness of the oxide (Ox) and hydroxyl (OH) layers based on the intensity ratios of OH/Ox obtained from *in situ* O-1s spectra [82-Anderson 1965]. This model is briefly depicted in figure 4.30.

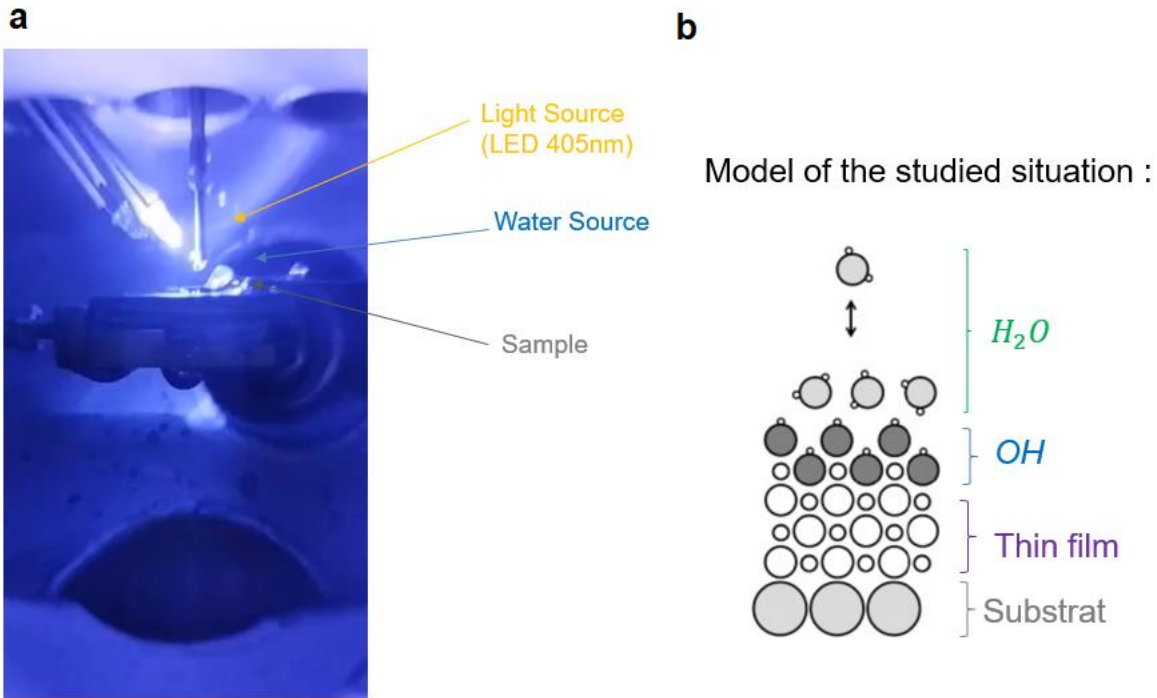


Figure 4.30: **a** picture of the reactor set-up. **b** simplified scheme of the model studied

In this model (figure 4.30b), the system is represented as a series of separated and homogeneous layers stacked on top of each other. A thin film covered of hydroxyls (OH) followed by layers of adsorbed water (H₂O).

The thickness of the OH layer (t_{OH}) and the H₂O layer (t_{H_2O}) is calculated using the following equations theorized by Aschaffenburg *et al.* [83- Aschaffenburg 2020]:

Equation (1):

$$t_{OH} = \lambda_{OH} \ln \left[1 + \frac{I_{OH}}{I_{Ox}} \left(\frac{\lambda_{Ox} N_{Ox}}{\lambda_{OH} N_{OH}} \right) \right]$$

Equation (2):

$$t_{H_2O} = \lambda_{H_2O} \ln \left[1 + \frac{I_{H_2O}}{I_{OH}} \left(\frac{\lambda_{OH} N_{OH}}{\lambda_{H_2O} N_{H_2O}} \right) \left(1 - e^{-\frac{t_{OH}}{\lambda_{OH}}} \right) \right]$$

In these equations, λ_{OH} and λ_{H_2O} represent the inelastic mean free path, N is the density of oxygen for the respective layers (OH, Ox, or H₂O) and I is the XPS intensity (for example I_{OH} is the intensity of the hydroxyl layer). The model assumes however, a uniform distribution of layers. It does not take into account surface morphology, surface termination, or the presence of isolated pockets or islands.

In the model, N_{OH} is assumed to be equal to the volume density of lattice oxygen in the sample, which is 46 nm⁻³. Similarly, for the H₂O layer, the number density N_{H₂O} can be directly determined from the bulk density, which is 33 nm⁻³.

In the case of the OH layer, the situation becomes more complex as there is Ti(OH)₄ formed at the surface, but its density was unknown. One assumption is that the density of the OH layer on the (100) surface is the same than the density on the (110) surface. In their reports Predota *et al.* and Zhang *et al.*, studied water on rutile (110) and demonstrate that the first water layer is located 3.8 Å above the surface, below which there is one monolayer of hydroxide. Assuming that we estimated N_{OH} = 46 nm⁻³ [84-Predota 2004, 85-zhang 2004].

4.3.7.3 Results and discussion

Figure 4.31 presents an example of the fitting results of the samples analyzed *post mortem* using XPS after undergoing various conditions.

The main peak corresponds to bulk oxygen (Ox) in the TiO₂ lattice and is used as a reference for binding energy (BE). The asymmetry in the Ox peak is fitted with an additional peak assigned at Ox+1.1 eV for every sample and is considered as surface OH. The adsorption of OH is present even after plasma treatment and increases under both water and light. After a drop of water, another peak emerges, assigned at 2.4+Ox eV, which is consistent with the presence of adsorbed molecular water. The intensities of both OH and H₂O peaks decrease after plasma cleaning and raise after water only, under both water and illumination.

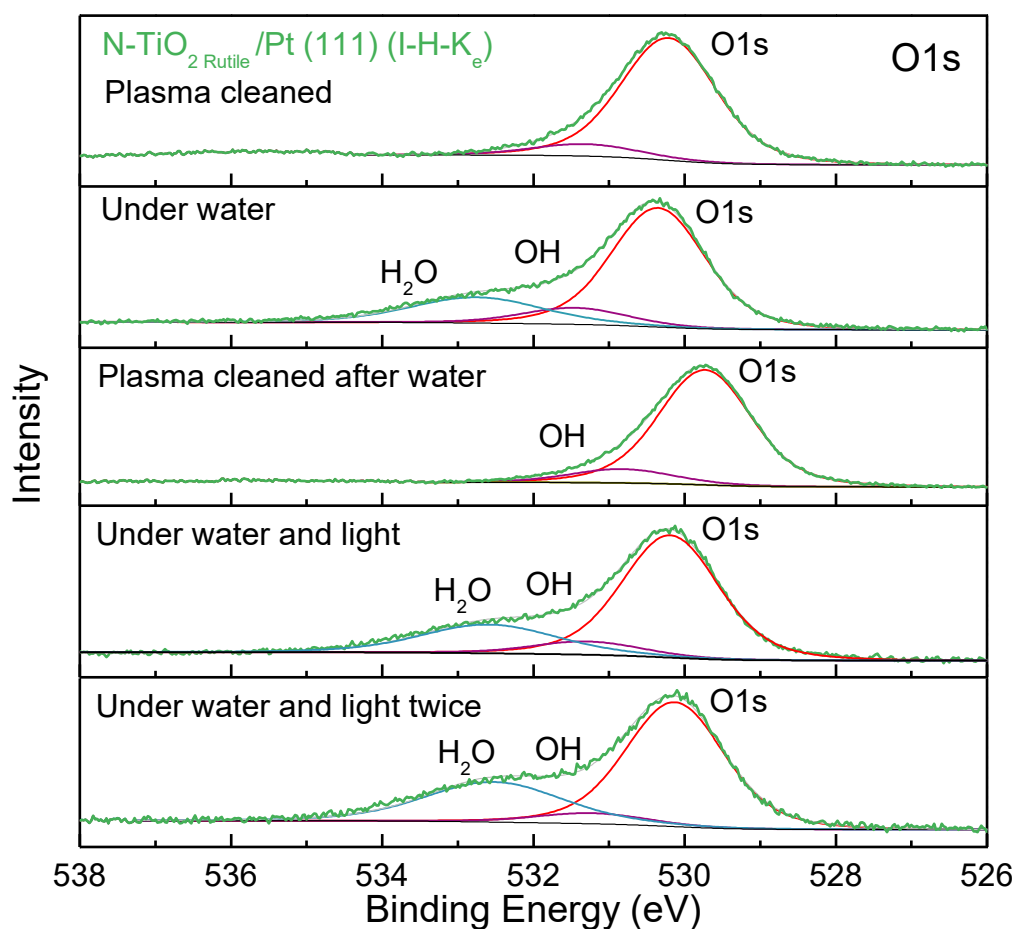
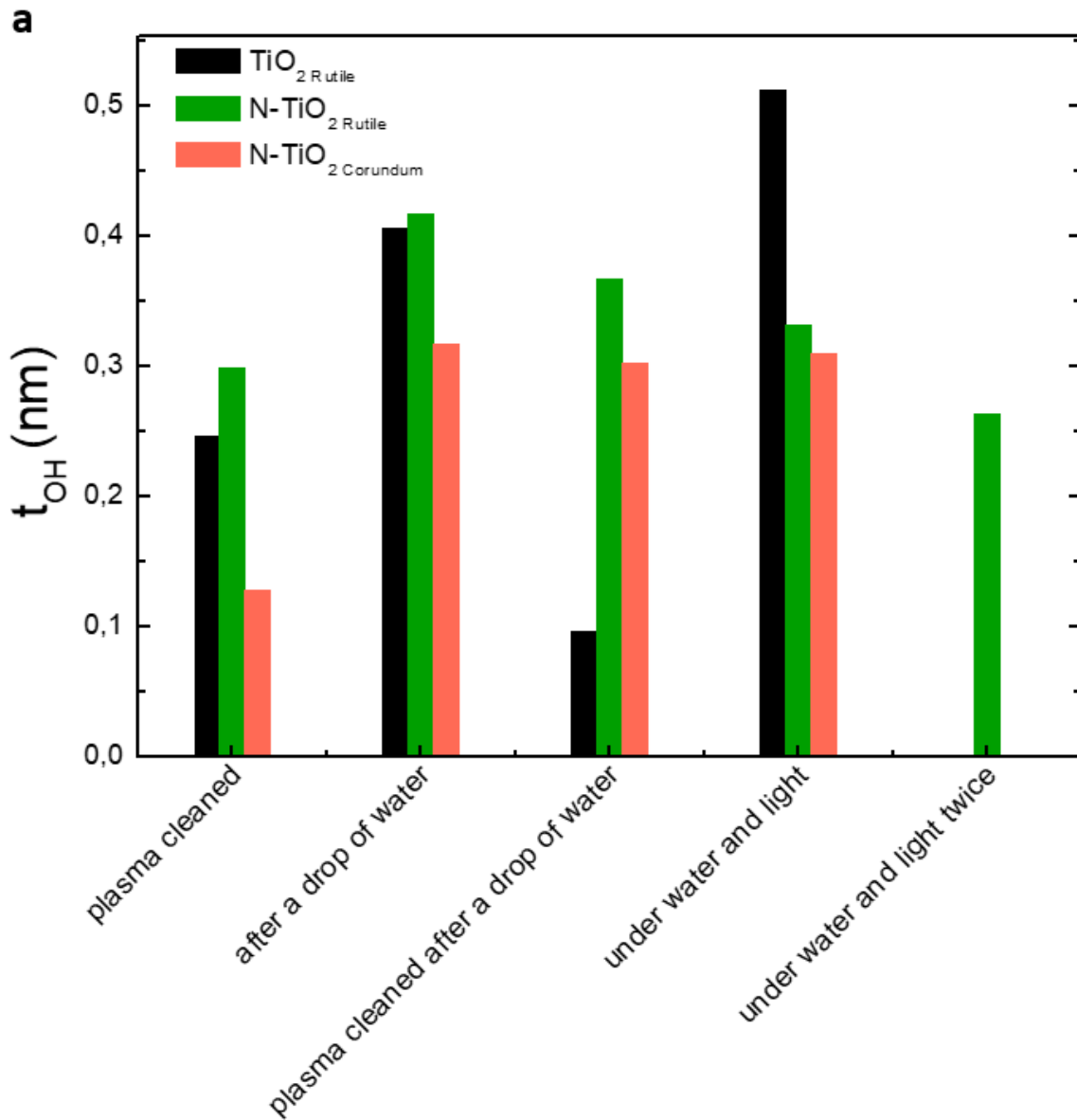


Figure 4.31: Examples of O1s XPS fitting for N-TiO_2 Rutile / Pt (111) (I-H-Ke) at select situation. The color-coding is as follows: Ox, (red); OH, (purple); H₂O, (blue); raw data, green lines; background black lines and envelopes, gray lines.

This model does not include an oxygen-containing carbon species; specifically carbonate (CO_3) would have been possible. Previous studies have assigned oxygen-containing carbonate species to a binding energy at ~ 532.7 eV. The content of carbon has been determined by the intensity of C-1s with respect to the O and is indicated on table 8. The C1s/O1s ratio is almost equivalent for each surfaces containing water. Its effect is thus, expected to be the same for all samples.

Sample: N-TiO_2 Rutile (I-H- K_e)	C1s/O1s
Plasma cleaned	14.43
Under a drop of water	30.55
Plasma cleaned after water	7.01
Under water and light	31.25
Under water and light twice	39.94

Table 8: Evolution of the C1s/O1s ratio and the FWHM of the Ox peak under every situation



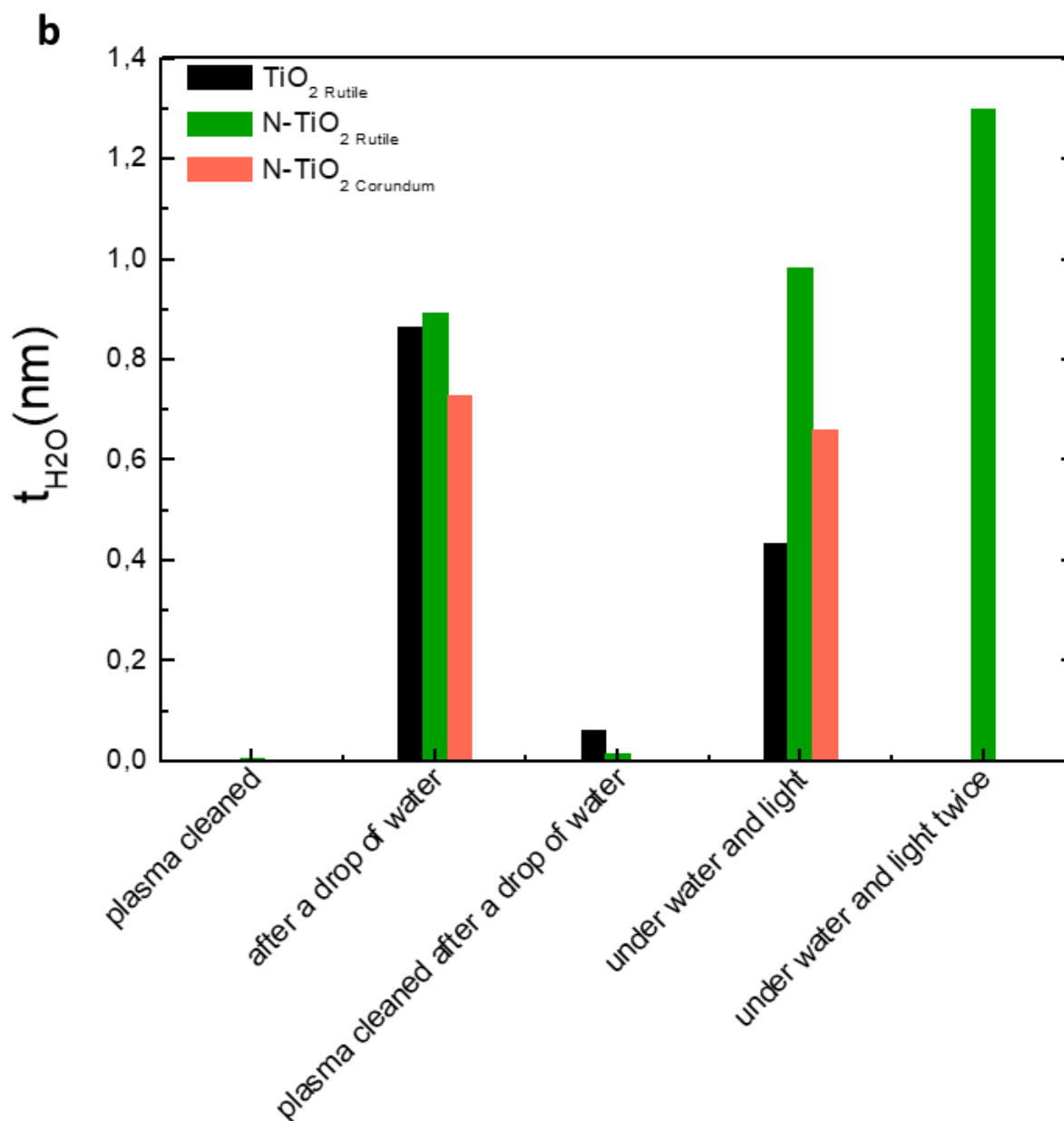


Figure 4.32: **a** Thickness of monolayers OH and **b** H₂O of three films ; undoped TiO₂, N-TiO₂ Rutile at I-H-K_e conditions and N-TiO₂ corundum at I-L-K_e deposited on Pt (111) as a function of each situation; plasma cleaned, under water, cleaned again and under water light on and two times. The values are the cumulative result of the fitting analysis from the three experiments. The data are analyzed by the multilayer model.

Figure 4.32 presents the results of the multilayer model, indicating that even in UHV conditions, in the absence of water and after plasma cleaning; a thin layer of hydroxyl is still present on the surface of the samples. After cleaning, the OH layer appears to be thicker in N-TiO₂ rutile phase compared to the other films. This hydroxyl layer appears to be even harder to remove by plasma oxygen in case

of nitrogen-doped samples. However, by comparing with the other samples, the corundum surface exhibits lower water absorption.

In contrast to the photocurrent results in figure 4.27, these films display different behaviors when exposed to water alone or water and light simultaneously. Although the three films have almost the same thickness of water when a drop is deposited in dark, the thickness is different when the drop is deposited with light. We note, that the films have now the same photocurrent (see figure 4.26). Despite having similar oxidized surfaces after plasma treatment, the volume properties associated with doping and crystallographic structure remain unchanged.

Furthermore, it is obvious that the N- TiO_2 rutile phase exhibits the highest hydrophilicity among the TiO_2 surfaces. The absorption of water by the TiO_2 films is influenced by light (see figure 4.32a). When the doped surfaces are illuminated, they become more hydrophilic, indicating that light enhances the interaction between water molecules and the film surface. Notably, the presence of nitrogen in the bulk of the film enhances light absorption, particularly in the visible range and at a wavelength of 405 nm, making light-induced modulation more effective for water absorption.

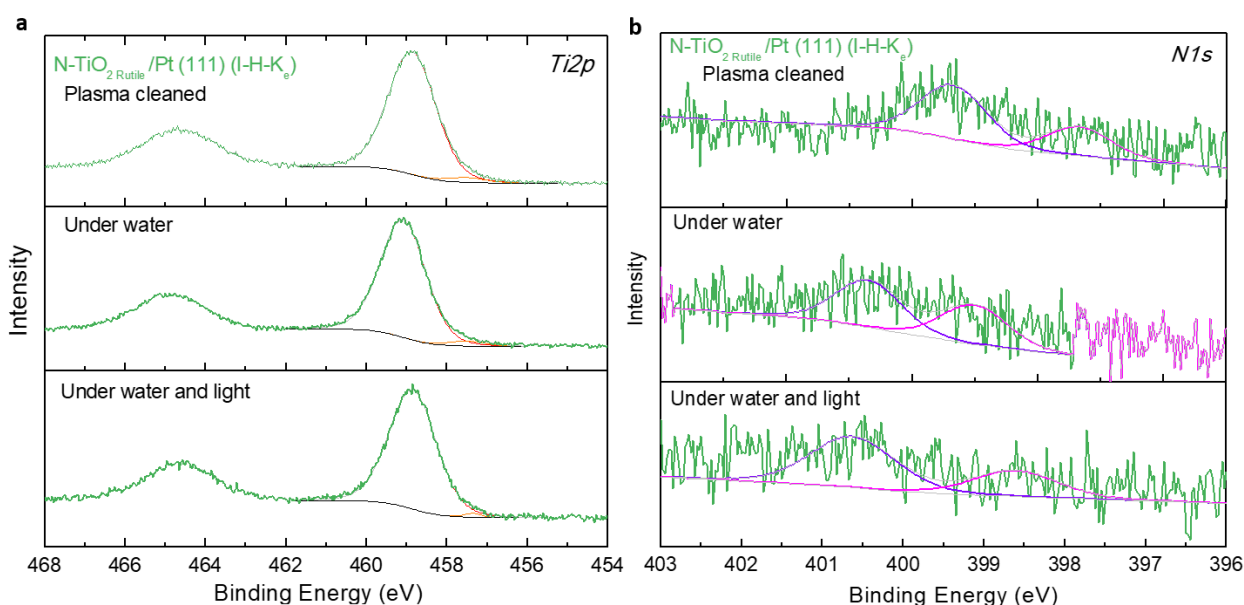


Figure 4.33: $\text{Ti}2p$ and $\text{N}1s$ core levels of N- TiO_2 Rutile /Pt (111) (I-H- K_e) during the reactivity with water and light study

Although, based on the results obtained from the measurement of $\text{Ti}2p$ and $\text{N}1s$ core levels in each material under the different conditions during the reactivity study under water and light. It can be concluded that no significant changes were observed in the electronic structure of Ti and N during the water reaction process (see figure 4.33).

In summary, the plasma oxygen cleaning treatment led to surface oxidation, causing the surfaces to exhibit similar behavior. The primary factor influencing the photocurrent was found to be the surface concentration of Ti³⁺, rather than the volume properties associated with doping or the crystallographic structure of the samples. Therefore, the objective was to optimize N-TiO₂ rutile thin films with an appropriate Ti³⁺ concentration of 9% without the need for reoxidation, in order to achieve the highest photocurrent. Moreover, light was observed to modulate water absorption by increasing the hydrophilicity of the surfaces.

4.4 General summary

In this chapter, at the same growth temperature, pure and nitrogen doped TiO₂ were found to have the same rutile (100) crystallographic structure. However, in the Ti-2p core level XPS spectra of the N doped samples, the presence of the Ti³⁺ feature induced by the reduction of Ti⁴⁺ into Ti³⁺ is linked to charge balance restoring due to oxygen vacancies. Such single crystalline samples deposited on non-oxide substrates proved advantageous as model systems, enabling the independent study of the effects of N-doping on the photoelectrochemical properties without the oxygen diffusion from the substrate.

According to the experimental results obtained, the enhancement in photocurrent density is attributed to the contributions of localized nitrogen states and oxygen vacancy (*i.e.* concentration of Ti³⁺ species). Furthermore, this observation enables us to provide a comprehensive understanding of their influences in factors related to the morphology, the crystalline structure, the intrinsic transport properties and the overall photoelectrochemical properties:

-We evidence by EXAFS that N incorporation induces a distortion of the oxygen octahedron without significant structural modifications. Nevertheless, the high content of Ti³⁺ in the material leads to pronounced anisotropy that can affect the properties of the film.

- For N-doping levels outside the optimum range, specifically beyond the optimal 9% Ti³⁺ content (~2.38% N/Ti), we observed similar trends in various photoelectrochemical parameters. The photoelectrochemical band gaps exhibit a narrowing effect when the Ti³⁺ content was below 9%, reaching a minimum value of 2.99 eV before increasing again with further doping. The range of wavelengths for 'efficient absorption' expanded until the Ti³⁺ content exceeded this optimal range. Similarly, the flat bands and the width of the depletion zones showed the same pattern, which causes a larger band bending at the surface. Consequently, the recombination of electron-hole pairs is hindered. This effect can thus contribute to the improvement of photoelectrochemical properties. Nonetheless, at a certain

point, the number of oxygen vacancies can act as recombination centers where charge carriers (electrons and holes) recombine instead of participating in the desired photoelectrochemical reactions.

- In the second set of samples, we observed a phase transition from rutile to corundum at higher temperature. Interestingly, the N doping level remained relatively constant at approximately 2.46% with respect to Ti. However, the Ti³⁺ content increases significantly up to 28%. The higher concentration of Ti³⁺ ions introduces a substantial number of vacancies, leading to an increase in crystallographic defects within the material. The presence of such a high number of vacancies and crystallographic defects has detrimental effects on the material's electrical conductivity. As a result, the photocurrent density of these samples was adversely affected, leading to poorer performance.

-The reactivity study conducted with our reactor setup in UHV conditions, combined with water and controlled light illumination, highlights the stability of the pure TiO₂ rutile configurations compared to doped samples against the plasma oxidation process. Therefore, further investigation focusing on developing the optimal nitrogen doping conditions to enhance the performance of solar water splitting while also aiming to create a stable and water-resistant structure is required.

Nitrogen doping is a very powerful degree of freedom for tuning the electrical properties of TiO₂, as well as its crystallographic structure. However, these results suggest that simply increasing the duration or quantity of nitrogen incorporation may not necessarily lead to the desired effects or improved performance. It seems more important to carefully consider the optimal conditions and parameters for nitrogen doping to achieve an optimal number of Ti³⁺ centers at the surface and thus the desired photoelectrochemical properties.

4.5 References

- [1] Magnan, H., Stanescu, D., Rioult, M., Fonda, E., & Barbier, A. (2019). Epitaxial TiO₂ thin film photoanodes: influence of crystallographic structure and substrate nature. *The Journal of Physical Chemistry C*, 123(9), 5240-5248.
- [2] Zhang YY, Hu HW, Chang ML et al (2017) Non-uniform doping outperforms uniform doping for enhancing the photocatalytic efficiency of Au-doped TiO₂ nanotubes in organic dye degradation. *Ceram Int* 43(12):9053–905
- [3] Wang, Z. S., Kawauchi, H., Kashima, T., & Arakawa, H. (2004). Significant influence of TiO₂ photoelectrode morphology on the energy conversion efficiency of N719 dye-sensitized solar cell. *Coordination chemistry reviews*, 248(13-14), 1381-1389.
- [4] Ahmad, M. S., Pandey, A. K., & Abd Rahim, N. (2017). Advancements in the development of TiO₂ photoanodes and its fabrication methods for dye sensitized solar cell (DSSC) applications. A review. *Renewable and Sustainable Energy Reviews*, 77, 89-108.
- [5] Lindblad, R., Bi, D., Park, B. W., Oscarsson, J., Gorgoi, M., Siegbahn, H., ... & Rensmo, H. (2014). Electronic structure of TiO₂/CH₃NH₃PbI₃ perovskite solar cell interfaces. *The journal of physical chemistry letters*, 5(4), 648-653.
- [6] Ke, W., Fang, G., Wang, J., Qin, P., Tao, H., Lei, H., ... & Zhao, X. (2014). Perovskite solar cell with an efficient TiO₂ compact film. *ACS applied materials & interfaces*, 6(18), 15959-15965.
- [7] Han, G. S., Song, Y. H., Jin, Y. U., Lee, J. W., Park, N. G., Kang, B. K., ... & Jung, H. S. (2015). Reduced graphene oxide/mesoporous TiO₂ nanocomposite based perovskite solar cells. *ACS applied materials & interfaces*, 7(42), 23521-23526.
- [8] Yamakata A, Vequizo JJM (2019) Curious behaviors of photogenerated electrons and holes at the defects on anatase, rutile, and brookite TiO₂ powders: a review. *J Photochem Photobiol C Photochem Rev* 40:234–243
- [9] T. Ohno, D. Haga, K. Fujihara, K. Kaizaki, M. Matsumura, (1997) Unique Effects of Iron(III) Ions on Photocatalytic and Photoelectrochemical Properties of Titanium Dioxide, *J. Phys. Chem. B* 101 6415-6419
- [10] R. Abe, K. Sayama, K. Domen, H. Arakawa, (2001) A New Type of Water Splitting System Composed of Two Different TiO₂ Photocatalysts (Anatase, Rutile) and a IO₃⁻/I⁻ Shuttle Redox Mediator, *Chem.Phys. Lett.* 344 339-344
- [11] K. Maeda, (2013) Direct splitting of pure water into hydrogen and oxygen using rutile titania powder as a photocatalyst, *Chem. Commun.* 49 8404-8406

- [12] B. Ohtani, J. Handa, S. Nishimoto, T. Kagiya, (1985) .Highly-Active Semiconductor Photocatalyst - Extra-Fine Crystallite of Brookite TiO₂ for Redox Reaction in Aqueous Propan-2-ol and or Silver Sulfate-Solution, Chem. Phys. Lett. 120 292-294
- [13] T. Ohno, T. Higo, H. Saito, S. Yuajn, Z. Jin, Y. Yang, T. Tsubota (2015), Dependence of Photocatalytic Activity on Aspect Ratio of a Brookite TiO₂ Nanorod and Dastic Improvement in Visible Light Responsibility of a Brookite TiO₂ Nanorod by Site-Selective Modification of Fe³⁺ on Exposed Faces, J. Mol. Catal. A: Chem. 396 261-267.
- [14] Ohno, T., Sarukawa, K., & Matsumura, M. (2002). Crystal faces of rutile and anatase TiO₂ particles and their roles in photocatalytic reactions. New journal of chemistry, 26(9), 1167-1170.
- [15] Bae, E., Murakami, N., & Ohno, T. (2009). Exposed crystal surface-controlled TiO₂ nanorods having rutile phase from TiCl₃ under hydrothermal conditions. Journal of Molecular Catalysis A: Chemical, 300(1-2), 72-79.
- [16] Murakami, N., Kurihara, Y., Tsubota, T., & Ohno, T. (2009). Shape-controlled anatase titanium (IV) oxide particles prepared by hydrothermal treatment of peroxy titanate in the presence of polyvinyl alcohol. The Journal of Physical Chemistry C, 113(8), 3062-3069.
- [17] Fujishima A, Honda K (1972) Electrochemical photolysis of water at a semiconductor electrode. Nature 238(5358):37–38
- [18] Hu Z, Li KN, Wu XF et al (2019) Dramatic promotion of visible light photoreactivity of TiO₂ hollow microspheres towards NO oxidation by introduction of oxygen vacancy. Appl Catal B Environ 256:117860
- [19] Lang Z, Lang XJ (2018) Visible light photocatalysis of dye-sensitized TiO₂: the selective aerobic oxidation of amines to imines. Appl Catal B Environ 224:404–409 15.
- [20] Lang XJ, Zhao JC, Chen XD (2016) Visible-light-induced photoredox catalysis of dye-sensitized titanium dioxide: selective aerobic oxidation of organic sulfides. Angew Chem Int Ed 55(15):4697–4700 16.
- [21] Dahlman C, Agrawal A, Staller CM et al (2019) Anisotropic origins of localized surface plasmon resonance in n-type anatase TiO₂ nanocrystals. Chem Mater 31(2):502–511 17. Gao YY, Nie W, Zhu QH et al (2020) The polarization effect in surface-plasmon-induced photocatalysis on Au/TiO₂ nanoparticles. Angew Chem Int Ed 59(41):18218–18223 18.
- [22] George S, Pokhrel S, Ji ZX et al (2011) Role of Fe doping in tuning the band gap of TiO₂ for the photo-oxidation-induced cytotoxicity paradigm. J Am Chem Soc 133(29):11270–11278 19.

- [23] Biswas A, Chakraborty A, Jana NR (2018) Nitrogen and fluorine codoped, colloidal TiO₂ nanoparticle: tunable doping, large red shifted band edge, visible light induced photocatalysis, and cell death. *ACS Appl Mater Interfaces* 10(2):1976–1986
- [24] Kapilashrami MY, Liu YS et al (2014) Probing the optical property and electronic structure of TiO₂ nanomaterials for renewable energy applications. *Chem Rev* 114(19):9662–9707
- [25] Sadanandam G, Lalitha K, Kumari VD et al (2013) Cobalt doped TiO₂: a stable and efficient photocatalyst for continuous hydrogen production from glycerol: water mixtures under solar light irradiation. *Int J Hydrog Energy* 38(23):9655–9664
- [26] Pérez-Larios A, Hernández-Gordillo A, Morales-Mendoza G et al (2016) Enhancing the H₂ evolution from water-methanol solution using Mn²⁺–Mn³⁺–Mn⁴⁺ redox species of Mn-doped TiO₂ sol-gel photocatalysts. *Catal Today* 266:9–16
- [27] Huang CY, Guo RT, Pan WG et al (2018) Eu-doped TiO₂ nanoparticles with enhanced activity for CO₂ photocatalytic reduction. *J CO₂ Util* 26:487–495
- [28] Kočí K, Troppová I, Reli M et al (2018) Nd/TiO₂ anatase-brookite photocatalysts for photocatalytic decomposition of methanol. *Front Chem* 6:44
- [29] Singh K, Harish S, Kristy AP et al (2018) Erbium doped TiO₂ interconnected mesoporous spheres as an efficient visible light catalyst for photocatalytic applications. *Appl Surf Sci* 449:755–763
- [30] Ribao P, Corredor J, Rivero MJ et al (2019) Role of reactive oxygen species on the activity of noble metal-doped TiO₂ photocatalysts. *J Hazard Mater* 372:45–5
- [31] Ida S, Sato K, Nagata T et al (2018) A cocatalyst that stabilizes a hydride intermediate during photocatalytic hydrogen evolution over a rhodium-doped TiO₂ nanosheet. *Angew Chem Int Ed Engl* 57(29):9073–9077
- [32] Wang WK, Chen JJ, Gao M et al (2016) Photocatalytic degradation of atrazine by boron-doped TiO₂ with a tunable rutile/ anatase ratio. *Appl Catal B Environ* 195:69–76 38.
- [33] Shao J, Sheng WC, Wang MS et al (2017) In situ synthesis of carbon-doped TiO₂ single-crystal nanorods with a remarkably photocatalytic efficiency. *Appl Catal B Environ* 209:311–319 39.
- [34] Jia GR, Wang Y, Cui XQ et al (2018) Highly carbon-doped TiO₂ derived from MXene boosting the photocatalytic hydrogen evolution. *ACS Sustain Chem Eng* 6(10):13480–13486
- [35] Boningari T, Inturi SNR, Suidan M et al (2018) Novel one-step synthesis of nitrogen-doped TiO₂ by flame aerosol technique for visible-light photocatalysis: effect of synthesis parameters and secondary nitrogen (N) source. *Chem Eng J* 350:324–334

- [36] Calisir, M.D.; Gungor, M.; Demir, A.; Kilic, A.; Khan, M.M. Nitrogen-doped TiO₂ Fibers for Visible-Light-Induced Photocatalytic Activities. *Ceram. Int.* **2020**, *46*, 16743–16753
- [37] Gao QZ, Si FY, Zhang SS et al (2019) Hydrogenated F-doped TiO₂ for photocatalytic hydrogen evolution and pollutant degradation. *Int J Hydrog Energy* 44(16):8011–8019 43.
- [38] Xie RJ, Lei DX, Zhan YJ et al (2020) Efficient photocatalytic oxidation of gaseous toluene over F-doped TiO₂ in a wet scrubbing process. *Chem Eng J* 386:121025
- [39] Yuan W, Cheng L, An Y et al (2018) Laminated hybrid junction of sulfur-doped TiO₂ and a carbon substrate derived from Ti₃C₂ MXenes: toward highly visible light-driven photocatalytic hydrogen evolution. *Adv Sci (Weinh)* 5(6):1700870 46.
- [40] Xu H, Zheng Z, Zhang L et al (2008) Hierarchical chlorine-doped rutile TiO₂ spherical clusters of nanorods: large-scale synthesis and high photocatalytic activity. *J Solid State Chem* 181(9):2516–2522 47.
- [41] Wang XK, Wang C, Jiang WQ et al (2012) Sonochemical synthesis and characterization of Cl-doped TiO₂ and its application. *Chemical Engineering Journal* 189–190:288–294.
- [42] Lin HY, Shih CY (2016) Efficient one-pot microwave-assisted hydrothermal synthesis of M (M = Cr, Ni, Cu, Nb) and nitrogen co-doped TiO₂ for hydrogen production by photocatalytic water splitting. *J Mol Catal A Chem* 411:128–137 49.
- [43] Kim TH, Rodríguez-González V, Gyawali G et al (2013) Synthesis of solar light responsive Fe, N co-doped TiO₂ photocatalyst by sonochemical method. *Catal Today* 212:75–80 51.
- [44] Shaban M, Ahmed AM, Shehata N et al (2019) Ni-doped and Ni/ Cr co-doped TiO₂ nanotubes for enhancement of photocatalytic degradation of methylene blue. *J Colloid Interface Sci* 555:31–41
- [45] Li YX, Ma GF, Peng SQ et al (2008) Boron and nitrogen codoped titania with enhanced visible-light photocatalytic activity for hydrogen evolution. *Appl Surf Sci* 254(21):6831–6836 53.
- [46] Khalilian H, Behpour M, Atouf V et al (2015) Immobilization of S, N-codoped TiO₂ nanoparticles on glass beads for photocatalytic degradation of methyl orange by fixed bed photoreactor under visible and sunlight irradiation. *Sol Energy* 112:239–245 54.
- [47] Divya Lakshmi KV, Siva Rao T, Swathi Padmaja J et al (2019) Structure, photocatalytic and antibacterial activity study of Meso porous Ni and S co-doped TiO₂ nano material under visible light irradiation.
- [48] Jibao Lu, Hao Jin, Ying Dai, Kesong Yang, Baibiao Huang, (2012) .Effect of Electronegativity and Charge Balance on the Visible-Light-Responsive Photocatalytic Activity of Nonmetal

Doped Anatase TiO₂, International Journal of Photoenergy, vol. 2012, Article ID 928503, 8 pages

- [49] Wong, M. S., Chou, H. P., & Yang, T. S. (2006). Reactively sputtered N-doped titanium oxide films as visible-light photocatalyst. *Thin Solid Films*, 494(1-2), 244-249.
- [50] Okato, T., Sakano, T., & Obara, M. (2005). Suppression of photocatalytic efficiency in highly N-doped anatase films. *Physical Review B*, 72(11), 115124.
- [51] Lee, J. Y., Park, J., & Cho, J. H. (2005). Electronic properties of N-and C-doped TiO₂. *Applied Physics Letters*, 87(1), 011904.
- [52] Batzill, M., Morales, E. H., & Diebold, U. (2006). Influence of nitrogen doping on the defect formation and surface properties of TiO₂ rutile and anatase. *Physical review letters*, 96(2), 026103.
- [53] Diwald, O., Thompson, T. L., Zubkov, T., Goralski, E. G., Walck, S. D., & Yates, J. T. (2004). Photochemical activity of nitrogen-doped rutile TiO₂ (110) in visible light. *The journal of physical chemistry B*, 108(19), 6004-6008.
- [54] Di Valentin, C., Pacchioni, G., & Selloni, A. (2004). Origin of the different photoactivity of N-doped anatase and rutile TiO₂. *Physical review B*, 70(8), 085116.
- [55] Asahi, R., Taga, Y., Mannstadt, W., & Freeman, A. J. (2000). Electronic and optical properties of anatase TiO₂. *Physical Review B*, 61(11), 7459.
- [56] Chambers, S. A., Cheung, S. H., Shutthanandan, V., Thevuthasan, S., Bowman, M. K., & Joly, A. G. (2007). Properties of structurally excellent N-doped TiO₂ rutile. *Chemical Physics*, 339(1-3), 27-35.
- [57] Cheung, S. H., Nachimuthu, P., Joly, A. G., Engelhard, M. H., Bowman, M. K., & Chambers, S. A. (2007). N incorporation and electronic structure in N-doped TiO₂ (1 1 0) rutile. *Surface Science*, 601(7), 1754-1762.
- [58] Ohsawa, T., Lyubinetsky, I., Du, Y., Henderson, M. A., Shutthanandan, V., & Chambers, S. A. (2009). Crystallographic dependence of visible-light photoactivity in epitaxial TiO_{2-x}N_x anatase and rutile. *Physical Review B*, 79(8), 085401.
- [59] Rioult, M.; Magnan, H.; Stanescu, D.; Barbier, A. (2014) Single Crystalline Hematite Films for Solar Water Splitting: Ti-Doping and Thickness Effects. *J. Phys. Chem. C* 118, 3007–3014.
- [60] Artiglia, L.; Zana, A.; Rizzi, G. A.; Agnoli, S.; Bondino, F.; Magnano, E.; Cavaliere, E.; Gavioli, L.; Granozzi, G. (2012) Water Adsorption on Different TiO₂ Polymorphs Grown as Ultrathin Films on Pt(111). *J. Phys. Chem. C*, 116, 12532–12540.

- [61] Barcaro, G.; Cavaliere, E.; Artiglia, L.; Sementa, L.; Gavioli, L.; Granozzi, G.; Fortunelli, (2012). A. Building Principles and Structural Motifs in TiO_x Ultrathin Films on a (111) Substrate. *J. Phys. Chem. C*, 116, 13302–133.
- [62] Zhang, Y.; Giordano, L.; Pacchioni, G.; Vittadini, A.; Sedona, F.; Finetti, P.; Granozzi, G. (2007) . The Structure of a Stoichiometric TiO₂ Nanophase on Pt(111). *Surf. Sci.* 601, 3488–3496.
- [63] Farstad, M. H.; Ragazzon, D.; Grönbeck, H.; Strømsheim, M. D.; C. Stavrakas, C.; Gustafson, J.; Sandell, A.; Borg, A. (2016). TiO_x Thin Films Grown on Pd(100) and Pd(111) by Chemical Vapor Deposition. *Surf. Sci.* 649, 80–89
- [64] Atrei, A.; Cortigiani, B.; Ferrari, A. M. (2012). Epitaxial Growth of TiO₂ Films with the Rutile (110) Structure on Ag(100). *J. Phys.: Condens. Matter* 24, No. 445005.
- [65] A. Fernandez, A. Caballero and A. R. Gonzalez-Elipe, (1992) Size and support effects in the photoelectron spectra of small TiO₂ particles, *Surface and interface analysis*, 18 392- 396
- [66] M. Guemaz, A. Mosser and J.-C. Parlebas, (2000) Electronic changes induced by vacancies on spectral and elastic properties of titanium carbides and nitrides, *Journal of electron spectroscopy and related phenomena*, 107 91-101.
- [67] F.-H. Lu and H.-Y. Chen, (2000) Characterization of titanium nitrides films deposited by cathodic arc plasma technique on copper substrates, *Surface and coatings technology*, 130 290-296
- [68] J. Zhao, E. G. Garza, K. Lam and C. M. Jones, (2000) Comparison study of physical vapor-deposited and chemical vapor-deposited titanium nitride thin films using x-ray photoelectron spectroscopy, *Applied surface science*, 158 246-251
- [69] I. Vaquila, M. C. G. P. Jr and J. Ferron, (1997) Oxidation process in titanium thin films, *Physical review B*, 55 (20) 13925-13931
- [70] I. Milosev, H. H. Strehblow, B. Navinsek and M. Metikos-Hukovic, (1995) Electrochemical and thermal oxidation of TiN coatings studied by XPS, *Surface and interface analysis*, 23 529-539.
- [71] Palgrave, R. G., Payne, D. J., & Egdell, R. G. (2009). Nitrogen diffusion in doped TiO₂ (110) single crystals: a combined XPS and SIMS study. *Journal of Materials Chemistry*, 19(44), 8418-8425.
- [72] Fujishima, Akira, Xintong Zhang, and Donald A. Tryk. (2008). TiO₂ photocatalysis and related surface phenomena. *Surface science reports* 63.12: 515-582.
- [73] Okato, T., Sakano, T., & Obara, M. (2005). Suppression of photocatalytic efficiency in highly N-doped anatase films. *Physical Review B*, 72(11), 115124.

- [74] Wang, J., Tafen, D. N., Lewis, J. P., Hong, Z., Manivannan, A., Zhi, M., ... & Wu, N. (2009). Origin of photocatalytic activity of nitrogen-doped TiO₂ nanobelts. *Journal of the American Chemical Society*, 131(34), 12290-12297.
- [75] Chen, H., Nambu, A., Wen, W., Graciani, J., Zhong, Z., Hanson, J. C., ... & Rodriguez, J. A. (2007). Reaction of NH₃ with titania: N-doping of the oxide and TiN formation. *The Journal of Physical Chemistry C*, 111(3), 1366-1372.
- [76] Esaka, F. F. K. S. H., Furuya, K., Shimada, H., Imamura, M., Matsubayashi, N., Sato, H., ... & Kikuchi, T. (1997). Comparison of surface oxidation of titanium nitride and chromium nitride films studied by x-ray absorption and photoelectron spectroscopy. *Journal of Vacuum Science & Technology A: Vacuum, Surfaces, and Films*, 15(5), 2521-2528.
- [77] Moulder, J. F., Stickle, W. F., Sobol, P. E. and Bomben, K. D. (1992). *Handbook of X-ray photoelectron Spectroscopy*; Eden Prairie
- [78] Ceotto, M., Lo Presti, L., Cappelletti, G., Meroni, D., Spadavecchia, F., Zecca, R., ... & Ardizzone, S. (2012). About the nitrogen location in nanocrystalline N-doped TiO₂: combined DFT and EXAFS approach. *The Journal of Physical Chemistry C*, 116(2), 1764-1771.
- [79] Belver, C., Bellod, R., Stewart, S. J., Requejo, F. G., & Fernández-García, M. (2006). Nitrogen-containing TiO₂ photocatalysts: Part 2. Photocatalytic behavior under sunlight excitation. *Applied Catalysis B: Environmental*, 65(3-4), 309-314.
- [80] Magnan, H., Stanescu, D., Rioult, M., Fonda, E., & Barbier, A. (2012). Enhanced photoanode properties of epitaxial Ti doped α -Fe₂O₃ (0001) thin films. *Applied Physics Letters*, 101(13).
- [81] Leitzke, F. P., Fonseca, R. O. C., Göttlicher, J., Steininger, R., Jahn, S., Prescher, C., & Lagos, M. (2018). Ti K-edge XANES study on the coordination number and oxidation state of Titanium in pyroxene, olivine, armalcolite, ilmenite, and silicate glass during mare basalt petrogenesis. *Contributions to Mineralogy and Petrology*, 173, 1-17.
- [82] Anderson, P. J., Horlock, R. F., & Oliver, J. F. (1965). Interaction of water with the magnesium oxide surface. *Transactions of the Faraday Society*, 61, 2754-2762.
- [83] Aschaffenburg, D. J., Kawasaki, S., Pemmaraju, C. D., & Cuk, T. (2020). Accuracy in resolving the first hydration layer on a transition-metal oxide surface: Experiment (AP-XPS) and theory. *The Journal of Physical Chemistry C*, 124(39), 21407-21417.
- [84] Předota, M., Bandura, A. V., Cummings, P. T., Kubicki, J. D., Wesolowski, D. J., Chialvo, A. A., & Machesky, M. L. (2004). Electric double layer at the rutile (110) surface. 1. Structure of surfaces and interfacial water from molecular dynamics by use of ab initio potentials. *The Journal of Physical Chemistry B*, 108(32), 12049-12060.

- [85] Zhang, Z., Fenter, P., Cheng, L., Sturchio, N. C., Bedzyk, M. J., Předota, M., ... & Wesolowski, D. J. (2004). Ion adsorption at the rutile– water interface: Linking molecular and macroscopic properties. *Langmuir*, 20(12), 4954-4969.

General conclusion and perspectives:

In the realm of solar energy-driven alternative fuel production, photoelectrochemical (PEC) technology emerges as a sustainable solution leveraging solar energy to generate clean energy vector: hydrogen. Nonetheless, oxide-based photoanodes, particularly TiO_2 and BaTiO_3 , face limitations such as limited solar photon absorption and poor charge separation, which impede their conversion efficiency.

To address these challenges, this thesis proposed the use of oxynitrides for solar water splitting, which theoretically exhibit stronger sensitivity to visible light and suitable band edge positions for water redox reactions. However, the practical application of oxynitrides has been hindered by poor photochemical activity attributed to high defect concentrations.

Herein, a novel approach consists in preparing epitaxial thin films of oxynitrides under ultra-high vacuum conditions by molecular beam epitaxy assisted by both oxygen and nitrogen plasma sources. This method allows the independent study of individual parameters, unlike chemical methods that may introduce multiple factors affecting the crystalline and electronic structure. On model samples, we explored the influence of nitrogen doping along with the calibration of a hybrid nitrogen ECR plasma source. The calibration process involved establishing a relationship between the nature of the species contained in the flow (atoms/ions), the flow rate and the level of N incorporation in the films. This critical step ensured reliable and reproducible experimental results

In a first attempt to elaborate oxynitrides epitaxial films, films were deposited on an oxide substrate using only a nitrogen atomic plasma source, resulting in $\text{TiO}_x\text{N}_{x-1-x}$ epitaxial films with a narrower band gap (3.31 eV) as compared to TiN (3.4 eV). We were also able to improve visible light absorption of BaTiO_3 even with modest N doping levels (~3.8% with respect to Ti) and improved the PEC photocurrent to up to 63% with respect to undoped BaTiO_3 .

In spite of the deposition technique, oxygen was always detected in the deposits. This is attributed to titanium and barium strong affinity to oxygen. There are two primary sources contributing to the presence of oxygen in the film. Firstly, oxygen diffuses into the film from the SrTiO_3 substrate through a self-diffusion process. Secondly, when the film is exposed to air, oxidation can occur on its surface. The oxidation of the surface is observed only for the $\text{TiO}_x\text{N}_{x-1-x}$ film, the N doped BaTiO_3 one remaining stable in air. However, for the $\text{TiO}_x\text{N}_{x-1-x}$ film, the quantity of oxygen in the film is influenced by its thickness, and it remains uncertain whether the distribution of oxygen is uniform across the entire film.

Subsequently, this method of deposition limits the number of nitrogen atoms that can be

introduced in the crystal structure. Therefore, we demonstrated that the co-doping of BaTiO₃ with tantalum allows to overcome the limitations of nitrogen incorporation even though the modification leads to poor crystallinity.

In chapter 4, we found that among the various N doped TiO₂ phases, the rutile phase is the most favorable phase for photoanodes. The photocurrent increased by a factor of two after the introduction of nitrogen and oxygen vacancies. This incorporation of N atoms is accompanied by the creation of oxygen vacancies and conversely to Ti³⁺ species. When the concentration of Ti³⁺ becomes too large, the film undergoes a crystallographic structure modification (distortion of the oxygen octahedron) and adopts a corundum structure, as it was seen by RHEED and EXAFS.

Investigating films deposited on a non-oxide substrate of Pt(111) using both atomic oxygen and hybrid nitrogen plasma sources made possible the study of the effects of the N-doping level independently with the Ti³⁺ content. We evidenced that the paramount parameter for understanding the crystallographic structure and properties is the content of Ti³⁺. The amount of nitrogen doping has a lesser effect in comparison. Among the different films studied, the film with 9% Ti³⁺ content (and N/Ti ratio of 2.38 at.%) exhibited the best performance for photoelectrolysis. In this film, the width of the depletion zone extended to up to 40% of the film's total thickness. This wider depletion zone allowed for effective charge separation and photoelectrochemical efficiency. For higher Ti³⁺ content, the width of the depletion zone increased up to 60% of the film thickness. Although, this increase in oxygen vacancies, act as detrimental recombination centers, ultimately reducing the photocurrent generated by the photoanode.

Surface reoxidation by oxygen plasma treatment alters also the photocurrent without affecting volume properties. Pure TiO₂ rutile demonstrated excellent resistance to plasma oxidation process. Further investigation aiming to create a stable and water-resistant N doped structure is desirable.

Doping is an influential parameter for tailoring the electrical properties and crystallographic structure of N doped BaTiO₃ and TiO₂. Since the amount of nitrogen incorporated in the lattices remains low, we tried other methods to elaborate oxynitrides. Such as annealing TiN films under air or forming heterojunction with double layers of, for example, both TiO₂ and TiN. However, these methods produced heterogeneous films with an overall TiO_xN_y composition hard to characterize.

This study focused on the use of Nb:SrTiO₃ and Pt (111) substrates, another path would be to

use different substrates and different substrate orientations to provide insights about the influence of the crystallographic structure and orientation of oxynitrides in PEC applications.

Another avenue of investigation is the use of the influence of ferroelectricity on charge carrier dynamics and structure-performance relationships in solar energy conversion. The LNO (Laboratoire Nano-Magnétisme et Oxydes) team has previously published research indicating that downward polarization in BaTiO₃ is beneficial for photoelectrolysis applications. However, the specific influence of charge compensation and nitrogen content on the photoelectrochemical properties of BaTiO₃ remains unknown.

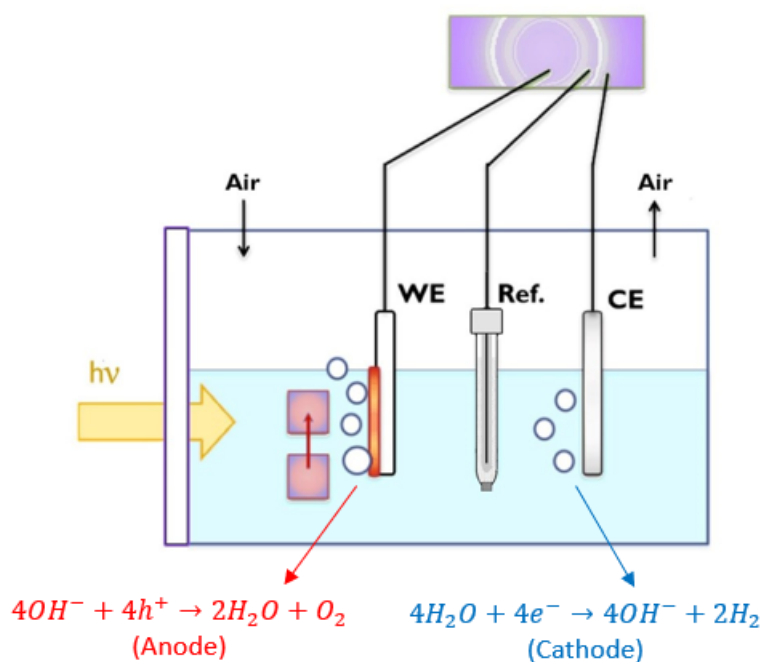
Finally, to further enhance the nitrogen content in epitaxial oxynitrides, co-doping could be a promising approach. However, achieving the desired N content in epitaxial oxynitrides through co-doping will require additional experimental work to identify the appropriate growth conditions.

Résumé étendu en français :

L'épuisement des réserves de combustibles fossiles et la pollution de l'environnement que leur combustion provoque ont incité à une course aux ressources alternatives d'énergie verte et renouvelable. Le fractionnement photoélectrochimique de l'eau à l'aide de semi-conducteurs est une solution prometteuse. Ce processus exploite l'énergie solaire abondante pour fractionner les molécules d'eau et générer de l'hydrogène comme vecteur d'énergie propre, exempt de émissions de dioxyde de carbone lors de son utilisation.

Pour utiliser l'énergie solaire dans la production d'hydrogène par photoélectrolyse, nous utilisons dans cette étude une cellule photoélectrochimique (PEC) comprenant généralement trois électrodes : une électrode photoactive de travail (WE) (photoanode ou photocathode, parfois les deux) composé d'un semi-conducteur qui absorbe l'énergie solaire pour générer des porteurs de charge photoexcités. Ces porteurs de charge peuvent ensuite se transférer vers l'électrolyte aqueux (NaOH dans notre cas) pour entraîner des réactions chimiques, telles que l'oxydation ou la réduction de l'eau, une contre-électrode (CE) (un matériau métallique, par exemple), et une électrode de référence (RE) pour observer les demi-réactions dans la cellule. En général, le réacteur de la cellule est soit transparent à la lumière, soit comprend une fenêtre optique permettant à l'irradiation d'atteindre la photoélectrode, dans ce cas, une fenêtre en quartz perméable à la lumière visible.

Le schéma suivant illustre le principe de base d'une cellule PEC :



Légende:











-  Matériaux photoactifs
-  Photoexcitation
-  Structure de bande du semi-conducteur
-  Solvant avec l'électrolyte
-  Fenêtre en quartz
-  Potentiostat
-  Contre électrode (CE)
-  Substrat conducteur pour l'électrode de travail (WE)
-  Gaz émis
-  Electrode de référence (Ref.)

Figure : Représentation schématique du principe de fonctionnement des cellules photoélectrochimiques basées sur une cellule photosynthétique générant de l'hydrogène par le fractionnement des molécules d'eau sous l'effet des photons.

Dans la quête d'une séparation efficace de l'eau, les films minces à base d'oxyde ont attiré l'attention en tant que photoanodes. Nombre de ces films offrent des avantages tels que l'abondance, la non-toxicité et le faible coût. Cependant, leurs performances sont encore limitées en raison de divers facteurs.

Pour surmonter ces limitations, des progrès significatifs dans les performances des matériaux photoactifs sont nécessaires. Les oxydes conventionnels sont confrontés à des défis tels qu'une absorption limitée des photons solaires et une mauvaise séparation des charges, qui entravent leur efficacité de conversion. Des recherches récentes ont mis en évidence certains nitrures en tant que semi-conducteurs à faible gap avec d'excellentes propriétés d'absorption et d'émission dans le spectre visible. Cependant, ces nitrures sont très sensibles à la corrosion en milieu aqueux. Pour surmonter ces limitations, l'utilisation d'oxynitrures dans le fractionnement photoélectrochimique de l'eau est apparue comme une approche prometteuse. Ces dernières années, les chercheurs se sont tournés vers les oxynitrures à structure pérovskite, en particulier des composés comme $AMO_{3-x}N_x$ ($A = La, Ca, Sr, Ba$; $M = Ti, Nb$ et Ta), comme photoélectrodes potentielles pour la photoélectrolyse de l'eau. Ces oxynitrures présentent une forte sensibilité à la lumière visible et possèdent des positions de bord de bande de conduction/valence adéquates par rapport aux niveaux de redox de l'eau. Cependant, expérimentalement, malgré leurs propriétés favorables, ces composés présentent souvent de mauvaises activités photochimiques. Cela peut être attribué à des concentrations élevées de défauts et à des conditions de surface inappropriées pour les réactions de l'eau, qui restent des défis importants dans ce domaine.

La production d'oxynitrures sous forme de films minces épitaxiés apparaît ainsi, comme une méthode prometteuse pour diminuer ces défauts. Dès lors que les méthodes traditionnelles de chimie à l'état solide impliquent la nitruration à haute température de poudres d'oxydes, ce qui donne des poudres oxynitrures difficiles à traiter. La nitruration est thermodynamiquement moins favorable par rapport à l'oxydation. Dans cette thèse, les films minces épitaxiés sont préparés en utilisant l'épitaxie par jets moléculaire et un plasma hybride d'azote atomique/ionique pour fournir l'azote nécessaire à la croissance des films épitaxiés dopés en N. Plus précisément, durant cette étude, nous étudions l'influence du dopage en N sur la structure cristalline, la structure électronique et les propriétés de photoanode pour la photoélectrolyse de l'eau.

Tout d'abord, les premiers films ont été déposés sur un substrat oxyde en utilisant un plasma atomique d'azote seul. Dans ces films, l'oxygène provient alors du substrat et nous avons fabriqué des films épitaxiés de TiO_xN_y et de BaTiO_3 dopés N (3.8 %). Une étude comparative avec des films non dopés de BaTiO_3 d'une épaisseur identique fabriqués à l'aide d'un plasma d'oxygène atomique montre que le dopage en N dans N : BaTiO_3 est auto-limitant en raison de l'incorporation de lacunes d'oxygène, assurant ainsi la neutralité de charge. Malgré, des niveaux de dopage faible, la structure électronique du matériau subit des modifications substantielles, améliorant l'absorption du spectre lumineux.

En s'appuyant sur les résultats de l'étude précédente, ce travail présente également des résultats préliminaires concernant le co-dopage de BaTiO_3 à l'aide d'atome de tantale (Ta) dans le but d'améliorer les performances photoélectrochimiques pour la photoélectrolyse de l'eau.

En introduisant du Ta dans le site B de N- BaTiO_3 ($\text{BaTa}_x\text{Ti}_{1-x}\text{O}_{3-x}\text{N}_x$) et même en l'absence de cristallinité, la présence de Ta dans la structure présente plusieurs effets positifs. Il réduit les centres Ti^{4+} en Ti^{3+} , crée des lacunes d'oxygène et permet un niveau de dopage en azote plus élevé.

La seconde partie, concerne ensuite, des films épitaxiés de TiO_2 dopé N, déposés sur du Pt(111) en utilisant à la fois un plasma d'oxygène atomique et un plasma d'azote. Nous avons montré qu'en changeant le taux d'ions d'azote et la température du substrat, on élabore des films minces de TiO_2 dopés N (~2.5%) de deux structures cristallographiques différentes : une structure quasi-rutile et une structure corindon. D'autre part, nous avons montré que le taux de Ti^{3+} influençait fortement les performances en photoélectrolyse. Le meilleur résultat est obtenu pour un film de structure quasi-rutile contenant 9 % de Ti^{3+} , avec un photocourant deux fois plus important que celui du TiO_2 rutile non dopé. La présence d'états $\text{Ti-}3d$, correspondant à la réduction de Ti^{4+} en Ti^{3+} , conduit à la formation d'états de défauts peu profonds qui peuvent piéger les trous bénéfiques pour les processus de photoélectrolyse, et permet une meilleure séparation de charge. Cependant, dès lors que la surface est réoxydée, par exemple, par un traitement au plasma d'oxygène, la surface adopte un comportement similaire à celle du TiO_2 entraînant ainsi un photocourant différent sans toutefois, modifier les propriétés de volume.

Pour relever les défis de l'obtention d'une structure de réseau plus stable pour les réactions d'oxydation de l'eau, des efforts supplémentaires de recherche et développement sont

nécessaires. Ces efforts impliquent un contrôle minutieux des conditions de croissance et une optimisation de la composition des films.

En résumé, en étudiant les composés d'oxydes dopés N en couches minces épitaxiées, nous visons à repousser les limites de la photoélectrolyse de l'eau et à rechercher des rendements de conversion plus élevés. Le développement de photoanodes oxynitrides efficaces et stables peut potentiellement révolutionner le domaine des énergies renouvelables. Ces composés, avec leurs propriétés électroniques et optiques uniques, offrent une voie pour surmonter les limites des oxydes traditionnels en termes de stabilité chimique et de performance. En exploitant les excellentes propriétés d'absorption de certains nitrures et en les combinant avec la stabilité et la résistance à la corrosion des oxydes, on vise à créer des matériaux capables d'exploiter efficacement l'énergie solaire pour le fractionnement des molécules l'eau.

Ainsi, l'objectif de cette thèse était d'examiner ces matériaux en étudiant un paramètre à la fois, ce qui la distingue des études traditionnelles en chimie du solide qui traitent de multiples paramètres simultanément.

بِسْمِ اللَّهِ الرَّحْمَنِ الرَّحِيمِ

كُتِبَ عَلَيْكُمُ الْقِتَالُ وَهُوَ كُرْهُ لَكُمْ وَعَسَى أَنْ تَكْرَهُوا شَيْئًا وَهُوَ خَيْرٌ لَكُمْ
وَعَسَى أَنْ تُحِبُّوا شَيْئًا وَهُوَ شَرٌّ لَكُمْ وَاللَّهُ يَعْلَمُ وَأَنْتُمْ لَا تَعْلَمُونَ
{سورة البقرة: ٢١٦}

Le combat vous a été prescrit alors qu'il vous est désagréable. Or, il se peut que vous ayez de l'aversion pour une chose alors qu'elle vous est un bien. Et il se peut que vous aimiez une chose alors qu'elle vous est mauvaise. C'est Allah qui sait, alors que vous ne savez pas

{Sourate Al-Baqara: 216}

صدق الله العظيم